Photoelectric amplification of variband photoresistors

V. G. Savitskiĭ and B. S. Sokolovskiĭ

I. Franko State University, 290602 L'vov, Ukraine
(Submitted December 6, 1995; accepted for publication January 26, 1996)
Fiz. Tekh. Poluprovdn. **31**, 3–5 (January 1997)

Characteristic features of the photoelectric amplification of variband photoresistors, whose energy gap increases linearly toward the contacts, are theoretically investigated. It is shown that such photoresistors are characterized by a nonmonotonic field-dependence of the photoelectric gain, whose maximum value increases with growth of the energy gap gradient and can substantially exceed the corresponding value for homogeneous samples. © *1997 American Institute of Physics.* [S1063-7826(97)00312-2]

One of the main factors limiting an enhancement of the sensitivity of bipolar photoresistors with small geometrical dimensions because of an increase in the bias voltage is the effect of expulsion (exclusion) of nonequilibrium charge carriers.[1–3] Under conditions in which the effect of expulsion of photocarriers is manifested, the effective lifetime of the latter τ_{eff} decreases as the voltage applied to the photoresistor is increased. This leads to saturation in strong electric fields of the photoelectric gain G, and in the case of a homogeneous n-type semiconductor the maximum value of the gain $G_0^{\max}=(1+b)/2$, where $b=\mu_n/\mu_p$ is the ratio of the electron and hole mobilities.[1] Therefore, a search for ways to eliminate, or at least reduce, the effect of photocarrier expulsion is an urgent task from the standpoint of the development of photoresistors. A number of ways have been proposed to increase the photoelectric gain of photoresistors, in particular, the creation along an ohmic contact of an abrupt isotypic homo- or heterojunction,[4–6] and layered-nonuniform doping of semiconductors.[7,8] In the present paper we give a theoretical proof of the possibility of increasing the photoelectric gain as a result of nonmonotonic coordinate variation in the width of the band gap E_g.

Let us consider a simple model of a variband photoresistor with n-type conductivity, in which $E_g(x)$ decreases linearly as one goes from the contacts ($x=\pm d$) toward the center of the photoresistor ($x=0$), where $E_g(-d)=E_g(d)$. The coordinate distribution of the concentration of excess holes Δp and electrons Δn ($\Delta n\approx\Delta p$), established in an illuminated photoresistor when an external electric field $\mathbf{E}$ (E_x,0,0) is applied to it, is described by the equations[9,10]

$$\frac{d^2\Delta p}{dx^2}-\frac{1}{kT}\left(eE_x\pm\left|\frac{dE_g}{dx}\right|\right)\frac{d\Delta p}{dx}-\frac{\Delta p}{L_p^2}=-\frac{\tau g}{L_p^2}, \qquad (1)$$

where the ''+'' and ''−'' signs pertain, respectively, to the regions $-d\leqslant x<0$ and $0<x\leqslant d$, L_p is the diffusion length of the holes, τ is the lifetime of the nonequilibrium charge carriers (τ, like L_p, is assumed to be independent of the coordinate), g is the photocarrier generation function, which for simplicity we assume to be constant over the sample, T is the temperature, e is the magnitude of the charge of the electron, and k is the Boltzmann constant. Equations (1), as written, assume that the photocarrier concentration is much lower than the equilibrium electron concentration.

It is necessary to augment Eqs. (1) by the boundary conditions

$$\Delta p(\pm d)=0, \qquad (2)$$

which correspond to ohmic contacts, and also by conditions of continuity of the photocarrier concentration and photocarrier fluxes at $x=0$, where dE_g/dx changes sign:

$$\Delta p(-0)=\Delta p(+0), \qquad (3)$$

$$\frac{d\Delta p}{dx}-\frac{1}{kT}\left(eE_x+\left|\frac{dE_g}{dx}\right|\right)\Delta p\Bigg|_{x=-0}=\frac{d\Delta p}{dx}-\frac{1}{kT}\left(eE_x-\left|\frac{dE_g}{dx}\right|\right)\Delta p\Bigg|_{x=+0}. \qquad (4)$$

Assigning the coordinate dependence of the photocarrier concentration from Eqs. (1)–(4), we calculate the photoelectric gain of a variband photoresistor (equal, by definition, to the number of electrons flowing through the outer circuit per absorbed photon):

$$G=\frac{(\mu_n+\mu_p)|E_x|}{4d^2g}\int_{-d}^{d}\Delta p(x)\,dx=\frac{2|\overline{E}|}{d^2}\,G_0^{\max}\left[\overline{d}+2\delta\left(1-\frac{f_1}{f_0}\right)-\frac{f_2}{2f_0}\right], \qquad (5)$$

where

$$\overline{d}=d/L_p,\quad \overline{E}=eE_xL_p/2kT,\quad \delta=L_p|\nabla E_g|2kT,$$

$$f_0=(\alpha_2-\alpha_1)(k_1'\alpha_1'-k_2'\alpha_2')-(\alpha_2'-\alpha_1')(k_1\alpha_1-k_2\alpha_2),$$

$$f_1=\alpha_1\alpha_2(\alpha_1'-\alpha_2')(k_1-k_2)-\alpha_1'\alpha_2'(\alpha_1-\alpha_2)(k_1'-k_2'),$$

$$f_2=(\alpha_2-\alpha_1')(\alpha_1-\alpha_2')(k_1'k_2+k_1k_2')+(\alpha_1-\alpha_1')(\alpha_2'-\alpha_2)\times(k_1k_1'+k_2k_2')-2(\alpha_1-\alpha_2)(\alpha_1'-\alpha_2'),$$

$$k_{1,2}=\overline{E}+\delta\pm\sqrt{(\overline{E}+\delta)^2+1},\quad k_{1,2}'=\overline{E}-\delta\pm\sqrt{(\overline{E}-\delta)^2+1},$$

$$\alpha_{1,2}=\exp(-k_{1,2}\overline{d}),\quad \alpha_{1,2}'=\exp(k_{1,2}'\overline{d}).$$

By virtue of the symmetry of the considered photoresistors, it is sufficient to analyze the properties of the photoelectric gain for one direction of the electric current; for con-

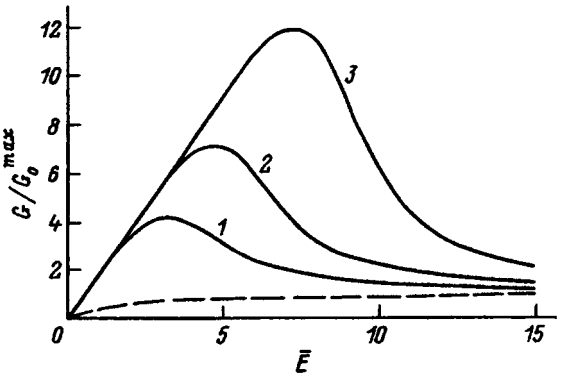

FIG. 1. Field dependence of the photoelectric gain of variband (solid lines) and homogeneous (dashed lines) photoresistors. Normalized length $\bar{d}=1$; for the parameter δ equal to 5 (*1*), 7 (*2*), and 10 (*3*).

creteness we assume that $\bar{E}>0$. It follows from Eq. (5) that for $E \ll \delta$ the photoelectric gain is proportional to the applied voltage, and for $\delta \gg 1$, d^{-1}

$$G=\frac{2\bar{E}}{d^2}\,G_0^{\max}[\bar{d}-4\delta^3\,\exp(-2\delta\bar{d})]. \tag{6}$$

In contrast to homogeneous photoresistors, in which the dependence $G(E)$ is linear only in weak electric fields[1] ($E \ll 1$), in variband photoresistors with large gradients of E_g ($\delta \gg 1$, d^{-1}) the linear segment of $G(E)$ is substantially longer; here, because the second term in Eq. (6) is small, the slope of the field dependence of the photoelectric gain is inversely proportional to d and essentially independent of δ.

For the case of strong electric fields $\bar{E} \gg \delta, \bar{d}^{-1}$, we can obtain the following expression for the photoelectric gain accurate to terms of the order of δ/E:

$$G=G_0^{\max}\left[1+\left(\frac{1}{2}-\frac{\bar{d}}{3\delta}\right)\frac{\delta}{E}\right]. \tag{7}$$

It follows from this expression that in strong electric fields $G(E)$ asymptotically approaches $G_0^{\max}$, decreasing with growth of E for $\delta > 2d/3$. This means that the field dependence of the photoelectric gain can have a nonmonotonic character with maximum value $G^{\max}$ in excess of the maximum value of the photoelectric gain of homogeneous photoresistors $G_0^{\max}$. Calculations based on Eq. (5) show that with growth of δ the coefficient $G^{\max}$ increases while the position of the maximum of $G(E)$ shifts toward higher fields (Figs. 1 and 2a).

The enhancement of the photosensitivity of the considered variband photoresistors in comparison with homogeneous photoresistors is due to the presence in the former of an internal quasi-electric field,[9] which pulls the photocarriers back toward the center of the variband structure, thereby blocking their diffusional and also their drift (in an external electric field) displacements toward the ohmic contacts. Diffusive movement of the photocarriers toward the contacts, which leads to a lower τ_{eff}, grows as the distance between the contacts decreases, especially for $d \lesssim 1$. Therefore, to ef-

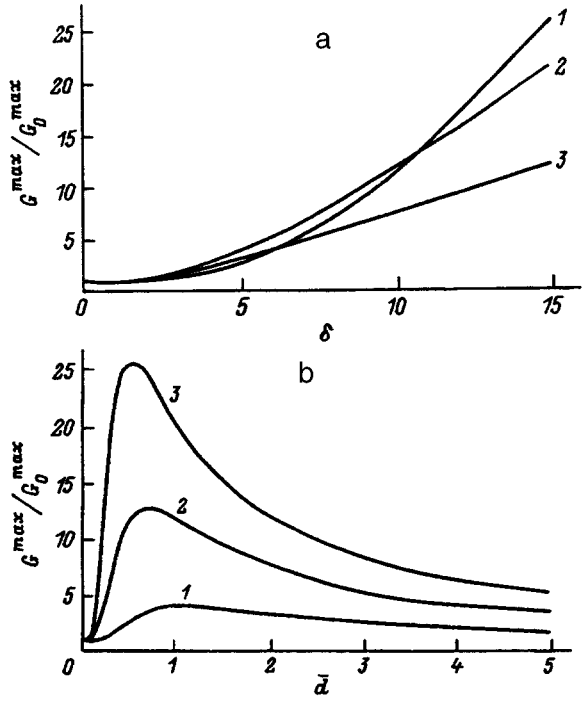

FIG. 2. Maximum value of the photoelectric gain of variband photoresistors plotted vs gradient of the width of the band gap (a) and vs the intercontact distance (b). The calculations were for a) d equal to 0.5 (*1*), 1 (*2*), and 2 (*3*), and b) δ equal to 5 (*1*), 10 (*2*), and 15 (*3*).

fectively counteract photocarrier diffusion, $|\nabla E_g|$ must be increased as d is decreased. Comparing the diffusion and drift times in a quasi-electric field for a given distance d, it is easy to show that in the case of thin samples with $d<1$ the varibandedness of the photoresistor has a marked effect on its photosensitivity (increasing it by a factor of 2 or more at low biases) if the condition $\delta > d^{-1}$ is satisfied. Note that this inequality, in combination with the inequality $\delta > 2d/3$, determines the region of values of $|\nabla E_g|$ for which $G^{\max} > G_0^{\max}$.

For a fixed value of $|\nabla E_g|$ the dependence $G^{\max}(\bar{d})$ is nonmonotonic (Fig. 2b). At first, growth of d leads to a growth of $G^{\max}$, due to an increase of τ_{eff} as a result of an increase in the characteristic time of diffusion–drift of the photocarriers toward the contacts. In the limit as τ_{eff} approaches the bulk lifetime τ, the dependence $G^{\text{eff}}(d) \sim \tau_{\text{eff}}(d)/\tau_E(d)$ is determined mainly by the transit time of the photocarriers in an external electric field $\tau_E = \tau d/E$; i.e., $G^{\max}$ decreases as d increases.

In conclusion, we will estimate the effect of varibandedness on the photoelectric gain of a photoresistor fabricated from epitaxial layers of CdHgTe with n-type conductivity. If we assume $T=77$ K and $d=L_p=17$ μm (Refs. 5 and 6), then for $E_g=0.1$ eV and $E_g(d)=0.3$ eV (which corresponds to $\delta=15$) the maximum value of the photoelectric gain that can be attained for $E_x=90$ V/cm is 20 times greater than for the case of homogeneous samples.

[1] R. L. Williams, Infrared Phys. **8**, 337 (1968).
[2] C. B. Burgett and R. L. Williams, Infrared Phys. **13**, 61 (1972).

[3] M. R. Johnson, J. Appl. Phys. **43**, 3090 (1972).
[4] T. Ashley and C. T. Elliott, Infrared Phys. **22**, 367 (1982).
[5] D. L. Smith, D. K. Arch, R. A. Wood, and M. Walter Scott, Appl. Phys. Lett. **45**, 83 (1983).
[6] D. K. Arch, R. A. Wood, J. Appl. Phys. **58**, 2360 (1985).
[7] O. G. Kondrat'eva, L. N. Neustroeva, V. V. Osipov, Fiz. Tekh. Poluprovodn. **22**, 2131 (1988) [Sov. Phys. Semicond. **22**, 1346 (1988)].
[8] O. G. Kondrat'eva, L. N. Neustroeva, V. V. Osipov, Fiz. Tekh. Poluprovodn. **23**, 536 (1989) [Sov. Phys. Semicond. **23**, 334 (1989)].
[9] O. V. Konstantinov, G. V. Tsarenkov, Fiz. Tekh. Poluprovodn. **10**, 720 (1976) [Sov. Phys. Semicond. **10**, 427 (1976)].
[10] V. G. Savitskiĭ and B. S. Sokolovskiĭ, Ukr. Zh. Fiz. **25**, 1919 (1980).

Translated by Paul F. Schippnick

Electrical and photoelectric properties of a Pd–p^0-Si–p-Si structure with a disordered intermediate p^0 layer

S. V. Slobodchikov, Kh. M. Salikhov, E. V. Russu, M. M. Meredov, and A. I. Yazlyeva

A. F. Ioffe Physicotechnical Institute, Russian Academy of Sciences, 194021 St. Petersburg, Russia
(Submitted January 31, 1996; accepted for publication February 5, 1996)
Fiz. Tekh. Poluprovodn. **31**, 15–18 (January 1997)

The electrical characteristics and the photovoltage on Pd–p^0-Si–p-Si diode structures with a disordered (porous) p^0 layer of Si have been measured. The current-transfer mechanism is assumed to be double injection of electrons and holes into the p^0 layer. In a hydrogen atmosphere, the photovoltage increases by a factor of 20 and the reverse current falls by a factor of 3–4. The increase of the photovoltage is associated with the growth of a Pd–p^0-Si Schottky barrier, while the decrease of the dark current is attributable to the variation in the amount of injected electrons. The relaxation of the photovoltage after turning off the H_2 flow has two time intervals, with lengths of about 130 and 420 sec. It is shown that these features of the relaxation are associated with heterogeneity of the structure of the p^0 layer, which includes unanodized sections and porous sections. These regions of the structure each contain their own set of deep traps and recombination centers. This set of traps and recombination centers can vary as a result of the introduction of hydrogen which creates induced ''temporary'' deep levels. © *1997 American Institute of Physics.* [S1063-7826(97)02112-6]

Many papers have recently been devoted to porous silicon and diode structures based on it, including the technology of obtaining them, studies of their microstructure, their physical and chemical properties, and especially the study of their photo- and electroluminescence. A review of a number of papers dealing with these topics, with corresponding citations, is given in Ref. 1. At the same time, it should be pointed out that data on the electrical and photoelectric characteristics of diode structures based on porous silicon are rather sparse and consist of short remarks or subsidiary fragments in papers on photo- or electroluminescence. The samples of porous silicon that are usually obtained by electrochemical etching with different variations essentially result in the creation of disordered layers on the substrate—a bulk Si crystal. The composition of these layers, their morphology, and their other properties depend on the etching regime and on the properties of the substrate.

In this paper we present some results of experimental studies of the electrical and photoelectric properties of Pd–p^0-Si–p-Si diode structures, with an intermediate disordered p^0 silicon layer, and their variation in a hydrogen atmosphere.

1. EXPERIMENTAL SAMPLES

The diode structures and disordered layers were based on p-Si with $\rho = 1\,\Omega\cdot$cm and orientation (100). Single crystals (the substrate) with a thickness of about 500 μm before electrochemical etching were cleaned chemically, rinsed, and dried. Ohmic contacts were created on the back side of the substrate by depositing a thin film of Al. Electrochemical etching was done in an HF solution with a current density of 25 mA/cm^2 and a duration of 5 min. Palladium was deposited on the resulting disordered layers, whose porosity was difficult to determine. This operation was carried out by deposition in a 10^{-5} Torr vacuum, and the palladium layer was about 400 Å thick.

The I-V characteristic, the voltage-capacitance characteristic, and the photocurrent of the test samples were measured, and the effect of the pulsed action of hydrogen on the dark current and the photovoltage was studied.

2. RESULTS OF THE MEASUREMENTS AND DISCUSSION

Figure 1 shows characteristic I-V curves of the test structures with forward (+ on the p-Si) and reverse bias. The forward current varies with voltage as $I \propto V^2$, and the reverse current varies as $I \propto V^{1.3}$. Based on the capacitance measurement, the computed thickness of the disordered layer was about 1 μm. It follows from the measured I-V characteristics that the Schottky-barrier contact does not play a decisive role in the mechanism for the current transport through the diode structure with forward bias and has a substantial effect with reverse polarity. The main contribution to the current-conduction mechanism with forward bias, in our opinion, comes from double injection of holes from the p region of the substrate and of electrons from the palladium contact into the disordered porous layer of p^0-Si. The dependence of the forward current on voltage found above is correct, provided that the hole and electron diffusion-displacement length $L_{n,p}$ is less than the thickness W of the p^0-Si layer. As a result, we find that $L_{n,p} < 1\,\mu$m. An approximate estimate of the averaged mobility at high injection levels, when the effect of the traps may be neglected, from the relation for the current density

$$J(\mathrm{A/cm^2}) = 10^{-13} V^2 \mu_p \varepsilon / W^3$$

with $V = 1$ V, $\varepsilon = 10$, and $W = 1\,\mu$m, gives a value of $\mu_p \simeq 0.6$ cm^2/(V·s), i.e., a very low value.

 1063-7826/97/010011-04$10.00

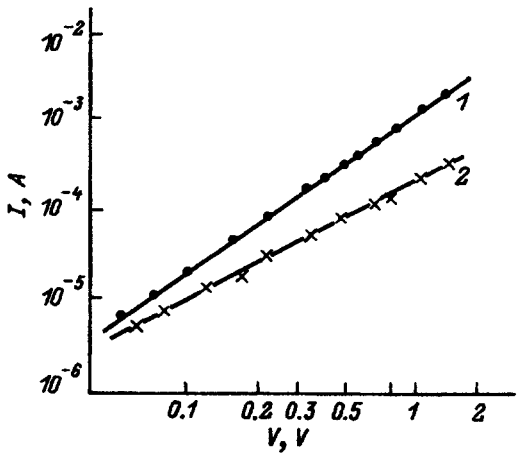

FIG. 1. The I-V characteristics of a Pd–p^0-Si–p-Si structure with a disordered p^0 layer: *1*—forward branch (+ on the p-Si), *2*—reverse branch.

The role of the palladium barrier contact is decisive when the photovoltage or the photocurrent (with no bias) is studied. In Ref. 2, we studied the electrical and photoelectric properties of Pd–SiO_2–$p(n)$-Si structures and their variation in a hydrogen atmosphere. We established that the photovoltage increases by almost two orders of magnitude in structures based on p-Si under the pulsed action of a H_2 flow. We associated this increase with an increase in the height of the Schottky barrier. A similar increase in the photovoltage was observed in the diode structures which we studied (Fig. 2), although it was smaller in magnitude: the photosignal increases by a factor of about 20. It is obvious that the cause of this increase is the same as in diodes with an ordered single-crystal substrate of p-Si. A difference is observed, however, in the relaxation mechanism of the photovoltage (or photocurrent) after the pulse of H_2 flow is switched off. In structures with a disordered (porous) layer, two sections are observed in the relaxation: The first (Fig. 2, section I) lies in the 50 to 180-s time interval, and approximately coincides with the relaxation time on Pd–SiO_2-p-Si structures,[2] whereas the second (section II) covers the 180 to 600-s interval. The minimum value of the photovoltage, V_{ph}^{min}, in the second interval is a factor of 5 lower than the starting value of V_{ph}^{st} (before the H_2 flow is started) and reaches the latter at the end of the observed time interval. It is characteristic that the total variation (decrease) of the forward dark current is 10–20%, with a relaxation time of about 180 s, while the reverse current decreases by a factor of 3–4, with a relaxation time of about 13 min (Fig. 3). We should point out that the increase of the photovoltage and the decrease of the dark current when the pulsed H_2 is started is virtually inertialess. We have already pointed out in Ref. 2 that the photoresponse relaxation time in the 50 to 180-s interval is associated with the effect of traps initiated by hydrogen diffusion. The presence of a disordered Si layer, which is mainly associated with the formation of voids, introduces additional centers that are deeper and with a greater concentration.

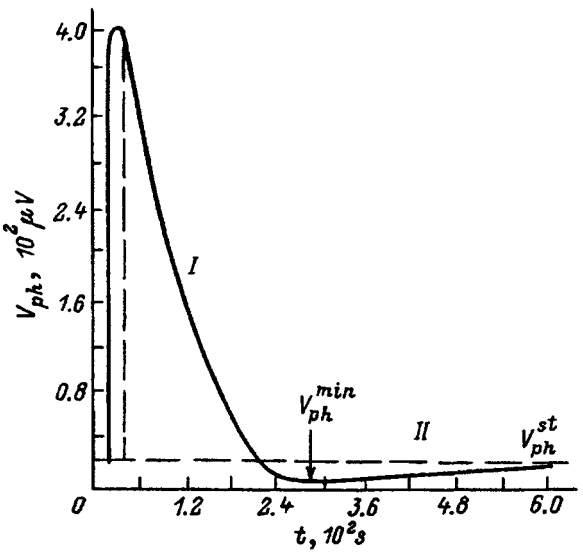

FIG. 2. Variation of the photovoltage of a Pd–p^0-Si–p-Si structure under the pulsed action of a hydrogen flow. I—relaxation region of the photovoltage after switching off the H_2 flow; II—relaxation region to the original value. Illumination with monochromatic light with $\lambda = 1.05\mu$m.

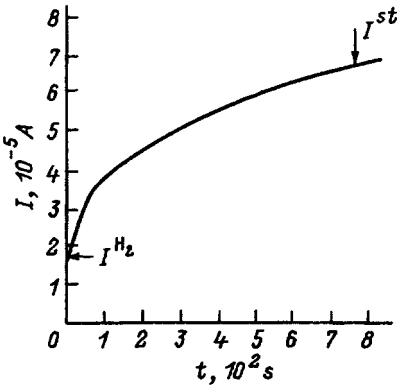

FIG. 3. Relaxation of the reverse current of a Pd–p^0-Si–p-Si structure after the H_2 flow is switched off ($I^{H_2} \rightarrow I^{st}$).

In our opinion, the common generation mechanism of the photovoltage and the photocurrent and their variation under the influence of hydrogen can be represented as follows: As can be seen from certain studies,[3,4] a disordered silicon layer can have a heterogeneous structure. Sugiyama and Nittono[4] detected acicular unanodized sections directed perpendicular to the surface layer, as well as a disorderly distribution of voids. The structure of the disordered porous layer includes, as is assumed in Ref. 5, a layer of large, longitudinal voids (about 0.5 μm in diameter) perpendicular to the surface and nanostructured layers. It is further assumed that the voids are almost completely filled with hydrogen during anodization, with clusters being formed in the Si with H of various compositions of the components.[6] The hydrogen atoms chemisorbed on the porous surfaces produce strong lattice distortions.

In view of these physicochemical and technological data, we assume that the spectra of the trapping and recombination levels in the depletion layers of the Schottky barrier will differ substantially in the void region and the unanodized region. The photocurrent of a Schottky diode, as is well

known, is determined by the sum of two main components,

$$I_{\text{ph}}=I_d+I_b, \tag{1}$$

where the current I_d of the depletion region is

$$I_d=qT(\lambda)F(\lambda)[1-\exp(-\alpha W_1)], \tag{2}$$

and the current of the base region, provided that its thickness is greater than the diffusion length L_n, is

$$I_b=\left[\frac{qF(\lambda)\alpha L_n}{(\alpha L_n+1)}\right]T(\lambda)\exp(-\alpha W_1). \tag{3}$$

Here $T(\lambda)$ is the transmittance of the Pd film, $F(\lambda)$ is the incident photon flux density, α is the absorption coefficient, and W_1 is the thickness of the depletion layer.

Equations (2) and (3) are valid if the intermediate states and the oxide layers are ignored. In the depletion layer, the set of trapping levels, including defect states, will obviously be substantially less in the unanodized sections than in the porous sections, which have a high density of defects and chemical impurities associated with the chemisorption of hydrogen. In this connection, the mobility of the current carriers and their lifetime will be greater in the first region than in the second, and consequently $L_{n1}>L_{n2}$. The rough estimate of the mobility made above probably reflects the averaged value over the entire disordered layer.

The variation of the photovoltage of the structure and its complete relaxation (Fig. 2) under the action of a pulse of H_2 flow is determined by the contribution of the two indicated regions and probably occurs as follows: When the H_2 starts, the barrier height increases in both regions, and the photovoltage consequently increases because the dark thermoelectron current and the generation–recombination current are reduced. The value of the photovoltage is given by $V_{\text{ph}}\simeq I_{\text{ph}}R_0$, where R_0 is the differential resistance at zero bias. In the structures studied here, the first region evidently makes the main contribution to V_{ph}, since its photocurrents, according to Eqs. (2) and (3), are larger. Moreover, for the generation–recombination current,

$$R_0S=2\tau_r/qn:\ W_1, \tag{4}$$

where S is the active area of the structure and n_i is the intrinsic carrier concentration in the Si. It is natural to assume that the recombination lifetime τ_r in the depletion region W_1 is greater in the first region than in the second; i.e., $R_0^{\text{I}}>R_0^{\text{II}}$. The relaxation decay of the photovoltage after switching off the pulse of H_2 flow reflects this inequality of the contributions to the photocurrent or photovoltage from the two regions of the diode structure. The photovoltage decay in the 50 to 180-s time interval is caused mainly by the contribution of the first region, while the longer-term relaxation is predominantly an effect of the second region.

Analytically, the photovoltage decay in the first section as a function of time can be approximately reppresented by $V_{\text{ph}}\propto\exp(-t)$, whereas the photovoltage rise in the second section from $V_{\text{ph}}^{\min}$ to the initial value (before starting the H_2) is approximated by the dependence $V_{\text{ph}}\propto(a_1+a_2t)$, with a coefficient $a_2\simeq 0.03\ \mu$V/s. The main cause of the relaxation variation of the photovoltage in the two regions of the barrier, i.e., in the unanodized and the porous regions, should be assumed to be the variation of the lifetime of the photocarriers, which is associated with their trapping and recombination at deep levels induced by diffusing hydrogen atoms. Before the H_2 is started, the lifetimes in both regions of the barrier can be represented, in general, as $1/\tau=\Sigma_i 1/\tau_i$, where τ_i is the lifetime corresponding to the ith recombination level. The number of levels and their energy position in the band gap can be different. It is natural that each level will have a different role in recombination. After the H_2 is started, new levels are induced in both regions because of lattice distortions that are no longer caused only by chemisorbed hydrogen atoms but also by hydrogen atoms that are diffused from outside; when this occurs, it is possible to form Si–H_x clusters, Si–O bonds, etc. In this case, we can write

$$1/\tau=\sum_i\ 1/\tau_i+\sum_j\ 1/\tau_j, \tag{5}$$

where the second sum includes the lifetimes associated with the newly created levels. In contrast with the first sum, the τ_j components contribute to τ only at the time that these levels exist. After the pulse of H_2 flow is turned off, the clusters decay, the lattice distortions decrease, and hydrogen atoms are given off in one form or another, including in the form of some compounds. The differential resistance given by Eq. (4), with allowance for the ''permanent'' and ''temporary'' deep centers, can be written as

$$R_0S=2/qn_iW_1\left(\sum_i\ v_{\tanh}\sigma_iN_i+\sum_j\ v_{\tanh}\sigma_jN_j\right), \tag{6}$$

where v_{th}, $\sigma_{i,j}$, and $N_{i,j}$ are the thermal velocity of the carriers, their capture cross section, and the density of recombination centers, respectively.

The dynamics of the relaxation process of the photovoltage under the action of the pulse of the hydrogen flow is represented as follows: At the time that the pulse of the H_2 flow acts, hydrogen atoms diffuse in both regions, unanodized and porous, which induces the appearance of new, ''temporary'' deep levels. Upon removal of H_2, the photovoltage relaxes. The relaxation is determined by trapping and recombination processes at the new levels. The decrease of the photoresponse is caused by the decrease of the photocurrent, because of active trapping of minority carriers (electrons) at the new levels, and by reduction of the differential resistance, according to Eq. (6).

In the 50 to 180-sec interval, the process is determined predominantly by the unanodized region of the structure and is approximately exponential with time. The relaxation for $t>180$ sec is already determined by the deep centers in the porous region, from which the probability of liberation of trapped electrons, $\gamma=\nu_0\exp(-E_j/kT)$, is substantially less (ν_0 is the burst frequency). As a result, a region with $V_{\text{ph}}<V_{\text{ph}}^{\text{st}}$ appears on the relaxation curve. Annihilation of the temporary deep levels in this region at a rate of about a_2t returns the photovoltage to its starting value.

In view of this explanation, we see more clearly why hydrogen affects the forward and reverse branches of the I-V curve, as mentioned earlier. With forward bias, the action of the H_2 is less appreciable, because the main component of

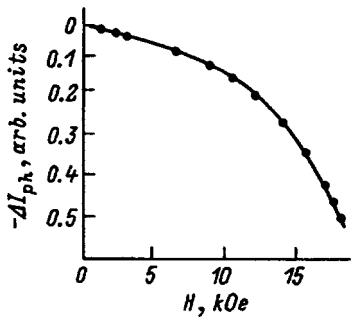

FIG. 4. Photocurrent of a Pd–p^0-Si–p-Si structure vs magnetic field; $-\Delta I_{\rm ph}=I^H_{\rm ph}-I^0_{\rm ph}$ and $I^H_{\rm ph}$ is the photocurrent in a magnetic field H.

the current through the structure is the hole current I_p, and decreasing the electron current in the p^0 region by trapping them on hydrogen-induced deep levels changes only slightly the total double-injection current $I=I_p+I_n$. With reverse bias, the injection coefficients are $I_p/(I_p+I_n)\neq 1$ for holes and $I_n/(I_p+I_n)\neq 1$ for electrons; the electron current can exceed the hole current, and the variation of the total current in an H_2 atmosphere is more significant, with the relaxation time being equal to 12–13 min, which is comparable to the corresponding relaxation time of the photovoltage.

The effect of a magnetic field on the photocurrent was checked (Fig. 4). The variation of the photocurrent in this case is probably also evidence in favor of heterogeneity of the disordered layer, with the acicular formations mentioned above. A relatively small decrease of the photocurrent at low fields is subsequently replaced by a sudden dropoff. Such a photocurrent variation can be attributed to a decrease of the photocarrier collection factor at the Schottky barrier, because L_n decreases when the electrons are deflected at the needles toward the void walls, where intense trapping and recombination occur.

The measurements of the electrical and photoelectric characteristics of diode structures with a disordered intermediate layer showed that both the dark-current transmission mechanism and the variation of the photovoltage (photocurrent) are determined by two regions of the structure, the unanodized and the porous regions, with each of them having its own set of deep traps and recombination centers, which can vary under the action of hydrogen, creating induced temporary deep levels.

[1] B. Hamilton, Semicond. Sci. Technol. **10**, 1187 (1995).
[2] G. G. Kovalevskaya, M. M. Mamedov, E. V. Russu, Kh. M. Salikhov, and S. V. Slobodchikov, Zh. Tekh. Fiz. **63**, No. 2, 185 (1993) [Tech. Phys. **38**, 149 (1993)].
[3] K. C. Mandal, F. Ozanam, and J.-N. Chazalviel, Appl. Phys. Lett. **57**, 2788 (1990).
[4] H. Sugiyama and O. Nittono, J. Cryst. Growth **103**, 156 (1990).
[5] F. Kozlowski and W. Lang, J. Appl. Phys. **72**, 5401 (1992).
[6] T. Ito, T. Yasumatsu, H. Watabe, and A. Hiraki, Jpn. J. Appl. Phys. **29**, L201 (1990).

Translated by W. J. Manthey

Influence of mismatch of the lattice parameters on the structural, optical, and transport properties of InGaAs layers grown by molecular beam epitaxy on InP(100) substrates

A. E. Zhukov, A. Yu. Egorov, V. M. Ustinov, A. F. Tsatsul'nikov, M. V. Maksimov, N. N. Faleev, and P. S. Kop'ev

A. F. Ioffe Physicotechnical Institute, Russian Academy of Sciences, 194021 St. Petersburg, Russia
(Submitted January 31, 1996; accepted for publication February 5, 1996)
Fiz. Tekh. Poluprovodn. **31**, 19–22 (January 1997)

The influence of mismatch stress on the structural, optical, and transport properties of thick InGaAs layers grown on InP(100) substrates by molecular-beam epitaxy is investigated. It is found that layers having tensile stress can be grown with a greater mismatch than compressively stressed layers before plastic relaxation sets in. The critical mismatch for thick InGaAs layers is not described with sufficient accuracy by either the mechanical equilibrium model or the energy balance model. The range of mismatches required to obtain high carrier mobilities and high radiative recombination efficiencies in InGaAs layers grown on InP substrates is much narrower than the pseudomorphic growth range. The maximum mobilities and minimum widths of the photoluminescence peak are attained in layers matched with the substrate in terms of the lattice parameter and also in slightly gallium-enriched layers. The compositional dependence of the width of the band gap is investigated with allowance for the influence of stress. [S1063-7826(97)00501-2]

The electronic properties of $In_xGa_{1-x}As$ solid solutions grown epitaxially on InP substrates make them well suited for applications in numerous optoelectronic and microelectronic device structures such as, for example, laser diodes operating at a wavelength of about 1.5 μm, transistors having a high electron mobility, and heterostructure bipolar transistors (HBTs).

In the event of a mismatch between the lattices of the epitaxial layer and the substrate, the resulting stress can be accommodated elastically if the thickness of the layer does not exceed a certain critical value h_c. The thickness of InGaAs layers designed for device applications should not exceed h_c, otherwise misfit dislocations, accompanied by severe degradation of both the optical and the electrical characteristics, will form. Relatively thick (several tens of micrometers) layers are used in certain applications such as collectors and HBTs, imposing stringent limitations on the range of accessible deviation from a lattice-matched configuration. In this article we investigate the influence of mismatch on the structural, optical, and transport properties of thick InGaAs layers grown on InP(100) by molecular-beam epitaxy (MBE).

The InGaAs layers were grown by MBE in a Riber 32P apparatus with a solid-state As_4 source on semiinsulating InP:Fe substrates oriented in the (100) plane without any kind of buffer layer. The temperature of the substrate during growth was measured with an IRCON V-series pyrometer and was set at 500–510 °C; the ratio of the fluxes of group-V and group-III elements was $\sim$20. The thickness of the InGaAs layers was 0.8 μm, and the growth rate was 0.4 μm/h. The In and Gas fluxes were precalibrated from the intensity oscillations of a reflected beam of fast electrons during the growth of GaAs and $In_xGa_{1-x}As$ ($x<0.3$) on GaAs(100) and were monitored according to the reading of an ion detector. The samples allocated for optical and transport investigations were lightly doped with Si at a concentration $n\sim 1\times 10^{16}$ cm^{-3}, which is typical of the doping levels used in HBT collectors.

The composition was determined from the flux ratios [In] / [Ga] and was then refined by two-crystal x-ray diffraction. The mismatch $\Delta x = x_{\mathrm{In}} - x_0$ (where x_{In} is the true mole fraction of InAs in the solid mixture, and x_0 is the mole fraction of InAs corresponding to matched lattice parameters of the epitaxial layer and the substrate) was varied in the interval from -7% to $+7\%$. A TRS-1 x-ray diffractometer, a Ge(001) monochromator, and the CuKα1 emission line (1.5405 Å) were used. The photoluminescence was investigated at 77 K, the excitation source was a He–Ne laser (1.96 eV) with a pump power density of 20 W/cm^2, and a cooled Ge photodiode was used for detection. The electron mobility was determined from Hall measurements by the van der Pauw method at 77 K and 300 K, and a unit Hall coefficient was assumed.

The usual measure of the crystal perfection of layers is the width of the layer diffraction peak.[1] Figure 1 shows the width $\Delta\theta$ of the diffraction peak of the epitaxial layer (004 reflection) as a function of the mismatch Δx. Clearly, $\Delta\theta$ falls between the limits 20–50″ in the interval of Δx from -3.7% to $+2.2\%$ [which corresponds to a mismatch of the InGaAs and InP lattice constants $\Delta d/d = (d_{\mathrm{InGaAs}} - d_{\mathrm{Inp}})/d_{I=nP} \simeq (-2.5 - 1.5)\times 10^{-3}$]. Values $\Delta\theta \simeq 20''$ are typical of InGaAs layers prepared by MBE on InP, taking into account the relatively small thicknesses of the investigated layers (<1 μm).

When the absolute value of the mismatch becomes higher than 3.7% for expansion and 2.2% for compression, $\Delta\theta$ exhibits a sudden jump to several hundred seconds of arc. This is accompanied by the disappearance of interference fringes in the x-ray rocking curves. Interference fringes (Pendellösung fringes) in a Bragg reflection geometry are

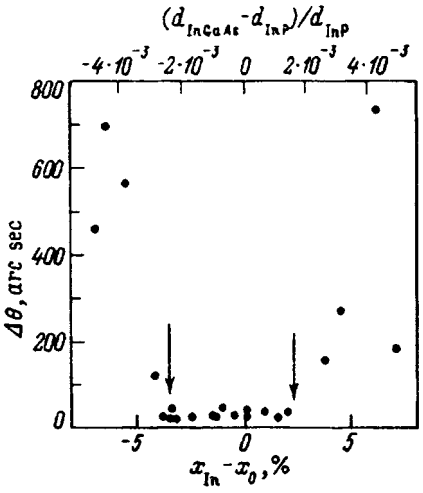

FIG. 1. Width of the diffraction peak of the epitaxial layer on the x-ray rocking curves near the (004) reflection for InGaAs layers of thickness $\sim 0.8\mu$m on InP(100) vs mismatch of the lattice constants. The arrows indicate the endpoints of the pseudomorphic growth interval (critical mismatch).

predicted by dynamic diffraction theory for perfect crystals as a consequence of interference of the wave fields created at the input and back surfaces of the crystal.[2] Their disappearance signifies a departure from parallelism between the surface of the epitaxial layer and the epitaxial layer/substrate interface as a result of the onset of misfit dislocations. Misfit dislocations partially relieve stress, producing the observed deviation of the value of x_{In} determined from the theory of elasticity on the assumption of pseudomorphic growth from the corresponding value determined from the flux ratio [In]/[Ga].

Two models have been proposed to predict the critical thickness for pseudomorphic growth: 1) mechanical equilibrium,[3] according to which

$$h_c/b \simeq \frac{1-1/4\nu}{4\pi(1+\nu)}\left(\frac{1}{\Delta d/d}\right)[\ln(h_c/b)+1], \tag{1}$$

and the energy balance model[4]

$$h_c/b \simeq \frac{1-\nu}{1+\nu}\,\frac{1}{16\pi\sqrt{2}}\left(\frac{b}{d_{\mathrm{InGaAs}}}\right)\left[\left(\frac{1}{\Delta d/d}\right)^2 \ln(h_c/b)\right], \tag{2}$$

where b is the magnitude of the Burgers vector, ν is the Poisson ratio, and

$$\frac{\Delta d}{d} \equiv \frac{d_{\mathrm{InGaAs}}-d_{\mathrm{InP}}}{d_{\mathrm{InP}}} = \frac{d_{\mathrm{InAs}}-d_{\mathrm{GaAs}}}{d_{\mathrm{InP}}}\Delta x. \tag{3}$$

The energy balance model well describes the critical thickness for InGaAs/InP in the interval $h_c \simeq 100$–1000 Å (Ref. 5).

For thick layers it is convenient to introduce the critical mismatch (Δx_c), defined as the lattice mismatch at which plastic relaxation begins for a layer of thickness h. We can therefore interpret the values $\Delta x = -3.7\%$ and 2.2% as corresponding to the critical mismatch for InGaAs layers of thicknesses 0.8 μm subjected to tensile or compressive stress, respectively. Similar results have been obtained in an earlier study,[1] where it was found that coherent growth is sustained up to $\Delta x_c \simeq 3\%$ for InGaAsP layers ($h \simeq 1$ μm on InP.

Setting $h = 0.8\mu$m for the case in question, we obtain the absolute values $\Delta x_c \simeq 0.5\%$ and 7% according to the mechanical equilibrium and energy balance models, respectively. Consequently, the mechanical equilibrium model yields too low a value, and the energy balance model yields too high a value for the critical mismatch in the case of thick (>1000 Å) layers. The discrepancy is probably attributable to the fact that the mechanical equilibrium model defines h_c as the thickness of a stressed film, for which existing threading dislocations can already begin to move, forming interface misfit dislocation lines. The energy balance model, on the other hand, is based on the assumption that the growing film starts out free of dislocations. The true situation is obviously intermediate between the two models.

From the data in Fig. 1 we note that the absolute value of the critical mismatch for tensile stress ($\Delta x_{\mathrm{In}} < 0$) is higher than the corresponding value for compressive stress ($\Delta x_{\mathrm{In}} > 0$). The difference is $\sim 1.5\%$, which corresponds to $\Delta d/d \simeq 1\times10^{-3}$ and is much greater than the experimental error. We assume that the given effect can be attributed to the difference in the thermal expansion coefficients of the epitaxial layer and the substrate.

The epitaxial layer has been determined experimentally for the system InGaAsP/InP.[6] It was found that the variation of the lattice mismatch as the temperature is varied from T_1 to T_2 is well described by the equation

$$\frac{\Delta d}{d}(T_2) = \frac{\Delta d}{d}(T_1) + \Delta\alpha(T_2 - T_1). \tag{4}$$

In the case of InGaAs/InP the difference $\Delta\alpha$ is approximately equal to 1×10^{-6} K^{-1}. Setting $T_1 = 20$ °C and $T_2 = 505$ °C (T_2 is the growth temperature), we obtain the variation of the lattice mismatch $\sim 5\times10^{-4}$. This is equivalent to a $\sim 0.7\%$ change of composition toward enrichment with Ga.

Consequently, layers having an excess (higher than x_0) content of In at room temperature are subjected to higher stress at the growth temperature. Proceeding from this model, we infer that the difference between the critical mismatches in tension and compression is $\sim 0.7\%$, which is close to the value obtained experimentally.

It is customarily assumed that the electrical and optical properties do not suffer any appreciable degradation as long as pseudomorphic growth is maintained. Figure 2 shows the experimental dependence of the Hall mobility on the mismatch for n-type layers nominally doped at the 1×10^{16} cm^{-3} level. We see that the mobility depends strongly on the mismatch at 77 K and has a maximum at $|\Delta d/d| < 1\times10^{-3}$ ($|\Delta x| < 1.7\%$). The value at the maximum is $\sim 1.9\times10^4$ cm^2/(V·s). An appreciable reduction in the mobility [to 1.2×10^4 cm^2/(V·s)] is observed in layers whose mismatch is close to, but not higher than the critical value determined by x-ray diffraction. A similar effect occurs at room temperature. In both cases the maximum is observed to shift slightly toward gallium-enriched compositions.

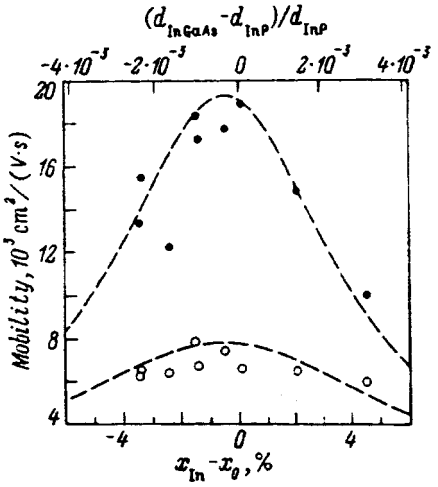

FIG. 2. Hall mobility at 77 K (graph *1*) and at 300 K (graph *2*) vs mismatch for InGaAs layers doped with Si at concentration $\sim 10^{16}$ cm^{-3}.

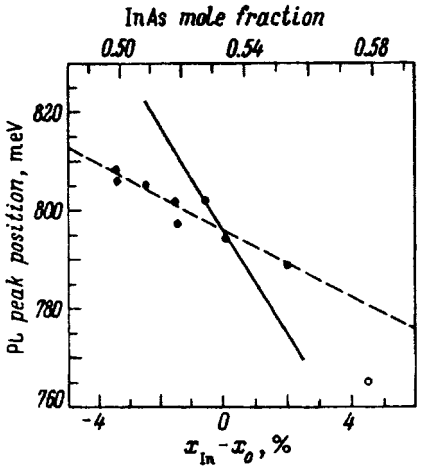

FIG. 4. Position of the photoluminescence peak at 77 K vs mismatch (mole fraction of InAs) (dots). The solid line represents the compositional dependence of the width of the band gap of InGaAs for the unstressed layer.

The total intensity (graph *1*) and half-maximum linewidth (graph *2*) of photoluminescence at 77 K are shown in Fig. 3 as functions of the mismatch. The photoluminescence intensity has a large scatter, but on the whole correlates well with the mobility. The minimum linewidth (15 meV) is also attained for small mismatches ($|\Delta x|<1.7\%$), corresponding to the maximum mobility. This effect is quite pronounced, because it is observed despite the doping-induced broadening of the line (the linewidth is 10 meV for undoped, matched layers).

The significant reduction in the mobility and the photoluminescence intensity in the layers with below-critical mismatch imposes more stringent limitations on the possible composition variations of thick InGaAs layers. It was noted[7] that tensile stress raises the potential barrier for surface diffusion and thereby lowers the migration rate of group III atoms. The result is increased roughness of the growing surface when observed by the diffraction of fast electrons by reflection, along with an increase in the number of crystal defects. In compressive stress the height of the potential barrier for surface diffusion is not expected to increase. On the other hand, it has been observed earlier[8] (in the deposition of InGaAs on GaAs) that the formation of In-enriched clusters in compressively stressed layers tends to lower the photoluminescence intensity, indicating that this cluster formation process invloves the formation of defects. The increase in the photoluminescence linewidth with increasing mismatch (Fig. 3) can also be attributed to increased cluster formation.

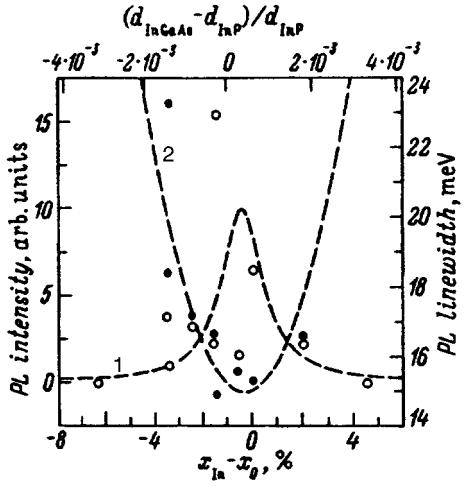

FIG. 3. Total intensity (graph *1*) and linewidth (graph *2*) of photoluminescence at 77 K vs mismatch for InGaAs layers doped with Si at concentration $\sim 10^{16}$ cm^{-3}.

The published values of the width of the band gap of InGaAs matched with InP substrates in terms of the lattice parameter reveal a large scatter. Reliable data at 77 K are particularly scarce. Figure 4 shows the experimental dependence of the position of the photoluminescence peak (E_{PL}) at 77 K on the chemical composition of the solid mixture. The following linear relation is well satisfied over the entire pseudomorphic growth range ($\Delta x=-3.7$–2.2%):

$$E_{PL}[\text{meV}]=796-3.36\Delta x, \tag{5}$$

where Δx is expressed in molar percent. The weaker compositional dependence of the gap width relative to unstressed InGaAs layers (-10.5 meV/%; Ref. 9) is a consequence of the displacement of the edges of the bands under the influence of stress. Calculations[10] show that this displacement partially offsets the variation of the band gap with composition and is approximately equal to $11.7\Delta d/d$ in tension and to $4.38\Delta d/d$ in compression. When both factors are taken into account, the rates of change of the gap width with composition are determined by the coefficients -2.5 meV/% and -7.4 meV/%, respectively. The dependence obtained by us is in good agreement with calculations for tensile stress up to critical mismatch. To the best of our knowledge, this effect was first demonstrated with thick InGaAs layers at-liquid-helium temperatures.

We have thus investigated the influence of mismatch of the lattice parameters of an epitaxial layer and a substrate on the structural, optical, and transport properties of InGaAs

deposited on a InP substrate. We found that the absolute value of the critical mismatch for layers under tensile stress is higher than the corresponding value in compression, because the difference in the thermal expansion coefficients of the epitaxial layer and the substrate. The range of mismatches required to obtain high carrier mobilities and high radiative recombination efficiencies in InGaAs layers grown on InP substrates is much narrower than the pseudomorphic growth range. Stress in the epitaxial layer modifies the band structure and weakens the compositional dependence of the width of the band gap relative to the expected dependence for unstressed layers.

This work has received support from the Hughes Research Laboratories in Malibu, California, USA, and from the Ministry of Science of the Russian Federation (''Physics of Solid State Nanostructures,'' Project 1-001).

[1] J. Lee, W. F. Mayo, and T. Tsakalakos, J. Electron. Mater. **21**, 867 (1992).
[2] W. J. Bartels and W. Nijman, J. Cryst. Growth **44**, 518 (1978); F. Genova, G. Morello, and C. Rigo, J. Vac. Sci. Technol. B **5**, 811 (1987).
[3] J. W. Matthews, J. Vac. Sci. Technol. **12**, 126 (1975).
[4] R. People and J. C. Bean, Appl. Phys. Lett. **47**, 322 (1985).
[5] M. Tacano, Y. Sugiyama, Y, Takeuchi, and Y. Ueno, J. Electron. Mater. **20**, 1081 (1991).
[6] N. A. Bert, A. T. Gorelenok, S. G. Konnikov, V. E. Umanskiĭ, and A. S. Usikov, Zh. Tekh. Fiz. **51**, 1018 (1981) [Sov. Phys. Tech. Phys. **26**, 610 (1981)].
[7] A. Salokatve and M. Hovinen, J. Appl. Phys. **67**, 3378 (1990).
[8] A. Yu. Egorov, A. E. Zhukov, P. S. Kop'ev, N. N. Ledentsov, M. V. Maksimov, and V. M. Ustinov, Fiz. Tekh. Poluprovodn. **28**, 604 (1994) [Semiconductors **28**, 363 (1994)].
[9] D. J. Arent, K. Deneffe, C. Van Hoof, J. DeBoek, and G. Borghs, J. Appl. Phys. **66**, 1739 (1989).
[10] G. Ji, D. Huang, U. K. Reddy, T. S. Henderson, R. Houdre, and H. Morkoc, J. Appl. Phys. **62**, 3366 (1987).

Translated by James S. Wood

Carrier accumulation and strong electrode sheath fields in illuminated, high-resistivity MISIM structures

B. I. Reznikov and G. V. Tsarenkov

A. F. Ioffe Physicotechnical Institute, Russian Academy of Sciences, 194021 St. Petersburg, Russia
(Submitted December 20, 1995; accepted for publication February 10, 1996)
Fiz. Tekh. Poluprovodn. **31**, 23–30 (January 1997)

The influence of the tunnel transmissivity $T_{n,p}$ of an insulation layer on the electric field distribution and the current–intensity j–I_i relation in a pure, highly biased, high-resistivity metal–insulator–semiconductor–insulator–metal (MISIM) structure is investigated theoretically. It is shown that as $T_{n,p}$ decreases, carriers accumulate near the oppositely polarized electrodes, and their density rises sharply in layers having a thickness of the order of $l_k = kT/eE_e$ ($E_e = V/d$). The domain of parameters is determined. In this domian the accumulation effects are so strong as to increase the near-electrode fields appreciably, to the extent that they significantly exceed the mean field. The dependence of the current on the transmissivity is determined by the height of the Schottky barrier. In moderate fields, if the photocurrent is much higher than the dark current, the current density increases slightly with decreasing $T_{n,p}$, tending to the maximum value eI_i. In strong fields the current rises sharply as a result of carrier injection across the lowered potential barrier. © *1997 American Institute of Physics.* [S1063-7826(97)00601-7]

INTRODUCTION

In metal–semiconductor–metal (MSM) structures the rates of carrier exchange across the boundaries of the semiconductor is of the order of the thermal exchange rates and is much greater than the carrier drift velocities in fields of the order of 10^3 V/cm. Consequently, carriers do not accumulate in the electrode sheaths, and in pure crystals illuminated at moderate intensities the electric field does not undergo sudden changes at the interfaces. The specific characteristics of the photoelectric effect in highly biased, high-resistivity MSM structures under various experimental conditions (i.e., various illumination intensities and applied voltages) and for various bulk parameters of the semiconductor (deep-level impurity concentration and impurity energy level) have been investigated in several papers.[1–5] The inclusion of insulating layers between the semiconductor and the metal imparts new significance to several surface parameters such as the barrier height φ_{Bn} between the semiconductor and the metal and the tunnel transmissivity $T_{n,p}$ of the insulator film. The influence of φ_{Bn} on the field distribution in the cathode zone of the illuminated structure at maximum carrier exchange rates has been studied previously.[6] For high-resistivity structures containing a deep-level impurity it has been shown[7] that to vary φ_{Bn} and $T_{n,p}$ by varying the filling factor of the deep impurity level significantly influences the dark field distribution in the interior (decompensation effect associated with thickening of the insulator film).

The discovery that tunnel transmission influences the dark field distributions in the interior volume makes it necessary to extend research to the case of illumination. The photoelectric effect in metal–insulator–semiconductor–insulator–metal (MISIM) structures with a tunnel-transmissive insulator have been studied previously in Ref. 8 and in several other papers.[9] However, these studies addressed conventionally doped, low-resistivity semiconductors with low biases of the order of 1–2 V. The distribution of the electric field in such structures is determined mainly by the doping and changes little under illumination.

The object of the present study is the influence of the tunnel transmissivity of the insulating layer between the semiconductor and metal on the electric field distribution in a highly biased, high-resistivity MISIM structure and the interdependence of the current and the illumination intensity. To isolate transmissivity effects, we consider a semiconductor without deep-level impurities, so that the volume recombination and charge exchange of traps are excluded from the model. Our investigation is therefore a generalization of Ref. 1 to the case of arbitrary boundary transmissivities.

1. STATEMENT OF THE PROBLEM

We consider an MISIM structure, to which we apply a voltage V much higher than all barriers. Natural monochromatic light ($h\nu \gtrsim E_g$) is incident on the semitransparent anode. Carrier transport in the semiconductor is analyzed on the basis of the system of equations of continuity in the diffusion-drift approximation and the Poisson equation.[1] The insulating layers are characterized by the transmissivities T_n and T_p (carrier tunneling probabilities), so that the boundary conditions at the semiconductor–insulator interfaces $x=0$ and $x=d$ have the form (see, e.g., Refs. 1, 9, and 10)

$$q_n(0) = -V_{n0}^T\left[n_0 - n_0^{eq}\exp\left(-\frac{eV_i^0}{kT}\right)\right] - q_s(0),$$
$$q_p(0) = -V_{p0}^T\left[p_0 - p_0^{eq}\exp\left(\frac{eV_i^0}{kT}\right)\right] - q_s(0), \tag{1}$$

$$q_n/(d)=V_{nd}^T\left[n_d-n_d^{eq}\exp\left(\frac{eV_i^d}{kT}\right)\right]+q_s(d),$$
$$q_p(d)=V_{pd}^T\left[p_d-p_d^{eq}\exp\left(-\frac{eV_i^d}{kT}\right)\right]+q_s(d). \quad (2)$$

Here $V_n^T=T_nV_n$, $V_p^T=T_pV_p$, $V_n=A_n^*T^2/eN_c$, $V_p=A_p^*T^2/eN_v$, A_n^* and A_p^* are the effective Richardson constants, and V_i^0 and V_i^d are the voltage drops across the films at the contacts $x=0$ and $x=d$. The recombination flux at the boundaries is written for the model of a single surface level.

The exponential factors in conditions (1) take into account the variations of the barriers on the metal side as a result of the voltage drops V_i^0 and V_i^d across the insulator films. We assume here that the latter are sufficiently thin, so that $eV_i/kT\ll 1$. For fields of the order of 10^3–10^4 V/cm the correction to the equilibrium concentrations does not exceed 10% if the layer thickness is bounded by the values 25–250 Å. Consequently, the boundary fluxes (1) practically coincide with the expressions discussed in Ref. 1 (additional allowance is made for surface recombination), but the emission rates V_n^T and V_p^T can vary over wide ranges, since they are proportional to the transmissivities of the insulating layers.

The tunnel transmissivities T_n and T_p depend exponentially on a function that contains the layer thickness δ, the tunneling mass $m_{n,p}$, the barrier height for tunneling $\Phi_{n,p}$, and the voltage drop across the layer V_i (see, e.g., Refs. 9, 11, and 12). In lieu of reliable information on these quantities, we ignore the details of the dependence of T_n and T_p on the film characteristics and use the transmissivity as an input parameter independent of V_i.

2. DARK CURRENT

2.1. We investigate a high-resistivity structure of width $d=0.3$ cm with an effective density of acceptors per unit volume $N_a=10^8$ cm^{-3}. The height of the barrier between the semiconductor and the metal is taken to be $\varphi_{Bn}=1$ V. This corresponds to the case in which the equilibrium hole density p^{eq} at the semiconductor boundaries is much higher than N_a, n_i, and n^{eq}. The voltage applied to the structure is varied between 1 V and 6000 V. All other parameters have the same values as in Ref. 1. The transmissivities are varied in the range $T_n=T_p=1$–10^{-5}.

Figure 1 shows the electric field distributions $\tilde{E}(X)$ ($\tilde{E}=E/E_e$, $E_e=V/d$, $X=x/d$) at various transmissivities. The graph of $\tilde{E}(X)$ is almost linear and, as the transmissivity decreases, tends to a near-uniform distribution [$\tilde{E}(X)\approx 1$] with a small negative slope. The density of holes in the interior decreases in this case, and their distribution becomes almost uniform (Fig. 2). Holes accumulate in a narrow boundary layer of thickness $\delta^-\simeq 10^4 d$ near the cathode, and the density p_d increases, tending to the value $2p_0^{eq}$. The behavior of the electrons is analogous to the hole behavior to within polarity. The density of electrons in the interior is much lower than the hole density and decays therein as the transmissivity decreases. The distribution $n(X)$ makes a sudden jump in the diffusion layer near the anode, tending to the

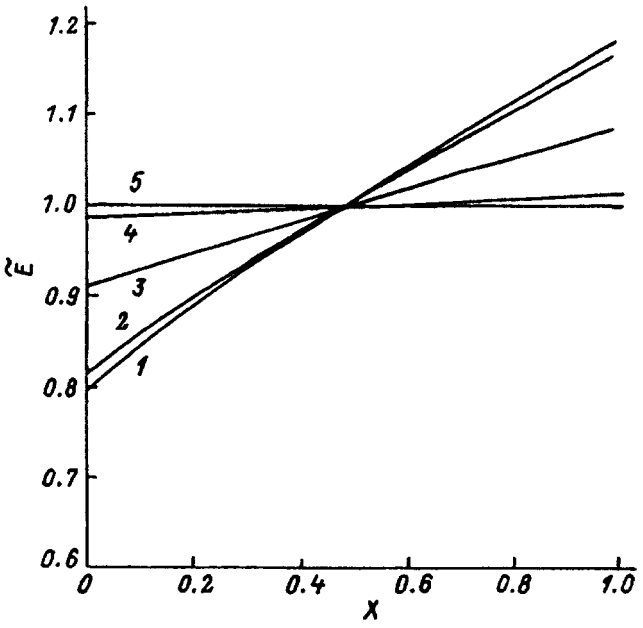

FIG. 1. Influence of the tunnel transmissivity of the boundaries on the dark electric field profiles, $\tilde{E}=E/E_e, E_e=V/d$. *1)* $T=1$; *2)* 10^{-1}; *3)* 10^{-2}; *4)* 10^{-3}; *5)* 10^{-5}.

value $2n_0^{eq}$ as the transmissivity decreases. The current–voltage (I–V) characteristic for various values of the transmissivity is shown in Fig. 3. In the transmissivity range 1–10^{-2} the current decreases relatively little, but with a further reduction in the transmissivity the $j(T)$ graph becomes more pronounced in the high-voltage range, of the order of several hundred volts. At high voltages the current tends to an asymptotic value, which depends on the transmissivity, reaching the asymptote at lower voltages as the transmissivity decreases.

2.2. The hole distribution $P(X)$ and the electric field distribution $\tilde{E}(X)$ in the dark case have been analyzed theoretically in Ref. 7 [see Eqs. (2), (4), (5), and (15) therein], where it is shown that the expressions derived in Ref. 1 for the boundary values of the carrier densities are also valid for arbitrary transmissivity. The graphs of $E(x)$, $P(x)$, and $j(T)$ obtained under the condition $p^{eq}\gg N_a$ (Figs. 1–3) are explained by a decrease in the hole fluxes from the metal and the space charge in the interior. A decrease in the transmissivity of the insulating layer causes carriers to accumulate around the electrodes of opposite polarity. It is also the prin-

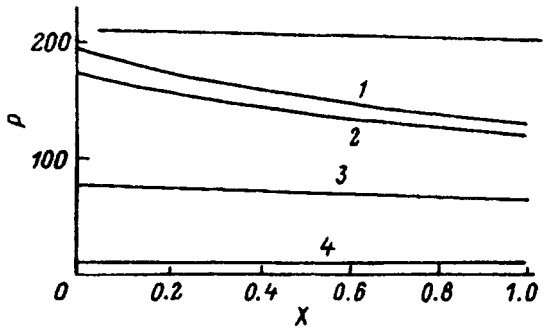

FIG. 2. Influence of tunnel transmissivity of the boundaries on the dark hole profiles, $P=p/N_a$. *1)* $T=1$; *2)* 10^{-1}; *3)* 10^{-2}; *4)* 10^{-3}.

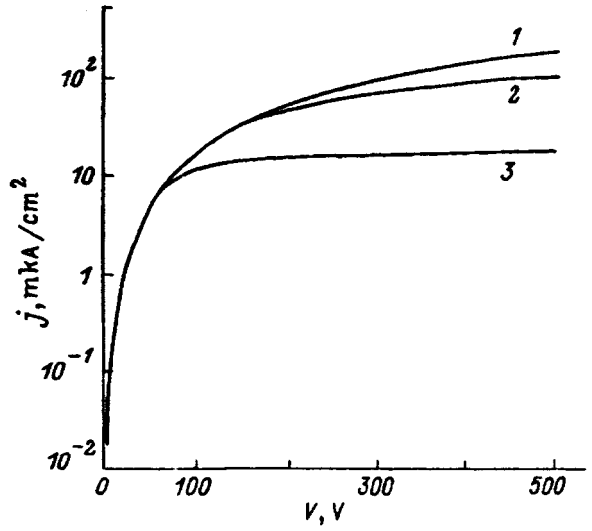

FIG. 3. Zero-illumination I–V characteristic for various tunnel transmissivities. *1)* $T=1$; *2)* 10^{-2}; *3)* 10^{-3}.

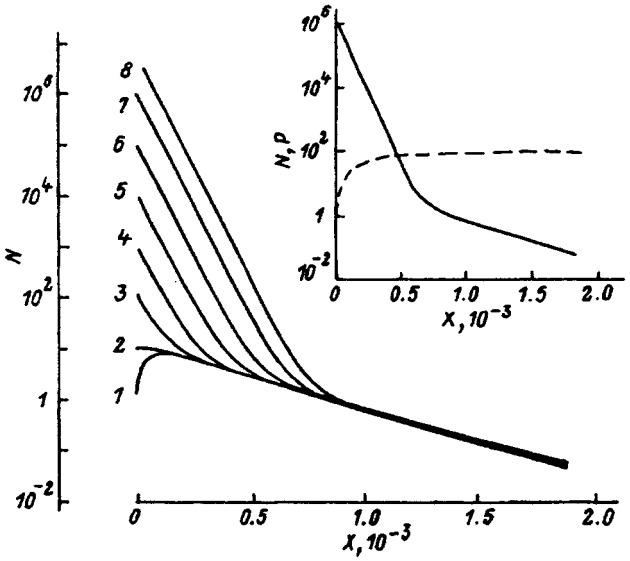

FIG. 4. Distribution of the electron density $N=n/N_a$ in the vicinity of the anode for various tunnel transmissivities of the insulating layer. *1)* $T=1$; *2)* 10^{-1}; *3)* 10^{-2}; *4)* 10^{-3}; *5)* 10^{-4}; *6)* 10^{-5}; *7)* 10^{-6}; *8)* 10^{-7}.

cipal effect in the case of photoproduction. However, since the density of photocarriers near the contacts can be much higher than their dark values, this phenomenon can produce, in thin sheaths around the electrodes, high space charge densities capable of influencing the electric fields themselves. The quantitative aspects of the phenomenon are investigated in Sec. 3.

3. PHOTOELECTRIC EFFECT: RESULTS OF NUMERICAL CALCULATIONS

The numerical calculations are carried out for an illumination intensity $I_i=10^{15}$ cm$^{-2}\cdot$s^{-1} and an applied voltage $V=600$ volts. The barrier heights at the boundaries of the semiconductor are assumed to be $\varphi_{Bn}=0.71$ V and 1 V. Surface recombination is included in the boundary conditions. It is assumed that the single surface level is situated in the middle of the band gap, and that $s_n=s_p=10^6$ cm/s. In view of the uncertainty of the numerical characteristics (the barrier heights and the effective masses of tunneling carriers) it is assumed that $T_n=T_p=T$. The transmissivity is varied within the range $T=1-10^{-8}$.

We first analyze the distribution $N(X)$ ($N=n/N_a$, $X=x/d$) in the vicinity of the anode. It is evident from Fig. 4 that lowering the transmissivity to a few hundredths has the effect of changing the sign of the derivative dN/dX in the electrode sheath and the formation of a layer whose electron density increases as the transmissivity is further reduced. The density N_0 increases inversely as the transmissivity, and the thickness of the negative-space-charge layer increases slightly (logarithmically). The form of the distribution $N(X)$ evinces an exponential dependence on the coordinate. At some distance from the anode there is a region where $N(X)$ is essentially independent of the transmissivity T. The $N(X,T)$ curves branch out in the depth of the semiconductor ($X<0.002$), the density $N(X)$ diminishing as T decreases (as in the dark case).

In a layer having an approximate thickness α^{-1} next to the anode the hole density $P(X)=p(x)/N_a$ increases and is much lower than $N(X)$ (see the inset to Fig. 4). This is associated with the applied bias and the influence of surface recombination, where the distribution of P near the anode and the value of P_0 depend weakly on the transmissivity of the boundaries. The variation of the hole density takes place in a thinner layer, because of the lower diffusion coefficient. As a result of the rapid decrease of the electron density immediately at $\gtrsim 5\alpha^{-1}$, the inequality $P\gg N$ holds. At $X\simeq 10\alpha^{-1}$ the hole density attains a maximum and subsequently in the interior of the semiconductor decays according to the law $pE=$const. It then passes through a minimum at a point located roughly at a distance $2l_E^d=2kT/eE_d$ from the cathode, and when the film has a low tunnel transmissivity, the hole density increases in the diffusion layer near the cathode (Fig. 5). The thickness of this layer, like that of the anode sheath, is of the order of a few times l_E and increases logarithmically as the transmissivity decreases. We call attention to the work of Gutkin and Sedov,[13] who previously suggested that carrier accumulation in the electrode sheaths plays a decisive role as a mechanism for maintaining a constant photocurrent at lowered transmissivity of the insulator.

We now consider the behavior of the field $\tilde{E}(X)$. At low transmissivities $T\lesssim 10^{-6}$ carrier accumulation at the oppositely polarized electrodes leads to appreciable variations of the field in the space charge layers. The values of the fields at the interfaces $\tilde{E}_0$ and $\tilde{E}_d$ increase (Fig. 6), and at $T\lesssim 10^{-7}$ (for $I_i=10^{15}$ cm$^{-2}\cdot$ s^{-1}) their variations are of the same order as the fields $\tilde{E}_0$ and $\tilde{E}_d$ themselves. Outside the electrode sheaths in the interior of the semiconductor the profile of the field closely resembles the previously investigated distribution[1] for an MSM structure and depends weakly on the tunnel transmissivities of the interfaces.

Next we consider the dependence of the current density in the structure on the transmissivity. A comparison of the

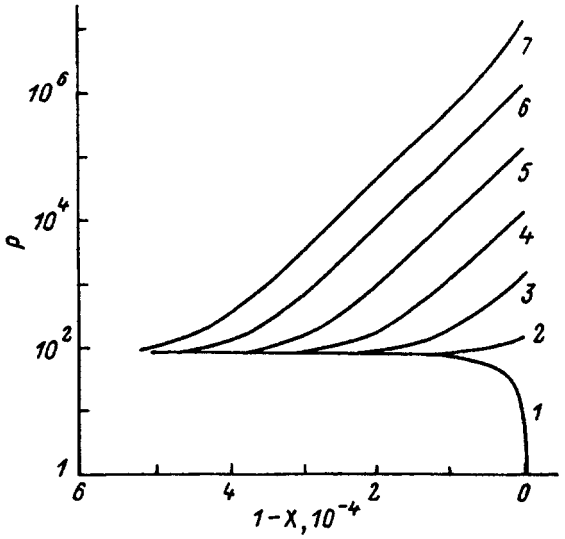

FIG. 5. Distribution of the hole density $P=p/N_a$ in the cathode sheath for various tunnel transmissivities of the insulating layer. *1)* $T=1$; *2)* 10^{-2}; *3)* 10^{-3}; *4)* 10^{-4}; *5)* 10^{-5}; *6)* 10^{-6}; *7)* 10^{-7}.

results for $\varphi_{Bn}=0.71$ V and 1 V shows that the function $j(T)$ is of different types in these cases. For $\varphi_{Bn}=0.71$ V, when the dark current is much lower than the photocurrent, the current density increases slightly with decreasing transmissivity, tending to the value eI_i., because of the large difference in the carrier densities in the vicinity of the electrodes, surface recombination is ineffective, and the quantity q_s is much lower than the emission flux of carriers across the boundary. The function $j(T)$ is more complex for $\varphi_{Bn}=1$ V. In this case (at $T_{n,p}\simeq 1$) the dark current, which is proportional to p_0^{eq}, is appreciable (at $I_i=10^{15}$ cm$^{-2}\cdot$s^{-1}). At high transmissivities $T\gtrsim 10^{-2}$ the hole density is even higher than its electron counterpart. In this case a decrease in the transmissivity drastically lowers the current (as in the dark case).

Since the densities N and P are now comparable, the recombination current $q_s(0)$ (depending on the value of the transmissivity) is equal to 50–99% of I_i. With a further reduction in the transmissivity, the contribution of the dark

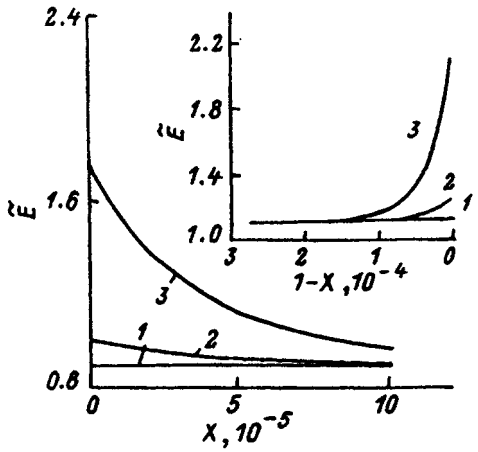

FIG. 6. Electric field distribution in the anode and cathode (inset) sheaths for various transmissivities. *1)* $T=10^{-5}$; *2)* 10^{-6}; *3)* 10^{-7}.

current becomes insignificant, and at $T\lesssim 10^{-4}$ the behavior of $j(T)$ is the same as in the case $\varphi_{Bn}=0.71$ V, i.e., it gradually tends to the value eI_i.

Consequently, a decrease in the transmissivity of the boundaries of a highly biased, high-resistivity MISIM structure results in the formation of space charge layers in the vicinity of the electrodes, where the density is so high as to make the variation of the fields near the electrodes comparable with E_e and even higher than the mean field. Illuminated MISIM structures with a transmissivity below a certain critical value ($T\lesssim 10^{-8}$–10^{-9} at $I_i=10^{16}$ cm$^{-2}\cdot$s^{-1}) are structures with large electric fields near the boundaries. Some particular features and quantitative relations are set forth in the next section, which addresses the cases of high and low boundary transmissivities.

4. ANALYTICAL TREATMENT OF THE PHOTOELECTRIC EFFECT

4.1. Without volume and surface recombination the analytical investigation of the photoelectric effect in an MISIM structure is identical to the previous investigation for an MSM structure[1] if the tunnel transmissivities T_n and T_p are such that the boundary values of the electric field are essentially constant ($T_{n,p}\gtrsim 10^{-6}$ at an illumination intensity $I_i=10^{15}$ cm$^{-2}\cdot$s^{-1}). In this case, when the conditions $eV/kT\gg 1$, $E_0>0$, $l_E/d\ll 1$, and $[(l_E/d)dE/dx]_{0d}\ll 1$ are satisfied, the equations derived in Ref. 1 can be used with V_n and V_p replaced by V_n^T and V_p^T respectively. In the presence of surface recombination the expressions for the densities and the current can also be found by solving the system of equations deduced from the boundary conditions (1) and the relations obtained by integrating the equations of continuity for electrons and holes by the steepest-descent method, using a procedure analogous to Ref. 1. The solution is rather cumbersome, but in the special case where $n_0\gg p_0$, $p_d\gg n_d$ and, hence, $q_s(0)=s_p p_0$, $q_s(d)=s_n n_d$, it is simplified and has the form

$$n_0=\frac{I_i}{V_n^T}\left(1-\frac{s_p}{V_\Sigma^p}\frac{\alpha l_E^0}{1+\alpha l_E^0}\right)+\left(1+\frac{v_{dr}^n}{V_\Sigma^n}\right)n_0^{eq}-\frac{s_p}{V_\Sigma^p}p_0^{eq}, \tag{3}$$

$$V_\Sigma^p=s_p+v_{dr}^p+V_p^T, \quad V_\Sigma^n=s_n+v_{dr}^n+V_n^T, \tag{4}$$

$$v_{dr}^p\equiv\mu_p E_0, \quad v_{dr}^n\equiv\mu_n E_d, \quad l_E^0=kT/eE_0, \tag{5}$$

$$n_d=\frac{V_n^T}{V_\Sigma^n}n_0^{eq}, \tag{6}$$

$$p_0=\frac{I_i}{V_\Sigma^p}\frac{\alpha l_E^0}{1+\alpha l_E^0}+\frac{V_p^T}{V_\Sigma^p}p_0^{eq}, \tag{7}$$

$$p_d=\frac{I_i}{V_p^T}\left(1-\frac{s_p+V_p^T}{V_\Sigma^p}\frac{\alpha l_E^0}{1+\alpha l_E^0}\right)+\left(1+\frac{v_{dr}^p}{V_\Sigma^p}\right)p_0^{eq}-\frac{s_n}{V_\Sigma^n}n_0^{eq}. \tag{8}$$

The total current flowing through the structure is

$$j = eI_i\left(1 - \frac{s_p + V_p^T}{V_\Sigma^p}\,\frac{\alpha l_E^0}{1+\alpha l_E^0}\right) + j_0, \tag{9}$$

$$j_0 = ev_{dr}^p p_0^{eq}\frac{V_p^T}{V_\Sigma^p} + ev_{dr}^n n_0^{eq}\frac{V_n^T}{V_\Sigma^n}. \tag{10}$$

Equations (3)–(10) describe:

• the accumulation of carriers at the electrodes of opposite sign as the transmissivity is lowered — $n_0 \sim 1/V_n^T$, $p_d \sim 1/V_p^T$;

• the fact that the hole density at the anode p_0 is independent of the transmissivity at low values of the latter;

• different, in general, monotonic dependences of the current on the transmissivity, which are determined by the ratio of the photocurrent and current of equilibrium electrons and holes j_0, expressed in terms of p_0^{eq} and n_0^{eq} by the quantity φ_{Bn}; here, if the exchange rate is much lower than the drift velocities and if $j_0 \ll I_i$, the current depends only very slightly on the transmissivity.

The latter result ties in with the fact that at low transmissivities the diffusion flux of photoelectrically generated holes toward the anode tends to zero, and in the structure without volume recombination complete charge separation takes place; i.e., the quantum efficiency is close to unity. As the transmissivity is lowered, a constant hole flux across the semiconductor–insulator interface is maintained by the increase in the gradient of the hole density near the cathode by virtue of the accumulation of holes in a layer of thickness a few times l_E (Fig. 5).

It is important to note that the transmissivities cannot tend to zero in Eqs. (3)–(10), because carrier accumulation in this case causes abrupt field changes to take place in layers having a thickness of several times l_E in the vicinity of the electrodes. The latter effect violates the conditions underlying the derivation of these relations, whereby the field varies smoothly near the boundaries.

It should also be noted that surface recombination does not restrict the growth of the densities n_0 and p_d as the boundary transmissivities decrease. This is attributable to the substantial difference between the electron and hole densities near the electrodes in the presence of high bias: $n_0 \gg p_0$, $p_d \gg n_d$. We note that the validity of Eqs. (3)–(10) is limited for nonzero values of s_n and s_p, since they have been derived for the special form of q_s implied by the above-stated inequalities.

4.2. We now give an analytical description of the physical picture in the case of transmissivities sufficiently small to meet the condition $\Delta E/E_e \gg 1$. We partition the semiconductor into four characteristic regions. In the vicinity of the anode is a high-field region, where the condition $n \gg p$ holds. Next in line is a region in which the field is of the order of E_e, but carrier production is still significant. In the interior is the drift zone, where $p \gg n$ and $pE = \text{const}$. In the vicinity of the cathode we again find a high-field region, where now $p \gg n$.

4.2.1. In the first region the space charge density in the Poisson equation depends only on the electron density. The distribution of the latter is quasiuniform, $n = n_0 e^{\psi}$ ($\psi = e\varphi/kT$), which follows from the conditions $q_n(x) = -D_n dn/dx - \mu_n En = 0$, because the drift and diffusion components are much greater than the total flux in large fields and in the presence of high gradients. In this approximation, which was used many years ago by Mott and Gurney[14] to determine the field in the vicinity of a metal–insulator contact, the potential equation has the form

$$d^2\psi/d\xi^2 = e^{\psi}, \tag{11}$$

where $\xi = x/L_D^n$ is the distance from the surface, normalized to the Debye length expressed in terms of the surface electron density n_0. When the field in the interior is much weaker than at the surface (i.e., when the conditions $d\varphi/d\xi \ll 1$, $\psi < 0$, and $|\psi| \gg 1$ are satisfied for $\xi \gg 1$), the solutions of the potential, the field, and the number densities have the form

$$\psi(\xi) = -2\ln\left(1 + \frac{\xi}{\sqrt{2}}\right), \tag{12}$$

$$E(x) = \frac{kT}{eL_D^n}\,\frac{\sqrt{2}}{1 + x/\sqrt{2}L_D^n} = \frac{E_0}{1 + x/\sqrt{2}L_D^n}, \tag{13}$$

$$n(x) = \frac{n_0}{(1 + x/\sqrt{2}L_D^n)^2}. \tag{14}$$

From Eqs. (12) and (13) follows the very interesting equality

$$\frac{\varepsilon E^2(x)}{8\pi} = kTn(x), \tag{15}$$

which asserts that the pressures of the electric field and electron gas balance equalize in the first region.

The solutions (12)–(14) are completely determined if the value of n_0 is known. The quantity n_0 can be determined with good approximation from the relations $q_n(d) - q_n(0) = I_i$ and $q_n(0) = -V_n^T(n_0 - n_0^{eq}) - s_p p_0$. If $q_n(d) - V_n^T n_0^{eq} + s_p p_0 \ll I_i$, then $n_0 = I_i/V_n^T$. We also note that the previously defined characteristic field length $l_E^0 = kT/eE_0$ is equal to $L_D^n/\sqrt{2}$ in the case discussed here. We estimate the width δ^+ of the first region, defining it by the condition $E(\delta^+) = E_e$. From expression (12) we obtain

$$\delta^+ = \frac{2kT}{eE_e} - \sqrt{2}L_D^n \approx \frac{2kT}{eE_e}. \tag{16}$$

4.2.2. In the high-field region near the cathode ($d - \delta^- \leqslant x \leqslant d$, $\delta^- \simeq \delta^+$), where $p \gg n$, the same considerations are valid as in the first region, except that the distance $d - x$ is normalized to the Debye length expressed in terms of the density $L_D^p = [\varepsilon kT/(4\pi e^2 p_d)]^{1/2}$, which is not expressed in terms of the density p_d. The solution in this region has a form analogous to (12)–(14) with ψ replaced by $\psi_d - \psi$, the coordinate x replaced by $d - x$, the density p by n, and the index 0 by d. A relation analogous to (15), expressing the equality of the pressures of the hole gas and the field, is satisfied in this region. The quantity p_d entering into L_D^p is given by the equation $p_d = I_i/V_p^T$ if the condition $|q_p(0) + V_p^T p_d^{eq} - s_n n_d| \ll I_i$. is satisfied.

4.2.3. The conditions $p \gg n$ and $q_p = \mu_p pE = \text{const}$ are satisfied in the drift region ($x_n \leqslant x \leqslant x_p$, $x_n \simeq 3\alpha^{-1}$, $x_p \simeq d - \delta^-$), so that

$$\frac{dE}{dx}=\frac{4\pi e}{\varepsilon}p(x)=\frac{4\pi e q_p}{\varepsilon\mu_p E}. \tag{17}$$

Integrating Eq. (16), for the quantity $\widetilde{E}=E(x)/E_e$, we obtain the expression

$$\widetilde{E}(X)=[\widetilde{E}(X_p)+a(X-X_p)]^{1/2},\quad a=2q_p/I_*,$$
$$X_p=x_p/d,\quad I_*=\frac{\varepsilon\mu_p V^2}{4\pi e d^3}. \tag{18}$$

Integrating (18) over the interval (X_n,X_p), for the pressure created by the voltage V_{sd} in the drift region of the semiconductor, we obtain

$$\frac{V_{sd}}{V}=\frac{2\widetilde{E}^3(X_p)}{3a}\left\{1-\left[1-\frac{a}{\widetilde{E}^2(X_p)}(X_p-X_n)\right]^{3/2}\right\}. \tag{19}$$

For $a\ll 1$ (which implies that $I_i\ll I_*/2$), this gives

$$\widetilde{E}(X_p)=\frac{V_{sd}}{V(X_p-X_n)}\left[1+\frac{a}{4}(X_p-X_n)^3\frac{V^2}{V_{sd}^2}\right]. \tag{20}$$

An analogous expression is obtained for $\widetilde{E}(X_n)$, except that the second term in the brackets is now preceded by a minus sign. It follows from (18) and (19) that for $X_n\simeq 0$, $X_p\simeq 1$, and $V_{sd}\simeq V$ the field $\widetilde{E}(X_n)$ decreases to zero, and $\widetilde{E}(X_p)\simeq 3/2$ when $q_p=9/8I_*$. This means that in the drift region the dependence of the field on the intensity is qualitatively the same as for a structure with a high carrier exchange rate.

The equations obtained in Subsecs. 4.2.1–4.2.3 completely determine the distribution of the field and the potential in the structure, making it possible to find the distribution of the carrier densities and the current.

4.2.4. Integrating the expression for q_p and proceeding as in Ref. 1, for $p_0\exp(\varphi_d)\ll p_0$, we obtain the relation

$$p_0=\frac{1}{D_p}\int_0^d q_p(x)e^{\psi(x)}dx=\frac{1}{D_p}\frac{V_p^T p_0^{eq}I_1+I_i(I_1-I_2)}{1+\dfrac{V_p^T+s_p}{D_p}I_1}, \tag{21}$$

where

$$I_1=\int_0^d\exp[\psi(x)]dx,\quad I_2=\int_0^d\exp[\psi(x)-\alpha x]dx. \tag{22}$$

In the derivation of the second expression on the right-hand side of Eq. (21) we have used the integral of the equation of continuity for holes $q_p(x)=q_p(0)+I_i(1-e^{-\alpha x})$ and the boundary condition $q_p(0)=-V_p^T(p_0-p_0^{eq})-s_p p_0$.

Partitioning the domain of integration into the high-field region near the anode $0\leqslant x\leqslant\delta^+$, on the one hand, and the rest of the structure $\delta^+\leqslant x\leqslant d$, on the other, and invoking the steepest-descent method, we obtain the following expression to within terms of the order of $[n(\delta^+)/n_0]^{1/2}$:

$$p_0=\frac{I_i\alpha l_E^0(-\psi_+-2\alpha\delta^+)+V_p^T p_0^{eq}}{s_p+V_p^T+v_{dr}^p/2}. \tag{23}$$

It is evident from Eq. (23) that the surface density of photoelectrically generated holes is a product of three factors. The first factor is the photon flux density divided by the rate of escape of holes from the surface. The second characterizes the reduction of the density by virtue of the fact that all holes generated over the length α^{-1} overcome the energy barrier with the characteristic field E_0. The last factor accounts for the inhomogeneity of the electric field in the region of width δ^+, which provides the main contribution to the hole flux toward the anode.

We now make some numerical estimates of characteristic quantities. We consider the initial parameters $I_i=10^{15}$ $\mathrm{cm^{-2}\cdot s^{-1}}$, $T_n=T_p=10^{-9}$, $V_p^T=6\times10^{-3}$ cm/s, $V_n^T=8.5\times10^{-3}$ cm/s, $s_p=s_n=10^7$ cm/s, $\varphi_{Vn}=0.71$ V, $p_0^{eq}=2.5\times10^5$ $\mathrm{cm^{-3}}$, $E_e=2\times10^3$ V/cm, and $\alpha=10^4$ $\mathrm{cm^{-1}}$.

We then have $n_0=1.2\times10^{17}$ $\mathrm{cm^{-3}}$, $L_D^n=1.2\times10^{-6}$ cm, $\delta^+=2.4\times10^{-5}$ cm, $n(\delta^+)/n_0=1/252$, $E_0/E_e=15.9$, $E_0=3.2\times10^4$ V/cm, $p_0=3.8\times10^6$ $\mathrm{cm^{-3}}$, $-\psi_+=5.52$, and $\alpha l_E^0=0.008$. For the given values of φ_{Bn} the relative contribution of the term containing p_0^{eq} in expression (23) is of the order of 10^{-9}.

Thus, under the given conditions ($T_{n,p}\simeq10^{-9}$, $I_i=10^{15}$ $\mathrm{cm^{-2}\cdot s^{-1}}$) an electron density $\simeq10^{17}$ $\mathrm{cm^{-3}}$ is formed in a layer of thickness $\simeq100$ Å near the anode. This creates fields that are an order of magnitude stronger than the external field but are not sufficient to produce appreciable voltage drops on the film. The physical picture in the electrode sheaths is reminiscent of phenomena in the high-field region of conventionally doped semiconductors (n–s or p–s structures), but in our case these layers are subjected to carrier enrichment rather than depletion. A further decrease in the transmissivity takes the analysis beyond the scope of the adopted model by virtue of the onset of high carrier densities near the electrodes and characteristic lengths commensurate with the carrier mean free path. The carrier gas becomes a two-dimensional system in this parameter domain.

4.2.5. To find the current density, we use the expression $j/e=q_p(0)-q_n(0)=I_i+q_p(0)-q_n(d)$, where the flux $q_p(0)=-V_p^T(p_0-p_0^{eq})-s_p p_0$ is determined by the density p_0 [Eq. (23)], and the electron flux $q_n=-V_n^T(n_d-n_d^{eq})+s_n n_d$ depends on the density n_d, whose calculation is analogous to that of p_0. We finally obtain

$$\frac{j}{e}=I_i\left[1-\frac{\alpha l_E^0(s_p+V_p^T)(-\psi_+-2\alpha\delta^+)}{s_p+V_p^T+v_{dr}^p/2}\right]+\frac{j_0}{e}, \tag{24}$$

where

$$\frac{j_0}{e}=\frac{V_p^T v_{dr}^p p_0^{eq}}{2(s_p+V_p^T+v_{dr}^p/2)}+\frac{V_n^T v_{dr}^n n_0^{eq}}{2(s_n+V_n^T+v_{dr}^n/2)}. \tag{25}$$

Equation (24) contains two different terms: the photocurrent and the thermal generation current j_0. The photocurrent, approximately proportional to I_i, increases slightly with decreasing transmissivity, tending to eI_i. This means that the resulting anode field completely inhibits the diffusion of holes toward the anode. It is also evident that surface recombination has little influence on the photocurrent, since $n_0\gg p_0$. The dependence of the photocurrent on the external voltage is taken into account through the quantity ψ_+ $[-\psi_+=2\ \ln(E_0 d/V)]$. The current decreases as the voltage is

lowered, but Eq. (24) should not be used for small V, because the conditions underlying its derivation are violated.

In contrast with the photocurrent, the thermal generation current j_0 is proportional to the transmissivity, and its contribution to the total current is determined mainly by the barrier height φ_{Bn}. In the numerical example discussed above ($\varphi_{Bn}=0.71$ V), the current j_0 is inconsequential. We note that surface recombination can significantly lower the value of j_0 and that the latter depends on I_i through the carrier drift rates.

5. DISCUSSION OF THE RESULTS

We wish to point out that there is one case in which the current–intensity dependence for small field variations (9) differs significantly from the analogous dependence (24) in the presence of large field variations near the electrodes. In the first case the shielding of a sizable portion of the external field by photoelectrically generated holes diminishes the anode field E_0 at intensities above the characteristic value I_*, producing a sublinear dependence $j(I_i)$ (Ref. 1). In the second case accumulation effects are dominant in the vicinity of the anode, $E_0<E_e$, and the dependence $j(I_i)$ is almost linear. What is the dependence $j(I_i)$ for structures with different interface tunnel transmissivities? We can assume that the form of the function $j(I_i)$ is dictated by competition between the two processes mentioned above, i.e., it depends on the relation between the intensity I_* (Ref. 1), which determines the lower limit of significance of shielding effects, and the intensity I_E, which determines the domain in which accumulation effects are significant. In the case $I_E \gtrsim I_*$, as the illumination intensity is increased, the function $j(I_i)$ has an initial sublinear interval, but then in the regions of large field variations near the semiconductor boundaries the function $j(I_i)$ is once again linear. In the opposite case $I_E<I_*$ the saturation regime is not achieved, and $j(I_i)$ remains linear, but its slope increases. A rough estimate of the intensity I_E can be obtained by integrating the Poisson equation over an interval of width δ^+. Assuming that the variation of the field in this layer is an ξ-fraction of E_e and that the density and thickness have values $n_0=I_i/V_n^T \gg n(\delta^+$ and $\delta^+=2l_E^e$, respectively, on the basis of the trapezoidal rule we obtain the expression $4\pi e n_0 l_E^e/\varepsilon=\xi E_e$, from which it follows that

$$I_E=\xi\,\frac{\varepsilon E_e^2 V_n}{4\pi kT}\,T_n. \tag{26}$$

For $E_e=2\times10^3$ V/cm, $\xi=0.1$, $V_n=8.5\times10^6$ cm/s, and $T_n=10^{-6}$ we obtain $I_E=10^{15}$ cm$^{-2}\cdot$s^{-1}, which is in good agreement with the numerical result. When the expressions for I_* (17) and I_E (25) are taken into account, the condition $I_E \gtrsim I_*$ acquires the form

$$T_n \gtrsim \frac{\varepsilon}{4\pi\xi}\,\frac{D_p}{dV_p}, \tag{27}$$

which implies that structures with high tunnel transmissivities at the boundaries have a sublinear interval in the dependence $j(I_i)$.

The onset of regions of high space charge density near the electrodes is a characteristic feature of illuminated, highly biased, high-resistivity MISIM structures. It is natural to inquire which processes slow down the growth of the densities and the field near the semiconductor boundaries. In our opinion, the responsible process is carrier injection from the metal due to the large film potential drop, which lowers the potential barrier that must be overcome by a tunneling particle when it falls within the corresponding band of the semiconductor. In particular, in an insulator of thickness $d_i=30$ Å subjected to a field $E_i=(\varepsilon_s/\varepsilon_i)E_0 \simeq 3\times10^5$ V/cm we have $V_i=0.1$ V. This effect causes the injection current and the enhancement of carrier recombination (through the surface level) to be accompanied by an increase in the values of p_0 and n_d, thereby diminishing the rate of increase of n_0, p_d, E_0, and E_d. The hole current can be calculated from (24) with p_0^{eq} replaced by $p_0\exp(eV_i^0/kT)$. To estimate the domain of parameters in which hole injection from the anode becomes significant, we set the current j_0 equal to the value $\xi e I_i$ ($\xi \gtrsim 0.1$). Disregarding the electron component of the current j_0, we obtain an equation for the dimensionless voltage $\psi=eV_i^0/kT$:

$$e^{\psi}=\gamma\beta\psi^2, \quad \gamma=\frac{\varepsilon_i^2}{8\pi\varepsilon_s}\,\frac{V_n^T}{V_p^T}\,\frac{kT}{e^2 d_i^2 p_0^{eq}}, \quad \beta=\xi\left(1+\frac{2s_p}{v_{dr}^p}\right). \tag{28}$$

For $\gamma\beta \gg 1$ Eq. (27) has the approximate solution

$$\psi \simeq \frac{\ln(\gamma\beta)(1+2\,\ln\ln(\gamma\beta)}{(\ln(\gamma\beta)-2)}. \tag{29}$$

For $\varphi_{Bn}=1$ V, $d_i=30$ Å, $\varepsilon_s=10.9$, $\varepsilon_i=3$, $V_n^T/V_p^T=1.4$, $T=300$ K, $\xi=0.1$, and $\beta=0.2$ we obtain $\gamma=4.7\times10^6$, $\psi=17.2$, $V_i^0=0.44$ V, $E_i=1.5\times10^6$ V/cm, and $E_0=4\times10^5$ V/cm.

It follows from Eq. (27) that the injection regime sets in at lower values of V_i^0 for higher values of φ_{Bn} and lower temperatures.

[1] P. G. Kasherininov, B. I. Reznikov, and G. V. Tsarenkov, Fiz. Tekh. Poluprovodn. **26**, 1480 (1992) [Sov. Phys. Semicond. **26**, 832 (1992)].
[2] B. I. Reznikov and G. V. Tsarenkov, Fiz. Tekh. Poluprovodn. **27**, 1262 (1993) [Semiconductors **27**, 699 (1993)].
[3] B. I. Reznikov and G. V. Tsarenkov, Fiz. Tekh. Poluprovodn. **28**, 242 (1994) [Semiconductors **28**, 146 (1994)].
[4] B. I. Reznikov and G. V. Tsarenkov, Fiz. Tekh. Poluprovodn. **28**, 867 (1994) [Semiconductors **28**, 506 (1994)].
[5] B. I. Reznikov and G. V. Tsarenkov, Fiz. Tekh. Poluprovodn. **28**, 1788 (1994) [Semiconductors **28**, 991 (1994)].
[6] B. I. Reznikov and G. V. Tsarenkov, Fiz. Tekh. Poluprovodn. **29**, 1430 (1995) [Semiconductors **29**, 743 (1995)].
[7] B. I. Reznikov and G. V. Tsarenkov, Fiz. Tekh. Poluprovodn. **29**, 2199 (1995) [Semiconductors **29**, 1147 (1995)].
[8] M. A. Green and J. Shewchun, Solid–State Electron. **17**, 349 (1974).
[9] A. A. Sachenko and O. V. Snitko, *Photoelectric Effects in the Surface Layers of Semiconductors* [in Russian], Naukova Dumka, Kiev (1984).
[10] B. I. Reznikov and G. V. Tsarenkov, Fiz. Tekh. Poluprovodn. **25**, 1922 (1991) [Sov. Phys. Semicond. **25**, 1158 (1991)].
[11] V. I. Strikha, *Theoretical Principles of the Operation of Metal–Semiconductor Contacts* [in Russian], Naukova Dumka, Kiev (1974), p. 36.
[12] J. G. Simmons and G. W. Taylor, Solid–State Electron. **29**, 287 (1986).
[13] A. A. Gutkin and V. E. Sedov, Fiz. Tekh. Poluprovodn. **10**, 1589 (1976) [Sov. Phys. Semicond. **10**, 945 (1976)].
[14] N. F. Mott and W. Gurney, *Electronic Processes in Ionic Crystals*, 2nd Ed., Dover, New York (1964).

Translated by James S. Wood

Growth of ZnSe films on GaAs(100) substrate by x-ray-enhanced, vapor-phase epitaxy

A. V. Kovalenko

Dnepropetrovsk State University, 320625 Dnepropetrovsk, Ukraine
(Submitted January 11, 1995; accepted for publication February 19, 1996)
Fiz. Tekh. Poluprovodn. **31**, 31–34 (January 1997)

Epitaxial films of ZnSe deposited on a GaAs(100) substrate are grown by x-ray-enhanced, vapor-phase epitaxy (XEVPE) using a URS-55a source (CuKα emission, $\lambda = 1.542$ Å, $P \sim 1-3$ mW/cm^2) from powdered raw material in a purified hydrogen flow. The differences in the photoluminescence and exciton reflection spectra are investigated for single-crystal ZnSe films on GaAs(100) at $T = 4.5$ K, which are subjected to compressive strain and are grown by x-ray enhanced and conventional VPE. The results indicate an improvement of the crystallographic structure of the epitaxial layer prepared by XEVPE. This is further corroborated by data from x-ray diffraction analysis. The observed phenomena are attributed to x-ray activated adsorption and desorption processes and to a change in the surface mobility of adsorbed atoms.
 [S1063-7826(97)00701-1]

The mass production of thin-film devices for microelectronic and optoelectronic applications is encouraging efforts to perfect technologies for the preparation of semiconductor films with prescribed optical properties. In the growth of high-quality films of II–VI compounds having a wide band gap, stringent requirements for chemical purity and structural perfection of the layers drastically limits the number of workable technologies. Among the latter are molecular beam epitaxy, deposition from the gaseous phase using organometallic compounds, atomic layer epitaxy, and vapor-phase epitaxy.[1–5] Holding special status in this regard are growth techniques that permit the properties of the film to be fine-tuned during growth by treating its surface with laser beams, plasma, etc.[4–8]

The objective of the present study is to compare the properties of ZnSe films on a GaAs(100) substrate, grown by vapor-phase epitaxy (VPE) and by x-ray-enhanced, vapor-phase epitaxy (XEVPE).

ZnSe/GaAs(100) heterostructures were grown from a Merck & Co. powder source in a flow of purified hydrogen. The technological parameters of the preparation of the layers and a description of the growth apparatus are detailed in Refs. 9 and 10. X-ray enhancement of the process was achieved using radiation with a power low enough not to induce direct desorption, which would degrade the surface morphology of the epitaxial layer. The x-rays (from a URS-55a source, CuKα emission, $\lambda = 1.542$ Å, $P = 1-3$ mW/cm^2) entered a quartz crystal-growth reactor through a special beryllium window and were directed onto the GaAs(100) substrate.

The objects chosen for the investigation were two samples found to be typical in a series of many repeated experiments. The first sample was grown by VPE at a temperature $T = 256°$, a carrier gas flow rate ~ 0.2 liters/min, a growth rate ~ 1.7 μm/h, and a thickness of the epitaxial layer ~ 0.5 μm. The second sample was prepared with the same technological growth parameters and with the same epitaxial layer thickness, but by XEVPE. For brevity we shall refer to the selected samples from now on as samples 1 and 2.

X-ray diffraction analysis data (Fig. 1) indicate a high degree of lattice perfection on the part of the sample grown by XEVPE. This quality is supported by the variation of the parameters of the diffraction peak associated with reflection from the ZnSe 400_β plane in this sample in comparison with the corresponding parameters of the same peak in sample 1: high intensity (the ratio of the two intensities is 3.97) and a small half-width (4–6′) for sample 2 and 6–9′ for sample 1). The improvement in the crystal quality of sample 2 is further indicated by the results of an analysis of the exciton photoluminescence (EPL) spectra excited by a He–Cd laser ($h\nu = 3.814$ eV). Besides the free exciton E_x ($h\nu = 2.8042$ eV), the following EPL lines associated with shallow donors were also observed in the investigated samples (Fig. 2): I_2 ($h\nu = 2.7990$ eV, $\Delta E = 5.2$ meV) — an exciton associated with a shallow donor, obviously Ga; I_3 ($h\nu = 2.7961$ eV, $\Delta E = 8.1$ meV) — an exciton associated with an ionized donor, Ga^+. The assumption that these EPL lines are associated with a shallow Ga donor is corroborated by recent survey data[1] and by secondary investigations of our own confirming an increase in the intensities of I_2 and I_3 bands in ZnSe epitaxial films specially doped with Ga during growth by means of an additional source situated in the quartz reactor. Also observed in the photoluminescence spectra of the investigated samples were EPL lines associated with shallow acceptors: I_1^y ($h\nu = 2.7935$ eV, $\Delta E = 10.7$ meV) — an exciton associated with a shallow acceptor, probably Na; I_1^x ($h\nu = 2.7890$ eV, $\Delta E = 15.2$ meV) — an exciton associated with a shallow acceptor, Li; I_1 ($h\nu = 2.7804$ eV, $\Delta E = 23.8$ meV) — an exciton associated with a shallow acceptor induced by a structural defect, V_{Zn}. The same EPL lines were recorded in sample 1. In analyzing the nature of the EPL bands, we relied on the results of our own preliminary investigations,[5] the results of a spectral analysis, and data from the cited survey.[1] According to earlier data,[11,12] the line I_v ($h\nu = 2.7743$ eV) is the result of nonexcitonic recombination at a local defect, possibly at a Se site. The improved lattice perfection of sample 2 is manifested in the high intensity of the free exciton line E_x, the sharper appearance of such EPL bands as I_2, I_3, I_1^y, and I_1^x and also in the reduction of the total inten-

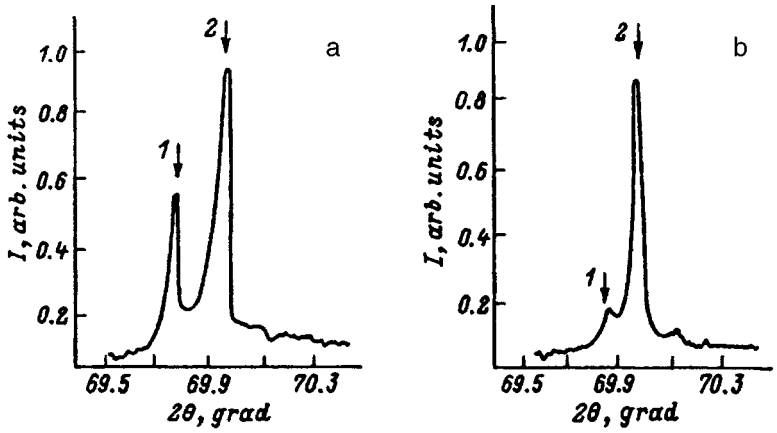

FIG. 1. Diffraction patterns of ZnSe/GaAs(100) heterostructures grown by: a) vapor-phase epitaxy; b) x-ray-enhanced VPE. *1*) $(400)_\beta$ ZnSe; *2*) $(400)_\beta$ GaAs.

sity of the emission bands associated with structural defects, i.e., the lines I_1 and I_v.

It should be emphasized at this point that, owing to internal deforming stresses present in a ZnSe/GaAs(100) heteroepitaxial structure, the degenerate (at the point Γ) valence band of bulk ZnSe in the epitaxial layer splits into subbands of ''light'' (E_{th}) and ''heavy'' (E_{hh}) holes. Compressive strain due to mismatch of the lattice parameters of the epitaxial layer and the substrate are predominant in films with $d_0<0.15$ μm. Here the split E_{lh} and E_{hh} subbands do not overlap, the E_{hh} subband is closer to the conduction band, and the width of the band gap of ZnSe increases. The compressive stress decreases in the interval of film thicknesses $d_0<d<d_c=0.88$ μm as a result of the emergence of misfit dislocations. The investigated samples with epitaxial layers of thickness $d=0.5$ μm are subjected to compressive strain (the exciton bands for this case are shown schematically in the inset to Fig. 3). For $d>d_c$ the film is dominated by tensile strain due to the difference in the coefficients of thermal expansion of ZnSe and GaAs. In this case the E_{ln} and E_{hh} bands overlap, the E_{ln} subband is closer to the conduction band, and the width of the band gap of ZnSe decreases. The influence of deforming stresses on the positions of the EPL bands in ZnSe/GaAs(100) heterostructures with epitaxial layers of various thicknesses have been analyzed in detail.[5]

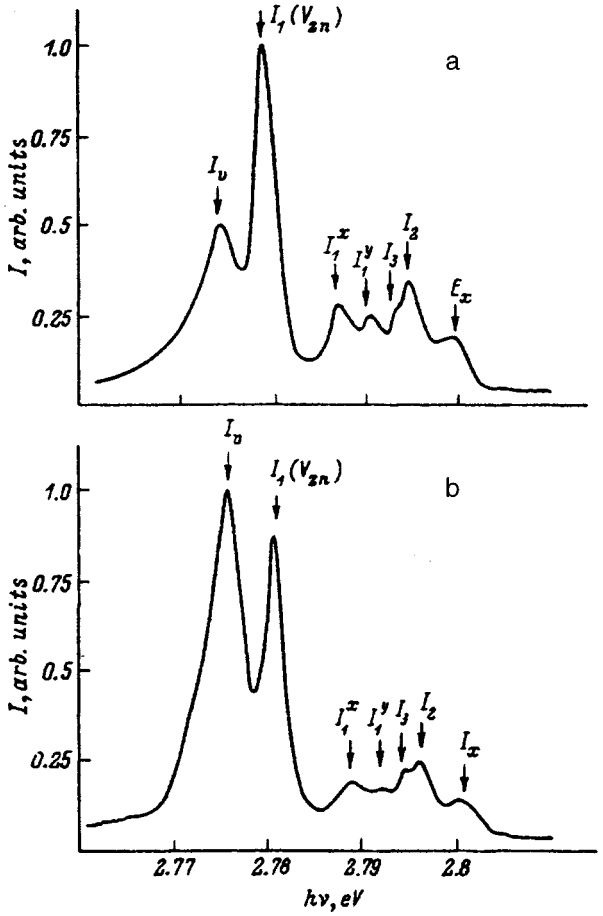

FIG. 2. Exciton photoluminescence spectra of ZnSe films grown on GaAs(100) by: a) VPE; b) XEVPE. $T=4.5$ K.

Processes of scattering by imperfections of the crystal structure of the ZnSe film and by acoustic phonons have important bearing on the establishment of thermodynamic equilibrium in the system light + heavy excitons. The role of the first processes diminishes as the quality of the epitaxial layer improves, while the role of the second diminishes as the driving frequency approaches exciton resonance.[13] Only the emission of heavy excitons is observed in films of poor quality. Nonequilibrium filling of the band of light excitons in thin epitaxial layers of ZnSe can be observed under conditions of the resonance excitation of EPL by a He–Cd laser ($h\nu=2.807$ eV). The emission of free excitons associated with light holes E_{ln} ($h\nu=2.8048$ eV) and heavy holes E_{hh} ($h\nu=2.8034$ eV) is distinctly observed in the EPL spectra in this case (Fig. 3). The splitting of the exciton bands, in turn, causes an exciton bound to a shallow donor I_2 to split into two components associated with light and heavy holes: I_{20}^{ln} ($h\nu=2.7998$ eV, $\Delta E=5.0$ meV) and I_{20}^{hh} ($h\nu=2.7988$ eV, $\Delta E=4.6$ meV), respectively. A notable feature of the illustrated EPL spectrum of sample 2 is the high intensity of the free exciton lines; as mentioned, this is evidence of the higher lattice perfection of the epitaxial layer. Such improved quality is also attested by the exciton reflection (ER) spectra of the investigated samples (Fig. 3). For example, in the ER spectrum of sample 2 an exciton state with quantum number $n=2$ ($h\nu=2.815$ eV) is recorded, and the exciton state with quantum number $n=1$ is characterized by sharper

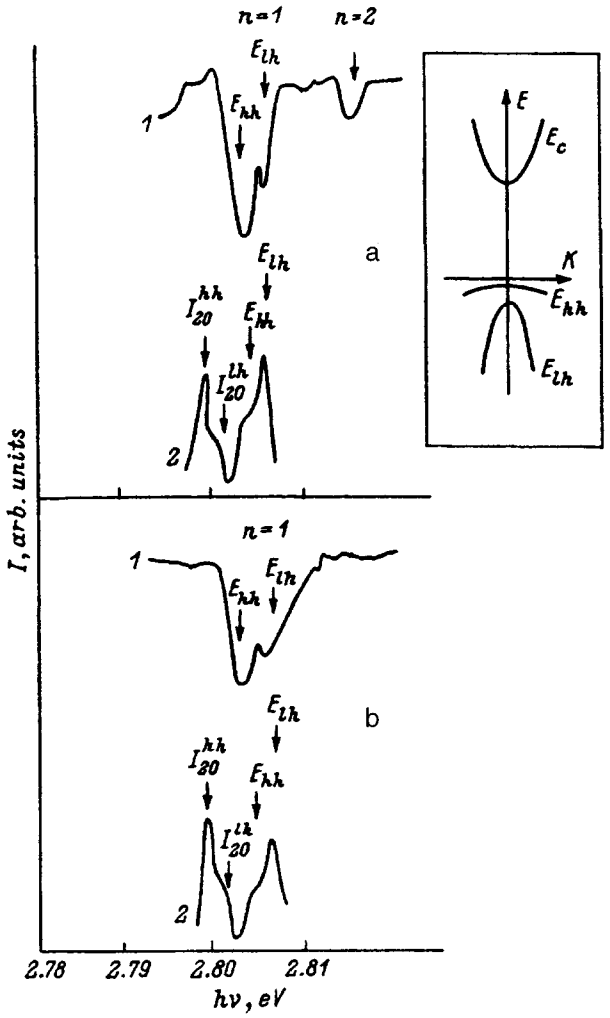

FIG. 3. Exciton reflection spectra (graphs 1) and resonance EPL (graphs 2) of ZnSe films grown on GaAs(100) by: a) VPE; b) XEVPE. $T=4.5$ K. Inset: schematic representation of the exciton bands of a ZnSe epitaxial layer under compressive strain.

lines of greater intensity. The free exciton energies E_{th} and E_{hh} determined from the EPL and ER spectra coincide.

These differences in the EPL and ER spectra of samples 1 and 2 are satisfactorily explained by the following growth model. The extinction of x-rays by the growing ZnSe layer with the formation of free $(e–h)$ pairs weakens the ionic bond, redistributes the density of electron states, and perturbs the sp^3 configuration, producing a metastable state. Direct desorption does not set in at low excitation intensities, and relaxation from the metastable state takes place through recombination involving deep-level centers. The energy released in this process is transferred to the skin layer of the ZnSe, lowering the heat of adsorption, enhancing the migration of adsorbed atoms over the surface, and ordering the crystal structure of the growing layer. X-rays can also induce the selective desorption of Se from the film surface. A similar phenomenon has been observed in laser-enhanced VPE.[5] This precludes any possibility of the growing film surface becoming ''contaminated'' with Se_2 molecules formed by chemical reactions in the vapor phase; it also prevents the formation of V_{Zn}, improves the crystal structure of the layer, and is manifested in suppression of the total luminescence intensity of the bands I_1 and I_v.

In summary, data from x-ray diffraction analysis and the results of an investigation of the EPL and ER spectra of samples grown by VPE and XEVPE indicate that irradiation of the surface of a single-crystal ZnSe film with x-rays during its growth on the GaAs(100) substrate improves the lattice perfection of the epitaxial layer. The results are analyzed on the basis of a qualitative model of the processes attending XEVPE.

The author is grateful to V. V. Tishchenko, N. V. Bondar', V. F. Katkov, and A. Yu. Mekekechko for their assistance and helpful discussions.

[1] J. Gutowski, N. Presser, and G. Kudlek, Phys. Status Solidi A **120**, 11 (1990).
[2] I. Yao, M. Fujimoto, S. Chang, and M. Tanino, J. Cryst. Growth **111**, 823 (1991).
[3] M. Umar-Syed and P. Lilley, J. Cryst. Growth **88**, 415 (1988).
[4] A. V. Kovalenko, A. Yu. Mekekechko, N. V. Bondar', V. V. Tishchenko, Yu. M. Shchekochikhin, S. M. Rumyantseva, and I. S. Malashenko, Fiz. Tekh. Poluprovodn. **26**, 1251 (1992) [Sov. Phys. Semicond. **26**, 698 (1992)].
[5] A. V. Kovalenko, A. Yu. Mekekechko, V. V. Tishchenko, and N. V. Bondar', Fiz. Tverd. Tela (St. Petersburg) **36**, 1350 (1994) [Phys. Solid State **36**, 737 (1994)].
[6] N. Matsumura, T. Fukada, and J. Saraie, J. Cryst. Growth **101**, 61 (1990).
[7] S. Fujita, A. Tanabe, T. Kinoshita, and S. Fujita, J. Cryst. Growth **101**, 48 (1990).
[8] T. Matsumoto, S. Yoshida, and T. Ishida, Jpn. J. Appl. Phys. **25**, L413 (1986).
[9] N. V. Bondar', A. V. Kovalenko, V. V. Tishchenko, and A. Yu. Mekekechko, Izv. Akad. Nauk SSSR Neorg. Mater. **27**, 2520 (1991).
[10] A. V. Kovalenko and P. Lilley, Izv. Akad. Nauk SSSR Neorg. Mater. **28**, 49 (1992).
[11] K. Shahzad, D. Olego, and D. Cammack, J. Cryst. Growth **101**, 763 (1990).
[12] K. Shahzad, D. Olego, and D. Cammack, Phys. Rev. B **39**, 13016 (1989).
[13] M. S. Brodin, V. V. Tishchenko, N. V. Bondar', A. V. Kovalenko, and A. Yu. Mekekechko, Ukr. Fiz. Zh. **37**, 1803 (1992).

Translated by James S. Wood

Photoelectric and photomagnetic properties of the gapless semiconductor $Cd_xHg_{1-x}Te$ in the infrared and millimeter spectral regions when an energy gap is opened

S. G. Gasan-zade, E. A. Sal'kov, and G. A. Shepel'skiĭ

Institute of Semiconductor Physics, National Academy of Sciences of Ukraine, 252650 Kiev, Ukraine
(Submitted December 19, 1995; accepted for publication February 19, 1996)
Fiz. Tekh. Poluprovodn. **31**, 35–42 (January 1997)

The magnetic-field and strain dependences of the photoelectric, photomagnetic, and photothermomagnetic characteristics are determined for the gapless semiconductor $Cd_xHg_{1-x}Te$ ($x=0.04$–0.16), in which an energy gap is opened by external effects. In excitation by infrared radiation the photosignal is observed to increase sharply with an increase in the applied magnetic field or uniaxial elastic deformation. For radiation in the millimeter spectral range the photoresponse exhibits giant oscillations associated with the variation of the electron density. This phenomenon is confirmed by the field dependence of the photomagnetic Hall effect. It is shown that the photothermomagnetic effect is a differential signal relative to the photoconductivity signal. © *1997 American Institute of Physics.* [S1063-7826(97)00801-6]

INTRODUCTION

In a broad range of compositions ($0<x<0.160$, $T=4.2$ K) the ternary semiconducting compound $Cd_xHg_{1-x}Te$ (CMT) is a semiconductor without a band gap, i.e., a so-called gapless (or zero-gap) semiconductor. The gapless stage in CMT is a result of the symmetry of the lattice and is characterized by several distinctive features: inversion of the positions of the bands, the presence of impurity resonance levels, etc. The degeneracy of the bands at the point $k=0$ (the point where the conduction and valence bands meet) can be lifted by subjecting the gapless semiconductor to some external effect that lowers the symmetry of the crystal. Such an influence can be, for example, a magnetic field or uniaxial elastic deformation. The result is the formation of an energy gap whose width increases more or less linearly with the strength of the magnetic field H or the uniaxial stress P. The width of the gap can be regulated over a fairly wide range. For example, a magnetic field $H=50$ kOe can regulate the energy gap in gapless CMT within the interval 0–40 meV, which encompasses a spectral range of radiation from millimeters to several tens of micrometers.

The high sensitivity of the band spectrum to an external influence qualifies gapless CMT as a promising material for the development of tunable photodetectors in the far infrared and millimeter ranges. It is instructive in this regard to study photoelectric and photomagnetic phenomena in gapless semiconductors when an energy gap is formed. Measurements of the photoconductivity of gapless CMT in a magnetic field have been reported previously for radiation in the infrared[1,2] and millimeter[3,4] ranges.

Here we give the results of an investigation of the photoconductivity, along with the photoelectromagnetic effect (PEME) and the photothermomagnetic effect (PTME) in gapless CMT after an energy gap has been induced in it by a magnetic field and uniaxial elastic deformation. Simultaneously we have measured the Hall coefficient R_H and the variation of the conductivity σ in the investigated samples under these conditions.

We briefly discuss the influence of a magnetic field and uniaxial deformation on the energy spectrum of a gapless semiconductor near the edges of the principal bands.[5] According to the inverse model of the energy spectrum of gapless CMT, the order of the Γ_6 and Γ_8 bands is reversed from a conventional semiconductor. The Γ_6 band in a gapless semiconductor has negative curvature and forms a band of light holes. The Γ_8 band remains degenerate at the point $k=0$. In this case the subband with light effective mass (with S symmetry) has positive curvature and comprises the conduction band. The curvature of the other Γ_8 subband (with P symmetry) remains negative, and it forms an ordinary band of heavy holes (Fig. 1a).

In a magnetic field an energy gap is formed between the Γ_8 bands (Fig. 1b) and is described in terms of the Luttinger parameters: $\delta(H)=(\gamma_1-\gamma)\hbar\omega_c$. Here $\omega_c=eH/m_n$ is the

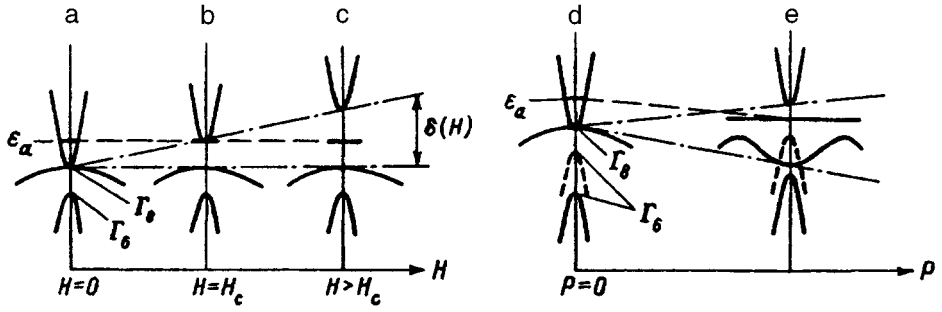

FIG. 1. Band structure of the gapless semiconductor $Cd_xHg_{1-x}Te$. a–c) In a magnetic field; d, e) under uniaxial stress (for two different compositions x.

 1063-7826/97/010029-07$10.00

TABLE I. Parameters of the investigated $Cd_xHg_{1-x}Te$ samples, $T=4.2$ K.

Sample No.	Composition x	n, cm^{-3}	μ_n, $cm^2/W\cdot s$
1	0.040	1.27×10^{15}	1.52×10^5
2	0.157	3.83×10^{14}	6.81×10^5
3	0.159	8.27×10^{14}	7.25×10^5
4	0.160	3.78×10^{14}	6.15×10^5
5	0.135	5.28×10^{14}	4.97×10^5

Note: The Hall coefficient was measured at $H=0.5$ kOe.

electron cyclotron frequency. If the contribution of distant bands is disregarded, the energy gap is well described by the simple expression $\delta(H)=\hbar\omega_c/4$. The acceptor level E_A moves after the top of the valence band and for $H>H_0$ enters the field-generated gap (Fig. 1c).

The energy spectrum of the gapless semiconductor is more complicated under uniaxial stress.[6–8] At the point $k=0$ the gap grows linearly with the stress and depends on the crystallographic direction. For example, in the direction $P\|[100]$ we have $E(P)=\frac{1}{4}b(S_{11}-S_{12})P$. Here b is the strain constant, and S_{ij} denotes the components of the compliance tensor. In addition to the energy gap at the point $k=0$, the valence band acquires side ($k\neq0$) extrema (Fig. 1e). Now, while the energy gap between the Γ_6 and Γ_8 bands is fairly small in the initial state, $|F_g|<100$ meV, at large stresses the Γ_6 band near $k=0$ can be higher than the Γ_8 band (Figs. 1d and 1e, dashed curves).[7]

EXPERIMENTAL RESULTS AND DISCUSSION

The transformation of the band spectrum of gapless CMT produces qualitative changes in its kinetic and optical characteristics. The changes are associated with variations of the density and the mobility of the charge carriers. As a rule, gapless CMT crystals exhibit *p*-type conductivity in the initial state. We have investigated *p*-CMT crystals with a concentration of electrically active impurities $N_A-N_D=3\times10^{16}$–5×10^{16} cm^{-3}, $N_A\gg N_D$. The differential densities of acceptors N_A and donors N_D was estimated from the saturation of the Hall coefficient R_H in a magnetic field $H=75$ kOe at the impurity depletion temperature ($T=78$ K). The density of electrons in the conduction band was determined from the period of the Shubnikov–de Haas oscillations, and the total donor density was determined from measurements of R_H at $T=1.8$ K. The samples had typical dimensions $0.5\times1.5\times7$ mm^3. The parameters of the samples are summarized in Table I. The radiation sources were lasers ($\lambda=3.39$–10.6 μm) and millimeter-range oscillators ($\lambda=2$–15 mm). Because of the low effective mass of the electrons, the donors in gapless CMT remain ionized down to the very lowest temperatures. The Fermi level in this case is fixed in the acceptor band.[5] Consequently, in the gapless state ($x<0.160$; $H=0$, $P=0$), despite the relation $N_A\gg N_D$, the Hall coefficient is determined by electrons with a density $1/eR_H$ and mobility $R_H\sigma$.

Figures 2 and 3 show the field and strain dependences of the electrical resistivity ρ and the coefficient R_H for gapless $Cd_xHg_{1-x}Te$ samples of various compositions x. The observed abrupt variations of the kinetic characteristics of the gapless semiconductor have a simple qualitative interpretation. In a quantizing magnetic field, when the energy of the lowest Landau level of the conduction band $\hbar\omega_c$ is higher than the acceptor energy E_A, electrons begin to freeze out of the conduction band into acceptor states. At $H>4E_A\cdot m_n/e\hbar$, $\hbar\omega_c\gg kT$, the electron density in the conduction band decreases exponentially, accounting for the observed field dependences of ρ and R_H.

The opening of the energy gap also becomes decisive under uniaxial deformation, along with the emergence of an acceptor level in it and the freezing out of electrons from the conduction band. This accounts for the complex form of the field and strain dependence of the kinetic coefficients (Figs. 2 and 3). The abrupt variation of the electron density with increasing stress occurs after the Fermi level intersects the bottom of the conduction band, i.e., for $P>4E_A/b(S_{11}-S_{12})$. However, for crystals with small values of E_g ($x=0.155$–0.159) R_H and ρ exhibit a very specific behavior in the range of large strains (Fig. 3). This kind of strain dependence is most likely associated with the change in order of the Γ_6 and Γ_8 bands and the appearance of free holes with low effective masses[7] (see Fig. 1e, dashed curve).

In the gapless state the photoconductivity induced by the radiation-induced departure of the carrier density from equilibrium is negligible. This is attributable to the very high

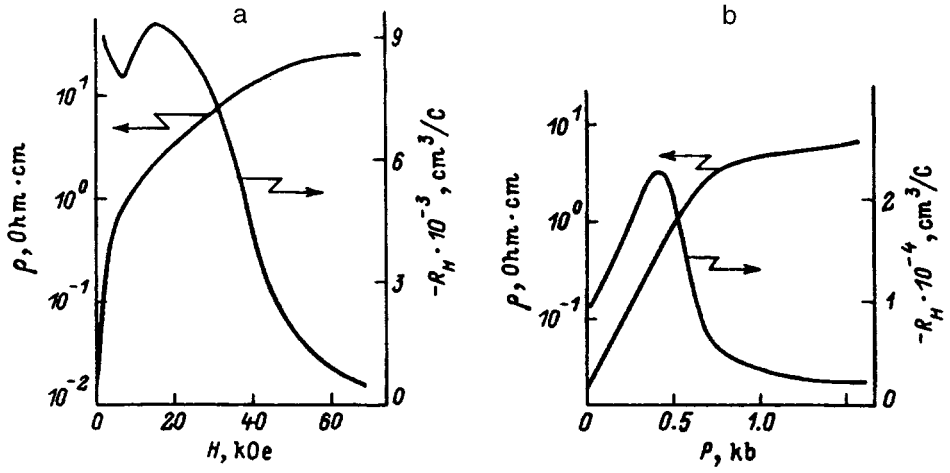

FIG. 2. Comparison of the field (a) and strain (b) dependences of ρ and R_H for sample 1, $T=1.7$ K.

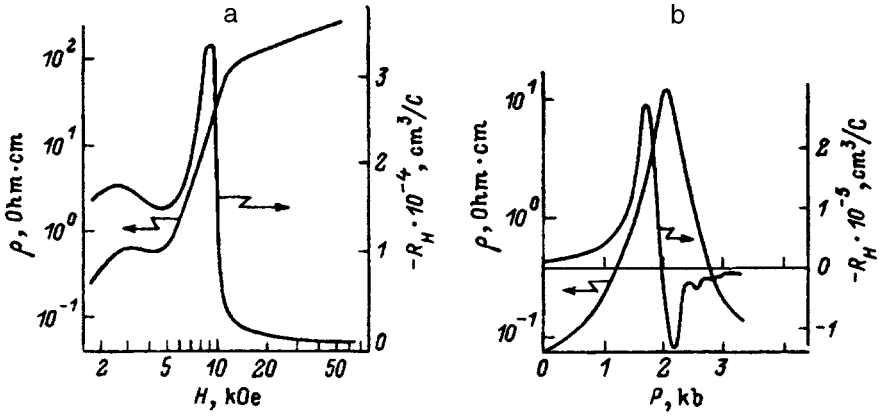

FIG. 3. Field (a) and strain (b) dependences of the electrical resistivity and the Hall coefficient for sample 2, $T=1.6$ K.

carrier recombination rate. As mentioned earlier,[8] the actual concept of recombination becomes meaningless in gapless semiconductors, because it is indistinguishable from the scattering process.

The emergence of an energy gap results in the generation of a strong interband photoconductivity signal at $\lambda=3-10$ μm (Fig. 4). The field dependence of the photoconductivity has several prominent features. Because the energy gap is small, and because the ratio between the effective masses of heavy holes and electrons is large ($m_h/m_n \sim 10^2$ for $x=0.155$), the main contribution to recombination is from interband transitions: radiative and impact (Auger type). The rapid growth of the photoconductivity signal as the magnetic field is increased ties in directly with the freezing out of free electrons from the conduction band at $H>4E_A \cdot m_n/e\hbar$. The fact that the field characteristic of the photoconductivity signal is steeper than for magnetoresistance indicates the predominance of the Auger recombination mechanism. Indeed, in the range of H corresponding to the freezing out of electrons the magnetoresistance is essentially a linear function of the electron density n. On the other hand, the rate of interband impact Auger recombination is a quadratic function of n.

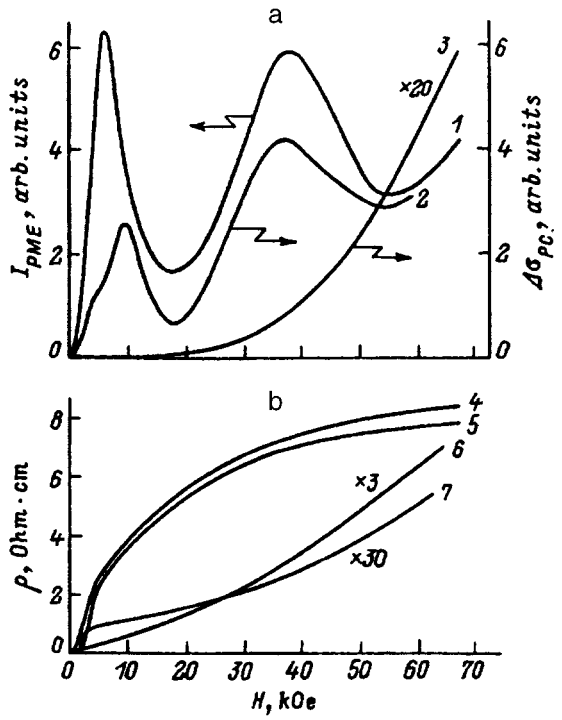

FIG. 4. Comparison of the voltage (a, curve *1*), the photoconductivity (a, curves *2* and *3*), and the longitudinal (b, curves *5* and *7*) and transverse (b, curves *4* and *6*) magnetoresistances as functions of the magnetic field at low temperatures for sample 3. 1, 2, 4, 5) 4.2 K; 3, 6, 7) 77 K.

Another important feature of the photoconductivity in a magnetic field is the low-temperature occurrence of large-amplitude oscillations in the range of H where the field dependences of R_H and ρ remain monotonic. The positions of the photoconductivity oscillations in a magnetic field is not affected by a variation of the radiation wavelength. This suggests that the oscillations are caused by a nonmonotonic dependence of the carrier lifetime τ on the magnetic field, and not by any specific characteristics of the absorption coefficient.

The positions of the photoconductivity minima in a magnetic field well satisfy the condition of equality of the energy gap $\delta(H)$ and the energy of a multiple number of longitudinal optical (LO) phonons: $\delta(H)=n\hbar\omega_{\mathrm{LO}}$ $(n=1,2,\ldots)$. This corresponds to resonance recombination transitions of electrons across the energy gap with the participation of LO phonons.[1] Invoking the expression $\hbar eH/4m_n=\hbar\omega_{\mathrm{LO}}$, we obtain, for the first minimum of V_{PC}, the width of the energy gap $\delta(H)=16.8$ meV, which is close to the LO phonon energy of HgTe, the principal sublattice of the $Hg_{0.855}Cd_{0.155}Te$ crystal: $\hbar\omega_{\mathrm{LO}}=17.2$ meV. The position of the second minimum corresponds quite well to twice the LO phonon energy. In this case a recombination transition takes place with the involvement of two optical phonons. Consequently, measurement of the interband photoconductivity can serve as a sensitive technique for detecting the formation of an energy gap in a gapless semiconductor and for determining its magnitude at a low temperature. On the other hand, by measuring $H_{\min}$ and knowing the LO phonon energy it is possible to determine the effective mass of electrons in the gapless semiconductor at the bottom of the conduction band.

At a higher temperature (77 K) the dark conductivity of the investigated gapless semiconductor samples is determined by the native electron density. Because of the high ratio $kT/\hbar\omega_c$ in this case, the appreciable radiation-induced

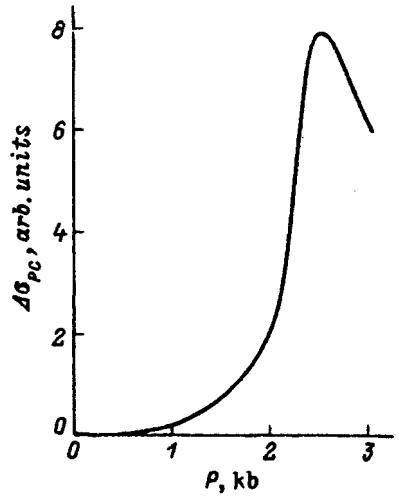

FIG. 5. Photoconductivity of sample 4 under uniaxial stress, $T=4.2$ K.

variation of the density n in the conduction band and the onset of a substantial photoconductivity signal occur in much higher fields H (Fig. 4, curve *3*). For this reason photoconductivity oscillations do not appear at $T=77$ K.

Oscillations that are multiples of the LO phonon energy also appear at a low temperature in the field dependences of the PEME (Fig. 4, curve *1*). In general, the characteristics of the bipolar PEME are determined by the minority carrier parameters, i.e., by electrons in our case. However, since the electron and hole lifetimes are equal for interband recombination mechanisms, the position of the PEME oscillations essentially coincides with that of the photoconductivity oscillations. In the gapless state a major contribution to the PEME comes from the radiative heating of electrons.[10–12] If the electron–electron interaction time τ_{ee} is much shorter than the relaxation time τ_r of the electron energy at lattice oscillations, the main part of the energy of a hot photoelectron is redistributed among equilibrium electrons of the conduction band. This results in the heating of electrons in the conduction band. As a result of the nonuniform absorption of light, the sample acquires an electron temperature gradient. In a transverse magnetic field this leads to the onset of a thermal PEME, an analog of the Nernst–Ettingshausen effect at hot electrons. The thermal component can dominate the total PEME signal at low temperatures.[11,12]

However, when the energy gap is opened up by a magnetic field, the electron density in the conduction band decreases rapidly as H is increased, becoming exponentially small at $H>4E_A\cdot m_n/eh$. And the density n is what determines the characteristic time n_{ee}: $\tau_{ee}=E^{3/2}/h$. Consequently, for appropriate values of H ($H_{cr}=4.5$ kOe for sample 2) the thermal component of the PEME can be disregarded. This assertion is based on a comparison of the results of the field dependences of the PEME and the photoconductivity.

The opening of the energy gap under uniaxial deformation also produces a strong photoconductivity signal (Fig. 5). As P is increased, the photoconductivity increases very rapidly, reaching a maximum at $P=2.2$–2.5 kbar.

Next we consider the interaction of millimeter (microwave) radiation with gapless CMT. In conventional semiconductors with a low effective mass and fairly high electron density ($n>5\times10^{14}$–10^{15} cm^3), for example, InSb, the microwave photoconductivity is known to be dominated by so-called μ-photoconductivity.[13] It is attributable to the variation of the density of electrons as their effective temperature T_e is raised by radiative heating. A distinctive feature of the gapless state is that the native carrier density exhibits a power-law rather than an activation dependence on the temperature: $n_i\sim T^{3/2}$. It has been found that this form of temperature dependence of n_i can be used to significantly alter the density of electrons as they are heated. The variation should be especially large at low temperature, where T_e can increase substantially. At low temperatures, however, n_i is much smaller than the density of impurity electrons n in the conduction band (at $T=4.2$ K we have $n/n_i=10^2$–10^3, $n=10^{15}$ cm^{-3}). We have therefore found it impossible to determine the variations of the electron density by measuring R_H for gapless CMT irradiated in the millimeter range. Consequently, in a gapless semiconductor without P or H the millimeter-range photoconductivity is probably of the same nature as in ordinary semiconductors, i.e., amounts to ordinary μ-photoconductivity.

When an energy gap is formed between the conduction and valence bands, other mechanisms of interaction of long-wavelength radiation with a gapless semiconductor can come into play. It is possible for electrons to be ejected directly across the gap by long-wavelength radiation quanta. The spectral dependence of such photoconductivity must have a threshold on the long-wavelength radiation side, influencing the bolometric effect, i.e., the direct heating of the sample by radiation, which can be disregarded at the applied power of 10^{-4} mW. The photosignal associated with the radiative heating of electrons is at least two orders of magnitude stronger than the signal from the bolometric effect.[3,14]

When the electrons are heated, the usual μ-photoconductivity can be accompanied by a concentration component of the photoconductivity due to the thermal ejection of electrons across the energy gap. This component of the photoconductivity is associated with the thermal redistribution of electrons between the acceptor band and the conduction band as T_e increases. Its occurrence is made possible by the abrupt drop in the initial density of electrons in the conduction band as a result of their being frozen out by a magnetic field or by deformation. Consequently, the variation of the conductivity of the gapless semiconductor with increasing value of T_e can be identified with variations of both the mobility and the density of electrons:

$$\Delta\sigma=e\left(n\cdot\frac{d\mu}{dT_e}+\mu\cdot\frac{dn}{dR_e}\right)\Delta T_e. \tag{1}$$

In a sufficiently weak magnetic field ($H<H_{cr}$) the first component must obviously be dominant in the expression for $\Delta\sigma$. For $H>H_{cr}$, on the other hand, the concentration component begins to be the main factor contributing to the photosignal as H increases.[3] To test these assumptions, in addition to the microwave photoconductivity, we have measured

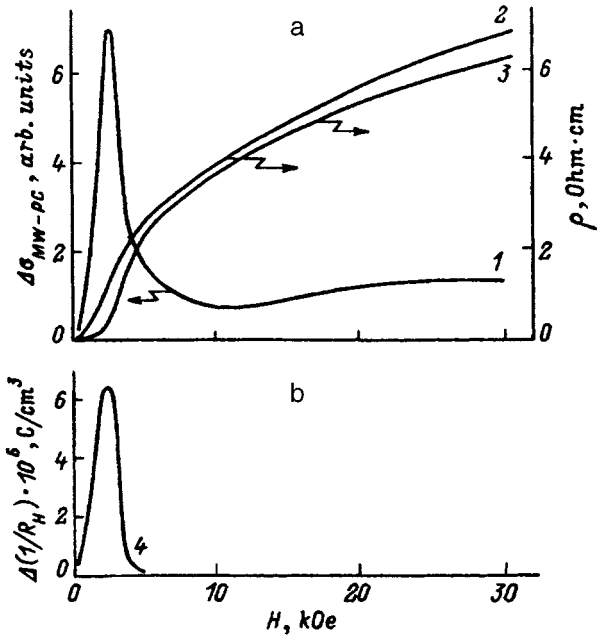

FIG. 6. Field dependence of the microwave photoconductivity (a, curve 1), the transverse (a, curve 2) and longitudinal (a, curve 3) magnetoresistances, and the carrier density increment $[\Delta(1/R_H)]$ (b, curve 4) for sample 4, $T=4.2$ K.

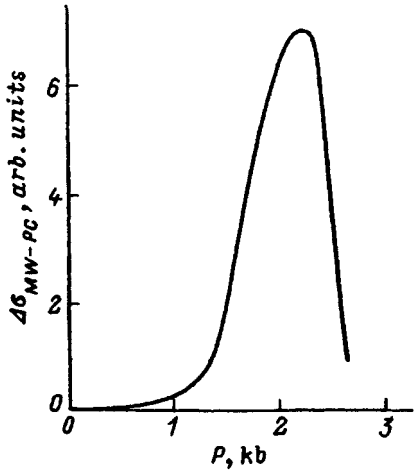

FIG. 7. Microwave photoconductivity of sample 5 vs uniaxial compression, $T=4.2$ K.

the Hall coefficient in the same samples under illumination and the PTME in the millimeter radiation range.

Figure 6 shows the field dependence of ρ and the microwave photoconductivity for sample 4. In the range of relatively weak fields ($H<3$ kOe) the photoconductivity oscillations practically coincide with the Shubnikov–de Haas oscillations for ρ. They have a small amplitude and, as a consequence, are not represented in the figure. As H is further increased, very large oscillations of the photoresponse are observed against the background of the monotonic growth of r. This field dependence of the microwave photoconductivity is in good agreement with the results in Ref. 3, in which the weak field (H) range, including the oscillations, is analyzed in detail. We therefore focus our attention primarily on the so-called giant maximum of the photosignal.

A variation of the frequency of the exciting radiation in the interval 2–15 mm does not alter the profile of the signal or the position of the maximum on the H scale. This means that the microwave photoconductivity is not associated with direct optical transitions of carriers across the energy gap created by the magnetic field. We can therefore assume that the main contribution to the photosignal is from the thermal concentration component of σ. In a strong field, when the Fermi level intersects the last Landau level, the variation of the dark conductivity is determined by electrons being frozen out of the conduction band into acceptor states. In this situation the microwave photoconductivity associated with the variation of T_e can be written as follows in the ultraquantum limit:[3]

$$\Delta\sigma \sim e\mu N_e \frac{\hbar\omega_c}{(kT)^2}\left(1+\frac{\hbar\omega_c}{|E_g|}\right)^{1/4}\Phi(\eta)\Delta T_e. \qquad (2)$$

Here the distribution function Φ can be written in the form of a one-parameter integral with parameter $\eta=[E_F-\delta(H)]/kT_e$, and N_e is the density of electron states with heating taken into account, $N_e=2(m_n kT_e/2\pi\hbar^2)^{3/2}$. The Fermi level is fixed in the acceptor band and does not depend on the magnetic field or the temperature in the low-temperature range ($T<4.2$–10 K). As the magnetic field is increased, the function Φ passes through a maximum at $\eta=-0.85$. The field strength H satisfying the above equation corresponds to the maximum of the microwave photoconductivity. This result has the physical significance that the width of the energy gap can be optimized for the given sample: $\delta(H_{\max})$. This optimum causes the electrons to be redistributed among states of the conduction band and the acceptor band in such a way as to maximize the photoconductivity signal as T_e is varied.

To test these estimates experimentally, we have measured the field dependence of the Hall coefficient of a gapless sample in two states: without irradiation (R_H) and with irradiation in the millimeter range (R_H^1). It is evident from curve *4* in Fig. 6 that the field dependence

$$\Delta\left(\frac{1}{R_H}\right)=\frac{1}{R_H^1}-\frac{1}{R_H}$$

has a distinct maximum, whose position virtually coincides with the maximum of the microwave photoconductivity on the H scale. This coincidence constitutes direct experimental proof of the concentration nature of the observed giant oscillations of the microwave photoconductivity in a strong magnetic field.

The application of uniaxial elastic deformation is also accompanied by the formation of an energy gap and a decrease in the electron density in the conduction band. Accordingly, as in a strong magnetic field, a strong microwave photoconductivity signal is generated with a characteristic maximum at a certain value $P_{\max}$ (Fig. 7). The value of $P_{\max}$ corresponds to the intersection of the Fermi level with the bottom of the conduction band: $E_F=b/4\times(S_{11}-S_{12})P_{\max}$ for the [100] direction.

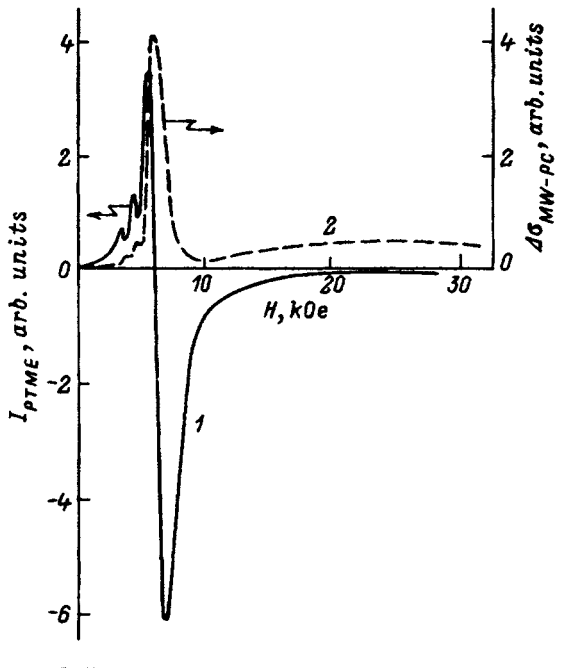

FIG. 8. Comparison of the field dependences of the photothermomagnetic effect (curve *1*) and the microwave photoconductivity (curve *2*) of sample 3, $T=4.2$ K.

The field dependences of the microwave photoconductivity and the PTME are compared in Fig. 8. It is generally known that a photothermomagnetic voltage is generated in a transverse magnetic field because of the presence of an electron temperature gradient associated with the nonuniform absorption of millimeter radiation by the sample.[15] The PTME is essentially an analog of the Nernst–Ettingshausen (N–E) effect at warm electrons, i.e., it takes place without any appreciable heating of the crystal lattice. It is noticeable that the field dependence of the PTME in the range of strong magnetic fields has a form similar to that of the first derivative of $V_{\mathrm{PC}}(H)$ with respect to H. To ascertain the cause of this characteristic feature of the PTME, we need to analyze the field dependence of the N–E coefficient in the quantum oscillation region.[16]

The PTME can be expressed in terms of the N–E coefficient Q:

$$E_{\mathrm{PTME}}=-Q\cdot\nabla T_e, \quad Q=\frac{\sigma_{11}\cdot\beta_{12}-\sigma_{12}\cdot\beta_{11}}{\sigma_{11}^2+\sigma_{12}^2}, \tag{3}$$

where σ_{ij} and β_{ij} are the kinetic coefficients in the equations for the galvanomagnetic and thermomagnetic effects, respectively.

The inequality $(\sigma_{12})^2\gg(\sigma_{11})^2$ holds in a classically strong magnetic field $(\mu H/c\gg 1)$.

The diagonal components of the tensors of kinetic coefficients can be written in the form

$$\sigma_{11}=\sigma_{11}^0\int dE\left(-\frac{\partial f}{\partial E}\right)g^2(E_F)W(E),$$

$$\beta_{11}=\beta_{11}^0\int dE\left(-\frac{\partial f}{\partial E}\right)g^2(E_F)W(E)\frac{E-E_F}{T}. \tag{4}$$

Here σ_{11}^0 and β_{11}^0 are dimensionless coefficients, $F(E)$ is a distribution function, $W(E)$ is a smooth function, and $g(E_F)$ is the density of states at the Fermi level.

In the presence of strong degeneracy of electrons we have

$$\sigma_{11}\sim g^2(E_F), \quad \beta_{11}\sim g(E_F)\frac{\partial g}{\partial E_F}.$$

In this case Q has the following form in a strong magnetic field:

$$Q\simeq\frac{\beta_{11}^0}{\sigma_{12}^0}C(E_F)\frac{\partial q}{\partial E_F}.$$

Here $G(E_F)$ is a smooth functions.

Consequently, in the region of oscillations where Q is highly nonmonotonic the term containing the derivative $\partial g/\partial E_F$ becomes dominant. For this reason, the oscillations of the N–E coefficient have a large amplitude and a phase shift relative to the conductivity oscillations, while the PTME is manifested in the form of the derivative of $V_{\mathrm{PC}}(H)$ with respect to H.

We can conclude from the foregoing discussion that gapless $Cd_xHg_{1-x}Te$ subjected to external influences such as a magnetic field and uniaxial elastic deformation exhibits photosensitivity over a wide range of the radiation spectrum. This range can be adjusted by varying the magnitude of the external influence. The volt–watt sensitivity of photodetectors utilizing a gapless semiconductor can surpass the sensitivity of detectors based on ordinary μ-photoconductivity. The latter assertion is based on the fact that the density of electrons, rather than their mobility, is the dominant factor in the conductivity of a gapless semiconductor.

The authors are grateful to the State Fundamental Research Foundation of the State Committee for Science and Technology of Ukraine for partial support of this work.

[1] R. Dornhaus, G. Nimtz, and B. Schlicht, *Narrow-Gap Semiconductors* [in Russian], Springer-Verlag, Berlin–New York (1985).
[2] S. G. Gasan-zade, V. A. Romaka, E. A. Sal'kov, and G. A. Shepel'skiĭ, JETP Lett. **39**, 678 (1984).
[3] Yu. G. Arapov, A. B. Davydov, and G. L. Shtrapenin, Fiz. Tekh. Poluprovodn. **18**, 1185 (1984) [Sov. Phys. Semicond. **18**, 742 (1984)].
[4] Yu. N. Gavrilyuk, S. G. Gasan-zade, E. A. Sal'kov, and G. A. Shepel'skiĭ, Fiz. Tekh. Poluprovodn. **13**, 1640 (1979) [Sov. Phys. Semicond. **13**, 955 (1979)]; S. G. Gasan-zade, E. A. Sal'kov, and G. A. Shepelsky, in *Digest of the Second International Conference on Millimeter Wave and Far-Infrared Technology*, Beijing (1992), p. 278.
[5] I. M. Tsidilkovski, G. I. Harus, and N. G. Shelushinina, Adv. Phys. **34**, 43 (1985).
[6] G. L. Bir and G. E. Pikus, *Symmetry and Strain-Induced Effects in Semiconductors*, Israel Program for Scientific Translations, Jerusalem; Wiley, New York (1975).
[7] F. T. Vas'ko, S. G. Gasan-zade, V. A. Romaka, and G. A. Shepel'skiĭ, JETP Lett. **41**, 120 (1987).
[8] A. V. Germanenko, G. M. Min'kov, E. L.Rumyantsev, and O. E. Rut, Zh. Éksp. Teor. Fiz. **94**, 242 (1988) [Sov. Phys. JETP **67**, 1654 (1988)].
[9] N. S. Baryshev, in *Proceedings of the Fourth All-Union Symposium on Narrow-Gap Semimetals and Semiconductors* [in Russian], Lvov (1975), Part 5, p. 7.
[10] R. I.Lyagushchenko, R. V. Parfen'ev, I. I. Farbshteĭn, S. S. Shalyt, and I. N. Yassievich, Fiz. Tverd. Tela (Leningrad) **10**, 2241 (1968) [Sov. Phys. Solid State **10**, 1764 (1969)].
[11] S. D. Lazarev, G. A. Shepel'skiĭ, and G. D. Efremova, Fiz. Tverd. Tela (Leningrad) **12**, 1718 (1970) [Sov. Phys. Solid State **12**, 1358 (1970)].

[12] Yu. N. Gavrilyuk, S. G. Gasan-zade, E. A. Sal'kov, and G. A. Shepel'skiĭ, Fiz. Tekh. Poluprovodn. **11**, 1571 (1977) [Sov. Phys. Semicond. **11**, 923 (1977)].
[13] Sh. M. Kogan, Fiz. Tverd. Tela (Leningrad) **4**, 1891 (1962) [Sov. Phys. Solid State **4**, 1386 (1963)].
[14] A. A. Manenkov, G. N. Mikhaĭlov, A. S. Severov, and V. D. Chernetskiĭ, Fiz. Tverd. Tela (Leningrad) **16**, 2719 (1974) [Sov, Phys. Solid State **16**, 1757 (1975)].
[15] A. N. Vystavkin, Sh. M. Kogan, T. M. Lifshits, and P. G. Mel'nik, Radiotekh. Élektron. **8**, 994 (1963).
[16] V. A. Pogrebnyak, D. D. Khalamwida, and V. V. Yakovenko, Solid State Commun. **68**, 891 (1988).

Translated by James S. Wood

Ion transfer processes in an insulating layer containing traps

E. I. Gol'dman

Institute of Radio Engineering and Electronics, Russian Academy of Sciences, 141120 Fryazino, Russia
(Submitted April 14, 1995; accepted for publication February 24, 1996)
Fiz. Tekh. Poluprovodn. **31**, 43–48 (January 1997)

A theory of ion transfer processes in an insulating layer containing a uniform distribution of traps throughout its volume is formulated. It is shown that free ions localized near the surface are held in a potential well created by repulsion from trapped carriers. Accordingly, the activation energy of the free-ion current is higher than the mobility activation energy and decreases as the voltage is increased, while detrapping takes place with a time delay. The temperature dependence of the depolarization current has two or three peaks, whose positions and profiles change with the voltage. A distinctive feature of the transfer of ions through an insulator containing traps is the ''memory'' of the electric field driving the carriers toward the surface prior to the start of the transfer process. © *1997 American Institute of Physics.* [S1063-7826(97)00901-0]

The thermally stimulated depolarization method has been used extensively for many years to determine the characteristics of mobile ions and their traps in insulators.[1–3] In the interpretation of the peaks of the polarization current–temperature curve it is customarily assumed that the ion traps are situated near the surface of the insulator at its boundaries with a metal or a semiconductor. In many cases, however, this approach cannot account for the experimentally observed profiles of the above-mentioned peaks or the dependence of their positions on the potential difference across the thickness of the insulator.[4,5] In this light we investigate the flow of ions across an insulation layer with a uniform volume distribution of traps having a density N_t. Let the insulator occupy the interval $0<z<h$, and at the initial time $t=0$ let all ions, each of which is assumed for definiteness to carry a single positive charge with a density per unit area k_s, be concentrated at the surface $z=0$. The relation between the volume densities of free ions k and those captured by traps k_t is described by the kinetic equation

$$\frac{dk_t}{dt}=\alpha_t(N_t-k_t)k-\frac{k_t}{\tau_t}, \tag{1}$$

and the ion energy potential well $U(z)$ is described by the Poisson equation

$$\frac{d^2U}{dz^2}=-\left(\frac{4\pi q^2}{\varkappa}\right)(k+k_t). \tag{2}$$

Here α_t is the capture coefficient, $\tau_t=\tau_0\exp(E_t/T)$ is the lifetime of an ion in a trap, E_t is the detrapping activation energy (temperature), T is the temperature in energy units, q is the elementary charge, and $\varkappa$ is the dielectric permittivity.

We assume that the ion system is in equilibrium initially, at $t<0$. Assuming that $dk_t/dt=0$ and that free ions have a Boltzmann distribution, we infer from Eqs. (1) and (2) that traps are filled in the layer $0<z<l$, where

$$l=\left[\left(\frac{\varkappa\mathcal{E}_-}{4\pi qN_t}\right)^2+l_{\max}^2\right]^{1/2}-\frac{\varkappa\mathcal{E}_-}{4\pi qN_t},$$

$$l_{\max}=\left\{\frac{\varkappa[E_t+T\ln(\alpha_tN_t\tau_0)]}{2\pi q^2N_t}\right\}^{1/2}, \tag{3}$$

$\mathcal{E}_-$ is the modulus of the electric field pushing ions toward the surface in the region $z>l$; free ions with a density (k_s-lN_t) are concentrated in a narrow channel immediately contiguous with the boundary $z=0$ and of width small in comparison with l. We emphasize that we are looking at the situation $h>2l_{\max}$, $\tau_t\gg(\alpha_tN_t)^{-1}$. In the case $k_s<lN_t$ all ions are held by traps in a layer of thickness k_s/N_t. Note the perfect physical analogy of the physical distribution of ions at the boundary of the insulator with the distribution pattern of electrons at the electron-enriched surface of a *p*-type semiconductor with a deep acceptor level. Obviously, the width of the trap filling layer is determined by the condition that the line representing the energy position of a trapping center on the energy diagram intersect the Fermi level of the charge carriers. The maximum $l=l_{\max}$ is attained at $\mathcal{E}_-=0$, which corresponds to the lowest voltage across the insulator gap U_I (in energy units) at which all ions transfer from one surface to the other,

$$U_I=\begin{cases}\dfrac{2\pi q^2N_tl_{\max}^2}{\varkappa}+2T\ln\left(1+\dfrac{k_s-l_{\max}N_t}{2l_{\max}N_t}\right), & k_s>N_tl_{\max},\\ \dfrac{2\pi q^2k_s^2}{\varkappa N_t}, & k_s<N_tl_{\max}.\end{cases} \tag{4}$$

The second term in the expression for U_I at $k_s>N_tl_{\max}$ is equal to the advance of the potential along the region of localization of free ions.

We now consider the expulsion of ions from the boundary $z=0$ after a voltage $U_d>U_I$ of opposite polarity from before (at $T>0$) is applied to the insulator at $t=0$. We disregard the trapping of ions as they pass through the body of the insulator. This assumption is valid if the inequality $\mu\mathcal{E}_+\gg h\alpha_tN_t$ is satisfied. Here $\mu=\mu_0\exp(-E_\mu/T)$ is the free-ion mobility, and $\mathcal{E}_+$ is the pulling electric field in the region $z>l$. The potential well in the insulator at the begin-

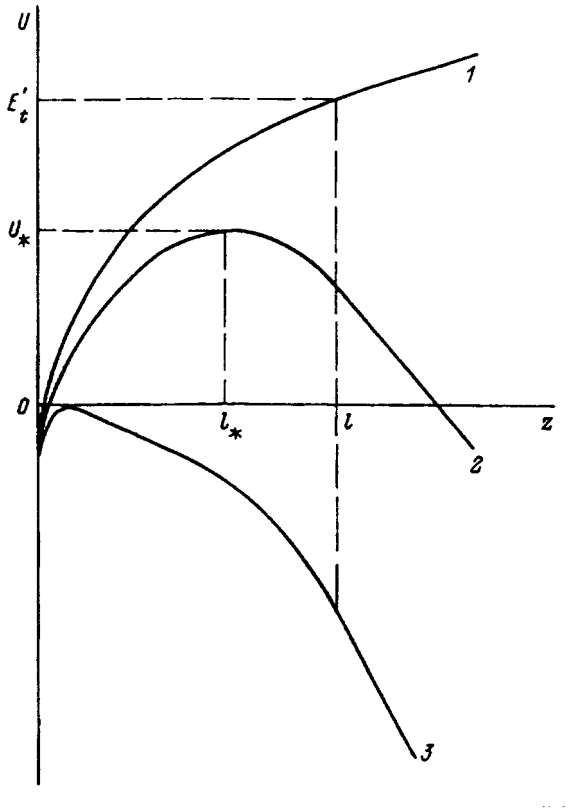

FIG. 1. Potential well at the surface of an insulator. Graphs of $U(z)$: *1*) before the start of the transfer process; *2*, *3*) at the first instant after the change of polarity of the voltage across the insulator gap, $E_t'=E_t+T\ln(\alpha_t\tau_0N_t)$: *2*) Pulling electric field $\mathcal{E}_+<4\pi qlN_t/\varkappa$; $\mathcal{E}_+>4\pi qlN_t/\varkappa$.

ning of the relaxation process is shown in Fig. 1. Let $k_s>lN_t$. If $\mathcal{E}_+<4\pi qlN_t/\varkappa$, which corresponds to the inequality $U_d<U_{II}$, where

$$U_{II}=\frac{4\pi q^2N_tlh}{\varkappa}-\frac{2\pi q^2N_tl^2}{\varkappa}-2T\ln\left(1+\frac{k_s-lN_t}{2N_tl+\varkappa\mathcal{E}_-/2\pi q}\right), \tag{5}$$

then in order for free ions to cross the insulator gap, they need to overcome the barrier of height $U_*=2\pi q^2l_*^2N_t/\varkappa$ created by repulsion from trapped carriers (Fig. 1, curve *2*). Here $z=l_*$ is the coordinate of the potential energy maximum, $l_*=l-(\varkappa\mathcal{E}_+/4\pi qN_t)$. The last term on the right-hand side of Eq. (5) describes the advance of the potential along the layer of free ions at $t<0$. The expression for the current density j of free ions escaping from the ''macroscopic trap'' associated with the potential barrier is obtained from the diffusion-drift equation $j=-\mu[k(dU/dz)+T(dk/dz)]$ in the approximations $U_*\gg T$ and $k|_{z=l}=0$:

$$j=\mu T\left(\frac{2q^2N_t}{\varkappa T}\right)^{1/2}k_0\exp\left[-\frac{U_0+U_*}{T}\right],$$

$$k_0\exp(-U_0/T)=\frac{4U_*N_t}{T}\frac{\tilde{k}_s}{(\tilde{k}_s+2N_tl_*)}, \tag{6}$$

where $k_0=k|_{z=0}$, U_0 is the advance of the potential along the free-ion layer, and $\tilde{k}_s=\tilde{k}_s(t)$ is the total number of such ions per unit area at time t.

A few remarks are in order. First, it follows from Eqs. (6) that the escape of ions from the macroscopic trap is characterized by the time constant

$$\tau=\frac{ql_*^2}{2\mu U_*}\left(\frac{\pi T}{U_*}\right)^{1/2}\exp(U_*/T).$$

It is much longer than the transit time $(ql_*^2/2\mu U_*)$ over the distance l_*. Consequently, free ions in the region $z<l_*$ far from the top of the barrier $U_*-U(z)\gg T$ exist in quasiequilibrium. Second, since $\tau_t=(\alpha_tN_t)^{-1}\exp(2\pi q^2N_tl_{\max}^2/\varkappa T)$ [see (Eq. 3)] and $l_*<l\leqslant l_{\max}$, we have $\tau\ll\tau_t$. Thus, detrapping can be ignored in the time that it takes for free ions to escape from the surface $z=0$. Third, strictly speaking, the length l_* and, accordingly, the barrier height U_*, increase with time, because the field $\mathcal{E}_+$ decreases as ions pile up at the boundary $z=h$.[1)] However, at $h\gg l$ under the condition $U_d\gg U_I$ (but $U_d<U_{II}$) we can disregard the time variation of the field $\mathcal{E}_+$ and assume that $\mathcal{E}_+=U_d/h$. Fourth, Eqs. (6) are valid for sufficiently high fields $\mathcal{E}_+$, since their derivation actually rests on the assumption that the time constant τ is much longer than the time to traverse the interval $l<z<h$, i.e., the time $(h-l)/\mu\mathcal{E}_+$ (otherwise, the condition $k|_{z=l}=0$ fails).

We now analyze the detrapping process. In the region $z>l_*$ liberated ions are ''driven'' toward the surface $z=h$ by the electric field, while in the region $z<l_*$ they stay close to the boundary $z=0$ and are therefore retrapped. We note that the coordinate of the potential maximum $z=\tilde{l}_*$ now becomes strongly time-dependent and, because of the transfer of free ions toward the surface $z=h$, its initial value $\tilde{l}_*|_{t=0}=l_*$ is greater than the value at the beginning of the relaxation process, the final value is $\tilde{l}_*=0$, and it is attained before the traps are fully discharged. The kinetic equation (1) can be rewritten in the form

$$\frac{dk_t}{dt}=\begin{cases}0, & z<\tilde{l}_*,\\ -k_t/\tau_t, & z>\tilde{l}_*.\end{cases} \tag{7}$$

Relations for the length $\tilde{l}_*$ and the insulator depolarization current density j (for the sum of the detrapping and displacement currents) are obtained from the Poisson equation (2):

$$\tilde{l}_*^2-\frac{2}{N_t}\int_{\tilde{l}_*}^{l}(h-z)k_tdz=-\frac{\varkappa}{2\pi q^2N_t}(U_d-U_h), \tag{8}$$

$$j=-\frac{\varkappa}{4\pi q}\left.\frac{\partial^2U}{\partial t\partial z}\right|_{z=0}=-q\frac{d}{dt}\int_0^l(1-z/h)k_tdz-\frac{\varkappa}{4\pi qh}\frac{dU_h}{dt}. \tag{9}$$

Here U_h is the advance of the potential along ions moving toward the surface $z=h$. Equation (9) is simplified in the case $\tilde{l}_*>0$:

$$j=-qN_t\frac{d\tilde{l}_x}{dt}. \tag{9a}$$

The solution of Eq. (7) for the thermal stimulation often used in experimental work, where $dT/dt=\beta>0$, has the form

$$k_t=\begin{cases} N_t, & z<\tilde{l}_*, \\ N_t e^{-(\theta_t-\theta_{tz})}, & \tilde{l}_*<z<l_*, \\ N_t e^{-\theta_t}, & l_*<z<l, \end{cases} \tag{10}$$

$$\theta_t=\int_0^t dt_1/\tau_t=t_{\text{eff}}^{(t)}/\tau_t,$$

$t_{\text{eff}}^{(t)}\simeq T^2/\beta E_t$ is the characteristic time for τ_t to decay by the factor $1/e=1/2.71\ldots$; and the function $\theta_{tz}(z)$ is defined as the inverse of the function $\tilde{l}_*(\theta_t)$, i.e., $\tilde{l}_*(\theta_{tz})\equiv z$. Physically, the function θ_{tz} corresponds to the time at which traps situated in the plane $z=\text{const}$ begin to empty. We assume below that either the layer of filled traps near the boundary $z=h$ has already formed (by virtue of the trapping of previously incoming carriers), and the increase in the potential U_h is mainly attributable to the increase in the density of free ions, or $h\gg l$ and $U_d\gg U_I$ (i.e., $\mathcal{E}_+=\text{const}$). In either case, $\tilde{l}_*^2$ varies far more strongly with time than the right-hand side of Eq. (8). Replacing this quantity by its initial value $l^2-2h(l-l_*)$ (with the observation that $[2h(l-l_*)-l^2]>0$ since $U_d>U_I>U_h$) and differentiating relation (8) with allowance for Eq. (7), we find

$$h\frac{d\tilde{l}_*}{d\theta_t}+\frac{\tilde{l}_*^2+2h(l-l_*)-l^2}{2}=0.$$

From this result we obtain

$$\tilde{l}_*=[2h(l-l_*)-l^2]^{1/2}\tan\left\{\frac{[2h(l-l_*)-l^2]^{1/2}}{2h}(\theta_{t0}-\theta_t)\right\}, \tag{11}$$

$$\theta_{tz}=\theta_{t0}-\frac{2h}{[2h(l-l_*)-l^2]^{1/2}}\arctan\left\{\frac{z}{[2h(l-l_*)-l^2]^{1/2}}\right\},$$

$$\theta_{t0}=\frac{2h}{[2h(l-l_*)-l^2]^{1/2}}\arctan\left\{\frac{l_*}{[2h(l-l_*)-l^2]^{1/2}}\right\}. \tag{12}$$

The value of the variable $\theta_t=\theta_{t0}=\theta_{tz}|_{z=0}$ corresponds to the time at which the maximum of the potential $U(z)$ vanishes ($\tilde{l}_*=0$). For $\theta_t<\theta_{t0}$ it follows from Eqs. (9a) and (11) that the current is expressed as

$$j=\frac{qN_t}{\tau_t}\frac{[2h(l-l_*)-l^2]}{2h}\cos^{-2}\left\{\frac{[2h(l-l_*)-l^2]^{1/2}}{2h}(\theta_{t0}-\theta_t)\right\}, \tag{13}$$

whereas for $\theta_t>\theta_{t0}$ we obtain the following expression from expressions (9), (10) and (12), disregarding the derivative dU_h/dt:

$$j=\frac{qN_t}{\tau_t}\frac{[2h(l-l_*)-l^2]}{2h}e^{-(\theta_t-\theta_{t0})}. \tag{14}$$

Note that Eqs. (10)–(14) remain valid in the isothermal regime ($T=\text{const}$ with $t_{\text{eff}}^{(t)}$ replaced by the real time t.

We now turn to the case $\mathcal{E}_+>4\pi qlN_t/\varkappa$ or $U_d>U_{II}$. The potential well at the beginning of the transient process is shown in Fig. 1, curve *3*. The theory of the transfer of a charge packet across an insulator gap is well known.[6] If $\mathcal{E}_+<4\pi qk_s/\varkappa$, the leading edge initially begins to move, while the trailing edge remains at the surface $z=0$, since $(dU/dz)|_{z=0}=0$. If $\mathcal{E}_+>4\pi qk_s/\varkappa$, the packet immediately moves as a whole unit, the leading and trailing edges coincide if diffusion is ignored, and the depolarization current in the thermal stimulation regime is given by the expression

$$j=\frac{q\mu(k_s-lN_t)}{h}\times\begin{cases}\left[\mathcal{E}_+-\dfrac{1\pi q}{\varkappa}(k_s+lN_t)\right] \\ \quad\times\exp\left\{\left[\dfrac{k_s+(h-l)N_t}{k_s-lN_t}\right]\theta\right\}, & \theta<\theta_l, \\ \left[\mathcal{E}_+-\dfrac{2\pi q}{\varkappa}(k_s-lN_t)(1-2l/h)\right] \\ \quad\times\exp(\theta-\theta_l), & \theta_l<\theta<\theta_h, \end{cases} \tag{15}$$

Here

$$\theta=\frac{4\pi q(k_s-lN_t}{\varkappa h}\int_0^t\mu dt_1=\frac{4\pi q(k_s-lN_t)\mu t_{\text{eff}}}{\varkappa h},$$

$t_{\text{eff}}\simeq T^2/\beta E_\mu$ is the characteristic time for the mobility to increase by the factor e, $\theta=\theta_l$ corresponds to the time at which the packet crosses the boundary of the filled-trap layer $z=l$,

$$\theta_l=\frac{k_s-lN_t}{k_s+(h-l)N_t}\ln\left\{1+\frac{4\pi ql[k_s+(h-l)N_t]}{\varkappa h[\mathcal{E}_+-(2\pi q/\varkappa)(k_s+lN_t)]}\right\},$$

and $\theta=\theta_h$ corresponds to the time to traverse the insulator gap,

$$\theta_h=\theta_l+\ln\left\{1+\frac{4\pi q(h-l)(k_s-lN_t)}{\varkappa h[\mathcal{E}_+-(2\pi q/\varkappa)(1-2l/h)(k_s-lN_t)]}\right\}.$$

The exponential factors in Eqs. (16) vary only slightly:

$$\exp\left\{\frac{[k_s+(h-l)N_t]\theta_l}{k_s-lN_t}\right\}<1+\frac{2l}{h}\left\{\frac{k_s+(h-l)N_t}{k_s-lN_t}\right\},$$

$$\exp(\theta_h-\theta_l)<3.$$

The current equations (15) retain their form in the isothermal regime with t_{eff} replaced by the real time t.

In this situation the potential $U(z)$ is a monotonically decreasing function of the coordinate. Consequently, all traps in the layer $0<z=l$ are emptied simultaneously, and the insulator depolarization current associated with their detrapping obeys the law (14), in which it is required to set $l_*=0$ and $\theta_{t0}=0$.

Now let us assume that initially there are no free ions, $k_s<lN_t$. The traps discharge in the same way as for $k_s>lN_t$. If $\mathcal{E}_+<4\pi qk_s/\varkappa$, which corresponds to the condition $U_d<U_{II}$ with U_{II} evaluated for $l=k_s/N_t$, the potential $U(z)$ has a maximum at the point $z=l_*=(k_s/N_t)-(\varkappa\mathcal{E}_+/4\pi qN_t)$. Disregarding the variation of the field $\mathcal{E}_+$

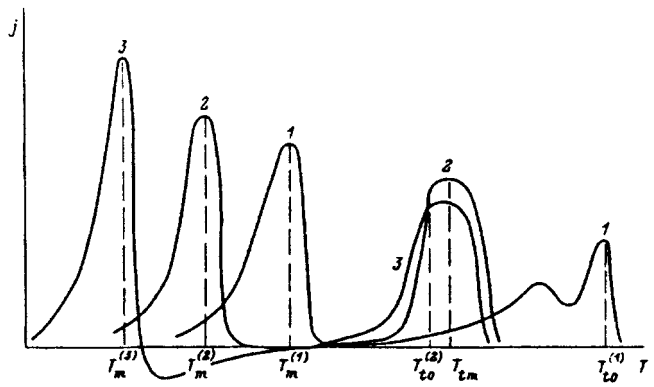

FIG. 2. Temperature curves of the depolarization current.) U_{d1}; *2*) U_{d2}; *3*) U_{d3} ($U_I<U_d<U_{d2}<U_{II}<U_{d3}$). The superscripts attached to the temperatures $T_m^{(i)}$ and $T_{t0}^{(i)}$ give the curve numbers.

on account of the redistribution of ions in the insulator, i.e., assuming that $h \gg k_s^2/(k_s - l_* N_t) N_t$ and setting $l = k_s/N_t$, from relations (13) and (14) we obtain

$$j = \frac{q(k_s - l_* N_t)}{\tau_t} \begin{cases} 1, & \theta_t < \theta_{t0}, \\ e^{-(\theta_t - \theta_{t0})}, & \theta_t > \theta_{t0}, \end{cases}$$

$$\theta_{t0} = \frac{l_* N_t}{k_s - l_* N_t}. \tag{16}$$

If $\mathcal{E}_+ > 4\pi q k_s/\varkappa$ (or $U_d > U_{II}$ for $l = k_s/N_t$), then $U(z)$ is a monotonically decreasing function of the coordinate z, and the depolarization current of the insulator gap for $h \gg k_s/N_t$ (this condition stipulates that the contribution to the displacement current from the redistribution of ions near the surface $z = h$ is small) obeys the lower equation (16), in which it is now required to set $l_* = 0$ and $\theta_{t0} = 0$.

Figure 2 shows the qualitative pattern of the temperature dependence of the depolarization current for various constant voltages U_d.[2)] It is identical in both the thermal stimulation regime and the isothermal regime (at a fixed observation time t). The $j(T)$ curves have two (or three) maxima: a low-temperature maximum associated with the migration of free ions and one or two high-temperature maxima corresponding to detrapping. The free-ion currents from the macroscopic trap (Fig. 2, curves *1* and *2*) increase according to the Arrhenius law almost up to the points of the maxima ($T_m^{(1)}$ and $T_m^{(2)}$), after which j drops very abruptly. This behavior is attributable to the fact that the carrier density near the base of the barrier $k_0 \exp(-U_0/T)$ [see Eq. (6)] for $k_s \gg l_* N_t$ remains practically invariant until depletion of the free-ion layer, which acts as an effective reservoir.[3)] As the voltage U_d is raised, the activation energy of the ascending branch of the current ($E_\mu + U_*$) is lowered, shifting the peak toward lower temperatures while simultaneously making it higher and narrower. In the case $U_d > U_{II}$ (Fig. 2, curve *3*) the low-temperature maximum is caused by the transfer of a packet of free ions across the insulator gap. The initial rise of the current with temperature according to the Arrhenius law accelerates near the maximum $T = T_m^{(3)}$ [this behavior is described by the exponential factor in the second equation (15)]; the steep descent of j after the maximum with increasing t is dictated by the smallness of the diffusion broadening of the packet. The activation energy of the ascending branch of the function $j(T)$ is equal to E_μ and is therefore independent of the voltage; the fact that the peak shifts more slowly toward low temperatures with increasing voltage U_d than in the case $U_d < U_{II}$ is attributable to a decrease in the transit time. After the packet is dislodged and driven toward the surface $z = h$, free ions begin to be captured by traps in the interior of the insulator. The charge center therefore shifts toward the boundary $z = 0$, and the current changes polarity (negative segment of curve *3* in Fig. 2). The capture of ions by distant traps is a self-inhibiting process, because the field squeezing free ions toward the surface $z = h$ also increases synchronously with the filling of the traps. For this reason $|j|$ increases abruptly at first and then gradually decreases as T is increased.

The profile of $j(T)$ in the high-temperature range is significantly affected by the delay in the emptying of traps situated in the layer $0 < z < l_*$. At sufficiently low stresses

$$\frac{\varkappa}{2\pi q^2 N_t}(U_d - U_h)$$

$$= [2h(l - l_*) - l^2] < l_*^2 \cot^2[(\pi/4) + 0.5] \cong 0.086 l_*^2$$

the function $j(T)$ has two maxima (see curve *1* in Fig. 2), where the absolute maximum is reached at $T = T_{t0}^{(1)}$. The temperature T_{t0} corresponds to the time at which the potential $U(z)$ loses its maximum, whereupon detrapping is no longer delayed, and its value is determined from the equation

$$\theta_t|_{T = T_{t0}} - \theta_{t0}.$$

At $T > T_{t0}$ the current density j drops abruptly with increasing T, moving to the descending branch of the ''ordinary'' peak of the current produced by the thermally stimulated discharge of microscopic traps [see expression (14)]. The ''ordinary,'' i.e., undelayed, detrapping leads to the relation[8]

$$j \sim \theta_t \exp(-\theta_t),$$

and j becomes a maximum at $T = T_{tm}$, where T_{tm} is the solution of the equation $\theta_t = 1$ (T_{tm} does not depend on the voltage U_d). Under the condition $l - l_* \ll l$ the inequality $\theta_{t0} \gg 1$ holds, and at the time the delay vanishes ($T = T_{t0}$) the majority of the traps have already been emptied, so that the current drop in the range $T > T_{t0}$ takes place within a far narrower temperature interval than its rise (see curve *1* in Fig. 2). As the voltage is increased (see curve 2 in Fig. 2), the values of l_* and T_{t0} decrease, the relative maximum of j at $T < T_{t0}$ vanishes, and in the case $[2h(l - l_*) - l^2] \gg l_*^2$ the ascending branch of the function $j(T)$ is described up to $T = T_{t0}$ by the Arrhenius law with activation energy E_t. At sufficiently high U_d (but with $U_d < U_{II}$) we have $\theta_{t0} < 1$, and T_{t0} is lower than T_{tm}. Under these conditions the current maximum is attained at $T = T_{tm}$, and the time at which detrapping ceases to be delayed ($T = T_{t0}$) corresponds to the kink in the $j(T)$ curve:

$$\left.\frac{dj}{dT}\right|_{T + T_{t0} + 0} = (1 - \theta_{t0}) \left.\frac{dj}{dT}\right|_{T = T_{t0} - 0}$$

If $U_d > U_{II}$ (Fig. 2, curve *3*), there is no delay at the outset of the depolarization process, and the graph of $j(T)$ represents an ordinary peak of the current produced by thermally stimulated detrapping.

An increase in the field $\mathcal{E}_+$ is accompanied by a decrease in the thickness of the layer in which ions are localized at the boundary $z=h$ after termination of the transfer process. The areas under the peaks of $j(T)$ must therefore increase somewhat as the voltage is raised. This is especially true of the low-temperature maximum, because in the high-temperature range traps at the boundary $z=h$ are filled by previously incoming ions. The pattern of the temperature curves of the depolarization current in Fig. 2 corresponds to the situation involving a large number of ions, $k_s > lN_t$. In the opposite situation, $k_s < lN_t$, there are no free ions, hence the $j(T)$ curve contains only the high-temperature peak.

An important characteristic of the ion transfer processes in an insulator with volume traps is the dependence of their parameters on the conditions underlying the initial localization of charge carriers near the surface $z=0$. In particular, if the ions are uniformly distributed at $t=-0$, the thickness l of the layer of filled traps is a function of the driving field $\mathcal{E}_-$ [see expression (3)]. Consequently, at the same voltage U_d the height of the barrier U_* for the escape of free ions from the potential well and the characteristic temperature T_{t0} corresponding to the cessation of delay of detrapping becomes lower as the field $\mathcal{E}_-$ increases. On the graph of the insulator depolarization current as a function of the temperature (see Fig. 2) the increase of $\mathcal{E}_-$ is manifested as an increase in the area under the low-temperature peak, which simultaneously shifts to the left and becomes narrower, along with a decrease in the area under the high-temperature maximum and a leftward shift of the kink in the $j(T)$ curve at $T=T_{t0}$. In the case $k_s < l_{\max}N_t$ the low-temperature peak does not exist for low fields $\mathcal{E}_-$, but when $\mathcal{E}_-$ increases, this peak appears as soon as

$$\mathcal{E}_- > \frac{2\pi q}{\varkappa}\,\frac{(l_{\max}N_t)^2 - k_s^2}{k_s}$$

(i.e., when $l < k_s/N_t$).

Strictly speaking, the results obtained in this study are valid for a more or less thick insulator, $h > 2l_{\max}$. If $h < 2l_{\max}$, the layers of filled traps corresponding to the boundaries $z=0$ and $z=h$ can overlap. Traps at the boundary $z=h$ are filled synchronously with the escape of free ions from the potential well near the surface $z=0$. The height of the barrier U_* therefore increases until traps throughout the entire interval $0<z<h$ are unoccupied. As a result, the low-temperature $j(T)$ curve must acquire an interval of quasi-saturation or even slow decay of the current, which changes over (after the filled-trap layers have merged) to growth of j with increasing T according to the Arrhenius law. If $h < \min(l, l_h, k_s/N_t)$, where l_h is the thickness of the filled-trap layer next to the surface $z=h$ at $t=\infty$, all ion trapping centers in the insulator remain filled during depolarization. The $j(T)$ curve loses the high-temperature part in this case.

In summary, ion transfer processes in an insulating layer with volume traps have a great many distinctive qualitative features in the temperature and voltage dependences of the depolarization current. Such features as the increase in the area under the peaks of the $j(T)$ curve as the voltage is increased, the interval of the $j(T)$ curve where the current changes polarity, and the ''memory'' of the field driving ions toward the surface prior to the onset of the transfer process are fundamentally unexplainable in terms of the presence of traps at the boundaries of the insulator. Consequently, these characteristic features in fact provide a test of the stated assumptions as to the presence of volume (nonsurface) traps in the insulator for the interpretation of experimental data.

The author is grateful to A. G. Zhdan for a discussion of the issues addressed in the work.

[1)] This explains why the insulator depolarization current differs from the current described by Eqs. (6) by the amount of the displacement current $(\varkappa/4\pi)(d\mathcal{E}_+/dt)$.

[2)] Highly nonequilibrium depolarization is discussed here. In the opposite, quasiequilibrium case, when the current is induced by slow variation of the voltage, the $j(U_d)$ curve is in the form of a peak of width $2U_I$ symmetric about $U_d=0$.

[3)] A similar ''reservoir effect'' has been observed in the thermal delocalization of electrons near a $Si-SiO_2$ interface.[7]

[1] T. W. Hickmott, J. Appl. Phys. **46**, 2583 (1975).
[2] M. R. Boudry and J. P. Stagg, J. Appl. Phys. **50**, 942 (1979).
[3] Yu. A. Gorokhovatskiĭ and G. A. Bordovskiĭ, *Thermally Stimulated Current Spectroscopy of High-Resistance Semiconductors and Insulators* [in Russian], Nauka, Moscow (1991).
[4] T. W. Hickmott, J. Appl. Phys. **51**, 4269 (1980).
[5] A. G. Zhdan and Yu. V. Markin, Fiz. Tekh. Poluprovodn. **28**, 756 (1994) [Semiconductors **28**, 444 (1994)].
[6] K. Kao and V. Huang, *Electron Transfer in Solids* [Russian translation], Vol. 2, Mir, Moscow (1994), p. 56.
[7] E. I. Gol'dman, A. G. Zhdan, and A. N. Ponomarev, Fiz. Tekh. Poluprovodn. **28**, 1947 (1994) [Semiconductors **28**, 1073 (1994)].
[8] R. Chen and Y. Kirsh, *Analysis of Thermally Stimulated Processes* (*Science of the Solid State*, Vol. 15), Pergamon Press, New York (1981).

Translated by James S. Wood

Relaxation spectra of photoluminescence from porous silicon obtained by chemical etching of laser-modified silicon

L. L. Fedorenko, A. D. Sardarly, É. B. Kaganovich, S. V. Svechnikov, S. P. Dikiĭ, and S. V. Baranets

Institute of Semiconductor Physics, Ukraine National Academy of Sciences, 252028 Kiev, Ukraine
(Submitted October 5, 1995; accepted for publication February 1, 1996)
Fiz. Tekh. Poluprovodn. **31**, 6–10 (January 1997)

The distinctive features of time-resolved photoluminescence spectra of porous silicon created by chemical etching of single-crystal silicon subjected to modification by laser light has been investigated. Two bands were seen upon examination of the amplitude spectra: a band with a maximum at a wavelength ($\lambda_{max} \simeq 530$ nm) and a band with $\lambda_{max} \simeq 420$ nm and twice the intensity of the first. The relaxation curves are characterized by two sets of times: $\tau_1 < 2\times10^{-8}$ s and 2×10^{-8} s$< \tau_2 \times 2\times10^{-4}$ s in the spectral ranges 420–700 nm and 500–850 nm, respectively. Upon increasing the energy density of the laser irradiation from ~ 10 to ~ 40 $J\cdot cm^{-2}$, the intensity of the photoluminescence and the contribution of the fast component increased as well. The difference in the photoluminescence spectra compared to the spectra of layers of porous silicon obtained by electrochemical etching is attributable to a shift in the distribution of nanocrystallite sizes toward smaller sizes, which leads to an increase in the area of the Si/SiO_x surface that separates the phases. Although our results can be explained within the framework of a quantum-well model, we do not rule out the contribution of local centers at the Si/SiO_x phase boundary. The slow component of the relaxation is approximated by a ''stretched'' exponential. It is assumed that the slow component is controlled by the rate at which photocarriers leave the quantum-well nanocrystallites by tunneling through the Si/SiO_x barrier. © *1997 American Institute of Physics.* [S1063-7826(97)01712-7]

INTRODUCTION

The interest in porous silicon layers derives from the observation of photoluminescence in the visible region of the spectrum coming from these films[1] and from recent reports of the first successful attempts to create electroluminescent sources based on them. However, despite complex investigations carried out by many authors, it is not yet possible to make any definitive assumptions about the nature of photoluminescence in porous silicon, although many of the results suggest that a quantum-well model is correct.[2–7]

Traditionally, layers of porous silicon are obtained either by electrochemical or by chemical (dye) etching. There is interest in finding new methods of directed creation of porous silicon layers with a specific topology using laser irradiation.

In the majority of papers to date, laser irradiation of porous layers of Si is used to stimulate chemical etching of single crystals of Si at the stage of void formation,[8] and also to observe the effect of light-induced degradation of the photoluminescence.[9–11] At the same time, it is known that the intensity of chemical etching processes depends considerably on the degree of defect content and the type of starting structure. In our previous paper,[12] we proposed to use laser irradiation before dye etching in order to create layers of porous silicon with a nanocrystalline structure like that shown in Figure 1. Our proposal was based on the idea that the etching efficiency should increase for those portions of the silicon layer with a high degree of disorder of the crystal lattice caused by an increased defect concentration.

We have investigated the time-resolved photoluminescence spectra of porous silicon layers obtained by laser modification of Si. Our goal is to analyze and compare the distinctive features of our spectra with photoluminescence spectra of porous silicon obtained by other technologies, and to seek new arguments in favor of this or some other model of porous silicon.

METHOD AND RESULTS OF EXPERIMENTS

Single crystals of p-type Si with resistivity $\rho = 10$ $\Omega\cdot$cm were processed by pulses from a YAG laser operating in the cw regime (the laser wavelength was $\lambda = 1.06$ μm, the energy $E_i =$ 0.3 J, and the pulse duration $t_i = 2\times10^{-4}$ s). The laser beam was focused by a SOK-1 optical block and was translated along the surface of the silicon film, thereby providing a prespecified power density and degree of blocking of the laser spot. The samples were then processed in a dye etch with composition $HF:HNO_3:H_2O = 1:3:5$ for 3–10 min at room temperature. The relaxation spectra of the photoluminescence were measured for excitation by a pulsed nitrogen laser LGI-21 ($\lambda = 0.34$ μm, $t_i = 7\times10^{-9}$ s, $E_i = 2\times10^{-5}$ J) as part of a setup assembled around a DFS-12 spectrometer, with the help of a cooled pulsed photomultiplier FEU-83 ($\lambda = 0.3$–1.2 μm). The setup allowed us to record amplitude values (in the peak-value detection regime) and time-integrated values of the photoluminescence intensity (I_{pl}), to make stroboscopic recordings of the relaxation spectra in the photon-counting regime with a time resolution of 10^{-8} s, and to accumulate and process the information on a computer.

Figure 1 shows spectra of the peak value of the photo-

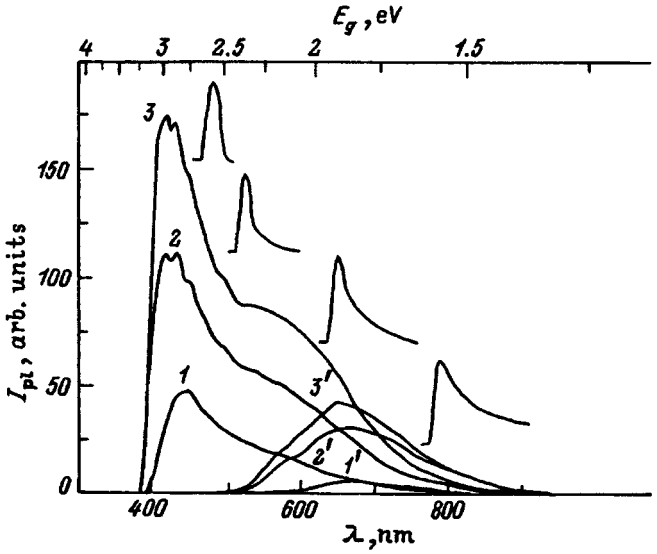

FIG. 1. Photoluminescence spectra of porous silicon layers obtained by laser modification. *1–3*—amplitude, *1′–3′*—time-integrated photoluminescence spectra. The energy density for laser processing W in $J \cdot cm^{-2}$ was: 1, *1′*—11.5; *2*, *2′*—20.0; *3*, *3′*—33.5. In the inset we show the decay of the photoluminesence at various wavelengths.

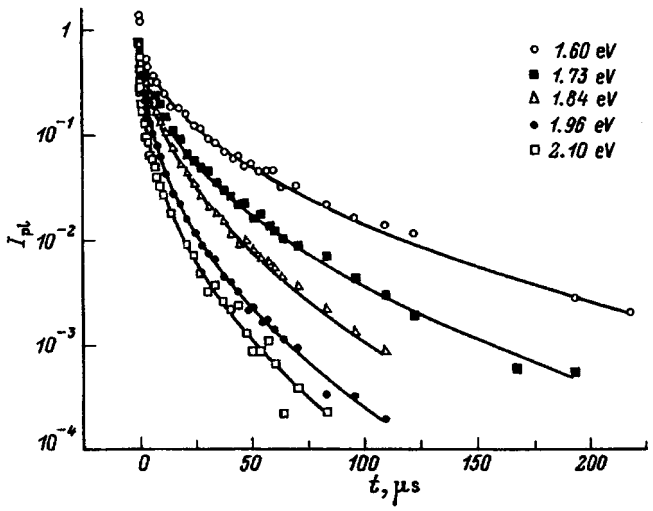

FIG. 2. Normalized decay of the slow component of the photoluminescence from porous silicon layers (dots) and approximation of the experimental results (solid curves) by a ''stretched'' exponential (2) for various energies of the luminescence radiation.

luminescent intensity (curves *1−3*) and its integration over time (curves *1′−3′)* for various optical energy densities W from the YAG laser. It is clear that as W increases, the intensity of the peak-value photoluminescence spectrum with a maximum at $\lambda_{max} \simeq 420$ nm increases along with its integral over time. In the longer-wavelength region (near $\lambda = 540$ nm) a distortion of the amplitude spectrum is observed due to an increase in the relative contribution of the short-lived component as the intensity of the laser processing increases. The relaxation spectra, as is clear from the insets in Fig. 1, are characterized by two sections of the photoluminescence decay curve with two sets of relaxation times—a rapid decay ($\tau_1 < 20$ ns) and a slow decay (20 ns$< \tau_2 <$200 μs). Although both components are present over most of the spectral range, the ratio of amplitudes of the two components changes, starting with the vanishing of the slow component for wavelengths less than 510 nm and ending with the vanishing of the fast component for wavelengths greater than 700 nm. Accordingly, the maximum in the photoluminescence spectrum shifts with time toward longer wavelengths, while the shape of the spectrum undergoes a time-dependent transformation similar to that observed in Ref. 13.

Typical relaxation curves for transient photoluminescence are shown in Fig. 2 for five wavelengths. It is clear that the relaxation curves for photoluminescence cannot be described by a single exponential dependence on time t over the entire spectral range. The relaxation times do not depend on the excitation intensity I of the light from the nitrogen laser anywhere within the entire range of nonstationary photoluminescence spectra, at least within the limits $I = 1–10$ W.

DISCUSSION OF RESULTS

1. Fast component. A noticeable feature of the peak-value photoluminescence spectra is a strong ''blue'' band. In contrast to observations of photoluminescence spectra from porous silicon layers obtained by electrochemical etching,[13] which peak at $\lambda_{max} \simeq 500$ nm, the maximum of this band is shifted toward the short-wavelength region of the spectrum ($\lambda_{max} \equiv 420$ nm), and the ratio of amplitudes of the intensities of the ''blue'' band and ''red'' band exceed those observed in Ref. 13 by more than a factor of 2 for equal time delays between the strobing pulse and the excitation pulse. This band, which is connected with transitions between levels with the highest energy and with relaxation times $\tau_1 < 20$ ns, may be due to: geminal recombination of photocarriers with the characteristic time for dispersal along the length of a Bohr radius,[14] radiative quasidirect transitions between bulk quantum states,[3] excitonic recombination, and radiative centers in siloxene, polysilane,[4] and silicon oxide.[15] The fact that the amplitude of this band greatly exceeds that of the red band, in contrast to the corresponding relation for photoluminescence spectra from samples obtained by other technologies,[13] we associate with intense laser-stimulated generation of structural defects in the single-crystal Si in the process of laser processing.[16] In fact, even at comparatively moderate concentration levels of these defects (10^{18} cm^{-3}), the average distance between defects as potential etch centers amounts to ~ 10 nm. Along with the decrease in the etch time, this limits the maximum size of the nanocrystallites, shifting the maximum of their size distribution toward smaller sizes. In accordance with the quantum-well model, this increases the energy gap E_g between quantum levels, shifting the blue band toward shorter wavelengths. At the same time, as the concentration of small particles increases the effective surface area of the porous layer increases, and consequently the concentration of possible radiative centers as well, for example, in the oxide.[15] It is reasonable to assume that in the band with $\lambda_{max} \simeq 420$ nm there is a parallel switching-on of two competing recombination channels for our case: bimolecular (geminal recombination, because it is excitonic according to theoretical

estimates,[14] gives a considerably larger value for the relaxation time $\tau_1 > 100$ ns) and monomolecular (for example, through centers in the oxide). Identification of these channels requires further investigation of nonstationary photoluminescence spectra with nanosecond and subnanosecond time resolution.

It should be noted that a similar blue band was also observed in photoluminescence spectra of fragments of porous silicon dispersed through a quartz substrate.[17]

The fact that a fast component is present ($\tau_1 < 20$ ns) over much of the spectral range ($420 < \lambda < 70$ nm) indicates a rapid exchange of a sizable amount of photocarrier energy (2.9–1.8=1.1 eV). This is most likely an indication of the predominance of some recombination process that is common over this spectral range. The most probable mechanism would appear to be that of geminal recombination coupled with the quantum-well model of Si nanocrystallites in the form of segments of wires of varying cross section (and accordingly varying E_g).[1] This model assumes transport of photocarriers along quantum fragments with subsequent photoluminescence in the more long-wavelength portion of the spectrum. Excitation within the volume of one of these crystallites can provide photoluminescence at any wavelength within the entire spectral range. In fact, transport of photocarriers from the volume of a nanocrystal to its surface should lead predominantly to nonradiative recombination[6] (which agrees with the smallness of the quantum efficiency in porous silicon). In this case, the radiative recombination in the volume of a nanocrystal of length 10 nm should occur within the transport time $u_{cr} \leqslant 10^{-12}$ s for photocarriers to move along such a fragment of (the mean-free path in Si at $T=300$ K is $l_{tr} \leqslant 150$ nm); i.e., nearly instantaneously on the time scale of our observations. Under conditions of ballistic transport, a mechanism of recombination of photocarriers at distances of their dispersal along the length of a Bohr radius is the most likely mechanism, which is similar to that observed in amorphous Si. The fast component of the photoluminescence is less likely to have such a wide spectrum in a model involving radiative centers in the oxide SiO_x, or centers of molecular nature.

2. Slow component. The second set of times (20 ns$<\tau_2<$200 μs) is characterized by a relaxation that cannot be described by a single exponential, and is similar to that observed in samples obtained by other methods, e.g., anodization.[18] Computer analysis of relaxation spectra measured in the photon counting regime over a range of more than three orders of magnitude in intensity show that the spectra are well approximated by a ''stretched'' exponential, which is used to describe disordered systems with a characteristic integration time[16]

$$\tau_{pl}=\frac{1}{I_{pl}(0)}\int_0^T I_{pl}(t)dt=\tau_0\beta^{-1}\Gamma(\beta^{-1}), \tag{1}$$

$$I_{pl}(t)=I_{pl}(0)\exp[-(t/\tau_0)^{\beta}], \tag{2}$$

where β is the dispersion parameter.

Other approximations used previously to describe the kinetics of photoluminescence spectra (for example, models that include re-emission (photon transport) of free electrons and holes,[19] the three-level model,[20] and also a model developed to describe the long-period relaxation of the photoresponse in nonuniform barrier semiconductor structures[21]) are inapplicable in our case.

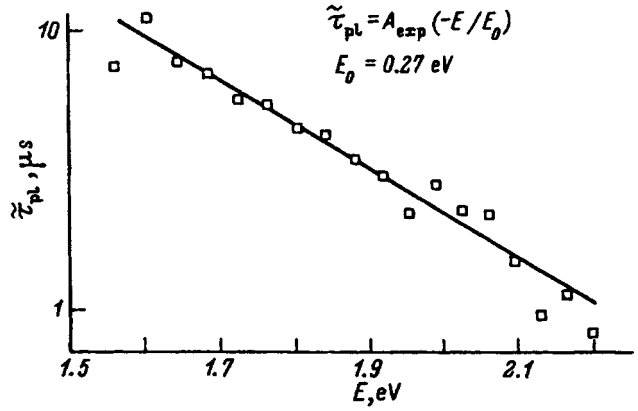

FIG. 3. Spectral dependence of the average decay time of the slow component of the photoluminescence from porous silicon layers.

The average time is characterized by a spectral dependence that falls off with the photon energy E at a rate close to exponential,

$$\tilde{\tau}_{pl}(E)\sim A\ \exp(-E[\text{eV}]/0.27) \tag{3}$$

in the range 1.47–2.48 eV (Fig. 3). Since the photoluminescence kinetics are independent of the intensity of excitation over the entire spectrum under observation, this fact argues in favor of a ''tunneling'' mechanism for the recombination,[15] according to which its rate is controlled by tunneling of carriers through potential barriers formed by layers of oxide that coat the surface of the crystallites. The recombination process itself can be associated with radiative transitions of free electrons and holes (or excitonic transitions) between bulk quantum levels, and also (in light of the smallness of the quantum efficiency, $\eta < 3\%$, in porous silicon[15,18]) with nonradiative transitions at bulk centers,[15] surfaces,[19] or at Si/SiO_x interfaces.[22] In addition, tunneling of carriers through oxide layers between neighboring crystallites is also quite probable. In the latter case, the resulting recombination rate will no longer be proportional to the sum of probabilities for the recombination processes $W_\Sigma = 1/\tau_r + 1/\tau_{nr}$, where τ_r and τ_{nr} are lifetimes of carriers with respect to radiative and nonradiative recombination, respectively. It can, however, be described by a series-parallel scheme that includes the transport and recombination channels with a certain effective time $\tau_{\Sigma\,eff} = \tau_{tun} + 1/W_\Sigma$, where τ_{tun} is the tunneling time. In any case, the recombination will take place in regions separated from the region where the carriers appear by tunneling barriers. The dispersion of characteristic times, which determines the nonmonoenergetic nature of the photoluminescence kinetics curves at a given wavelength λ, can arise from a scatter in the thickness of barriers x which determines their transparency T:

$$T=T_0\ \exp\left[-(4\pi/h)\int_0^{\delta}(2m^*\Delta U)^{1/2}dx, \right. \tag{4}$$

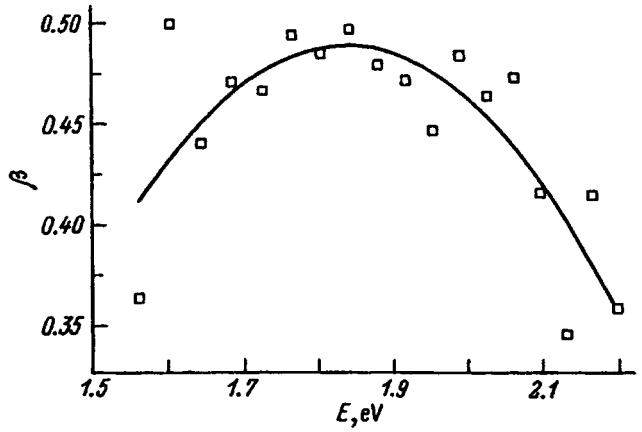

FIG. 4. Spectral dependence of the dispersion parameter β for porous silicon layers.

where m^* is the reduced effective mass of the photocarriers, ΔU is the height, and δ is the maximum thickness of the barrier.

An additional argument in favor of the model of tunneling recombination is the reproducibility which we observe in the slope of the function $\tau_{pl}(E)$ for $T=77$ K.

The dispersion parameter β is also spectrally dependent with a maximum in the neighborhood of $E_g=1.9$ eV (Fig. 4), which corresponds to the smallest scatter in characteristic times (or the largest density of states). This is found to be in agreement with the position of the maximum of the integrated photoluminescence band ($\lambda_{\max}\simeq 650$ nm) (Fig. 1).

Thus, our investigation of time-resolved photoluminescence spectra of porous silicon layers made from silicon, modified by laser light and dye etching, and its subsequent analysis leads us to assume that the fast component of the photoluminescence is caused by transitions between quantum bulk states in nanocrystallites of variable cross section (geminal recombination), while the band $\lambda_{\max}\simeq 420$ nm exhibits evidence that quantum-size effects and local centers are involved. The slow component is controlled by the rate of tunneling of carriers through the Si/SiO_x energy barrier, which also argues in favor of a quantum-well model.

The method we propose for creating porous silicon layers using laser modification, combined with selective chemical etching of Si, can be a useful alternative to methods that use photoresist and ion implantation to obtain a given figure.[23]

This work was carried out with partial support by a grant from the George Soros International Science Fund.

[1] L. T. Canham, Appl. Phys. Lett. **57**, 1046 (1990).
[2] G. D. Sanders and Yia-Chung Chang, Appl. Phys. Lett. **60**, 2525 (1992).
[3] Chin Yu Yeh, S. B. Zhang, and Alex Zunger, Appl. Phys. Lett. **63**, 3455 (1993).
[4] E. Bustarret, M. E. Ligeon, and L. Ortega, Solid State Commun. **83**, 461 (1992).
[5] M. S. Brandt, H. D. Fuchs, M. Stutsmann, J. Weber, and M. Cardona, Solid State Commun. **81**, 307 (1992).
[6] J. C. Vial, S. Billat, A. Bsiesy, G. Fishman, F. Gaspard, R. Herino, M. Ligeon, F. Madeore, I. Mihalcescu, F. Muller, and R. Romestain, Physics B **185**, 593 (1993).
[7] F. Koch, V. Petrova-Koch, T. Muschik, A. Nikolov, and V. Gavrilenko, Proc. Mater. Res. Soc. Symp. **283**, 197 (1993).
[8] S. Shih, K. H. Jung, and D. L. Kwong, Appl. Phys. Lett. **62**, 12 (1993).
[9] H. Nishitani and H. Nakota, J. Appl. Phys. **31**, L1577 (1992).
[10] S. Shih, K. H. Jung, D. L. Kwong, M. Kovar, J. M. White, T. George, and S. Kim, Appl. Phys. Lett. **63**, 3306 (1993).
[11] S. V. Svechnikov, L. L. Fedorenko, E. B. Kaganovich, A. D. Sardardi, S. P. Dikiĭ, and S. V. Baranets, Ukr. Fiz. Zh. **39**, 704 (1994).
[12] A. V. Andirianov, D. I. Kovalev, V. B. Shuman, and I. D. Yaroshetskiĭ, JETP Lett. **56**, 236 (1992).
[13] M. S. Bresler and I. N. Yassievich, Fiz. Tekh. Poluprovodn. **27**, 873 (1993) [Semiconductors **27**, 475 (1993)].
[14] A. J. Kontkiewicz, A. M. Kontkiewicz, J. Siejka, S. Sen, G. Nowak, A. M. Hoff, P. Sakthivel, K. Ahmed, P. Mukherjee, S. Witanachchi, and J. Lagowski, Appl. Phys. Lett. **65**, 1436 (1994).
[15] A. F. Banishev and L. V. Novikova, Phys. Chem. Processed Mater. **5**, 55 (1992) [in Russian].
[16] M. E. Kompan and I. Yu. Shabanov, Fiz. Tverd. Tela (Leningrad) **36**, 125 (1994) [Phys. Solid State **36**, 68 (1994)].
[17] L. Pavesi, M. Geschini, and F. Rossi, J. Luminescence **57**, 131 (1993).
[18] H. Sher, M. F. Shlesinger, and J. T. Bender, *Physics Today*, No. 1, 26 (1991).
[19] S. Finkbeiner, J. Weber, M. Rosenbauer, and M. Stutsmann, J. Luminescence **57**, 231 (1993).
[20] R. Laiho, A. Pavlov, and O. Hovi, Appl. Phys. Lett. **63**, 275 (1993).
[21] M. K. Sheĭnkman, I. V. Markevich, and V. A. Khvostov, Fiz. Tekh. Poluprovodn. **5**, 1904 (1971) [Sov. Phys. Semicond. **5**, 1654 (1971)].
[22] A. Ya. Shik and A. Ya. Vul', Fiz. Tekh. Poluprovodn. **28**, 1645 (1994) [Semiconductors **28**, 917 (1994)].
[23] Y. Kanemitsu, T. Ogawa, K. Shiraishi, and K. Takeda, J. Luminescence **60/61**, 337 (1994).
[24] S. Gardelis, J. S. Rimmer, P. Dawson, B. Hamilton, R. A. Kubiak, T. E. Whall, and E. H. C. Parker, Appl. Phys. Lett. **69**, 2118 (1991).
[25] A. J. Steckl, J. Xu, H. C. Mogul, and S. Morgen, Appl. Phys. Lett. **62**, 1982 (1993).

Translated by Frank J. Crowne

Vibrational spectra of $CuInS_{2x}Se_{2(1-x)}$ solid solutions

I. V. Bodnar'

Belarus State University of Information Science and Radio Electronics, 220069 Minsk, Belarus
(Submitted October 3, 1995; accepted for publication February 28, 1996)
Fiz. Tekh. Poluprovodn. **31**, 49–52 (January 1997)

The reflection spectra in the infrared range and the optical Raman spectra are investigated in single crystals of the ternary compounds $CuInS_2$ and $CuInSe_2$ and in $CuInS_{2x}Se_{2(1-x)}$ solid solutions, all grown by the method of chemical transport reactions. The frequencies of the optical modes in the given materials are determined, and the type of behavior of these modes in the solid solutions are established. © *1997 American Institute of Physics.*
[S1063-7826(97)01001-6]

In addition to providing information about the phonon frequencies in solid solutions, the study of the vibrational spectra of these materials can also facilitate the identification of the spectral bands of the constituent compounds forming a given solid solution. By investigating the vibrational spectra of such materials it is possible to analyze how disorder in them influences the phonon frequencies at the center of the Brillouin zone in contrast with the constituent substances.[1]

It is a well-known fact that solid solutions can be classified as unimodal or bimodal according to the type of behavior of the optical modes.[2,3] Among the unimodal type are solid solutions, for which the optical mode frequencies vary with the composition in the range extending from frequencies typical of one of the constituent compounds to frequencies typical of another compound, while the mode intensity remains constant. The bimodal classification encompasses solid solutions, in which twice as many modes are observed for all intermediate compositions as for the constituent compounds, and the intensity of each mode is proportional to the mole fraction of the basic components.

The objective of the present study is to determine the optical mode frequencies and to establish their type of behavior in $CuIn_{2x}Se_{2(1-x)}$. The indicated substances crystallize in a chalcopyrite structure with space group of symmetry $D_{2d}^{12}(142m)$. Since the primitive cell of such a structure contains two formula units, the number of vibrational modes at the center of the Brillouin zone, which determines the number of degrees of freedom, is equal to 24 (Refs. 4 and 5). Here the optical modes in the infrared (IR) region of the spectrum and in the spectral range of the Raman effect (RE) are classified as

$$\Gamma^{\text{opt}} = 1A_1(\text{RE}) + 2A_2 + 3B_1(\text{RE}) + 3B_2(\text{IR,RE}) + 6E(\text{IR,RE}),$$

and the acoustic modes are classified as

$$\Gamma^{\text{ac}} = B_2 + E.$$

The B_2 modes are polarized $\mathbf{E} \| \mathbf{c}$, and the E modes are polarized $\mathbf{E} \perp \mathbf{c}$.

The vibrational spectra of $CuIn_{2x}Se_{2(1-x)}$ were investigated by IR and Raman spectroscopy, and the IR reflection spectra were recorded on a Perkin Elmer 180 spectrophotometer in the frequency range 150–400 cm^{-1} in polarized light at room temperature. The optical Raman spectra were excited by an argon laser with $\lambda = 4880$ Å. The scattered light was analyzed by a DFS-24 dual monochromator and was recorded by means of an FÉU-79 photomultiplier operating in the photon-counting mode. The spectral resolution was 2–3 cm^{-1}.

The homogeneous single crystals investigated in this work were prepared by the method of chemical transport reactions according to the procedure described in Ref. 6. They were made in the form of wafers with an even mirror surface corresponding to the (112) plane. The composition of the grown crystals was determined by an x-ray technique based on the satisfaction of Vegard's law within error limits of ± 1.0 mol.%. The homogeneity of the single crystal was monitored by microradiographic spectral probe analysis.

The IR reflection spectra of the ternary compounds $CuInSe_2$ and $CuInS_2$, and of the $CuInS_{2x}Se_{2(1-x)}$ solid solutions are shown in Fig. 1. Clearly, three reflection bands are observed in the spectra measured in the $\mathbf{E} \perp \mathbf{c}$ polarization for $CuInS_2$, and they agree with previous results[7] for this polarization. On the other hand, the reflection spectra for this compound in what we denote as the $\mathbf{E} \| \mathbf{c}$ polarization differ significantly from the spectra published in Ref. 7, which can be attributed to the following causes. A typical feature of the growth of crystals of the I-III-VI compounds by the method of chemical transport reactions is their preferential growth in the [111] direction. This direction forms a 35.3° angle with the optical axis of the crystal, so that the optical axis forms this angle with the natural face of the crystal (112). This causes the $\mathbf{E} \| \mathbf{c}$ polarization to be achieved partially (66%), and it has been shown[8] that the strict $\mathbf{E} \| \mathbf{c}$ polarization is impossible in the given geometry. Consequently, the spectra of this polarization can contain attenuated bands from the $\mathbf{E} \perp \mathbf{c}$ polarization. The $\mathbf{E} \perp \mathbf{c}$ conditions, however, are satisfied 100% (Ref. 8).

The reflection spectra were processed by a combined sequential analysis (so-called DAKK) technique,[9] which has lower systematic errors than either dispersion analysis (DA) or the Kramers–Kronig (KK) method used separately. It is evident from Fig. 1 that, when sulfur atoms are replaced by selenium, the spectra of the solid solutions acquire a new band (absent from the spectra of pure $CuInS_2$), which we label with the number 4 for $\mathbf{E} \perp \mathbf{c}$ and 5 for $\mathbf{E} \| \mathbf{c}$. The presence of bands 1 and 3 in the $\mathbf{E} \| \mathbf{c}$ polarization is associated

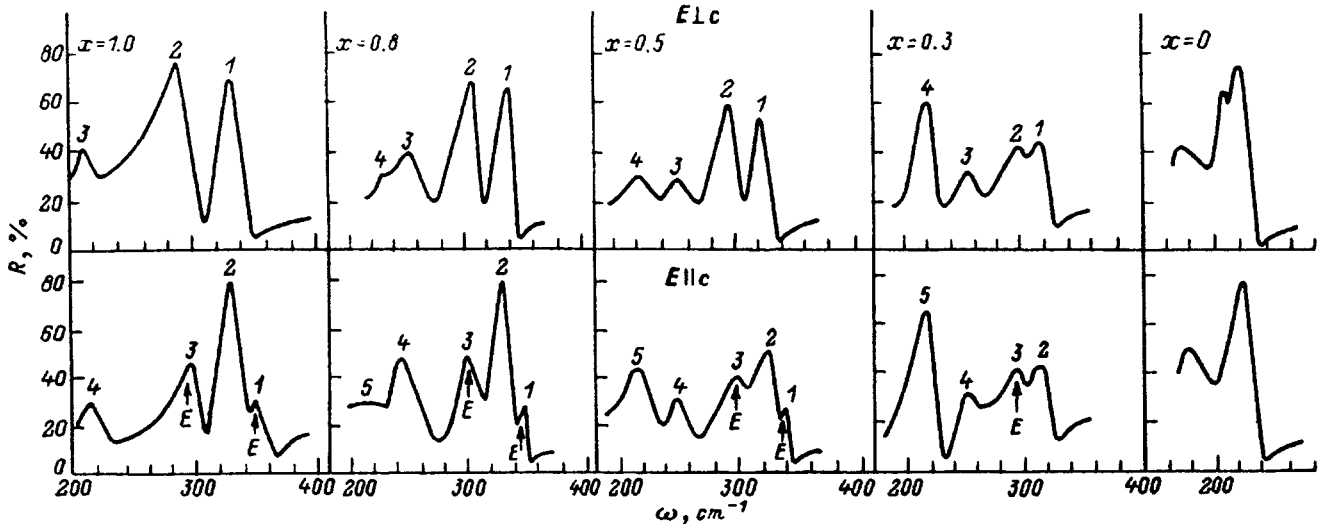

FIG. 1. Reflection spectra in the infrared range for the $CuInSe_2$ and $CuInS_2$ compounds and $CuInS_{2x}Se_{2(1-x)}$ solid solutions. The upper half of the figure corresponds to light with polarization $\mathbf{E}\perp\mathbf{c}$, and the lower half to $\mathbf{E}\parallel\mathbf{c}$.

with the above-stated causes. As the selenium content of the solid solutions is increased, the intensity of bands 4 ($\mathbf{E}\perp\mathbf{c}$) and 5 ($\mathbf{E}\parallel\mathbf{c}$) increase, while the intensities of the high-frequency bands (bands 1–3 for $\mathbf{E}\perp\mathbf{c}$, bands 2 and 4 for $\mathbf{E}\parallel\mathbf{c}$) decrease. The high-frequency bands do not occur in pure $CuInSe_2$ (Fig. 1). The concentration dependence of the TO and LO photon frequencies for $CuInS_{2x}Se_{2(1-x)}$ are shown in Fig. 2, from which we infer that, as the selenium content of the solid solutions is increased, the frequencies of bands 1–3 for $\mathbf{E}\perp\mathbf{c}$ and of bands 2 and 4 for $\mathbf{E}\parallel\mathbf{c}$ vary from the eigenfrequencies of $CuInS_2$ to the frequencies of local vibrations of the sulfur atoms in $CuInSe_2$. On the other hand, for bands 4 ($\mathbf{E}\perp\mathbf{c}$) and 5 ($\mathbf{E}\parallel\mathbf{c}$) a transition is observed from the gap mode frequency of selenium in $CuInS_2$ to the eigenfrequencies of $CuInSe_2$.

A comparison of the reflection spectra of $CuInS_{2x}Se_{2(1-x)}$ for the frequency positions of the bands with previously published data[4,7] leads to the conclusion that the modes of the solid solutions for $\mathbf{E}\perp\mathbf{c}$ (bands 1 and 2) and $\mathbf{E}\parallel\mathbf{c}$ (bad 2) are determined by the vibrations of the In–S bond, because such bands are not observed in this frequency range in $CuInSe_2$. The low-frequency bands 3 for $\mathbf{E}\perp\mathbf{c}$ and 4 for $\mathbf{E}\parallel\mathbf{c}$ also correspond to vibrations of the In–S bond with an escalating contribution to these vibrations from copper cations. The remaining modes of the solid solutions for $\mathbf{E}\perp\mathbf{c}$ (band 4) and $\mathbf{E}\parallel\mathbf{c}$ (band 5) correspond to vibrations of the In–Se bond, since they do not occur in pure $CuInS_2$.

The foregoing considerations indicate that the vibrational bands corresponding to E and V_2 modes exhibit a bimodal behavior in that their intensities and frequency positions both vary.

Figure 3 shows the Raman spectra for the ternary compounds $CuInSe_2$ and $CuInS_2$, and of certain solid solutions $CuInS_{2x}Se_{2(1-x)}$. A distinguishing feature of these spectra is the coexistence of two A_1 modes, which are pure anion modes and which correspond to vibrations of sulfur and selenium atoms surrounded by motionless neighboring atoms. Clearly, the A_1 mode corresponding to vibrations of sulfur atoms has the predominant intensity in solid solutions with $x>0.5$. The introduction of selenium atoms in $CuInS_2$ broadens and lowers the intensity of this mode. In solid solutions with $x<0.5$ the A_1 corresponding to vibrations of selenium atoms is stronger. The frequency position of the band corresponding to vibrations of sulfur atoms shifts slightly as the composition of the solid solution is varied. On the other hand, the position of the band corresponding to vibrations of

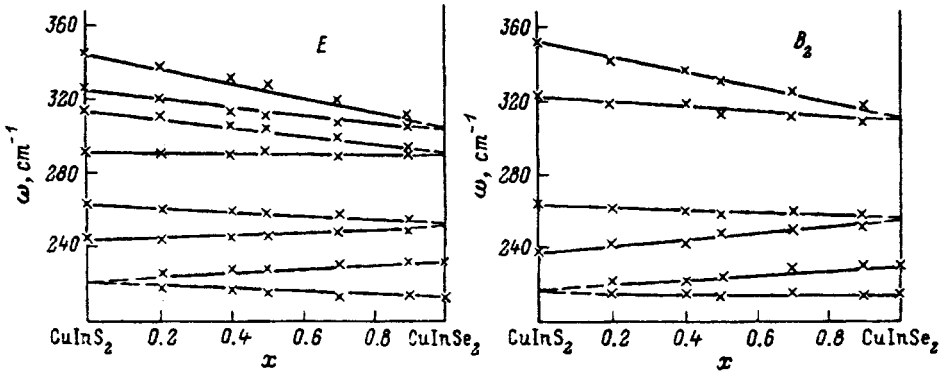

FIG. 2. Concentration dependence of the phonon frequencies (E and B_2 modes) for $CuInS_{2x}Se_{2(1-x)}$ solid solutions, determined from the reflection spectra in Fig. 1.

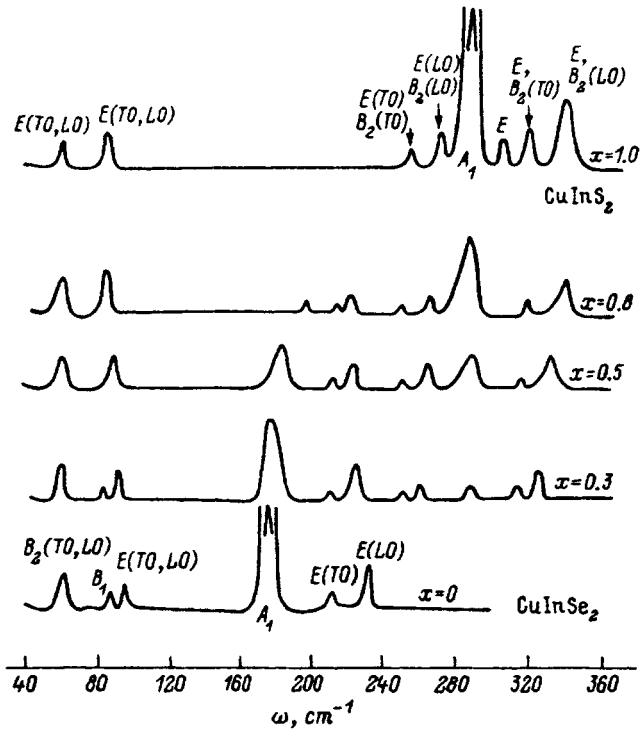

FIG. 3. Optical Raman spectra of the compounds $CuInSe_2$ and $CuInS_2$ and $CuInS_{2x}Se_{2(1-x)}$ solid solutions.

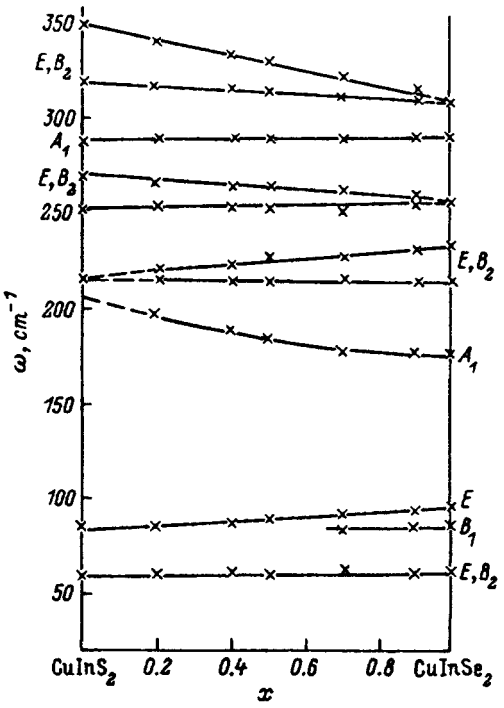

FIG. 4. Concentration dependence of the phonon frequencies for $CuInS_{2x}Se_{2(1-x)}$ solid solutions, determined from the spectra in Fig. 3.

selenium atoms in the interval $0.5<x<1.0$ varies slightly as x is increased and, beginning with $x<0.5$, its frequency gradually increases. Our results on the behavior of the A_1 mode for $CuInS_{2x}Se_{2(1-x)}$ solid solutions are in satisfactory agreement with the results of Ref. 10. The broadening of the vibrational bands of symmetry A_1 is attributable to disorder processes in an anonymous sublattice of the solid solutions, the degree of disorder becoming a maximum for the 50–50 composition.

The behavior of the high-frequency bands in the Raman spectra corresponding to E and B_2 modes is similar to the behavior of these modes in the IR reflection spectra. They exhibit a bimodal behavior (Fig. 4). The low-frequency bands corresponding to E and B_2 modes are induced by Cu–S(Se) vibrations and exhibit unimodal behavior.

Our investigations have thus shown that the optical modes in $CuInS_{2x}Se_{2(1-x)}$ solid solutions exhibit a mixed (unimodal and bimodal) type of behavior.

[1] I. V. Bodnar', G. F. Smirnova, A. G. Koroza, and A. P. Chernyakova, Phys. Status Solidi B **158**, 469 (1990).
[2] G. M. Zinger, I. P. Ipatova, and A. V. Subashiev, Fiz. Tekh. Poluprovodn. **10**, 479 (1976) [Sov. Phys. Semicond. **10**, 286 (1976)].
[3] J. F. Chang and S. S. Mitra, Phys. Rev. **172**, 924 (1968).
[4] W. H. Koschel, F. Sorger, and J. Baars, J. Phys. (Paris) **36**, 177 (1975).
[5] R. Sandbrock and J. Treusch, Z. Naturforsch. Teil A **19**, 884 (1964).
[6] I. V. Bodnar', A. P. Bologa, and B. V. Korzun, Krist. Tech. **15**, 1285 (1980).
[7] H. Neumann, W. Kissinger, H. Sobotta, V. Riede, R. D. Tomlinson, and N. Avgerinos, Czech. J. Phys. B **34**, 69 (1974).
[8] N. Jamamoto and T. Miyauchi, Bull. Univ. Osaka Prefect Ser. A **23**, 147 (1974).
[9] V. M. Burakov, D. A. Rzaev, and V. N. Pyrkov, Inst. Spektrosk. Akad. Nauk SSSR Preprint [in Russian], Institute of Spectroscopy, Academy of Sciences of the USSR (1984).
[10] R. Vacewicz, W. Gebicki, and J. Filipowicz, J. Phys. **6**, 777 (1994).

Translated by James S. Wood

Charge instability effects in the system silicon carbide–insulator

V. A. Karachinov

Novgorod State University, 173003 Novgorod, Russia
(Submitted December 14, 1995; accepted for publication January 16, 1996)
Fiz. Tekh. Poluprovodn. **31**, 53–55 (January 1997)

The influence of laser radiation on the electric strength and characteristics of the interface of the system silicon carbide–insulator is investigated by nondestructive inspection according to the noise characteristics and by means of the capacitance–voltage characteristics. It is found that a laser beam can be used to control the fixed charge in the insulating layer and to modify the distribution of the density of surface states. Possible mechanisms underlying the observed effects are discussed. © *1997 American Institute of Physics.* [S1063-7826(97)01101-0]

INTRODUCTION

The laser irradiation of such well-studied semiconductors as silicon, germanium, and gallium arsenide in the implementation of cutting (scribing) operations, the annealing of implanted layers, evaporation, etc., is known to be capable of producing various modifications of their crystal structure as well as their electrical and optical properties.[1,2] Laser technologies are especially valuable in application to high-temperature semiconductors, including silicon carbide.

For example, studies associated with the influence of a laser beam on layered structures, SiC–insulator structures in particular, which not only have interesting properties but are also typical in the planar technology of semiconductor devices, have important bearing on a number of engineering applications.[3–6]

Here we give the results of experimental investigations of the influence of millisecond laser pulses on the properties of insulating films and interfaces in insulator–semiconductor structures made from 6*H*-SiC.

EXPERIMENTAL PROCEDURE

Silicon dioxide films of thickness $d \approx 0.2$ μm were deposited on the (0001)*C* face of silicon carbide substrates by the following methods: thermal oxidation of SiC in dry and wet oxygen SiO_{2t}; oxidation of silane with oxygen SiO_{2s}. Silicon nitride films of thickness $d \approx 0.2$ μm were prepared by the reactive cathode sputtering of silicon in a nitrogen atmosphere. The substrates were 6*H*-SiC single crystals with a density of uncompensated donors $N_d - N_a = (1-3) \times 10^{18}$ cm^{-3} and a dislocation density $N_D = 10^3 - 10^4$ cm^{-2}. The deposition of the insulating films was preceded by chemical etching of the substrates in a KOH melt at a temperature $T = 450$ °C for 20 min. Some of the substrates were further etched in an argon plasma.

The SiC–insulator structures were irradiated with laser pulses ($\lambda = 1.06$ μm, $\tau = 0.8 \times 10^{-4}$ s, pulse energy density $E_p = 0.3$–20 J/cm^2).

The electric strength of the insulating films was estimated by nondestructive inspection from the noise characteristics.[7] The properties of the SiC–insulator interface were investigated on the basis of the high-frequency capacitance–voltage characteristics.[8]

EXPERIMENTAL RESULTS AND DISCUSSION

By performing the measurements under nondestructive conditions we were able to compare the electric strengths of the untreated and irradiated insulating films. The measurements showed that the electric strength of nonirradiated SiO_{2t} films on SiC is one third the value for SiO_{2s} films. This fact is obviously attributable to defects of the initial structure of the substrates and the presence of unbonded carbon at the SiC–SiO_{2t} interface formed during the oxidation of silicon carbide.[9] The irradiation of the untreated insulator–silicon carbide structures in the interval of pulse energies $\sim(0.3$–$7)$ J/cm^2 increased the electric strength of the SiO_{2t}, SiO_{2s}, and Si_3N_4 films. The dependence of E_s on the energy density in the pulse exhibits a complex behavior (Fig. 1). It can only be assumed that the increase in E_s is associ-

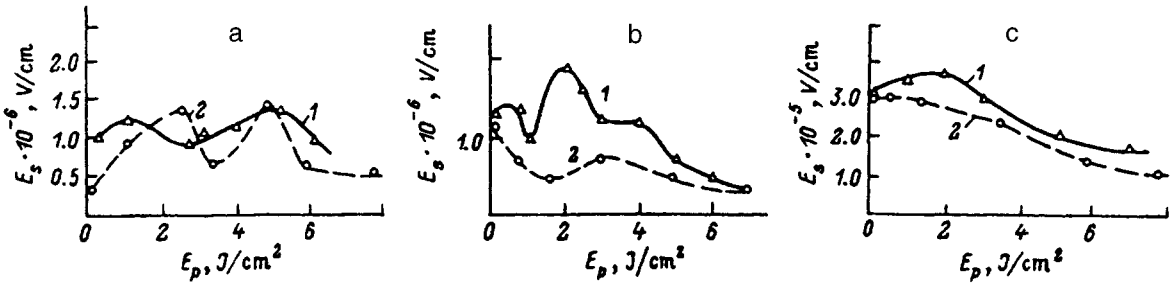

FIG. 1. Experimental graphs of the electric strength of insulating films vs laser energy density. *1)* After chemical + ion-plasma (Ar) etching of the substrate; *2*) after chemical etching of the substrate in a KOH melt; a) SiC–SiO_{2t}; b) SiC–SiO_{2s}; c) SiC–Si_3N_4.

 1063-7826/97/010044-02$10.00

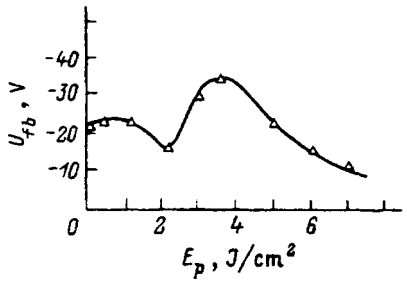

FIG. 2. Flat-band voltage of the systems SiC–SiO_{2t} vs laser energy density (experimental).

ated mainly with variations in the properties of the interface. In particular, for SiO_{2t} it can be attributed to a decrease in the concentration of nonuniformly distributed carbon as a result of diffusion toward the surface, the formation of Si–O–C bonds, and chemical reactions, which result in the synthesis of CO from CO_2 accumulated during oxidation of the interface.[10]

From all appearances, the decrease in E_s is explained by purely mechanical disturbances that set in at high pulse energy densities and by the nonuniform energy distribution in the laser spot.

The results of our investigation of the characteristics of the insulator–SiC interface suggest an apparent correlation between the variations of E_s and the charge state. In the case of SiC–SiO_{2t} structures, for example, beginning with energies $E_p=4$ J/cm^2 and higher, the flat-band voltage and, hence, the fixed charge in the oxide decrease (Fig. 2). It is important to note that the slope of the capacitance–voltage characteristics vary only slightly over the entire investigated range of laser energies. In the interval $E_p=(3–5)$ J/cm^2, however, the characteristic acquires a step, and at $E_p=5.98$ J/cm^2 the path traversed around the hysteresis loop changes (Fig. 3). In this case hysteresis is caused by the electrons falling into traps situated in the oxide layer near the silicon carbide surface, and beginning with energy $E_p=6$ J/cm^2, the traversal of the hysteresis loop reverts to its original path, and ion drift becomes predominant in the silicon dioxide film.[8] The appearance of the step on the high-frequency capacitance–voltage characteristic is obviously associated with flaws in the crystal structure at the SiC–SiO_{2t} interface under the influence of laser irradiation. This creates a distribution of the density of surface states in the form of a monoenergic surface level. The presence of such a level alters the dependence of the surface potential on the displacement voltage of the SiC–SiO_{2t} structure, and its shielding action merely causes isolated segments of the capacitance–voltage characteristic to shift relative to the initial characteristic. We can assume that we have a monoenergic surface level in the form of a trap, which exchanges charge with the SiC. Here the maximum density of surface states, calculated from Ref. 8, is $N_{ss}=2.5\times10^{11}$ eV·cm^{-2}.

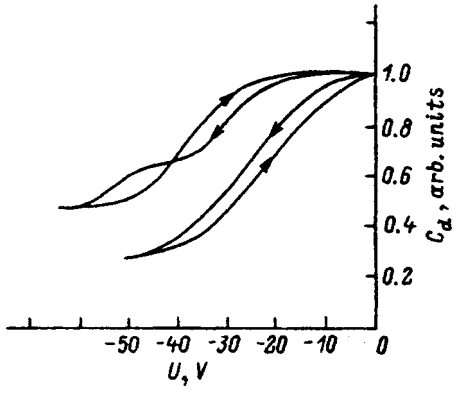

FIG. 3. High-frequency capacitance–voltage characteristics of the system SiC–SiO_{2t} (experimental). *1*) After laser irradiation $E_p=(3–5)$ J/cm^2; *2*) untreated.

CONCLUSION

1. The system silicon carbide–insulator has been irradiated with a laser, producing significant structural changes both in the insulating films and in the vicinity of the interface.

2. A laser beam can be used to control the fixed charge in the insulating layer and to alter the nature of the distribution of surface states.

[1] A. V. Marsanov, Itogi Nauki Tekh. Élektron. **13**, 73 (1981).
[2] A. G. Grigor'yants, *Fundamentals of the Laser Processing of Materials* [in Russian], Mashinostroenie, Moscow (1989).
[3] I. Lundström, Phys. Scr. **18**, 424 (1978).
[4] V. A. Karachinov, in *Digests of the International Seminar on Semiconducting Silicon Carbide and Devices Utilizing It* [in Russian], Novgorod (1995), p. 72.
[5] É. E. Violin, O. N. Voron'ko, F. Noĭbert, and E. N. Potapov, Fiz. Tekh. Poluprovodn. **18**, 954 (1984) [Sov. Phys. Semicond. **18**, 596 (1984)].
[6] P. A. Ivanov, V. N. Panteleev, T. P. Samsonova, and V. E. Chelnokov, Fiz. Tekh. Poluprovodn. **29**, 271 (1995) [Semiconductors **29**, 135 (1995)].
[7] L. P. Karba and L. N. Krutyakov, Élektron. Tekh., Ser. 8, **3**, 68 (1978).
[8] V. M. Koleshko and G. D. Kaplan, Obzory Élektron. Tekh. Mikroélektron. **2**, 79 (1977).
[9] R. W. Kee, K. M. Geib, and C. W. Wilmsen, J. Vac. Sci. Technol. **15**, 1520 (1978).
[10] A. Suzuki, H. Matsuami, and T. Tanaka, J. Electrochem. Soc. **125**, 1896 (1978).

Translated by James S. Wood

Optical properties of quasiperiodic and aperiodic PbS–CdS superlattices

S. F. Musikhin, V. I. Il'in, O. V. Rabizo, L. G. Bakueva, and T. V. Yudintseva

St. Petersburg State Technical University, 195251 St. Petersburg, Russia
(Submitted February 26, 1996; accepted for publication February 28, 1996)
Fiz. Tekh. Poluprovodn. **31**, 56–62 (January 1997)

The transmission spectra of quasiperiodic Fibonacci superlattices and aperiodic Thue–Morse superlattices of the system PbS–CdS at room temperature and at 77 K are investigated. The superlattices are fabricated by pulsed laser-beam evaporation. The spectrum of optical transitions of the aperiodic superlattice is much richer than implied by a calculation of the spectrum of periodic superlattices. This is a consequence of the fractal structure of the energy spectrum of the aperiodic superlattices. Self-similarity is observed in the energy spectra of Thue–Morse lattices. © *1997 American Institute of Physics.* [S1063-7826(97)01201-5]

1. INTRODUCTION

The capability of creating artificial media on the basis of layered structures using materials endowed with extremely diverse properties is a reality today. Of special interest are layered structures with quantum-well layers. Electronic circuitry components with distinctive new properties can be constructed on the basis of such quantum-well structures or superlattices. Intriguing attributes can be expected in structures composed of lead sulfide and cadmium sulfide layers. Lead sulfide is a photosensitive material with a narrow band gap ($E_g = 0.41$ eV), a high static dielectric permittivity, and a nonparabolic conduction band. Cadmium sulfide is a wide-gap semiconductor ($E_g = 2.4$–2.6 eV) that exhibits photosensitivity and piezoelectric properties. The consolidation of these materials into a superlattice can lead to the creation of a structure in which photostimulated nonequilibrium carriers and piezoelectric excitations closely interact with one another.

Here we report an investigation of the optical transmission spectra of multilayer structures consisting of quantum-size lead sulfide and cadmium sulfide layers, which are combined in such a way as to form two types of superlattice: a Fibonacci quasiperiodic superlattice or a Thue–Morse superlattice.

The quasiperiodic Fibonacci superlattice, which is grown in the pattern of a Fibonacci sequence, is classified as intermediate between periodic and disordered media. Certain salient features of the energy spectrum of such structures have already been studied in the example of GaAs–GaAlAs Fibonacci superlattices.[1]

The Thue–Morse superlattice is based on a sequence in which each term is defined by the rule $T_r = T_{r-1} + T_{r-1}^+$, where r enumerates the elements in the sequence, and T_{r-1}^+ is the complement of the term T_{r-1}. For example, given two structural elements A and B of a Thue–Morse sequence, the complement of element A is B ($A^+ = B$) and, conversely, the complement of element B is A ($B^+ = A$). In the complement, which consists of several layers, the position of element A is occupied by B, and vice versa. A Thue–Morse superlattice constructed by this rule never repeats itself. Despite the aperiodicity, it is inherently self-similar.[2]

2. OBJECT OF INVESTIGATION

The investigated superlattices were constructed from two structural elements: Element A comprised a lead sulfide layer of thickness 20 Å and a lead sulfide layer of thickness 10 Å; element B comprised a lead sulfide layer of thickness 40 Å and a cadmium sulfide layer of thickness 10 Å. Elements A and B were combined to form structures $S^* = ABABAABABAABAABABABAA$ in conformity with a Fibonacci number sequence and $T^* = ABBABAABBAABABBA$ in accordance with a Thue–Morse sequence. The structures were prepared by pulsed laser-beam vacuum evaporation.[3]

3. EXPERIMENTAL RESULTS AND DISCUSSION

The spectra of the optical transmission T of the superlattices were investigated in the infrared, visible, and ultraviolet regions at room temperature and at liquid-nitrogen temperature. In this article all the spectra are displayed with the ordinate $1 - T$, which is proportional to the absorption coefficient.

The one-to-one relation between the absorption spectra and the density of states function in superlattices is well known.[4,5] Minibands are formed in periodic superlattices, whereas in aperiodic superlattices levels common to the entire lattice coexist with energy levels associated with localized states in solitary quantum wells and in groups of maximally tight-coupled wells. The result is an energy spectrum having a stepped character with several diffuse transitions from one step to another. The electron energy levels were calculated in the Kronig-Penney model for isolated quantum wells separated by barriers. The previously used[6] energy diagram of a type-II PbS–CdS superlattice with overlap of the CdS conduction bands and the PbS valence band at room temperature was employed in the present study. The distinctive features of the carrier energy spectrum show up in the optical spectra and are a consequence of intraband and interband transitions in the superlattices.

The widths of the band gaps of the superlattice components were measured at liquid-nitrogen temperature; the gap width decreases for lead sulfide ($E_g = 0.31$ eV) and increases for cadmium sulfide ($E_g = 2.5$ eV).

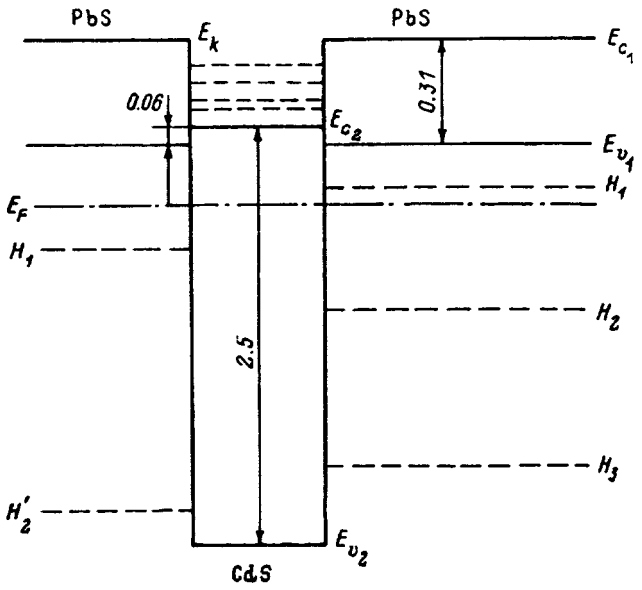

FIG. 1. Energy band diagram of a CdS–PbS superlattice at 77 K. The numbers indicate the widths of the energy intervals in electron-volts.

If we assume, for example, that the discontinuity of the valence bands of the superlattice components ($\Delta E_v = \text{const}$) remains constant,[1)] then the partial overlap of the allowed bands of the superlattice components is eliminated, and the band gaps overlap (Fig. 1).

Calculations show that the quantum well formed by the conduction band of cadmium sulfide contains one quantum level $E_1 = 0.257$ eV, which is not occupied by electrons. At 77 K, depending on the width of the barrier, whether a lead sulfide layer of thickness 20 Å or 40 Å, the quantum well for cadmium sulfide has four closely spaced quantum levels in the energy interval 0.171–0.183 eV. The hole quantum wells formed by lead sulfide layers contain from five to ten quantum levels in the valence band for lead sulfide layers of thickness 20 Å and 40 Å, respectively.

Investigations of the Hall effect on films of satellite samples yield values of the concentration such that the Fermi level at the given doping levels of the superlattice components is situated below the top of the cadmium sulfide valence band. In this case the first H_1 level in the quantum well of the lead sulfide layer of width 40 Å is free. Accordingly, interband transitions between free electron levels in the cadmium sulfide conduction band and filled levels in the lead sulfide valence bands are possible, along with intraband transitions between the first unfilled level in the valence band of the lead sulfide layer of thickness 40 Å and deeper filled levels in the valence bands of lead sulfide. Table I gives calculated and experimental data on the possible energy transitions in the superlattices.

Figures 2–4 give the optical spectra of the Fibonacci and Thue–Morse superlattices at room temperature and at liquid-nitrogen temperature in the IR region of the spectrum on barium fluoride and glass substrates. An absorption peak appears in the IR range of the transmission spectrum for BaF_2 substrates at a temperature of 77 K, making it difficult to analyze the transmission spectra of the superlattices. We therefore constructed superlattices on glass and investigated them in the same spectral range as the superlattices on a BaF_2 substrate. Against the background of the transmission spectrum in all the structures there is a stepped structure, which characterizes the prominent features of the superlattice and does not occur in the spectrum of the substrates. Typically, the spectrum of the Fibonacci superlattices is stepped, whereas the spectra of the Thue–Morse superlattices disclose absorption peaks in addition to the steps (see, e.g., Fig. 2 for energies of 0.389 eV and 0.434 eV). The numbers in the figures indicate transitions, whose order numbers coincide with those of the transitions in Table I.

The spectra for lattices constructed on BaF_2 substrates (Fig. 2) have a distinct stepped profile. The greatest number of steps is observed in the spectra of the Thue–Morse superlattices at room temperature. The experimentally determined spectrum discloses a far greater number of steps for the Thue–Morse superlattices than predicted by calculations for the solitary quantum wells (see Table I). These results are consistent with recent theoretical studies of the electron spectra of Thue–Morse superlattices,[2,7,8] which show that in aperiodic superlattices of the given form the spectra contain a greater number of energy steps than for periodic and quasiperiodic superlattices. As mentioned above, despite the change in the shape of the spectrum, the elements of self-similarity or fragmentation are preserved in the Thue–Morse superlattices. This fact is revealed in the observation of two

TABLE I. Calculated and experimental data for the energy transitions in superlattices in the infrared region of the spectrum.

Transition No.	Type of transition	Transition energy, eV: Calculated	Experiment on superlattices (BaF_2 substrate): Fibonacci	Thue–Morse	Experimental temperature, K
1	H_1'–H_1	0.148	0.150–0.236	0.144–0.164	300
2	H_2–H_1	0.206	0.150–0.236	0.198–0.216	300
3	H_3–H_1	0.438	0.423–0.439	0.440	300
4	H_1'–E_1	0.476	0.445–0.487	0.459–0.473	300
1′	H_1'–H_1	0.141	0.139–0.155	0.144–0.164	77
2′	H_1'–E_1	0.486	0.478–0.483	0.482–0.496	77

Note: H_k denotes the quantum levels in the valence band of a PbS layer of thickness 40 Å, H_k' is the same in a layer of thickness 20 Å, and E_1 is the quantum level in the conduction band of CdS.

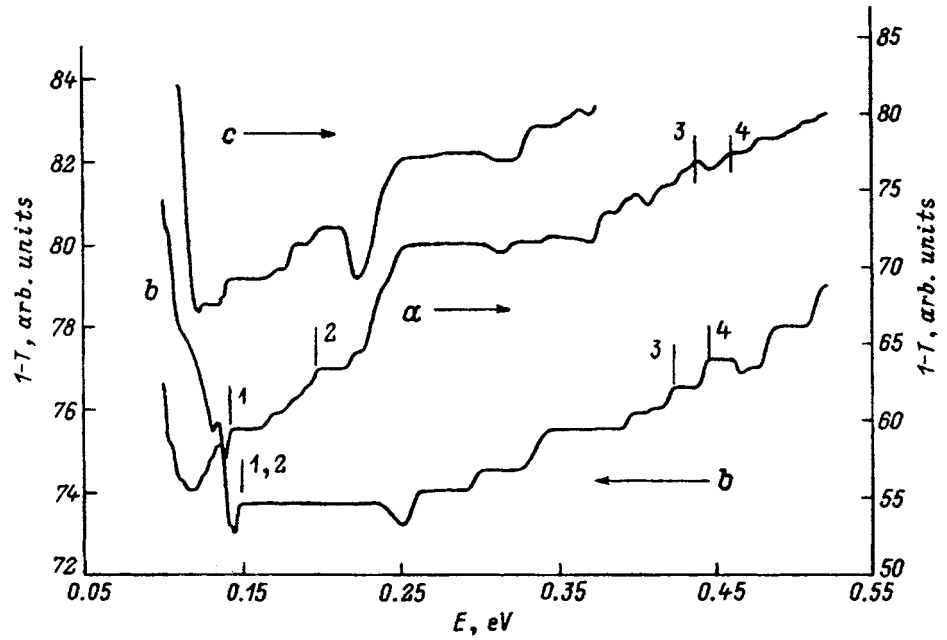

FIG. 2. Absorption spectra in the IR region for superlattices fabricated on a BaF_2 substrate. a) Thue–Morse superlattice at 300 K; b) Fibonacci superlattice at 300 K; c) Thue–Morse superlattice at 77 K. The transitions are numbered along the spectra in accordance with the order numbers in Table I.

narrow steps between two broader steps in the absorption spectra.[7]

A lucid example of self-similarity is the absorption spectrum of a Fibonacci superlattice on a barium fluoride substrate, shown in Fig. 2. Three broad steps are observed in the spectrum in the energy intervals 0.150–0.240, 0.340–0.395, and 0.445–0.480 eV, etc. This arrangement of the steps in the spectrum exhibits the self-similarity of the energy spectrum and corroborates the existence of a bona fide Fibonacci superlattice.

The spectrum of a Thue–Morse superlattice at room temperature (Fig. 2) consists almost entirely of energy steps. Self-similarity elements can be seen in the low-energy range in the interval 0.107–0.250 eV. For example, several narrow steps are interspersed between the broad steps 0.144–0.164 eV, 0.205–0.220, and 0.255–0.280 eV. This pattern of the spectrum persisted at liquid-nitrogen temperature with a certain energy shift of the broad steps. At higher energies in the IR range 0.280–0.500 eV the room-temperature spectrum comprises a sequence of steps of approximately identical width.

Figures 3 and 4 show the absorption spectra in the IR range for superlattices prepared on a glass substrate. A series of prominent features associated with the grown structures is observed in the superlattice spectra against the background of the substrate transmission spectrum. The energy positions of the majority of the steps for superlattices on BaF_2 and glass substrates practically coincide. In fact, the spectra of the Fibonacci superlattices on glass also have a stepped profile. Lowering the temperature does not alter the general appearance of the spectrum. The analyzed part of the spectrum of a structure on a glass substrate is a fragment of the spec-

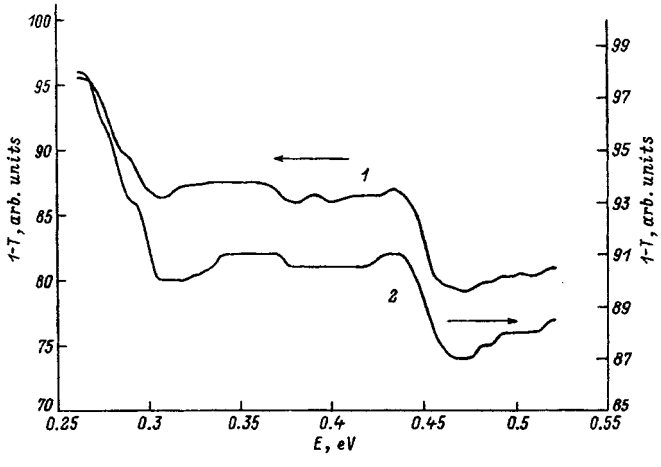

FIG. 3. Absorption spectra at 300 K in the IR region for superlattices fabricated on a glass substrate. *1)* Thue–Morse superlattice; *2)* Fibonacci superlattice.

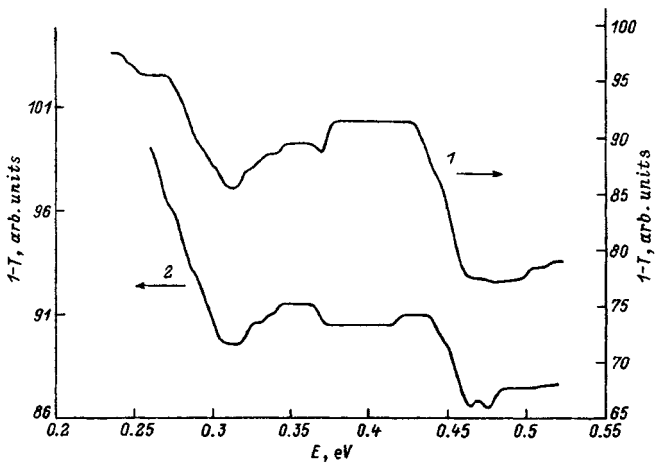

FIG. 4. Absorption spectra at 77 K in the IR region for superlattices fabricated on a glass substrate. *1)* Thue–Morse superlattice; *2)* Fibonacci superlattice.

TABLE II. Calculated and experimental data for the energy transitions in superlattices in the infrared region of the spectrum.

Transition No.	Type of transition	Transition energy, eV: Calculated	Experiment on superlattices (BaF_2 substrate): Fibonacci	Thue–Morse
1	H_8–H_1	1.72	0.160	1.70–1.754
2	H_7–E_1	1.79	1.75–1.80	1.70–1.75
3	H_4–E_1	1.84	1.86–1.89	1.85
4	H_9–E_1	1.92	1.86–1.89	1.85
5	H_9–H_1	1.99	2.02	2.06
6	H_5–H_1	2.01	2.02	2.06
7	H_8–E_1	2.05	2.02	2.06
8	H_{10}–H_1	2.25	2.30	2.28–2.32
9	H_5–E_1	2.34	2.43	2.34–2.41
10	H_{10}–E_1	2.58	2.58	2.58
1′	H_8–H_1	1.62	0.162	1.62
2′	H_7–E	1.71–1.83	1.70–1.73	1.70
3′	H_9–H_1	1.87	1.86	1.83
4′	H_4–E	1.76–1.88	1.86	1.85
5′	H_8–E	1.96–2.08	1.97	1.97–2.00
6′	H_5–H_1	2.00	1.97	1.97–2.00
7′	H_{10}–H_1	2.12	2.13	2.16–2.24
8′	H_9–E	2.15–2.27	2.24	2.16–2.24
9′	H_5–E	2.24–2.27	2.24	2.30
10′	H_{10}–E	2.58	2.58	2.50–2.53

Note: Transitions 1–10 were observed at 300 K, and transitions 1′–10′ at 77 K.

trum of the structure grown on a BaF_2, and the general features of the two spectra concur quite well. For example, steps are observed in the energy intervals 0.340–370 eV, 0.429–0.440 eV, and 0.493–0.521 eV. An exception is the step 0.269–0.300 eV, which splits into two narrow steps for a structure grown on a glass substrate.

Prominent features in the form of steps and in the form of absorption peaks are observed in the spectra measured at room temperature for Thue–Morse superlattices grown on a glass substrate. However, the number of such features is much smaller than in the analogous spectrum of the structure on a BaF_2 substrate. An exception is the energy interval 0.475–0.525 eV, where the positions of the steps for both types of substrates essentially coincide. The absorption peak at an energy of 0.390 eV, which is observed in structures on both glass and BaF_2 substrates, can be explained on the assumption that the superlattice exhibits a common energy level situated 0.501 eV below the top of the lead sulfide valence band. The absorption peak in the vicinity of 0.434 eV is associated with an intraband H_3–H_1 transition in the valence band of a lead sulfide layer of thickness 40 Å. The presence of an absorption peak at energy 1.83 eV in the spectra is associated with a transition of the type L^6–$L_3^{6'}$ in lead sulfide.

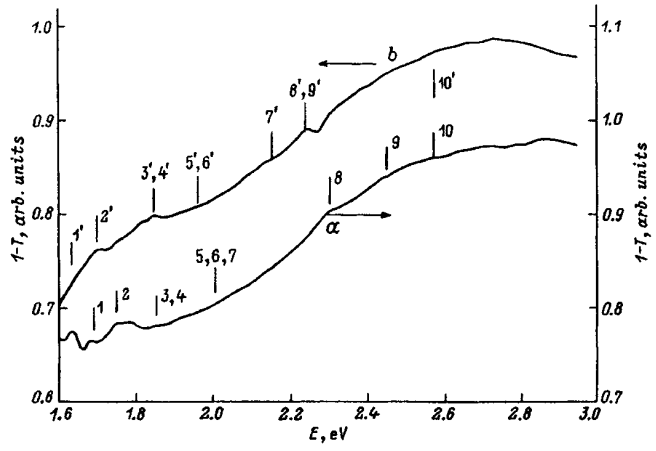

FIG. 5. Absorption spectra in the UV spectral region for Thue–Morse superlattices fabricated on a glass substrate. a) 300 K; b) 77 K. The transitions are numbered along the spectra in accordance with the order numbers in Table II.

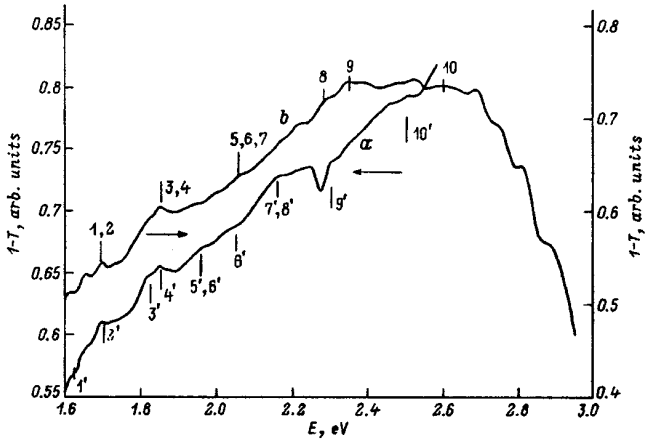

FIG. 6. Absorption spectra in the UV spectral region for Fibonacci superlattices fabricated on a glass substrate. a) 300 K; b) 77 K. The transitions are numbered along the spectra in accordance with the order numbers in Table II.

Table II summarizes the calculated and experimental data for energy transitions in the superlattices in the visible and UV spectral ranges. The calculations were carried out in the approximation of two quantum wells. It is evident from these data that good agreement is observed between theory and experiment.

CONCLUSION

Laser-beam vacuum evaporation has been used to fabricate two types of structures on barium fluoride and glass substrates: quasiperiodic superlattices fabricated in a Fibonacci sequence and aperiodic superlattices fabricated in a Thue–Morse sequence. The coincidence of the positions of the steps on an orienting substrate (BaF_2) and on a nonorienting amorphous substrate (glass) does not have a decisive influence on the growth of quantum-well structures fabricated by pulsed laser-beam evaporation.

An investigation of the optical transmission spectra of the fabricated structures in the infrared, visible, and ultraviolet ranges of the spectrum has shown that the spectra have a series of prominent features (steps and absorption peaks), whose presence, as we know,[4,5] evinces a stepped behavior of the density of states function. This knowledge has enabled us to identify the synthesized structures as superlattices. The

investigations have shown that the spectrum of the Fibonacci superlattices exhibits a self-similarity effect inherent in quasiperiodic structures.[1]

It was found for the first time that self-similarity elements are also present in the spectra of periodic structures constructed in accordance with a Thue–Morse sequence, corroborating recent theoretical work.[1,2]

A calculation of superlattice energy levels in the Kronig-Penney model for isolated quantum wells gives good agreement between theory and experiment. The results lead to the conclusion that the fabricated structures are quasiperiodic Fibonacci superlattices and aperiodic Thue–Morse superlattices.

This work has received support from the Russian Fund for Fundamental Research, Grants 94-02-05886 and 96-02-17200, and from the International Soros Science Education Program (ISSEP), Grant 1027P.

[1)]Being deeper, the valence bands should be less prone to changes induced by temperature variations.

[1] D. Munzar, L. Bocáek, J. Humlicek, and K. Ploog, J. Phys. C **6**, 4107 (1994).
[2] D. Huang, G. Gumbs, and M. Kolar, Phys. Rev. B **46**, 1147 (1992).
[3] L. G. Baueva, V. I. Il'in, S. F. Musikhin, and L. V. Sharonova, Fiz. Tekh. Poluprovodn. **27**, 1868 (1993) [Semiconductors **27**, 1029 (1993)].
[4] M. Herman, *Semiconductor Superlattices* [Russian translation], Mir, Moscow (1989).
[5] A. Ya. Shik, *Two-Dimensional Electronic Systems* [in Russian], SPbGTU, St. Petersburg (1993).
[6] S. F. Musikhin, L. G. Bakueva, V. I. Il'in, O. V. Rabizo, and L. V. Sharonova, Superlat. Microstr. **15**, 495 (1994).
[7] D. Barache and J. M. Luck, Phys. Rev. B **49**, 15004 (1994).
[8] Q. Niu and F. Nori, Phys. Rev. B **42**, 10329 (1990).

Translated by James S. Wood

Waveguide properties of gallium, aluminum, and indium nitride heterostructures

V. E. Bugrov and A. S. Zubrilov

A. F. Ioffe Physicotechnical Institute, Russian Academy of Sciences; Cree Research EED Inc., 194021 St. Petersburg, Russia

(Submitted February 21, 1996; accepted for publication February 29, 1996)
Fiz. Tekh. Poluprovodn. **31**, 63–67 (January 1997)

The waveguide properties of double heterostructures constructed from nitrides of group-III elements are investigated. It is established that a maximum 8–10% AlN is sufficient (for limiting the optical mode inside the active region) in the solid solution of the wide-gap layer. The influence of light absorption in the wide-gap layers on the threshold current density of heterostructure lasers is taken into account. This form of light absorption is probably a decisive factor for heterostructures utilizing III-nitrides. A threshold current density at levels of the order of 10 kA/cm^2 is expected for lasers utilizing such structures. Because of strong light absorption in the waveguide layer, the threshold current density for lasers with solitary quantum wells cannot be expected to be any lower than that of conventional double-heterostructure lasers. The threshold current density can be lowered to a few kA/cm^2 in the case of lasers with a large number of quantum wells.
[S1063-7826(97)01301-X]

1. INTRODUCTION AND PRINCIPAL RESULTS

The nitrides of group-III elements (III-nitrides), specifically In, GaN, AIN, and their solid solutions are promising materials for the fabrication of short-wavelength laser diodes.[1,2] Recent advances in nitride technology have made the construction of such diodes an entirely real possibility. The fabrication of the world's first injection laser utilizing III-nitrides was announced in January of 1996 (Ref. 3). The present-day theory of semiconductor injection lasers using heterostructures is tailored to the properties of III-arsenides, III-antimonides, and III-phosphides. For heterostructure lasers utilizing these materials both theory and experiment show[4] that the threshold current density decreases regularly as the thickness of the active narrow-gap zone is decreased. The phenomenon is very simple in essence: The thinner the zone, the fewer the carriers that need to be injected into it to induce population inversion.

In the case of the simplest double heterostructure (DH) lasers, where the active zone serves in the additional capacity of waveguide, the curve representing the threshold current density as a function of the thickness of the active zone has a minimum. This is attributable to the fact that only the part of the optical mode propagating through the active zone is amplified, so that too much of a reduction in the thickness of the active zone leads to extremely rapid degradation of optical mode confinement to the active zone and, as a consequence, an increase in the current required to achieve lasing.

In double heterostructure lasers with separate mode confinement (SCDH lasers) nonequilibrium carriers are confined within the active zone, whereas the optical field is confined within the relatively thick waveguide layer. In this case optical confinement is not significantly diminished; hence the threshold current decreases monotonically with the thickness of the active zone. This decrease is particularly noticeable in transition from lasers using a bulk material to lasers operating on quantum wells or even quantum points, where a lower carrier pump level is required to attain the same gains in the active zone.

However, these considerations are valid when light absorption does not take place in the passive wide-gap layers of the structure. This is, in fact, the case for the majority of direct-band-gap materials characterized by sharp absorption edges. In particular, for the photon energy of a GaAs/AlGaAs laser, which corresponds to a shift of the order of 40-meV into the red part of the spectrum from the width of the band gap, the absorption coefficient of GaA is approximately 10 cm^{-1} (Ref. 4), and the absorption coefficient of AlGaAs solid solutions used as materials for wide-gap layers is only a few reciprocal centimeters.

Existing data on the absorption coefficients of gallium and aluminum nitrides[1,5] show that the absorption spectra in these materials have a low-energy ''tail,'' which leads to appreciable absorption of the generated light in the wide-gap layers. For nitride materials the absorption coefficient at the emission wavelength of the laser is clearly of the order of 10^3 cm^{-1}. The present study has shown that a consequence of this figure is the fact that the curve of the threshold current density as a function of the thickness of the active zone has a pronounced minimum for DH and — especially important — SCDH lasers made from III-nitrides.

It is evident from Fig. 1 that allowance for strong absorption in the wide-gap claddings has the effect of shifting the optimum thickness of the active zone from a value of the order of 0.05 μm to values of the order of 0.2 μm. Here the expected threshold current density of the laser increases severalfold, arriving at the level 10 kA/cm^2. Figure 1 shows the dependence of the threshold current density on the thickness of the active zone for a DH laser with various wide-gap regions containing from 2% to 20% aluminum nitride and a narrow-gap region of pure gallium nitride. This dependence has a minimum, which becomes lower as the wide-gap addition of aluminum nitride is increased. This tendency reaches saturation: Curves 3 and 4 in Fig. 1 scarcely differ from one

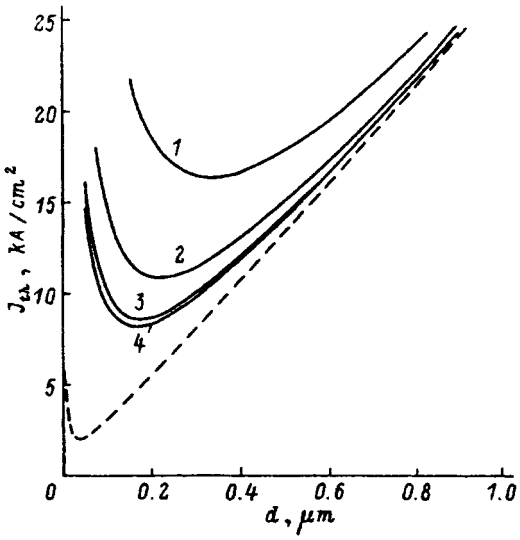

FIG. 1. Threshold current density j_{th} in laser double heterostructures of the type GaN/AlGaN ($\lambda=370$ nm) vs thickness of the active zone d for four solid solution compositions (percentage AlN) in the wide-gap layers. *1*) 2%; *2*) 5%; *3*) 10%; *4*) 20%. The graphs represent the results of calculations with (solid curves) and without (dashed curves) regard for light absorption in the wide-gap layers.

another, even though curve 3 refers to a 10% content of aluminum nitride, and curve 4 to a 20% content.

The nature of the dependence of the threshold current density on the thickness of the active zone changes in the case of a SCDH laser. This variation is shown in Fig. 2. It is evident from the figure that in the range of the most significant practical thicknesses of the active zone the threshold current density is not observed to decrease with diminishing

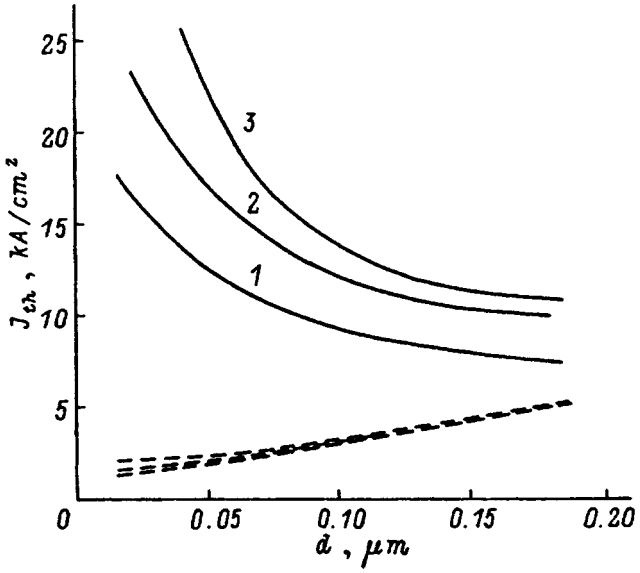

FIG. 2. Threshold current density j_{th} for a laser utilizing a double heterostructure with separate confinement of the type $In_{0.1}Ga_{0.9}N/GaN/Al_{0.1}Ga_{0.9}N$ ($\lambda=395$ nm) vs thickness of the active zone d for three thicknesses of the GaN waveguide layer. *1*) 0.2 μm; *2*) 0.4 μm; *3*) 0.8 μm. The graphs represent the results of calculations with (solid curves) and without (dashed curves) regard for light absorption in the wide-gap layers.

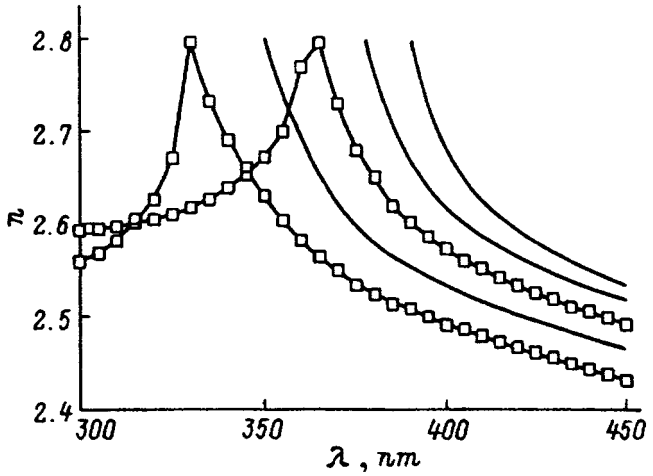

FIG. 3. Spectrum of the refractive index of GaN and various compositions of AlGaN and InGaN solid solutions at room temperature. *1*) 10% AlN, 0% InN; *2*) 5% AlN, 0% InN; *3*) 0% AlN, 0% InN; *4*) 0% AlN, 5% InN; *5*) 0% AlN, 10% InN. *6*) Experimental data from Ref. 6; the curves represent the approximation proposed in the present article.

thickness of the active zone but, conversely, to grow. The optimum thickness of the active zone in this case is once again approximately 0.2 μm. As a result, the minimum attainable threshold current density is found at the level of the threshold current densities in ordinary DH lasers.

2. THEORY

Here we consider planar heterostructures, for which the GaN active zone (DH) or the GaN waveguide layer with an InGaN active zone in the center (SCDH) is contained between two thick, wide-gap AlGaN (cladding) layers so that the optical mode cannot penetrate the outer layers of the structure. An end-fire laser geometry is assumed everywhere in this case.

All the calculations for the modeled heterostructures with a GaN active zone are carried out for a laser emission wavelength $\lambda=370$ nm in accordance with existing data on stimulated emission in a GaN/AlGaN DH ($\sim$368 nm; Ref. 6) at 300 K. The laser wavelengths λ for a SCDH with an InGaN active zone corresponds to the composition of the solid solution.

The distribution of the optical field in the structure (transverse mode) is determined from the standard wave equation

$$E''(x)+k^2[n^2(x)-N^2]E(x)=0, \tag{1}$$

where x is the direction normal to the planes of the layers, k is the light wave vector in vacuum, $n(x)$ is the refractive index, and N is an effective refractive index, which must be determined for each mode separately. All the results are given for the fundamental laser mode.

In solving the wave equation, we assume that the refractive indices of the GaN and AlGaN (InGaN) solid solutions correspond to those in Fig. 3, and that they do not depend on the temperature, the doping level, or the type of electrical conductivity. In plotting the refractive-index spectra in Fig. 3, we have taken into account the dependence of the width of

the band gap of the AlGaN (Refs. 1 and 2) and InGaN Ref. 7) solid solutions on the compositions of the solid solutions. The refractive indices of the materials used have values $\alpha_s \sim 10^3$ cm^{-1} (Refs. 1 and 5) at the given wavelengths, and the values obtained for the gain in the active zone are much lower than the magnitude of the light wave vector $k \sim 10^5$ cm^{-1}. Consequently, the imaginary parts of the refractive indices $\alpha_s(x)/2k$ do not have any appreciable influence on the profiles of the intensity distribution of the field, and they can be disregarded in solving the wave equation.

The required gain in the active zone to achieve lasing is determined by the rate of losses that must be overcome in the structure. The losses are made up of the losses in the emission of radiation $\alpha_L = (1/L)\ln(1/R)$, where L is the length of the cavity, and R is the reflection coefficient of the mirror, plus the internal losses in the structure α_i, which cannot be determined by knowing only the parameters of the structure. The internal losses can, for example, encompass losses at free carriers in the active zone or losses in the scattering of radiation by the heterointerfaces and scattering centers (inhomogeneities). As mentioned above, the losses due to light absorption in the passive layers, α_s, must also be taken into account in III-nitrides. Once the above-described loss mechanisms have been taken into account, the expression for the gain in the active zone at the lasing threshold assumes the form

$$g_{\text{th}} = (1/\Gamma)(\alpha_i + \alpha_L + \Gamma_w \alpha_s^w + \Gamma_c \alpha_s^c), \tag{2}$$

where Γ_w and Γ_c are the fractions of the optical mode associated with the waveguide and cladding layers, respectively, and Γ is the fraction of the optical mode associated with the active zone (the optical confinement factor[4]). The standard relation for bulk materials is[4]:

$$g_{\text{th}} = \beta(j_{\text{nom}} - j_0), \tag{3}$$

where β and j_0 are constants, and j_{nom} is the nominal current density required to maintain the existing rate of pumping of a uniformly excited layer of thickness 1 μm. For bulk GaN at 300 K we can set $\beta = 8.33$ cm/kA and $j_0 = 22$ kA/cm^2 (Ref. 8). If the injection efficiency and the injection coefficient are equal to unity, the threshold current density of the laser can be defined as

$$j_{\text{th}} = d j_{\text{nom}} = d(j_0 + g_{\text{th}}/\beta), \tag{4}$$

where d is a dimensionless quantity corresponding to the thickness of the active zone in micrometers.

3. DISCUSSION OF THE RESULTS

The most important parameter of a heterostructure in the design of injection lasers is the thickness of the active zone. It has already been mentioned that the optimum thicknesses of the active zone differ significantly in III-nitride and classical III-arsenide, etc., lasers. Figure 1 illustrates the influence of the thickness of the active zone on the threshold current density for a GaN/AlGaN DH for various compositions of the solid solution in the claddings. In the calculations it is assumed that $\alpha_L = 40$ cm^{-1} (corresponding to a cavity length of approximately 400 μm and a mirror reflection coefficient of the order of 0.2), $\alpha_i = 0$, and $a_s^c = 800$ cm^{-1}. It follows from Fig. 1 that for an AlN content in the claddings greater than or of the order of 5% the optimum thickness of the active zone is approximately 0.15–0.2 μm.

Separately confined DH lasers are widely used. Lasers of this configuration not only have far superior degradation characteristics and less beam divergence, but also, as mentioned, have lower current thresholds than conventional DH lasers. Two fundamentally different situations need to be distinguished in the case of SCDH lasers.

1. The active zone is not too thin and cannot be regarded as a quantum well. The threshold current densities in InGaN/GaN/AlGaN SCDH lasers with this kind of active zone can be determined from relation (3) with the same values of β and j_0 as in the case of GaN/AlGaN DH lasers. Calculations without regard for absorption in the wide-gap layers show that even when a SCDH of this type is used, the expected threshold current density is lowered in comparison with conventional DH lasers (e.g, by 1/2 to 1/3 for GaAs/AlGaAs DH lasers[4]). In nitride lasers, however, a GaN waveguide layer is highly absorbing. The absorption coefficient of GaN at the wavelength $\lambda = 395$ nm (10% InN in the active zone) is approximately 800 cm^{-1} (Refs. 1 and 5). Such large light absorption raises the threshold gain. Figure 2 shows the dependence of the threshold current density on the thickness of the active zone for three $In_{0.1}Ga_{0.9}N/GaN/Al_{0.1}Ga_{0.9}N$ DH lasers with GaN waveguide layers of thickness 0.2 μm, 0.4 μm, and 0.8 μm. In the calculations it is assumed that $\alpha_s^c = 500$ cm^{-1}, $\alpha_s^w = 800$ cm^{-1}, $\alpha_i = 0$, and $\alpha_L = 40$ cm^{-1}.

The calculations show that the expected current densities in SCDH lasers are approximately equal to those expected in conventional DH lasers. Also shown for comparison in Fig. 2 are data from calculations of the threshold current density without regard for the absorption ($\alpha_s = 0$) in the waveguide and adjacent layers. The strong influence of this absorption on the expected value of the threshold current is clearly evident.

2. Quite a different situation is encountered for SCDH lasers with one or several quantum wells. The dependence of the gain in the active zone on the current density through the structure differs from that used for bulk GaN. The scarcity of data on this dependence for the quantum wells of InGaN/GaN makes it impossible to run detailed calculations on SCDH lasers with quantum wells (e.g., to calculate the influence of the thickness of the active zone on the threshold current density).

The known[9] dependence of the gain on the current for the quantum well of $In_{0.1}Ga_{0.9}N/Al_{0.2}Ga_{0.8}N$ with a thickness of 50 Å can presumably be used to estimate the expected threshold current in these lasers and to compare with conventional DH lasers.

The calculations show that the optical confinement factor in the case of an $In_{0.1}Ga_{0.9}N/GaN/Al_{0.1}Ga_{0.9}N$ SCDH laser with a quantum well in the role of an active zone of thickness 50 Å is approximately equal to 0.025 for optimum thicknesses of the waveguide layer. If absorption in the passive layers of the structure is ignored, this result means that a gain of 200 cm^{-1} can be expected in the active zone at the lasing threshold, along with (according to Ref. 9) a threshold current density of about 600 A/cm^2. The inclusion of absorp-

tion produces dramatic changes in these values. Assuming that $\alpha_s^c = 500\ \text{cm}^{-1}$ and $\alpha_s^w = 800\ \text{cm}^{-1}$, we obtain a threshold gain in the active zone at the level $(2-3)\times 10^4\ \text{cm}^{-1}$. So far the literature does not offer any data on the expected values of the threshold current density at such gains. Taking into account the well-known phenomenon of gain saturation as the current increases, we infer that the attainment of such a high gain level at threshold current densities lower than those needed to operate a conventional DH laser is clearly impossible.

It appears most certain that this situation can be avoided in the design of SCDH lasers by using structures with a large number of quantum wells. The fraction of the optical mode associated with the passive layers in these structures is much smaller, which means a reduction in the losses due to light absorption in the wide-gap layers and, hence, lowering of the threshold current density. Let us consider, for example, a structure consisting of ten $In_{0.1}Ga_{0.9}N/GaN$ quantum wells 50 Å thick, contained between $In_{0.1}Ga_{0.9}N$ cladding layers. The fraction of the optical mode dedicated to the active zones of this structure is approximately 0.3. Setting $\alpha_s^w = 500\ \text{cm}^{-1}$ and $\alpha_L = 40\ \text{cm}^{-1}$, we obtain a threshold gain in the active zones of the order of $1300\ \text{cm}^{-1}$ and, as a consequence, a threshold current density of approximately 5 kA/cm^2. Clearly, the expected threshold current density is half the value in conventional DH lasers. Further lowering of the threshold current density can be expected when the degree of confinement of the light field in the active zone is increased and the thicknesses of the quantum wells are decreased.

By way of comparison we note that the first demonstrated laser using a III-nitride heterostructure[3] as the active zone had 26 $In_{0.1}Ga_{0.9}N/In_{0.05}Ga_{0.95}N$ quantum wells of thickness 25 Å and had a threshold current density of 4 kA/cm^2.

An obvious feature common to all heterostructures made from III-nitrides is the very unfavorable configuration of the light field in III-nitride layers in that the generated waveguide mode is present, for the most part, in all layers. The ''leakage'' of the mode beyond the active zone produces strong absorption of the emitted radiation and a corresponding increase of the required gain in the active zone. Stronger localization of the light field in the active zone is preferable for III-nitride lasers.

In closing, we should mention one other important feature of III-nitride heterostructures. It is evident from Fig. 1 that the influence of the composition of the cladding layers on the threshold current is no longer significant when the claddings contain more than 10% AlN. Such a small content of the wide-gap component in the solid solutions of the claddings has not been sufficient in lasers utilizing arsenides, etc. Two factors account for the adequacy of such a low AlN level for achieving good optical confinement. First, the emission wavelength of III-nitride lasers is shorter than in III-arsenide lasers. Second, the III-nitrides are characterized by large dispersion of the refractive index (Fig. 3). It follows, therefore, that the required AlN content in the solid solution of the wide-gap layers for good confinement of the optical mode to the active zone should be relatively low. This result is important in light of the fact that the difficulties associated with doping of the AlGaN layers are still encountered in nitride technology.

4. CONCLUSIONS

1. In the investigation of laser configurations utilizing double heterostructures and double heterostructures with separate confinement the threshold current densities are expected to have levels of approximately 10 kA/cm^2 (for ideal laser structures with 100% internal quantum efficiencies and injection efficiencies).

2. The low-energy ''tails'' in the absorption spectra of the III-nitrides clearly play a very important role in the design of laser structures in that they raise considerably the attainable threshold currents. The influence of the absorption ''tails'' is particularly strong in the case of SCDH lasers with quantum wells, where a large fraction of the optical mode propagates in the highly absorbing passive zones. For SCDH lasers with single quantum wells the required gains in the active zone at the lasing threshold, calculated with allowance for interband absorption in the wide-gap layers adjacent to the active zone, are ten or more times the gains calculated without absorption taken into account.

3. For lasers utilizing III-nitride heterostructures with single quantum wells, clearly, one cannot expect the threshold current density to be lowered from that of conventional DH lasers. The threshold current densities can be lowered to values of the order of a few kA/cm^2 in heterostructures with a large number of quantum wells.

4. For a DH with a GaN active zone the optimum thickness of this zone is approximately 0.15–0.2 μm.

5. Because of the short emission wavelengths and appreciable dispersion of the refractive index in III-nitride DH lasers, an AlN level of the order of 8–10% in the solid solution of the wide-gap layer is definitely sufficient for achieving good optical mode confinement.

The authors are grateful to O. V. Konstantinov for major assistance in the investigation.

[1] S. Strite and H. Morkoc, J. Vac. Sci. Technol. B **10**, 1237 (1992).
[2] H. Morkoc, S. Strite, G. B. Gao, M. E. Lin, B. Sverdlov, and M. Burns, J. Appl. Phys. **76**, 1363 (1994).
[3] S. Nakamura, *InterNet Communication Report* (January 15, 1996).
[4] H. C. Casey Jr. and M. B. Panish, *Heterostructure Lasers*, Academic Press, New York (1978).
[5] O. Ambacher, W. Rieger, and M. Stutzmann, in *Abstracts of Topical Workshop on III–V Nitrides TWN'95*, F-5, Nagoya, Japan (1995).
[6] H. Amano, N. Watanabe, N. Koide, and I. Akasaki, Jpn. J. Appl. Phys. **32**, L1000 (1993).
[7] K. Osamura, S. Naka, and Y. Murakami, J. Appl. Phys. **46**, 3432 (1975).
[8] W. Fang and S. L. Chuang, Appl. Phys. Lett. **67**, 751 (1995).
[9] S. Kamiyama, M. Suzuki, T. Uenoyama, and Y. Ban, in *Abstracts of Topical Workshop on III–V Nitrides TWN'95*, SP-5, Nagoya, Japan (1995).

Translated by James S. Wood

Photoluminescence of InSb quantum dots in GaAs and GaSb matrices

A. F. Tsatsul'nikov, N. N. Ledentsov, M. V. Maksimov, B. Ya. Mel'tser, P. V. Neklyudov, S. V. Shaposhnikov, B. V. Volovik, I. L. Krestnikov, A. V. Sakharov, N. A. Bert, P. S. Kop'ev, and Zh. I. Alferov

A. F. Ioffe Physicotechnical Institute, Russian Academy of Sciences, 194021 St. Petersburg, Russia

D. Bimberg

Institute für Festkörperphysik, Technische Universität Berlin, D-10623 Berlin, Germany
(Submitted February 27, 1996; accepted for publication March 2, 1996)
Fiz. Tekh. Poluprovodn. **31**, 68–71 (January 1997)

The photoluminescent properties of quantum dots formed in the deposition of an InSb thin film (1–3 monolayers) on GaAs(100) and GaSb(100) surface are investigated. The results indicate the importance of As–Sb substitution reactions in the formation of quantum dots on a GaAs surface. © *1997 American Institute of Physics.* [S1063-7826(97)01401-4]

The fabrication of optoelectronic light-emitting devices (LEDs) with emission wavelengths close to 1.3 μm and 1.5 μm is an important task in the physics of semiconductors in view of the sharp reduction of the absorption coefficient in optical fibers at these wavelengths. Adequate techniques have not been developed to date for the preparation of dislocation-free GaAs heterostructures capable of emitting radiation in the vicinity of 1.5 μm at a temperature of 300 K. This deficit is explained by the fact that materials with a narrow band gap such as, for example, $Ga_xIn_{1-x}As_yP_{1-y}$ and $In_xGa_{1-x}As$ have a lattice constant that differs substantially from that of GaAs. This difference means that the layer of narrow-gap material deposited on GaAs must have a very small critical thickness, making it impossible to achieve a substantial shift of the photoluminescence line to the long-wavelength side of the absorption edge of GaAs, because of quantum size effects. The growth of layers with greater than critical thickness leads to the formation of misfit dislocations and to catastrophic degradation of the optical properties.

Major progress in the physics and technology of semiconductors has been achieved lately through the creation and study of the properties of objects of limited dimension in all directions: quantum dots. One method for the *in situ* formation of quantum dots is through the spontaneous transformation of an elastically stressed layer of one material grown on the surface of another material having a different lattice constant.[1] When the deposited layer has greater than critical thickness, it begins to fragment. The greatest progress has been achieved in the formation of (In,Ga)As quantum dots on a GaAs(100) surface. The resulting dislocation-free quantum dots are distinguished by a high degree of dimensional homogeneity. This method can be used to obtain islands of a narrow-gap material in a wide-gap matrix material with a height much greater than the critical thickness, thereby lowering the quantum-dot energy and shifting the photoluminescence line to lower energies. The advantages of quantum-dot lasers — a high characteristic temperature and low threshold current density — have been successfully exploited on the basis of structures with InAs quantum dots obtained by molecular beam epitaxy (MBE).[2–4]

We have prepared and investigated the properties of quantum dots formed in the deposition of an InSb thin film [$\sim$1–3 monolayers (ML)] on GaAs(100) and GaSb(100) surfaces by MBE. The width of the band gap for InSb ($E_g \approx 0.17$ eV) is small in comparison with the width of the band gap for GaAs ($E_g \approx 1.42$ eV) and GaSb ($E_g \approx 0.72$ eV). Even more important is the fact that the discontinuity in the valence band for the InSb/GaAs heterojunction constitutes a large part of the total discontinuity of the bands, and this fact, coupled with the large effective mass of a heavy hole, radically increases the localization energy. On the other hand, the lattice constant of InSb ($a = 6.4794$ Å) is $\sim$15% times greater than the lattice constant of GaAs ($a = 5.6533$ Å). Such a marked difference means that transformation of the surface with the formation of three-dimensional (3D) islands must take place in the deposition of a very thin, $\sim$1 ML, InSb layer.

The investigated structures were grown by means of a Riber 32 MBE apparatus on GaAs(100) and GaSb(100) substrates. For the structures grown on GaAs substrates InSb films of various thicknesses and a 200-Å GaAs layer were deposited on a 1000-Å GaAs layer. The structure was clad on both sides by a (20-Å $Al_{0.4}Ga_{0.6}As$/20-Å GaAs)$\times$10 superlattice. The substrate temperature during growth of the structure was 610 °C. The temperature was lowered to 420 °C prior to the deposition of InSb and was raised back to 610 °C after deposition of the InSb film and 50-Å GaAs. The InSb growth rate was 18 Å/min. The structures grown on GaSb substrates consisted of the following sequence of layers: 0.3-μm GaSb, a five-period 55-Å AlSb/20-Å GaSb superlattice, 1000-Å GaSb, an InSb film of various effective thicknesses, 300-Å GaSb, a superlattice analogous to the one described above, and 20-Å GaSb. The substrate temperature was 500 °C; the temperature was lowered to 420 °C prior to deposition of the dots and was maintained at that temperature until completion of the growth of the structure. The surface transformation process was monitored from the fast-electron diffraction pattern. Photoluminescence was induced by Ar^+ (quantum energy $\sim$2.56 eV, power $\sim$200 W/cm^2) and a semiconductor laser (excitation energy 1.55 eV, power $\sim$60 W/cm^2) and was detected by means of a Ge photodiode. It has been shown[5] that the transformation of a GaSb surface with the formation of quantum dots takes place in the deposition of an InSb film having an effective thickness

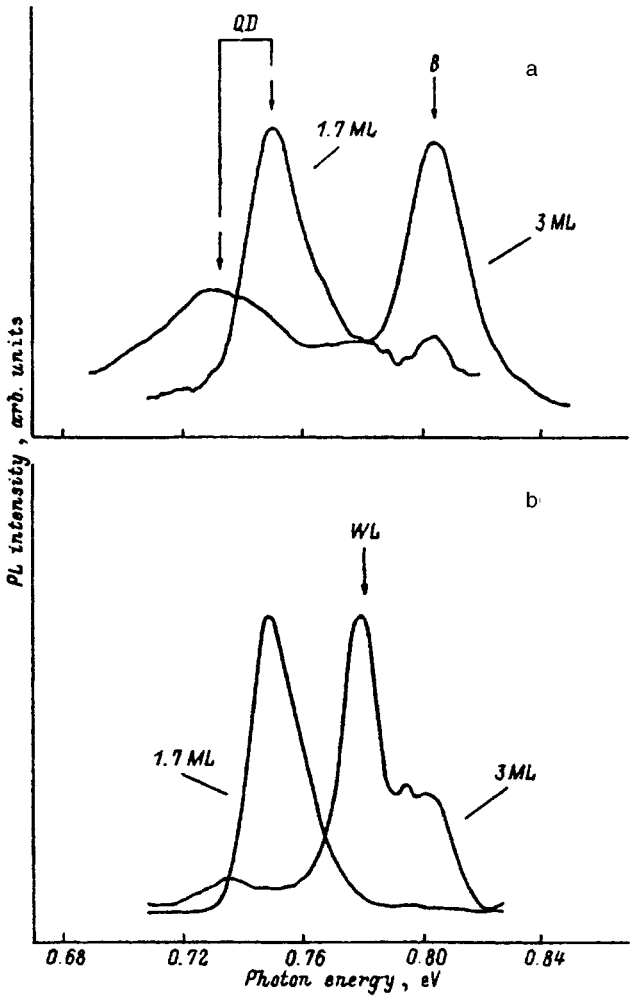

FIG. 1. Photoluminescence spectra of structures with InSb layers of thickness 1.7 ML and 3 ML deposited on the surface of GaSb at temperatures of 77 K (a) and 4 K (b).

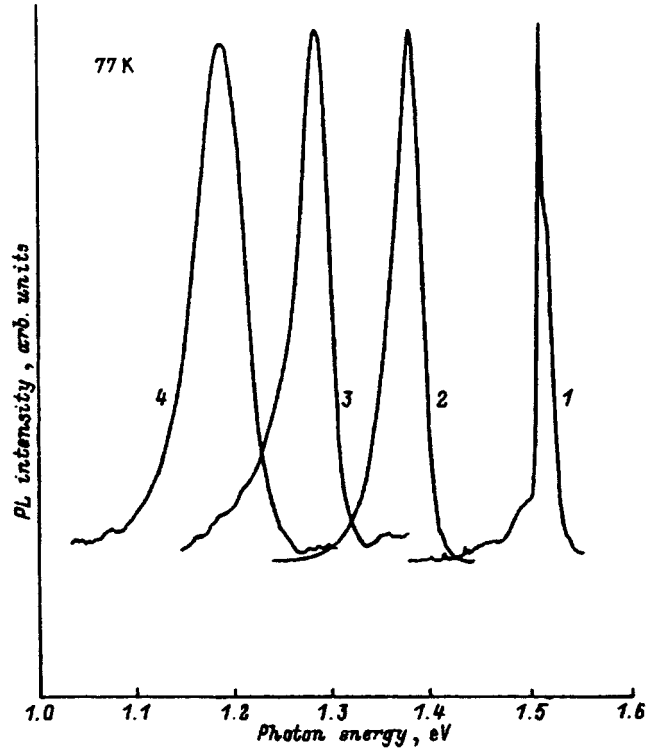

FIG. 2. Photoluminescence spectra of structures grown on GaAs and exposed to an Sb flux for 10 s at various temperatures. *1*) 550 °C; *2*) 470 °C; *3*) 420 °C. Curve 4 corresponds to a sample in which a 10-s exposure to an Sb flux was followed by the deposition of an InSb film of effective thickness 1.7 ML.

~1.7–2.8 ML. According to the Stransky–Krastanov growth model, quantum dots are formed on a thin film (wetting layer) of InSb. Figure 1a shows the photoluminescence spectra of structures with effective thicknesses of the deposited InSb film ~1.7 and ~3 ML at $T=77$ K. For both structures the formation of quantum dots was monitored by fast-electron diffraction. The deposition of ~1.7-ML InSb produces, in addition to the B line associated with the recombination of nonequilibrium carriers in the GaSb region, a strong QD line with maximum at ~0.75 eV due to carrier recombination through the quantum dots. The fringe width is ~25 meV. An increase in the thickness of the InSb causes the QD line to shift in the long-wavelength direction to ~0.73 eV and to broaden to ~40 meV. This behavior of the photoluminescence is attributable to an increase in the dimensions of the newly formed quantum dots and an increase in the size dispersion. Figure 1b shows the photoluminescence spectra of these structures at $T=5$ K. It is evident from the figure that lowering the temperature causes the spectrum of a sample with 3-ML InSb to acquire a strong WL line with maximum at ~0.78 eV. The appearance of this fringe is most likely associated with the recombination of electron–hole pairs in the InSb wetting layer. Raising the temperature produces an increase in the thermal ejection of carriers from states of the wetting layer and a decrease in the intensity of the WL line.

An important problem encountered in the deposition of InSb on a GaAs surface is the substitution of Sb atoms for As atoms, which results in the formation of a GaSb thin film on the GaAs surface. Since the lattice constant of GaSb ($a=66.0959$ Å) differs from that of GaAs by ~7.8%, the surface can acquire a long-wavelength undulation which accounts for the partial stress relaxation. Moreover, after the deposition of ~3 ML GaSb the GaSb layer begins to fragment into quantum drops. These phenomena can influence the kinetics of the transformation process.

We have investigated the influence of the InSb deposition conditions on the formation of quantum dots. We know[6,7] that a GaSb layer of thickness ~1 ML is formed on the surface of GaAs exposed for 10 s to a flux of Sb atoms at a temperature ~470 °C. Figure 2 shows the spectra of structures in which growth has been halted for ~10 s while exposed to a flux of Sb atoms at various substrate temperatures. It is evident from the figure that raising the temperature shifts the photoluminescence line into the high-energy range until it vanishes at a temperature ~550 °C, probably because of the decrease in the thickness of the GaSb layer. Comparing the position of the maximum of the line with previous results,[7] we conclude that exposure at $T=420$ °C results in the formation of a GaSb layer of thickness ~3 ML, while exposure at $T=470$ °C produces a layer of thickness ~1

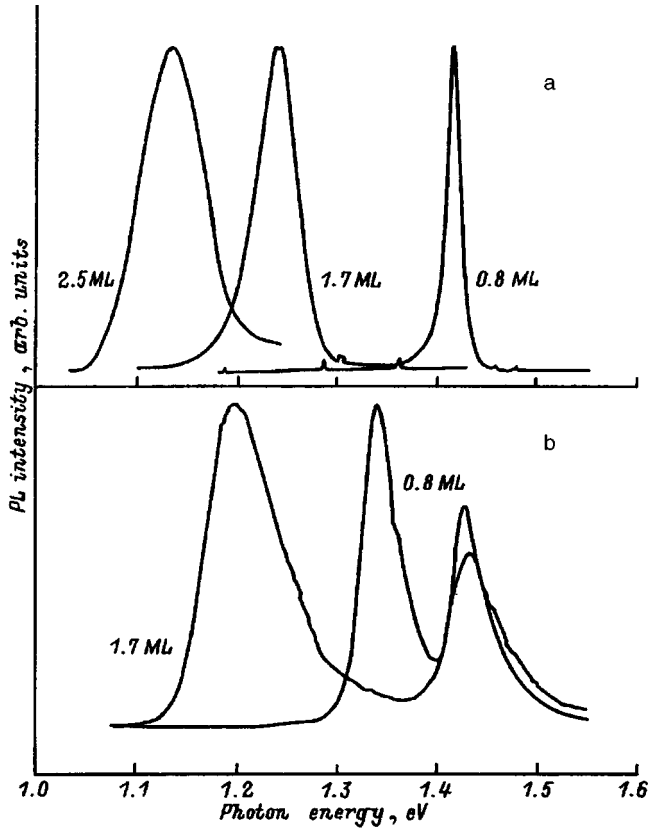

FIG. 3. Photoluminescence spectra of structures grown on GaAs with effective thicknesses of the InSb layer 0.8 ML, 1.7 ML, and 2.5 ML at temperatures of 77 K (a) and 300 K (b).

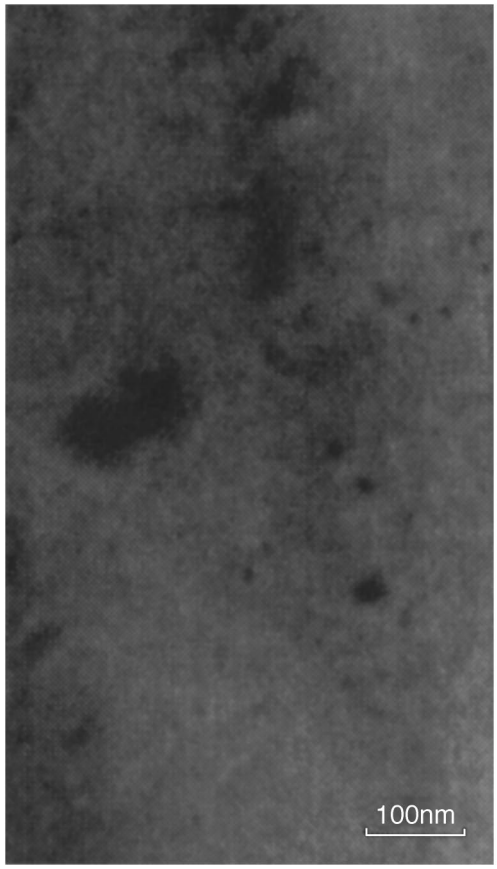

FIG. 4. TEM photomicrographs (top view) of islands for a structure with 1.7 ML InSb on a GaAs surface.

ML, which indicates that arsenic atoms are being rapidly replaced by antimony atoms at low growth temperatures. Figure 2 also shows the photoluminescence spectrum of a structure in which an InSb layer of thickness 1.7 ML was deposited after 10-s exposure to an Sb flux at $T=420$ °C. This process broadened the photoluminescence line and shifted it in the long-wavelength direction.

Figure 3a shows the photoluminescence spectra of structures with various thicknesses of the deposited InSb film at $T=77$ K. In the deposition of ~0.8 ML InSb a narrow line with maximum at ~1.415 eV and width ~15 meV is observed in the spectrum. An increase in the quantity of material deposited causes the energy of the maximum of the line to shift far into the long-wavelength range and to broaden to ~75 meV. This fact is consistent with fast-electron diffraction data, illustrating the broadening of the diffraction orders as evidence of morphological transformation of the InSb film. Raising the temperature to 300 K causes the line to shift to longer wavelengths and to broaden (Fig. 3 b).

Figure 4 shows a picture obtained with a transmission electron microscope (top view) of the surface of GaAs after the deposition of 1 ML InSb. It is evident from the micrograph that surface transformation has taken place in this structure with the formation of islands. These islands have typical lateral dimensions ~200 Å.

Consequently, the reported investigations have established that the deposition of an InSb thin film of thickness greater than ~1.7 ML on GaAs and GaSb surfaces is accompanied by its spontaneous transformation into quantum dots. The results of the study reveal the importance of As–Sb substitution reactions in the formation of islands.

[1] P. M. Petroff and S. P. DenBaars, Superlattices Microstr. **15**, 15 (1994).
[2] N. Kirstaedter, N. N. Ledentsov, M. Grundmann, D. Bimberg, V. M. Ustinov, S. S. Ruvimov, M. V. Maximov, P. S. Kop'ev, Zh. I. Alferov, U. Richter, P. Werner, U. Gosele, and J. Heydenreich, Electron. Lett. **30**, 1416 (1994).
[3] Zh. I. Alferov, N. A. Bert, A. F. Egorov, A. E. Zhukov, P. S. Kop'ev, A. O. Kosogov, I. L. Krestnikov, N. N. Ledentsov, A. V. Lunev, M. V. Maksimov, A. V. Sakharov, V. M. Ustinov, A. F. Tsatsul'nikov, Yu. M. Shernyakov, and D. Bimberg, Fiz. Tekh. Poluprovodn. **30**, 351 (1996) [Semiconductors **30**, 194 (1996)].
[4] Zh. I. Alferov, N. Yu. Gordeev, S. V. Zaĭtsev, P. S. Kop'ev, I. V. Kochnev, V. V. Komin, I. L. Krestnikov, N. N. Ledentsov, A. V. Lunev, M. V. Maksimov, S. S. Ruvimov, A. V. Sakharov, A. F. Tsatsul'nikov, Yu. M. Shernyakov, and D. Bimberg, Fiz. Tekh. Poluprovodn. **30**, 357 (1996) [Semiconductors **30**, 197 (1996)].
[5] N. Bertu, O. Brandt, M. Wessermcier, and K. Ploog, Appl. Phys. Lett. **68**, 31 (1996).
[6] F. Hatami, N. N. Ledentsov, M. Grundmann, J. Bohrer, F. Heinrichsdorff, M. Beer, D. Bimberg, S. S. Ruvimov, P. Werner, U. Gosele, J. Heydenreich, U. Richter, S. V. Ivanov, B. Ya. Meltser, P. S. Kop'ev, and Zh. I. Alferov, Appl. Phys. Lett. **67**, 656 (1995).
[7] N. N. Ledentsov, J. Bohrer, M. Beer, F. Heinrichsdorff, M. Grundmann, D. Bimberg, S. V. Ivanov, B. Ya. Meltser, I. N. Yassievich, N. N. Faleev, S. V. Shaposhnikov, P. S. Kop'ev, and Zh. I. Alferov, Phys. Rev. B **52**, 14058 (1995).

Translated by James S. Wood

Investigation of the structure of the edge of the valence band of $Cd_{1-x}Mn_xS$ crystals on the basis of magnetooptical measurements

V. G. Abramishvili, A. V. Komarov, and S. M. Ryabchenko

Institute of Physics, National Academy of Sciences of Ukraine, 252650 Kiev, Ukraine

Yu. G. Semenov

Institute of Semiconductor Physics, National Academy of Sciences of Ukraine, 252650 Kiev, Ukraine
(Submitted February 29, 1996; accepted for publication March 6, 1996)
Fiz. Tekh. Poluprovodn. **31**, 72–77 (January 1997)

The results of magnetooptical studies are reported for $Cd_{1-x}Mn_xS$ crystals with concentrations of the magnetic component $x_1=0.0056$, and $x_2=0.0013$, $x_1=0.0002$ at $T=2$ K in a magnetic field $H\leqslant 3.5$ T for $\mathbf{H}\perp\mathbf{c}$ and $\mathbf{H}\|\mathbf{c}$, where $\mathbf{c}$ is the hexagonal axis of the crystal. The first reliable confirmation of spin splitting of the exciton reflection spectra of the *B* exciton transition is successfully obtained as a result of working in an $\mathbf{H}\perp\mathbf{c}$ experimental geometry. The values of the crystal-field and spin–orbit interaction parameters $\Delta_1,\Delta_2,\Delta_3$ and the exchange constants J_e and J_h of $Cd_{1-x}Mn_xS$ crystals for achieving the best description of the experimental results in the mean exchange field approximation are found on the basis of the data obtained for $\mathbf{H}\perp\mathbf{c}$ and for $\mathbf{H}\|\mathbf{c}$. An analysis shows that the main qualitative features of the observed reflection spectra for the entire series of investigated $Cd_{1-x}Mn_xS$ crystals can be described only if the condition $(\Delta_1-\Delta_2)<0$ is satisfied.
[S1063-7826(97)01501-9]

INTRODUCTION

Investigations of giant spin splittings of the exciton reflection spectra in $Cd_{1-x}Mn_xS$ crystals have revealed[1–5] a number of distinctive features of the giant spin splittings of this compound in contrast with other $A^{II}_{1-x}Mn_xB^{VI}$ compounds. The most widely discussed topic is the dependence of the exchange interaction constant of J_h carriers of the valence band (holes) with Mn^{2+} ions on the content of magnetic ions x (Ref. 3).

On the other hand, beginning with the earliest experiments,[1,2] difficulties were noted in attempting to describe simultaneously the magnetic field splittings of the *A* and *B* exciton reflection bands when using the notions generally accepted by most researchers as to the parameters of the crystal field and spin–orbit interaction, which form the structure of the edge of the valence band of CdS crystals.

Since the publication of the papers of Birman[6] and Thomas and Hopfield[7] a keen debate has been waged regarding the genesis of the *A*, *B*, and *C* subbands for CdS, which are ordered according to decreasing energy and which correspond to symmetries Γ_9, Γ_7, and Γ_7, respectively. It is obvious (see Fig. 33 in Bir and Pikus[8]) that the Γ_9 subband and one of the Γ_7 subbands originate from spin–orbit splitting of the Γ_5 band, while the other Γ_7 subband originates from the Γ_7 subband split off by the crystal field. It has also been argued which of the subbands *B* or *C* is identified with these two Γ_7 subbands of different origins. In the case of CdSe, for example, the *A* and *C* subbands are associated with spin–orbit splitting of Γ_5, and the *B* subband with Γ_1. This kind of scheme has been proposed for CdS by Thomas and Hopfield (TH scheme).[7] Birman[6] has proposed a scheme whereby the *B* subband is identified with Γ_5, and the *C* subband with Γ_1 (B scheme).

In the wake of experiments[9] to study the influence of external strains on the positions of the exciton spectra in CdS and their interpretation on the basis of the Birman's scheme, most researchers began to express a preference for this scheme of the origin of the valence subbands in CdS.[1,4,8]

The group of *A*, *B*, and *C* levels is described in the basis of the wave functions *X*, *Y*, and *Z* for valence electrons by the Hamiltonian (see, e.g., Ref. 10)

$$H=\Delta_1 L_z^2+2\Delta L_z S_z+2\Delta_3(L_xS_x+L_yS_y), \tag{1}$$

where $\mathbf{L}$ and $\mathbf{S}$ are the orbital momentum ($L=1$) and spin ($S=1/2$) operators, respectively; Δ_1 is the crystal field parameters, Δ_2 and Δ_3 are the anisotropic spin–orbit interaction parameters, and the *z* axis coincides with the hexagonal $\mathbf{c}$ axis of the crystal.

The solution of the Hamiltonian (1) for states *B* and *C* in the basis functions corresponding to Γ_5 and Γ_1 is written in the form

$$|B^{\pm}\rangle=\sqrt{(1+\xi_0)/2}|\Gamma_5^{\pm}\rangle\mp\sqrt{(1-\xi_0)/2}|\Gamma_1^{\pm}\rangle,$$
$$|C^{\pm}\rangle=\pm\sqrt{(1-\xi_0)/2}|\Gamma_5^{\pm}\rangle+\sqrt{(1+\xi_0)/2}|\Gamma_1^{\pm}\rangle, \tag{2}$$

where in the notation of the functions *B* and *C* the symbols Γ_5 and Γ_1 refer to the description of the orbital parts of the corresponding functions, and the symbols $\pm$ refer to the description of the twofold (spin) degeneracy of the corresponding states.

The quantity ξ_0 is related to the parameters Δ_1, Δ_2, and Δ_3:

$$\xi_0=(\Delta_1-\Delta_2)/\omega_0, \tag{3}$$

where $\omega_0=\sqrt{(\Delta_1-\Delta_2)^2+8\Delta_3^2}$.

It is evident that states *B* and *C* are a mixture of Γ_5 and Γ_1. As to which scheme each should be identified with re-

duces to estimating the sign of $(\Delta_1-\Delta_2)$. Any experimentally determined value of $p=(E_A-E_B)/(E_A-E_C)$, where $E_{A,B,C}$ are the energies of tops of the corresponding subbands, corresponds to two different values of $q=(\Delta_1-\Delta_2)/(\Delta_1+\Delta_2)$, even in the approximation $\Delta_2\neq\Delta_3$. The problem is more complex yet for $\Delta_2 \neq \Delta_3$.

Experiments aimed at the influence of external strains on the *A*, *B*, and *C* exciton positions (Ref. 9) do not provide a qualitative answer as to the sign of $(\Delta_1-\Delta_2)$, and their quantitative interpretation could lead to a reliable conclusion in this regard only if the deformation potential constants are known with sufficient accuracy. In view of the limited accuracy ($\pm 20\%$) with which these constants are known, the possibility of ambiguity in the choice of sign for $(\Delta_1-\Delta_2)$ persists.

Here we report measurements of the magnetic field splittings of the exciton reflection spectra in $Cd_{1-x}Mn_xS$ crystals with significantly different concentrations of Mn ions, where we have attempted to surmount the above-mentioned difficulties of interpreting the magnetic field splittings of a *B* exciton by performing measurements not only with the magnetic field orientation $\mathbf{H}\|\mathbf{c}$, but also, for the first time, with $\mathbf{H}\perp\mathbf{c}$.

It will be shown below that an analysis of the reported experiments favors the TH scheme associated with $(\Delta_1-\Delta_2)<0$ for the investigated $Cd_{1-x}Mn_xS$ crystals. We have obtained data on the behavior of Δ_1, Δ_2, and Δ_3 as functions of *x*. At the same time, we have obtained an unexpected result for a crystal with minimal concentration *x*, grown from the vapor phase. We have found the magnetic field splittings in it to be anomalously small, contradicting the previously established[3,12] trend of $|J_h|$ to increase as the Mn concentration of the solid mixture is lowered.

EXPERIMENTAL

The light reflection spectra in the *A*, *B*, and *C* exciton regions of $Cd_{1-x}Mn_xS$ crystals with Mn contents $x_1=0.0056$, $x_2=0.0013$, and $x_3=0.0002$ were investigated at the temperature $T=2$ K in magnetic fields $H\leqslant 3.5$ T for $\mathbf{H}\|\mathbf{c}$ and $\mathbf{H}\perp\mathbf{c}$. The values of *x* were measured by x-ray microscopic analysis and were additionally verified from the comparative total intensities of the electron spin resonance (ESR) spectra of the Mn^{2+} ions. The crystals with $x=x_1,x_2$ were grown from the melt by the Bridgman method at the Institute of Solid State Physics of the Russian Academy of Sciences in Chernogolovka, and the crystal with $x=x_3$ was grown from the vapor phase at the Institute of Semiconductor Physics of the National Academy of Sciences of Ukraine in Kiev. The optical measurements were performed on a DFS-12 double grid spectrophotometer with a linear dispersion of 5 Å/mm.

Figure 1 shows examples of *A* and *B* exciton reflection spectra for the sample with $x=x_1$ at $H=0$ (curves 1 and 3 for polarizations $\mathbf{E}\|\mathbf{c}$ and $\mathbf{E}\perp\mathbf{c}$, respectively) and in a field $H=3$ T perpendicular to the crystal **c** axis ($\mathbf{H}\perp\mathbf{c}$); curve 2 corresponds to $\mathbf{E}\|\mathbf{c}$, $\mathbf{k}\|\mathbf{H}$, $\mathbf{E}\perp\mathbf{H}$, curve 4 to $\mathbf{E}\perp\mathbf{c}$, $\mathbf{k}\|\mathbf{H}$, $\mathbf{E}\perp\mathbf{H}$, and curve 5 to $\mathbf{E}\perp\mathbf{c}$, $\mathbf{k}\perp\mathbf{H}$, $\mathbf{E}\|\mathbf{H}$. Here **E** and **k** denote the electric and wave vectors of the light wave.

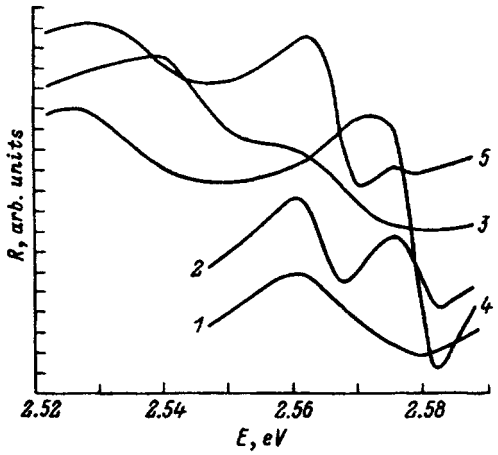

FIG. 1. Reflection spectrum in a $Cd_{1-x}Mn_xS$ crystal with $x_1=0.0056$ for $\mathbf{H}\perp\mathbf{c}$ at $T=2$ K. 1, 3) $H=0$; 2, 4, 5) $H=30$ kOe; 1, 2) measurements in the polarization $\mathbf{E}\|\mathbf{c}\|z$, $\mathbf{k}\|\mathbf{H}$, $\mathbf{E}\|\mathbf{H}$; 3, 4) $\mathbf{E}\perp\mathbf{c}$, $\mathbf{k}\|\mathbf{H}$, $\mathbf{E}\perp\mathbf{H}$; 5) $\mathbf{E}\perp\mathbf{c}$, $\mathbf{k}\perp\mathbf{H}$, $\mathbf{E}\|\mathbf{H}$.

Recorded spectra similar to those shown here were obtained for the samples with $x=x_1,x_2$ for various fixed values of $0<H\leqslant 3.5$ T. The positions of the inflection points of the exciton reflection lines were used to plot the magnetic field dependences of the energies and splittings of the exciton bands. The magnetic field dependences of the spectra for $\mathbf{H}\|\mathbf{c}$ were recorded analogously for the samples with $x=x_1,x_2$, except that circularly polarized light with polarizations σ^+ and σ^- were used for $\mathbf{k}\|\mathbf{H}$. For the sample with $x=x_3$ the magnetic field was found to have an appreciable influence only in the *A* exciton band. These spectra were processed to incorporate the recommendations of Dmitrenko et al.[13] The measurements with $x=x_3$ were carried out only for $\mathbf{H}\|\mathbf{c}$.

The reflection lines in the *C* exciton region were determined for all the investigated crystals, making it possible to find E_A-E_C and E_B-E_C for them. On the other hand, magnetic field splittings for the *C* exciton could not be observed against the background linewidth. The values of E_B-E_C for $H=0$ were then taken into account by fitting the experiment to the calculations. These values were equal to 67 meV, 60 meV, and 60 meV for $x=x_1,x_2,x_3$, respectively. The results of the measurements for x_1 and x_2 with $\mathbf{H}\|\mathbf{c}$ and $\mathbf{H}\perp\mathbf{c}$ were coprocessed according to equations in Refs. 10, 11, and 14 describing the splittings of *A* and *B* excitons as a function of the exchange fields G_e and G_h acting on the electron and the hole:

$$G_{e(h)}=J_{e(h)}x\langle S_z\rangle. \tag{4}$$

Here $\langle S_z\rangle$ is the thermodynamic average of the projection of the spin of Mn^{2+} ions onto the *z* axis, which coincides with the direction of the external magnetic field **H**; J_e is the exchange interaction constant between the electron and Mn ions, and J_h is the same between the hole and Mn ions. The quantity $\langle S_z\rangle$ is related to *H* and *T* by the Brillouin function for $S=5/2$. Only for the concentration $x=x_3$ was the direct action of the magnetic field on the electron and hole spins at all significant against the background of the exchange fields. To describe it, we used the difference between the electron

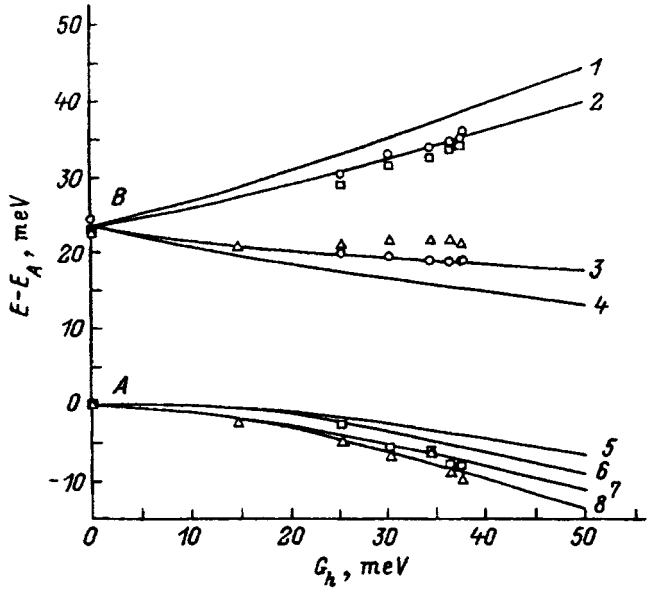

FIG. 2. Energies of the A and B exciton spin components vs exchange interaction parameter G_h in a $Cd_{1-x}Mn_xS$ crystal with $x_1=0.0056$ for $\mathbf{H}\perp\mathbf{c}$ at $T=2$ K. The curves represent the results of calculations with the fitting parameters given in Table I, and the point symbols represent the experimental data: 1–4) transitions resolved in the polarization $\mathbf{E}\|\mathbf{c}$, $\mathbf{k}\|\mathbf{H}$, $\mathbf{E}\perp\mathbf{H}$; ○) experimental data for this polarization; 1, 2, 6, 8, □) $\mathbf{E}\perp\mathbf{c}$, $\mathbf{k}\|\mathbf{H}$, $\mathbf{E}\perp\mathbf{H}$; 3, 4, 5, 7, △) $\mathbf{E}\perp\mathbf{c}$, $\mathbf{k}\perp\mathbf{H}$, $\mathbf{E}\|\mathbf{H}$.

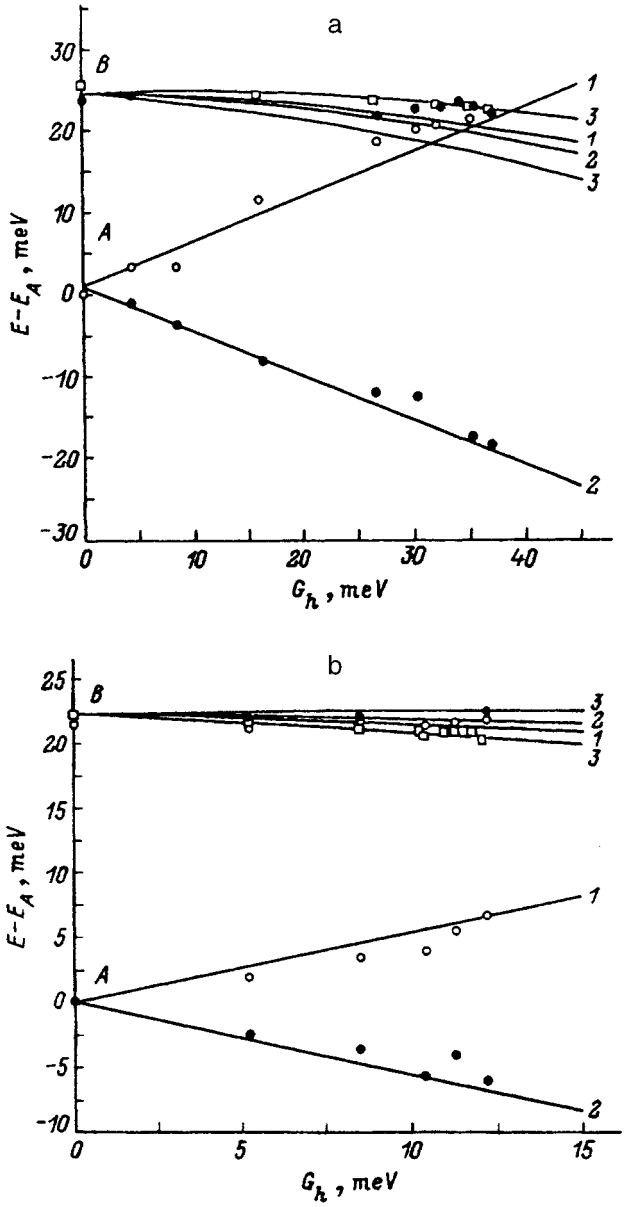

FIG. 3. Energies of the A and B exciton spin components vs exchange interaction parameter G_h for $\mathbf{H}\|\mathbf{c}$ at $T=2$ K in $Cd_{1-x}Mn_xS$ crystals with: a) $x_1=0.0056$; b) $x_2=0.0013$. The curves represent the results of calculations with the fitting parameters given in Table I, and the point symbols represent the experimental data: 1, ○) σ^- polarization ($\mathbf{E}\perp\mathbf{H}$); 2, ●) σ^+ polarization ($\mathbf{E}\perp\mathbf{H}$); 3, □) π polarization ($\mathbf{E}\|\mathbf{H}$).

and hole g factors from Ref. 15: $(g_e-g_h)=0.63$. The following parameters were chosen to achieve the best match between the calculated and experimental data: $\eta=J_h/J_e$, $\Delta_1,\Delta_2,\Delta_3$. Moreover, an attempt was made to include the anisotropy of the exchange interaction of holes with Mn ions in much the same way as in Ref. 4 (for $\mathbf{H}\perp\mathbf{c}$). It is important to note that large experimental errors and large widths of the exciton reflection lines limited the possibility of optimal selection. For $\mathbf{H}\perp\mathbf{c}$ the closely spaced lines predicted by the calculations to be resolvable in the same polarization were generally unresolved experimentally, and for comparison with experiment the calculated transition probabilities in different, simultaneously resolved polarizations were taken into account, along with the widths of the observed combined reflection lines.

It is essential to note that the position of the B exciton reflection line for $H=0$ differs by 0.8 meV in the polarizations $\mathbf{E}\|\mathbf{c}$ and $\mathbf{E}\perp\mathbf{c}$. This difference is not described by the model used for the calculations. It could be associated with electron–hole exchange interaction within the exciton,[2,16] which we have ignored to simplify the problem. It must also be noted that the indicated anomalies have resulted in less than full correspondence between the experimental and calculated results, creating instead a conflict in the comparison of the calculations with the experiment within the existing error limits.

The parameters $\eta=3DJ_h/J_e,\Delta_1,\Delta_2,\Delta_3$ were chosen by fitting the measured magnetic field dependences of the positions of the inflection points of the exciton reflection spectra to the calculated curves. As a matter of convenience the magnetic field dependences have been transformed into dependences on G_h with selective fitting of the parameter η, these curves having initially been matched with the observed splittings of the A exciton reflection line for $\mathbf{H}\|\mathbf{c}$ in the corresponding crystal, followed by variation of the parameters Δ_1, Δ_2, and Δ_3. Experiment the optimal graphs of these dependences from the standpoint of matching the calculations with are shown in Figs. 2 and 3. The values of the parameters corresponding to the calculated curves in Figs. 2 and 3 are given in Table I. The parameters Δ_1, Δ_2, and Δ_3 were also chosen with due regard for the requirement that the C exciton position be described correctly for $H=0$. It is important to note that the strongest qualitative argument in support of assigning values of $\Delta_1<\Delta_2$ are the results on the splitting of the B exciton in the geometry $\mathbf{H}\|\mathbf{c}$ (Fig. 3); spe-

TABLE I. Band parameters and exchange constants of $Cd_{1-x}Mn_xS$, obtained by numerical fitting of the calculated energies and experimentally observed inflection points of the exciton reflection spectra.

	x	Δ_1, meV	Δ_2, meV	Δ_3, meV	J_h, eV	J_e, eV
x_1	0.0056	25±1	30±3	24±2	−2.82 ±0.2	0.23±0.02
x_2	0.0013	23±1	27±2	21±1	−4.0 ±0.3	0.30±0.02
x_3	0.0002	16±2	25±2	21±1	−0.7 ±0.3	0.21±0.02

cifically: 1) observed in the crystals with $x=x_1,x_2$, the absence of any visible splitting between the components σ^+ and σ^-; 2) a shift of one observed π-component in the crystal with $x=x_2$ such as to become external relative to the unsplit σ^+ and σ^-; 3) relative positioning of the components σ^+ and σ^- as observed in Ref. 4 for $x=0.014$, where the energy of the component σ^+ is lower than that of σ^-. This distinctive feature of the *B* exciton spin splittings in a magnetic field can occur only when the sign of the difference satisfies the condition $\Delta_1-\Delta_2<0$.

DISCUSSION OF THE RESULTS

Table I gives the parameters of the valence band Δ_1, Δ_2, and Δ_3 that best describe the splittings between the *A*, *B*, and *C* components of the exciton spectrum at $H=0$ and give the necessary correspondence of experimental *A* and *B* exciton splittings in a magnetic field. In view of the deviation of these parameters of the valence band of $Cd_{1-x}Mn_xS$ crystals from those used in the literature, it is natural to inquire into the possibility of using our band parameters to describe experiments[9] on uniaxial strains in CdS. We have analyzed this question on the basis of data for the crystal with $x=x_3$. For this purpose we have followed a procedure for numerical diagonalization of the strain matrix, similar to that in Ref. 9. As a result, using the values of Δ_1, Δ_2, and Δ_3 for $x=x_3$ from Table I, we have succeeded in completely describing the *A* and *B* exciton energy shifts for deformations applied in all the directions used in Ref. 9, and the description with these parameters is as good as for those used in Ref. 9, because of the insignificant variations of the deformation potential constants. The necessary values of the deformation potential constants C_i^* to achieve such agreement are given in Table II. Also shown for comparison in the table are the corresponding values of C_i from Ref. 9. Clearly, the two sets of values are acceptably close to one another within admissible error limits for these constants.

According to the data in Table I, the valence band parameters Δ_i for $Cd_{1-x}Mn_xS$ crystals are also observed to depend on the content of the magnetic component *x*. This effect is most conspicuous in the rather abrupt increase (by 5 meV) of the crystal field constant Δ_1 in the interval $x_3<x<x_2$. Here the composition with x_3 corresponds to the value of Δ_1 that should be chosen for pure CdS in the TH scheme, whereas for the crystal with $x=x_1$ the value of Δ_1 increases, as in a crystal with $x=0.014$ (Ref. 4). This type of dependence could be a consequence of carrier–ion exchange interaction of a biquadratic-spin magnetic ion and the effective hole spin when included in higher perturbation orders.[16] On the other hand, constant growth of Δ_1 with increasing concentration *x* is not observed within the framework of our data, making it difficult to apply the theory of Ref 16 directly to the given results.

TABLE II. Deformation potential parameters obtained by numerical fitting to data in Ref. 9 according to the energy shifts of the exciton reflection spectra.

i	1	2	3	4	5	6
C_i^*, eV	−2.7	−3.8	−1.1	2.6	−1.3	1.2
C_i, eV	−2.8	−4.5	−1.3	2.9	−1.5	1.2

The exchange interaction constant J_h given in Table I for $x=x_1$ exhibits good agreement with previously published values for this composition[2,3,5,17]; for $x=x_2$ the constant is more accurate than in Refs. 1, 3, and 5. Here the tendency for J_h to increase as *x* is lowered, which was noted in Ref. 3 and subsequently interpreted theoretically in Ref. 18, is corroborated for the two given concentrations. An unexpected result for x_3 is the fact that the value of J_h does not increase, but is actually much lower than in crystals with $x=x_2,x_3$. This violates the previously established trend in the dependence of J_h on *x*; however, investigations for such a low concentration *x* as x_3 have not been carried out before. We note that a dependence $J_h(x)$ somewhat different from that established previously for $Cd_{1-x}Mn_xS$ has also been recorded in another sulfide compound $Zn_{1-x}Mn_xS$ (Ref. 19). In Ref. 19 J_h was observed to increase in the interval of concentrations $x=0.001-0.01$. The explanation of the new features observed in the dependence $J_h=J_h(x)$ for the case $x=x_3$ may well require further modification of the theory.[18] An alternative possibility is the persistence of special aspects of the doping of the crystal with Mn ions in growth from the vapor phase.

CONCLUSIONS

We have found that the *A* and *C* valence subbands of a $Cd_{1-x}Mn_xS$ crystal with all the investigated concentrations *x* are formed from the Γ_5 as a result of its spin–orbit splitting, as postulated in the Thomas–Hopfield band genesis scheme.[7] Since as the optical properties of CdS are described in most papers on the basis of the set of parameters Δ_i corresponding to the Birman's scheme,[6] the interpretation of several previous results might have to be reexamined.

We have obtained data on the variation of the behavior of $|J_h(x)|$ in the range of extremely low concentrations *x*. In this range we have discovered a strong dependence of the crystal field parameter Δ_1 on *x*. To make use of the theoretical models, therefore, it is important to study these phenomena further in the interval of concentrations of the magnetic component $0.0002<x<0.0015$.

The authors are grateful to S. I. Gubarev for furnishing the crystal with x_1 and x_2 and to G. S. Pekar' for the crystal grown with x_3.

[1] S. I. Gubarev, Zh. Éksp. Teor. Fiz. **80**, 1174 (1981) [Sov. Phys. JETP **53**, 601 (1981)].
[2] V. G. Abramishvili, S. I. Gubarev, A. V. Komarov, and S. M. Ryab-

chenko, Fiz. Tverd. Tela (Leningrad) **26**, 1095 (1984) [Sov. Phys. Solid State **26**, 666 (1984)].
[3] S. I. Gubarev and M. G. Tyazhlov, JETP Lett. **44**, 494 (1986).
[4] M. Nawrocki, J. P. Lascaray *et al.*, MRS Symp. Proc. **89**, 65 (1987).
[5] V. G. Abramishvili, A. V. Komarov, Yu. G. Semenov, and S. M. Ryabchenko, in *Digests of the First Scientific Conference on Defects in Semiconductors* [in Russian], St. Petersburg (1992), p. 57.
[6] J. L. Birman, Phys. Rev. **114**, 1490 (1959).
[7] D. G. Thomas and J. J. Hopfield, Phys. Rev. **116**, 573 (1959); Phys. Rev. **119**, 570 (1960).
[8] G. L. Bir and G. E. Pikus, *Symmetry and Strain-Induced Effects in Semiconductors*, Israel Program for Scientific Translations, Jerusalem; Wiley, New York (1975).
[9] D. W Langer, R. N. Euwema, K. Era, and T. Koda, Phys. Rev. B **2**, 4005 (1970).
[10] S. M. Ryabchenko and Yu. G. Semenov, in *Spectroscopy of Crystals* [in Russian], Nauka, Leningrad (1983), p. 206.
[11] A. V. Komarov, S. M. Ryabchenko, Yu. G. Semenov, V. D. Shanina, and N. I. Vitrikhovskiĭ, Zh. Éksp. Teor. Fiz. **79**, 1554 (1980) [Sov. Phys. JETP **52**, 783 (1980)].
[12] Yu. G. Semenov and V. A. Stephanovich, Semicond. Sci. Technol **7**, 364 (1992).
[13] K. D. Dmitrenko, L. V. Taranenko, S. G. Shevel', and A. V. Marinchenko, Fiz. Tekh. Poluprovodn. **19**, 788 (1985) [Sov. Phys. Semicond. **19**, 487 (1985)].
[14] S. I. Gubarev, Phys. Status Solidi B **134**, 211 (1986).
[15] J. J. Hopfield and D. G. Thomas, Phys. Rev. **122**, 35 (1961).
[16] S. M. Ryabchenko, Yu. G. Semenov, and O. V. Terletskii, Phys. Stat. Solidi B **144**, 661 (1987).
[17] S. I. Gubarev, J. Lumin. **52**, 193 (1992).
[18] C. Benoit a la Guillaume, D. Scalbert, and T. Dietl, Phys. Rev. B **46**, 9853 (1992).
[19] V. G. Abramishvili, S. M. Ryabchenko, and O. V. Terletskiĭ, Fiz. Tverd. Tela (Leningrad) **31**, 33 (1989) [Sov. Phys. Solid State **31**, 564 (1989)].

Translated by James S. Wood

Analysis of the temporal instability of the parameters of an insulator/III–V compound by the isothermal capacitance relaxation method

L. S. Berman

A. F. Ioffe Physicotechnical Institute, Russian Academy of Sciences, 194021 St. Petersburg, Russia
(Submitted December 14, 1995; accepted for publication March 12, 1996)
Fiz. Tekh. Poluprovodn. **31**, 78–82 (January 1997)

Existing diagnostic techniques used to evaluate the temporal instability of the parameters of a semiconductor–insulator interface with deep-level centers are analyzed. A method is proposed for evaluating temporal instability according to the long-term isothermal transient behavior of the capacitance of a metal–insulator–semiconductor structure. The energy spectrum of the effective density of surface states is determined for *n*-type InP–SiO_2–Al structures prepared by chemical vapor deposition. The variation of the capacitance during long-term isothermal relaxation provides a criterion of temporal instability of a semiconductor–insulator interface. © *1997 American Institute of Physics.* [S1063-7826(97)01601-3]

INTRODUCTION

The foremost unsolved problem in the physics of insulator/III–V compound interface structures is the temporal instability of the interface parameters.

A unified procedure for evaluating the temporal instability of the interface does not exist at present. Estimates based on the capacitance properties of a metal–insulator–semiconductor (MIS) are preferred over estimates based on the drift current of an MIS transistor, because the fabrication of an MIS structure requires fewer auxiliary technological operations affecting the interface parameters; moreover, the stability of an MIS structure does not depend on the carrier mobility. In a number of papers, therefore, it has been the practice to characterize the instability of the interface by the width of the hysteresis loop of the capacitance–voltage (C–V) characteristic and/or the flat-band voltage shift[1–3] ΔV_{FB}, and also by deep-level transient spectroscopy (DLTS) signals.[4–6]

However, the behavior of the C–V characteristic depends significantly on the measurement technique, i.e., the initial filling of surface states and deep-level (DL) centers in the insulator, the voltage amplitude, and the direction and rate of change of the voltage (see, e.g., Ref. 7). The results of DLTS measurements depend on the initial filling of the DL centers. If the period and duration of the filling pulses are shorter than or commensurate with the carrier tunneling time, the initial filling of the DL centers is ambiguous.

A more reliable approach is to analyze the temporal instability of the interface by the method of long-term isothermal relaxation of the capacitance after switching of the MIS structure, for example, from enrichment to depletion (after prolonged holding in the enrichment mode). We propose to carry out such an analysis in the present article.

THEORY

(A) Statement of the Problem

The thickness of the insulator d exceeds a few hundred angstroms, and tunneling clear through the insulator can be disregarded. There is a fragmented layer with a thickness of the order of several tens of angstroms near the insulator–semiconductor interface and a fragmented layer near the metal–insulator interface. Upon integration of the Poisson equation the space charge density in the insulator is multiplied by the distance from the charge to the electrode on the insulator. Consequently, if the densities of DL centers in the two both layers are of the same order of magnitude, then the second layer exerts a much weaker influence than the first on the capacitance of the MIS structure. We shall consider only the first fragmented layer and ignore the influence of the second on the capacitance of the MIS structure. We assume that the DL centers in the fragmented layer of the insulator exchange charge carriers only with the surface of the semiconductor by tunneling but not by tunneling between DL centers. For definiteness the calculations are carried out for *n*-type semiconductors.

(B) Basic Equations

We specify long-term holding of the MIS structure at $V=V_1$ (Fig. 1a) for a time exceeding the subsequent time to measure the transient process by more than an order of magnitude. Surface states with energies $E<F_n$ are filled with electrons, which tunnel from the surface states into the depth of the insulator with a time constant τ_T, which is determined from the approximate equation[6,8]

$$\tau_T=\alpha^{-1}\exp[z(b\Phi)^{1/2}], \tag{1}$$

where z is the tunneling depth (in angstroms), b is the ratio of the effective mass of an electron in the insulator to the free-electron mass, Φ is the height of the potential barrier (in electron-volts), and α is the preexponential factor, which depends on Φ and z and on the parameters of the insulator (see Fig. 4 in Ref. 6).

During the holding period at $V=V_1$, the DL centers in the insulator with energies $E<F_n$ are filled with electrons in the layer 0–z_1.

The following relation holds at $V=V_1$:

$$V_1-V_{bi}=\Psi_{s1}-C_i^{-1}[Q_{sc1}+Q_{ss1}+Q_{i\text{eff}}], \tag{2}$$

 1063-7826/97/010063-04$10.00

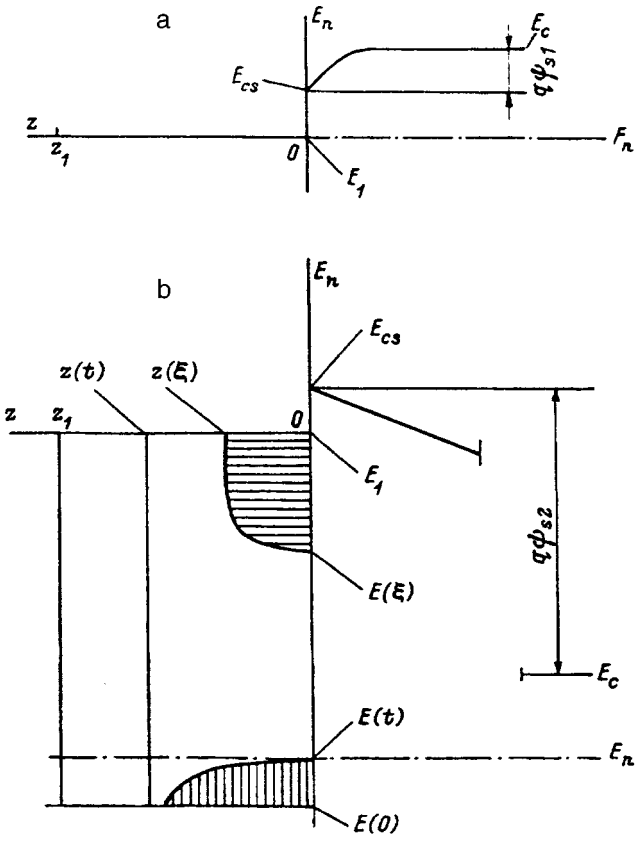

FIG. 1. Filling of surface states and deep-level centers with electrons in the insulator. a) In enrichment, $V=V_1$; b) in depletion, $V=V_2$. Here F_n is the Fermi level in the semiconductor, E_n is the electron energy, E_c is the energy of the lower edge of the conduction band, and E_{cs} is the value of E_c on the surface of the semiconductor.

where V_1-V_{bi} is the difference between the work functions of the metal and the semiconductor, q is the electron charge, Ψ_{s1} is the surface potential, C_i is the capacitance of the insulator, Q_{sc1} is the charge in the space charge region of the semiconductor, Q_{ss1} is the charge of the surface states and DL centers in the δ layer of the insulator, $Q_{i\text{eff}}$ is the effective (averaged) charge in the insulator, determined from the expression

$$Q_{i\text{eff}}=(d-\delta)^{-1}\int_0^{d-\delta} x\rho(x)dx, \tag{3}$$

δ is the thickness of the layer (of the order of several tens of angstroms) in which charge carriers are exchanged between the insulator and the semiconductor during the measurement, ρ is the space charge density, and the coordinate x is measured from the metal (the capacitances and charges are given per unit area).

At $t=0$, we switch the structure from V_1 to V_2 (from enrichment to depletion; see Fig. 1). Switching is followed by the thermionic emission of electrons from surface states into the conduction band with a time constant τ_{th}, which is determined from standard relations.[9,10] After thermionic emission from surface states with energies $E>E(\xi)$ electrons tunnel their way to these surface states from DL centers in the insulator with a time constant τ_T determined from (1); the electrons then experience thermionic emission from the surface states into the conduction band. The layer from which the electrons arrive is marked with horizontal striations in Fig. 1b.

The following relation holds at $V=V_2$:

$$V_2-V_{bi}=\Psi_{s2}-C_i^{-1}[Q_{sc2}+Q_{ss1}+\Delta Q_{ss}+Q_{i\text{eff}} +\Delta Q_{i\text{eff}}], \tag{4}$$

where ΔQ_{ss} is the charge variation of the surface states and DL centers in the δ layer after switching; from now on we regard these two interacting charges as a single charge of DL centers with a number density N_t; $\Delta Q_{i\text{eff}}$ is the charge variation in the insulator in strong fields (avalanche injection or the Fowler–Nordheim effect). The rest of the notation has the same significance as in (2), and the subscript 2 corresponds to $V=V_2$.

After Ψ_{s2} is increased (diminishing band bending) to a certain value Ψ_{s2}^*, the charge $\Delta Q_{i\text{eff}}$ does not change. We assume that after switching from V_1 to V_2 the inequality $\Psi_{s2}>\Psi_{s2}^*$ holds during the entire transient process, so that $\Delta Q_{i\text{eff}}$ can be disregarded.

(C) Solution

Subtracting Eq. (4) from (2), we obtain

$$V_1-V_2=\Psi_{s1}-\Psi_{s2}-C_i^{-1}[Q_{sc1}-Q_{sc2}-\Delta Q_{ss}]. \tag{5}$$

a) We specify V_1 in such a way as to satisfy the inequality $C_{sc1}\gg C_{ss1}$, where C_{sc1} and C_{ss1} are the capacitance of the space charge region and the capacitance of the surface states, respectively; at $V=V_1$[1)], this inequality can be satisfied in the enrichment mode. We then have

$$C_{sc1}=[C(V_1)^{-1}-C_i^{-1}]^{-1}, \tag{6}$$

where $C(V_1)$ is the capacitance of the MIS structure at $V=V_1$. The capacitance C_{sc1} can be calculated from (6) using the known values of $C(V_1)$ and C_i. Since C_{sc} and Q_{cs} are known functions of Ψ_s (Refs. 9 and 10), Ψ_{s1} and Q_{sc1} can be calculated from the known value of C_{sc1}.

b) We specify V_1 in such a way as to satisfy the inequality $\Psi_{s1}<\Psi_{\text{scr}}$, where Ψ_{scr} is determined from the condition

$$2\pi f\tau_{th}(\Psi_{\text{scr}})=1, \tag{7}$$

in which $\tau_{th}(\Psi_{\text{scr}})$ is the time of thermionic emission from the level $E=F_n$ when $\Psi_s=\Psi_{\text{scr}}$; in other words, the rf capacitance is measured at $V=V_1$ (see also Ref. 11). Now C_{sc1}, Q_{sc1}, and Ψ_{s1} can be calculated as in case a).

Let us assume that the inequality $\Psi_{s2}<\Psi_{\text{scr}}$ holds after switching. We also assume that the MIS structure stays in the depletion mode (without forming an inversion layer). At $V=V_2$ the values of C_{sc2}, Q_{sc2}, and Ψ_{s2} can then be calculated as for $V=V_1$, i.e., from the experimental values of the measured capacitance. Consequently, $\Delta Q_{ss}(t)$ can be determined from (5).

We now examine limiting cases.

a) The inequality $\tau_T\ll\tau_{th}$ is satisfied for δ of the order of a few angstroms. Methods for determining the energy spectrum of the surface states $N_{ss}(E)$ in this case have been developed in detail.[9,10,12]

b) $\tau_T \gg \tau_{th}$. In this case the tunneling depth z is calculated from (1) over the entire energy interval $E(0)<E<E_1$, where $E_1=F_n$ for $V=V_1$, and $E(0)=F_n$ for $V=V_2$ at $t=0$. From now on we restrict the discussion to case b).

We consider two methods for the analysis of the transient processes.

1) Constant capacitance method. After switching, the voltage $V_2(t)$ is varied in such a way as to keep the capacitance of the structure constant, i.e., we have $\Psi_{s2}=\text{const}$ and $Q_{sc2}=\text{const}$; $\Delta Q_{ss}(t)$ is determined from (5) according to the experimental dependence $V_2(t)$.

On the other hand, $\Delta Q_{ss}(t)$ is calculated from the expression

$$q^{-1}\Delta Q_{ss}(t)=\int_0^{z(t,E)}\int_{E(0)}^{E_1} N_t(E,y)\,dE\,dy, \tag{8}$$

where E_1 and $E(0)$ are determined from the expressions

$$E_{cs}-E_1=E_c-F_n-q\Psi_{s1}, \tag{9}$$

$$E_{cs}-E(0)=E_c-F_n-q\Psi_{s2}(0) \tag{10}$$

(see Fig. 1). From Eqs. (9) and (10) we deduce the relation

$$E_1-E(0)=q[\Psi_{s1}-\Psi_{s2}(0)], \tag{11}$$

where $\Psi_{s2}(0)$ is the value of Ψ_{s2} at $t=0$.

For n-n-type InP/SiO_2 and n-n-type Si/SiO_2 structures we have $\Phi\approx 3$ eV. For $\Phi\approx 3$ eV and $E_1-E(0)$ of the order of several tens of electron-volts we can ignore the dependence of z on E; in addition, we can set $\Phi=\text{const}$ in the layer $\delta \ll d$. We therefore assume from now on that z does not depend on E.

We now consider the special case where $N_t(E,z)$ decreases into the depth of the insulator as

$$N_t(E,z)=N_t(E,0)\exp(-\beta z), \tag{12}$$

and β does not depend on E. Expression (8) is then transformed to

$$q^{-1}\Delta Q_{ss}(t)=z^*\overline{N_t}(0)[E_1-E(0)]=z^*\overline{N_t}(0)q[\Psi_{s1}-\Psi_{s2}(0)], \tag{13}$$

where

$$\overline{N}(0)[E_1-E(0)]=\int_{E(0)}^{E_1} N_t(E,0)\,dE,$$

$$z^*=\frac{1-\exp[-\beta z(t)]}{\beta}, \tag{14}$$

$\overline{N_t}(0)$ is the average value of $N_t(0)$ in the interval $\Psi_{s1}-\Psi_{s2}(0)$, $N_t(0)z^*$ is the average value of the effective density of surface states in the interval $\Psi_{s1}-\Psi_{s2}(0)$, and z^* is the effective thickness of the fragmented layer [this concept is useful in situations where the decrease of N_t into the depth of the insulator is not described by expression (12)].

Consequently, having determined ΔQ_{ss} from (5), we then use (13) to calculate the average value of the effective density of surface states in the interval $\Psi_{s1}-\Psi_{s2}(0)$. The long-term variation of the charge ΔQ_{ss} is also a criterion of the temporal stability of the interface.

The dependence of $N_t(0)z^*$ on E can also be determined by switching from V_1 to various values of V_2; this switching technique can be used to determine $N_t(0)z^*$ in different energy intervals but within one time interval, i.e., for identical values of z^*. Comparing $N_t(0)z^*$ in the intervals $\Psi_{s1}-\Psi_{s2}(0)$ and $\Psi_{s1}-\Psi_{s2}(0)+\Delta\Psi_{s2}$, we determine $N_t(0)z^*$ in a narrow energy interval $\Delta\Psi_{s2}$. After a series of switchings we find the dependence of $N_t(0)z^*$ on E.

2) Constant voltage method. After switching, we have $V_2=\text{const}$; Ψ_{s2}, Q_{sc2}, and ΔQ_{sc} are time-dependent. The tunneling of electrons from the insulator into surface states and their thermionic emission into the conduction band reduce band bending and increase the capacitance of the structure, and levels with energies $E(0)<E<F_n$ are again filled with electrons (this layer is marked by vertical striations in Fig. 1b). We assume that for $E<F_n$ all DL centers in the 0–z layer are filled with electrons; this assumption is justified by the logarithmic dependence of z on τ_T. Now $N_t(0)z^*$ can be calculated in the interval $\Psi_{s1}-\Psi_{s2}(t)$ from Eq. (13) with $\Psi_{s2}(0)$, replaced by $\Psi_{s2}(t)$. The dependence of $N_t(0)z^*$ on E can be determined as in the constant capacitance method.

EXPERIMENTAL

Samples were prepared from n-InP(111), $N_d=2\times10^{16}$ cm^{-3}. A SiO_2 layer was formed by chemical vapor deposition at 350 °C. An Al film was deposited on the SiO_2 by vacuum evaporation at room temperature. An ohmic contact to the InP was created by depositing Au+Ge according to standard technology.

Measurement results. The current density I was $<10^{-12}$ A/cm^2 as the voltage was varied from -3 V to $+3$ V. The isothermal capacitance relaxation was measured on an apparatus described in Ref. 13. The constant voltage method was used, as it permits the measurement of faster transient processes than the constant capacitance method. After the samples were switched from enrichment to the boundary between depletion and mild inversion, the relative increment of the capacitance in the time interval 0.1–1300 s was $\Delta C/C=0.05$–0.06.

The value of $N_t(0)z^*$ and the dependence of $N_t(0)z^*$ on E were determined by switching from V_1 to various values of V_2. The dependence of $N_t(0)z^*$ on E is shown in Fig. 2; at the minimum $N_t(0)z^*_{\min}=5\times10^{-11}$ $\text{cm}^{-2}\cdot\text{eV}^{-1}$. In the interval $E_c=-(0.28$–$0.80)$ eV we have $N_t(0)z^*=2.4\times10^{12}$ $\text{cm}^{-2}\cdot\text{eV}^{-1}$ for this sample.

We have also compared the width of the hysteresis loop with the amplitude of the long-term isothermal capacitance relaxation for our n-n-type InP–SiO_2–Al samples and for control samples of n-n-type Si on low-temperature SiO_2. The experimental results show that no detectable correlation exists between these quantities.

CONCLUSION

It follows from the analysis above that the energy spectrum of the effective density of surface states can be determined by switching the MIS structure from enrichment to depletion or from depletion to stronger depletion according to one of two methods:

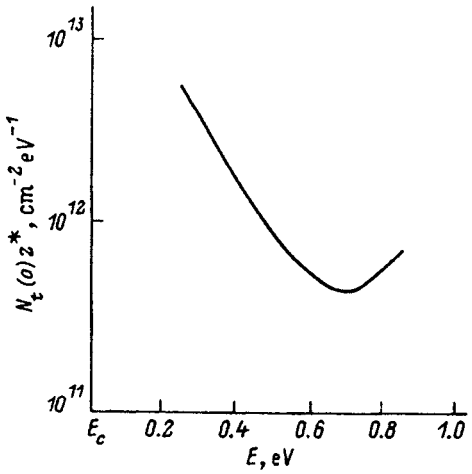

FIG. 2. Effective density of states vs energy.

1) the constant capacitance method, using the experimental time dependence of the voltage on the sample;

2) the constant voltage method, using the time dependence of the capacitance.

Moreover, a simple criterion of the stability of the semiconductor–insulator interface is the relative variation of the capacitance in a given time interval after the indicated switching.

The author is grateful to L. E. Klyachkin for preparing the samples and to N. M. Shmidt for valuable discussions.

This work has received financial support from the International Science Foundation, the Ministry of Science and Engineering Policy of the Russian Federation, and the Russian Fund for Fundamental Research (Grant No. NU2300).

[1)]In the stated problem the capacitance of the surface states is the capacitance of those DL centers on and in the vicinity of the surface whose filling can keep pace with an alternating voltage with the frequency at which the capacitance is measured.

[1] J. Tardy, I. Thomas, P. Viktorovich, M. Gendry, J. L. Perrossier, C. Santinelli, M. P. Besland, P. Lous, and G. Post, Appl. Surf. Sci. **50**, 383 (1991).
[2] M. O. Bakshin, A. V. Emel'yanov, O. D. Men'shikov, S. M. Portnov, and V. B. Ufimtsev, Élektron. Tekh. Ser. Mikroélektron., **1**, 32 (1990).
[3] M. O. Bakshin, A. V. Emel'yanov, S. M. Portnov, and N. S. Samsonov, Élektron. Prom. **6/92**, 2 (1992).
[4] P. V. Staa, H. Rombach, and R. Kassing, J. Appl. Phys. **54**, 4014 (1983).
[5] D. Vuilaume, J. C. Bourgoin, and M. Lanoo, Phys. Rev. B **34**, 1171 (1986).
[6] H. Lakhadri, D. Vuilaume, J. C. Bourgoin, and M. Lanoo, Phys. Rev. B **38**, 13124 (1988).
[7] H. Hasegawa, Li He, H. Ohno, T. Sawada, T. Haga, Y. Abe, and H. Takahashi, J. Vac. Sci. Technol. B **5**, 1097 (1987).
[8] V. Kumar and W. E. Dahlke, Solid State Electron. **20**, 143 (1977).
[9] S. M. Sze, *Physics of Semiconductor Devices*, 2nd Ed., Wiley–Interscience, New York (1981).
[10] E. H. Niccollian and J. R. Brews, *MOS (Metal–Oxide–Semiconductor) Physics and Technology*, New York (1982), p. 972.
[11] L. S. Berman, I. V. Grekhov, I. N. Karimov, and N. V. Ostroumova, Fiz. Tekh. Poluprovodn. **27**, 917 (1993) [Semiconductors **27**, 497 (1993)].
[12] K. Yamasaki, M. Yoshida, and T. Sugano, Jpn. J. Appl. Phys. **18**, 113 (1979).
[13] L. S. Berman, A. D. Remenyuk, and M. G. Tolstobrov, FTI Preprint No. 974 [in Russian], A. F. Ioffe Physicotechnical Institute, Academy of Sciences of the USSR, Leningrad (1985), p. 25.

Translated by James S. Wood

Depth distribution of deep-level centers in silicon dioxide near an interface with indium phosphide

L. S. Berman

A. F. Ioffe Physicotechnical Institute, Russian Academy of Sciences, 194021 St. Petersburg, Russia
(Submitted December 29, 1995; accepted for publication March 12, 1996)
Fiz. Tekh. Poluprovodn. **31**, 83–84 (January 1997)

The constant capacitance method with measurement of the voltage–time dependence over a long period of time is used to determine the profile of the density of deep-level centers in an insulator at an interface with a semiconductor. The distribution of deep-level centers in silicon dioxide near an interface with indium phosphide is measured. It is shown that the density of deep-level centers does not depend on the coordinate at distances in the interval 22–27 Å from the interface. © *1997 American Institute of Physics.* [S1063-7826(97)01701-8]

The long-term temporal instability of an insulator/III–V compound interface presents a major obstacle to the utilization of such structures. The instability is caused by the presence of deep-level (DL) centers near the interface and their distribution with depth in the insulator $N_t(z)$.

This distribution can be estimated qualitatively from the dependence of the flat-band voltage shift on the time that the metal–insulator–semiconductor (MIS) structure is held in the enrichment mode.[1] When deep-level transient spectroscopy (DLTS) is used and tunneling is taken into account,[2] the depth resolution is limited by the duration or the period (or both) of the filling pulses.

In the present article the constant capacitance method[3,4] is used to determine $N_t(z)$, with the time dependence of the voltage measured over a long period of time with a view toward enhancing the depth resolution. The theory of the method is given in Ref. 5. The initial carrier population of the DL centers is set by holding the MIS structure for a long time in, say, the enrichment mode so that the holding time is much longer than the subsequent measurement time. At $t=0$ the MIS structure is switched from enrichment to depletion. We write the function $N_t(z)$ in the form $N_t(z)=N_t(0)f(z)$, where $N_t(0)$ is the density of DL centers at the interface, and z is the distance from the interface. We assume that $f(z)$ does not depend on the energy E. For a potential barrier having a height of several electron-volts and a narrow energy interval we can assume that z does not depend on E. After switching, therefore, the charge increment ΔQ_t of DL centers near the interface is described by the expression

$$\Delta Q_t(t)=q\overline{N_t}(0)\Delta E z^*, \tag{1}$$

where $z^*=\int_0^z f(y)dy$, q is the electron charge, $\overline{N_t}(0)$ is the average value of $N_t(0)$ in the energy interval ΔE, and z is the tunneling depth after a time t. The interval ΔE is specified by the choice of switching regime. The function $\Delta Q_t(t)$ is determined by processing experimental results.[5]

Differentiating Eq. (1) with respect to the time, we obtain

$$\frac{d}{dt}(\Delta Q_t)=q\overline{N_t}(0)\Delta E f(z)\frac{dz}{dt}. \tag{2}$$

The function $z(t)$ and its derivative dz/dt are calculated according to the theory in Refs. 2 and 6. The profile of the density of DL centers is then determined from the expression

$$\overline{N_t}(0)f(z)=\frac{d(\Delta Q_t)/dt}{q\Delta E dz/dt}. \tag{3}$$

Samples were prepared from n-InP(111), $N_d=2\times10^{16}$ cm^{-3}. A SiO_2 layer was applied by chemical vapor deposition at $T=350$ °C.

The measurements were performed on an apparatus described in Ref. 7 at $T\approx300$ K. The capacitance of the sample was held constant by means of a negative feedback circuit; the output voltage of the phase detector of an MTsE-12 AM

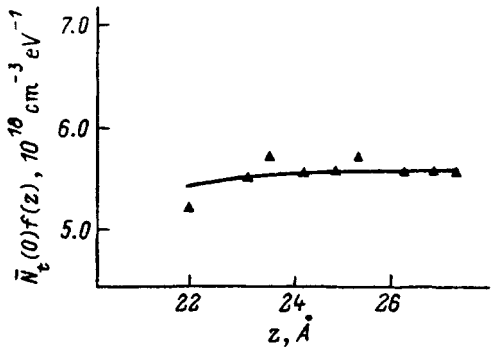

FIG. 1. Density of deep-level centers vs the depth coordinate.

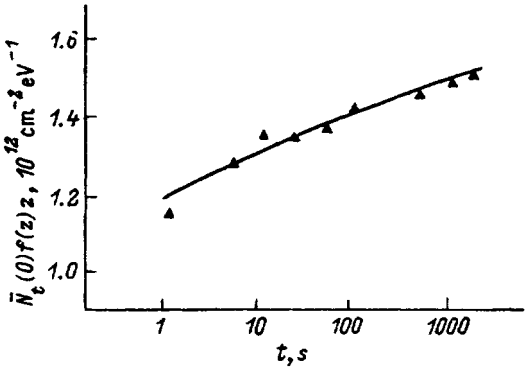

FIG. 2. Effective density of surface states vs time.

 1063-7826/97/010067-02$10.00

bridge was sent through an operational amplifier to the sample in series with an initial constant voltage.

Figure 1 shows a typical dependence of $N_t(0)f(z)$ on z in the energy interval $E_c=(0.4–0.6)$ eV. In the interval $z=22–27$ Å the density of DL centers is almost independent of the coordinate, i.e., we have $f(z)\approx 1$ and $z=z^*$. Figure 2 shows the time variation of $N(0)f(z)z$ due to widening of the insulator layer in which electrons escape from DL centers to the surface of the semiconductor.

An imminent objective is to investigate the behavior of $N_t(z)$ for different insulator deposition techniques and in various energy intervals; such a study can provide new information about the physical nature of the instability of an interface formed between a semiconductor and an insulator with deep-level centers.

The author is indebted to L. E. Klyachin for preparing the samples and to N. M. Shmidt for a discussion of the problem and valuable consultations.

This work has received financial support from the International Science Foundation, the Ministry of Science and Engineering Policy of the Russian Federation, and the Russian Fund for Fundamental Research (Grant No. NU2300).

[1] J. Tardy, T. Thomas, P. Viktorovich, M. Gendry, J. L. Perrsier, C. Santinelli, M. P. Besland, P. Lous, and G. Post, Appl. Surf. Sci. **50**, 383 (1991).
[2] H. Lakhadri, D. Vuilaume, and J. C. Bourgoin, Phys. Rev. B **38**, 13124 (1988).
[3] J. A. Pals, Solid–State Electron. **17**, 1139 (1974).
[4] L. S. Berman and A. A. Lebedev, *Capacitative Spectroscopy of Deep-Level Centers in Semiconductors* [in Russian], Nauka, Leningrad (1981).
[5] L. S. Berman, Fiz. Tekh. Poluprovodn. **31**, 78 (1997) [Semiconductors **31**, 63 (1997)].
[6] V. Kumar and W. E. Dahlke, Solid–State Electron. **20**, 143 (1977).
[7] L. S. Berman, A. D. Remenyuk, and M. G. Tolstobrov, FTI Preprint No. 974 [in Russian], A. F. Ioffe Physicotechnical Institute, Academy of Sciences of the USSR, Leningrad (1985).

Translated by James S. Wood

Electron-phonon scattering engineering

J. Požela, V. Jucienė, A. Namajūnas, and K. Požela

Semiconductor Physics Institute, Vilnius, Lithuania
(Received May 20, 1996; accepted for publication May 21, 1996)
Fiz. Tekh. Poluprovodn. **31**, 85–88 (January 1997)

We present calculations which show that independent quantization of electrons and phonons allows the intra- and intersubband electron-phonon scattering rate in two-dimensional structures to be changed. It is considered how the design of multi-heterostructure quantum well (QW) changes the electron mobility and population of subbands in the QW. It was shown that the insertion of the phonon wall (a few AlAs monolayers) into an AlAs/GaAs/AlAs double heterostructure allows the electron mobility in the QW to be enhanced and electron intersubband population to be inverted. © *1997 American Institute of Physics.* [S1063-7826(97)01801-2]

INTRODUCTION

In pure GaAs electron scattering by optical phonons is a dominating scattering mechanism. The electron-optical phonon scattering limits the electron mobility and determines the intersubband population of optically excited (or injected) electrons. A method for changing the electron-optical phonon scattering rate in a two-dimensional ($2D$) structure was recently proposed by Požela.[1,2] According to this method, an insertion of a phonon wall (*Ph*-wall) (a few AlAs monolayers) into an AlAs/GaAs/AlAs QW is a good tool for changing the electron-phonon scattering rate.[3] In this paper we consider an enhancement of electron mobility by inserting a *Ph*-wall into a rectangular QW and the possibility of inverting the intersubband population of optically excited electrons in the QW with a *Ph*-wall. The large increase in the electron-optical phonon scattering rate in a MODFET channel by inserting a *Ph*-wall is also considered.

Electron mobility enhancement in GaAs QW with an inserted AlAs *Ph*-wall

The division of a QW by a *Ph*-wall changes the frequencies of phonon modes, the electron-phonon coupling, and the shape of confined electron and phonon wavefunctions. As a result, the electron-optical phonon scattering rate and the electron mobility change significantly.[1,3] We performed the electron-optical phonon scattering rate calculations in an AlAs/GaAs/AlAs QW with a GaAs *Ph*-wall inserted at the center of the QW (Fig. 1).

The electron-phonon scattering rate is treated within the dielectric continuum approach. Assuming that the one-phonon process is the only process, the rate of the intrasubband ($1\rightarrow 1$) scattering of an electron with the initial wave vector $\mathbf{k}$ by nth mode phonon emission or absorption in the heterostructure quantized in the $\mathbf{z}$-direction is given by[3–5]

$$W_{11n}(\mathbf{k})=\frac{e^2 m}{\pi\hbar^3}\int_0^{2\pi} C_n\left(N_{qn}+\frac{1}{2}\pm\frac{1}{2}\right)\frac{|G_n|^2}{2q_n^2}\,d\Theta, \qquad (1)$$

where e and m are the electron charge and effective mass, h is Planck's constant, N_{qn} is the number of nth mode phonons, the ''+'' sign represents emission, the ''−'' denotes absorption,

$$C_n=\left(\frac{\partial\varepsilon_n}{\partial\omega}\right)^{-1} \qquad (2)$$

is the electron-phonon coupling coefficient,

$$G_n=\int_L \varphi_e^{*}\varphi_e\varphi_{qn}\,dz, \qquad (3)$$

L is the width of the electron QW, $\mathbf{q}_n=\mathbf{q}_\parallel+\mathbf{q}_z$ is the emitted or absorbed phonon wave vector in the plane of the heterostructure

$$q_\parallel=\sqrt{k^2+k_0^2-2kk_0\cos\Theta}, \qquad (4)$$

$k_0=\sqrt{k^2-k_n^2}$, $k_n=\sqrt{(2m/\hbar^2)}\hbar\omega_n$, and $\hbar\omega_n$ is the energy of the nth mode phonon. The z-components of the electron and phonon wave functions, φ_e and φ_{qn}, and the dielectric function ε_n are determined by the structure of the heterosystem.

The total scattering rate W_{11} is considered as a sum of the scattering rates of each n-phonon mode:

$$W_{11}=\sum_n W_{11n}. \qquad (5)$$

We use the slab model for confined phonon modes. We can therefore write the z-component of the confined phonon potential wave function in the phonon well for $z\geqslant 0$ as follows:

$$\varphi_q=\sqrt{\frac{2}{d_w}}\sin\left(q_z\left[z-\frac{d}{2}\right]\right),$$
$$q_z=n\,\frac{2\pi}{(L-d)}, \quad n=1,2,\ldots, \qquad (6)$$

where $d_w=(L-d)/2$ is the confined phonon QW width, and d is the AlAs *Ph Ph*-wall thickness (Fig. 1). The interface (IF) phonon wave functions in the double heterostructure with the AlAs *Ph*-wall centered at $z=0$ can be written for $z\geqslant 0$ in the form

$$\varphi_{q1}=B\,\frac{\cosh(q_\parallel z)}{\cosh(q_\parallel d/2)} \quad z<d/2,$$
$$\varphi_{q21}=B\cdot e^{-q_\parallel(z-d/2)} \quad d/2<z<L/2,$$
$$\varphi_{q23}=B\cdot e^{+q_\parallel(z-L/2)} \quad d/2<z<L/2,$$
$$\varphi_{q3}=B\cdot e^{-q_\parallel(z-L/2)} \quad z<L/2, \qquad (7)$$

where B is the normalization coefficient.

 1063-7826/97/010069-03$10.00

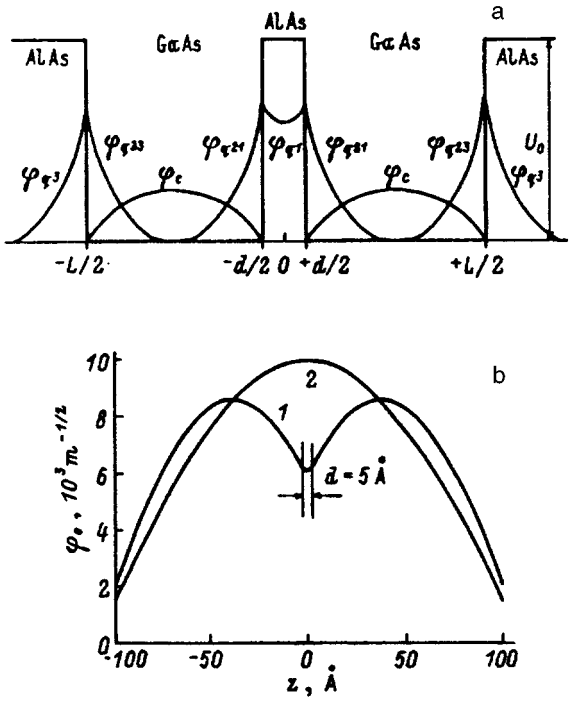

FIG. 1. a—The double AlAs/GaAs/AlAs heterojunction QW which contains the AlAs *Ph*-wall at the center of the structure. The wave functions of interface, φ_q, and confined, φ_c, phonon modes are shown schematically. b—The numerically calculated electron wave function in the AlAs/GaAs/AlAs QW with a AlAs *Ph*-wall of thickness $d=5$ Å (curve *1*). The electron wavefunction in the structure without the *Ph*-wall is shown for comparison (curve *2*).

We have assumed that in the region $d/2<z<L/2$ the IF phonon wave functions consist of two independent branches, φ_{21} and φ_{23}, which have different phonon frequencies and do not interact with each other (Fig. 1).

On the basis of this assumption the dielectric function ε determined from the boundary conditions for the wave function and their derivatives is different for the φ_{21} and φ_{23} branches of IF phonons:

$$\varepsilon_{21}\equiv\varepsilon_1\tanh(q_\parallel d/2)+\varepsilon_2=0, \quad \varphi_{q21}\text{ branch mode}, \tag{8}$$

$$\varepsilon_{23}\equiv\varepsilon_1+\varepsilon_2=0, \quad \varphi_{q23}\text{ branch mode}, \tag{9}$$

where

$$\varepsilon_{1(2)}=\varepsilon_{\infty 1(2)}\frac{\omega^2-\omega_{L1(2)}^2}{\omega^2-\omega_{T1(2)}^2}. \tag{10}$$

The Indexes 1(2) stand for AlAs (GaAs), ω_L and ω_T are the longitudinal and transverse phonon frequencies, respectively, and ε_∞ is the high-frequency dielectric constant. The frequencies of phonon modes are obtained from the dispersion relation $\varepsilon=0$. Note that the frequencies and the coupling coefficients $C_n(\omega)$ [Eq. (2)] for the φ_{q21} and φ_{23} IF phonon modes are different.

The z-component of the lower subband electron envelope function can be approximated by the functions (for $z\geqslant 0$)

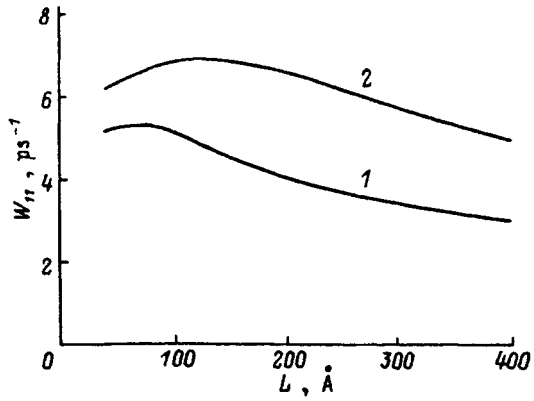

FIG. 2. The rate of intrasubband electron scattering W_{11} by phonon emission in a AlAs/GaAs/AlAs QW of thickness L without (curve *2*) and with (curve *1*) the AlAs *Ph*-wall ($d=5$ Å). Electron energy $E_e=1.4\hbar\omega_{L2}$, $T=300$ K.

$$\varphi_{e1}=A\frac{\cosh(k_1 z)}{\cosh(k_1 d/2)} \quad z\leqslant d/2,$$

$$\varphi_{e2}=A\frac{\cos(k_2 z+\varphi_0)}{\cos(k_2 d/2+\varphi_0)} \quad d/2\leqslant z\leqslant L/2,$$

$$\varphi_{e3}=A\frac{\cos(k_2 L/2+\varphi_0)}{\cos(k_2 d/2+\varphi_0)}e^{-k_1(z-L/2)} \quad z\geqslant L/2, \tag{11}$$

where A is the normalization coefficient, $k_1=k_2\sqrt{(U_0/E_1)-1}$, $k_2=\sqrt{(2m/\hbar^2)E_1}$, the AlAs/GaAs heterojunction height is $U_0=0.5$ eV, and E_1 is the lower subband energy. Using the boundary conditions for φ_e and their derivatives, we obtain the equations for the subband energy E_1 and the phase φ_0

$$\arctan\left(\frac{k_1}{k_2}\right)-\arctan\left(\frac{k_1}{k_2}\frac{e^{-k_1 d}-1}{e^{-k_1 d}+1}\right)=k_2\frac{L-d}{2}, \tag{12}$$

$$\arctan\left(\frac{k_1}{k_2}\right)=k_2\frac{L}{2}+\varphi_0. \tag{13}$$

It is worth noting that division of the GaAs QW by the AlAs barrier at its center simultaneously changes the subband energy E_1 in both parts of the QW. For $d\to 0$ and $U_0\to\infty$ the electron envelope function in the QW is

$$\varphi_e=\sqrt{\frac{2}{L}}\cos(k_z z), \quad k_z=\pi/L.$$

The numerically calculated electron wave functions in the GaAs QW, divided by the AlAs *Ph*-wall, are shown in Fig. 1b.

Figure 2 shows the calculated rates of the scattering of electrons with an energy of $1.4\hbar\omega_{1,2}$ by the emission of all optical phonon modes in the AlAs/GaAs/AlAs QW with and without the inserted AlAs *Ph*-wall. We see that the insertion of the *Ph*-wall decreases the total intrasubband scattering rate by more than a factor of 1.5 in a wide range of the QW widths. This decrease is greater than that obtained in the case of an idealized QW.[3] In a pure GaAs in a wide temperature range (100–400 K) electron scattering by polar optical

phonons is a dominant mechanism that determines the electron mobility. Since the ratio of the phonon scattering rates in the GaAs QW with and without the *Ph*-wall depends only slightly on the scattered electron energy, we can assume that the electron mobility changes proportionally to the scattering rate change. This means that in a pure GaAs QW with a *Ph*-wall the electron mobility increases by more than a factor of 1.5 and can reach 1.2 $m^2/(V \cdot s)$ at $T=300$ K.

Intersubband scattering in a QW with a *Ph*-wall

In recently demonstrated intersubband lasers the confined electron-phonon scattering is used to achieve the population inversion. In a three-subband-level laser the inverted population of electrons, which are photoexcited from the first level to the third, is achieved when the rate of the nonradiative electron transition by phonon emission from the third level to the second (W_{32}) is much less than the transition rate from the second level to the first (W_{21}). The population inversion take place when

$$\Delta n = n_3 - n_2 \approx \left(1 - \frac{W_{32}}{W_{21}}\right) n_3, \quad W_{32} \ll W_{21}. \tag{14}$$

In order to maximize the population inversion we need to minimize the nonradiative transitions between the upper levels (W_{32}) and to maximize the transition between the lower levels (W_{21}).

Let us consider how the insertion of the *Ph*-wall into an electron QW allows us to attain intersubband population inversion. For simplicity we shall consider the intersubband electron transition by emission of IF phonon only. This is a reasonable approximation in the QW with a width less than 100 Å, where the electron-IF phonon scattering rate is dominating.

We can write the intersubband scattering rate W_{if} in an approximate form as follows:

$$W_{if} \approx W_{oif} \frac{|G_{if}|^2}{\sqrt{E_{si} - E_{sf} - \hbar\omega_0}}, \tag{15}$$

where E_{si} and E_{sf} are the initial and final subband energies, $\hbar\omega_0$ is the IF optical phonon energy, and G_{if} is the overlap integral (3). The electron kinetic energy in the initial state is assumed to be zero.

The intersubband transition rate is sensitive to the design of a heterostructure because of the dependence of electron and phonon wave function overlap integrals and the subband energies on the heterostructure parameters.

We shall consider the electron population in the first three subband levels. First of all, we shall determine how the design of the electron and phonon wave function overlap integrals allows us to obtain population inversion. In a single QW the electron wave functions are symmetric in the first and third levels and asymmetric in the second level. Because of this circumstance, the rate of the $E_2 \to E_1$ transition by emission of symmetric IF phonons is very low.

In order to obtain the inversion population we need to maximize the $E_2 \to E_1$ transition. The insertion of the *Ph*-wall into the electron QW splits the first subband level into two sublevels. Note that the electron wave functions of these sublevels have the same symmetry, and that the scattering rate between the sublevels increases. In the QW with a *Ph*-wall the split levels become the lower two levels in the three-level laser model. The increase of W_{21} in this case creates the population inversion between the third level and the new, second subband level.

The insertion of the *Ph*-wall into the QW changes the subband energies and, according to Eq. (15), the intersubband scattering rate. The intersubband scattering rate increases when the energy difference between the subbands decreases. The population inversion between the third and the second subband levels can occur when $E_3 - E_2 > E_2 - E_1$. Especially great is the increase of the intersubband scattering rate when the energy difference between the subbands is equal to the emitted phonon energy ($W_{if} \to \infty$ at $E_i - E_f - \hbar\omega_0 - 0$). The resonance phonon scattering is used in many papers in order to obtain population inversion in intersubband lasers (see, for example, Ref. 6).

The insertion of the *Ph*-wall at the boundary of MODFET channel (triangular QW) separately shifts up the energy levels of subbands with higher quantum numbers. The resonance optical phonon scattering arises under the conditions where the energy difference between the lower subband and the shifted subband (with the same wave function symmetry) is equal to the emitted optical phonon energy. As a result, the electron mobility in the MODFET channel decreases significantly.

CONCLUSIONS

The insertion of the *Ph*-wall into the QW is a good tool for the electron-phonon scattering engineering. The insertion of the AlAs *Ph*-wall into the center of rectangular GaAs QW enhances the electron mobility 1.5 times. The insertion of the *Ph*-wall at the boundary of the MODFET channel decreases the electron mobility. The insertion of the *Ph*-wall into the QW changes the intersubband scattering rate because of the change in symmetry of the subband electron wave functions and the intersubband energies. Both mechanisms can create population inversion.

This work was supported by Human Capital and Mobility Programme of the EC (project contract ERBCIPDCT 940007) and Grant 5/94 from the Lithuanian State Sciences and Studies Foundation.

[1] J. Požela, V. Jucienė, V. Jucienė, Fiz. Tekh. Poluprovodn. **29**, 459 (1995) [Semiconductors **29**, 236 (1995)].
[2] J. Požela, V. Jucienė, K. Požela, Semicond. Sci. Technol. **10**, 1076 (1995).
[3] J. Požela, V. Jucienė, K. Požela, Semicond. Sci. Technol. **10**, 1555 (1995).
[4] N. Mori, T. Ando, Phys. Rev. B **40**, 6175 (1989).
[5] P. Bordone, P. Lugli, Phys. Rev. B **49**, 8178 (1994).
[6] F. H. Julien, A. Sa'ar, J. Wang, J.-P. Leburton, Electron. Lett. **31**, 838 (1995).

Published in English in the original Russian journal. Edited by S.J. Amoretty.

Monte Carlo simulation of the low-temperature mobility of two-dimensional electrons in a silicon inversion layer

V. M. Borzdov and T. A. Petrovich

Belarus State University, 220050 Minsk, Belarus
(Submitted December 19, 1995; accepted for publication March 23, 1996)
Fiz. Tekh. Poluprovodn. **31**, 89–92 (January 1997)

The transport of two-dimensional electrons in a silicon inversion layer is determined by Monte Carlo simulation in the temperature range 4.2–40 K, where the electrical quantum limit occurs and only the lowest subband is populated. Two scattering mechanisms are taken into account: scattering by distant ionized impurities and scattering by surface roughness elements, along with their dependence on the polarizability of the two-dimensional electron gas. The mobility and coefficient of warm electrons in weak electric fields are calculated. The data are compared with previously published results. © *1997 American Institute of Physics.*
[S1063-7826(97)01901-7]

The characteristics of the transfer of two-dimensional (2D) electrons in a silicon inversion layer at temperatures and concentrations such that the electric quantum limit is valid, where only the lowest energy subband is populated, have been studied long and diligently.[1] In view of the widespread application of silicon *n*-channel metal-oxide-semiconductor (MOS) field-effect transistors in integrated electronics, these studies are of great theoretical and practical importance. It is a well-known fact[1] that the principal mechanism underlying the scattering of inversion layer electrons at low temperatures, in cases where electron–electron scattering can be neglected,[2] is scattering by ionized impurities and surface roughness. The rigorous calculation of the kinetic properties of the 2D electron gas in this case requires that screening of the scattering potential be taken into account.[1,3–10] For example, it has been shown analytically[5] that the low-temperature dependence of the screening causes the conductivity of the 2D electron gas to decrease linearly with increasing temperature.

Of unquestionable interest in this regard is the Monte Carlo numerical method as a means of calculating the kinetic parameters characterizing electron transfer in the inversion layer at low temperatures; it affords a powerful tool for the investigation of kinetic effects in semiconductors and semiconducting structures.[11] To the best of our knowledge, however, this simulation method has never been employed for a degenerate electron gas in the electric quantum limit, despite the fair abundance of papers published for the range of temperatures and electric fields wherein not only the lowest, but also higher subbands are populated. Noteworthy among these publications are Refs. 12–14, along with several recent papers[15–17] in which the heating of 2D electrons is simulated with allowance for their transition to the 3D state.

Here we give the results of single-frequency Monte Carlo computations of the dependence of the mobility of 2D electrons in the inversion layer of silicon with surface orientation (100) on their number density N_s and the temperature T. We also estimate the warm-electron coefficient β in weak warming fields in the range of electric field strengths E from 10 V/m to 100 V/m. In the simulation we assume that all conduction electrons are situated in the lowest subband with a bottom energy equal to E_0 (Refs. 1 and 18).

The mobility μ is calculated according to an expression based on the assumption of a linear relation between the average electron drift velocity $\overline{V_d}$ and the strength E of the longitudinal electric field in the channel.[12,13] In this case the average mobility $\overline{\mu}$ can be calculated from the equation

$$\overline{\mu}=\frac{\overline{V_d}}{E}=\frac{e\Sigma_i t_i(k'_{xi}-k_{xi})}{m^*\Sigma_i(k'_{xi}-k_{xi})}, \tag{1}$$

where e is the electron charge, t_i is the time of the ith free transit of an electron, k_{xi} and k'_{xi} are the projections of the 2D electron wave vector onto the field direction x at the beginning and end of the given free transit, respectively. We also assume that the constant-energy contour formed by the projections of twofold-degenerate silicon valleys onto the (100) plane is a circle, whereupon we interpret the effective mass of an electron in its 2D motion in the plane as the mass $m^*=m_t^*=0.19\cdot m_0$, where m_t^* is the transverse effective electron mass in bulk silicon, and m_0 is the free-electron mass.

The simulation algorithm includes all the basic steps typical of the single-frequency Monte Carlo method in bulk semiconductors. In the ensuing discussion we shall indicate only the following salient characteristics of the method used in our work.

First of all, the accuracy of the Monte Carlo method is known to deteriorate in weak electric fields,[11,19] because the electron drift velocity becomes small in comparison with the electron thermal velocity. For this reason, a simulated sample of sufficient volume must be chosen if data are to be obtained with acceptable accuracy. Estimate have shown that good convergence and the required accuracy of the results in our case are attained for a sample size of at least 5×10^4 collisions. Second, since the electron gas is degenerate in the investigated range of temperatures and concentrations,[1] the Pauli principle must be taken into account in statistical sampling of the postscattering electron energy states; this is accomplished by incorporating into the general simulation algorithm a procedure proposed[20] for degenerate semiconductors.

According to Refs. 1,3, and 7, the intensity $W_i(k)$ of scattering by distant ionized impurities is calculated from the equation

$$W_i(k)=\frac{m^*N_i}{4\pi\hbar^3}\int_{\vartheta_{\min}}^{2\pi}\left[\frac{e^2}{(\varepsilon_{sc}+\varepsilon_{ox})\varepsilon_0\epsilon(q,T,N_s)}\right]^2 \times\left(1+\frac{q}{b}\right)^{-6}\frac{d\vartheta}{q}, \quad (2)$$

where $q=2k\sin(\vartheta/2)$, k is the modulus of the 2D electron wave vector, ϑ is the scattering angle, $\vartheta_{\min}$ is its minimum value, N_i is the density of ionized impurities per unit volume, $\hbar$ is the reduced Planck's constant, ε_{sc} and ε_{ox} are the dielectric constants of the semiconductor and the oxide, respectively, b is a parameter of the Fang–Howard variational wave function,[21] and $\epsilon(q,T,N_s)$ is the dielectric function. The parameter b is[1] $b=(12m_z^*e^2N^*/\varepsilon_{sc}\varepsilon_0\hbar^2)^{1/3}$, where m_z^* is the effective mass of an electron in the direction perpendicular to the surface, and $N^*=N_{\text{depl}}+(11/32)N_s$, and N_{depl} is the surface charge density in the depletion layer.

The dependence of the dielectric function on the parameters q, T, and N_s in the linear approximation can be written as follows on the basis of Refs. 1 and 5:

$$\epsilon(q,t,N_s)=1+\frac{e^2}{q(\varepsilon_{sc}+\varepsilon_{ox})\varepsilon_0}F(q,N_s)P(q,T,N_s), \quad (3)$$

where $F(q,N_s)$ is the form factor, which is given by the equation[1]

$$F(q,N_s)=\frac{1}{16}\left(1+\frac{\varepsilon_{ox}}{\varepsilon_{sc}}\right)\left(1+\frac{q}{b}\right)^{-3}\left[8+9\frac{q}{b}+3\left(\frac{q}{b}\right)^2\right] +\frac{1}{2}\left(1-\frac{\varepsilon_{ox}}{\varepsilon_{sc}}\right)\left(1+\frac{q}{b}\right)^{-6}, \quad (4)$$

and $P(q,T,N_s)$ is the polarizability of the 2D electron gas, whose temperature dependence is given in Ref. 22. According to this paper, in the electric quantum limit at sufficiently low temperatures, when the chemical potential can be regarded as equal to the Fermi energy,[5,6,9,10] $P(q,T,N_s)$ is written in the form

$$P(q,T,N_s)=\int_0^\infty\frac{P(q,0,E)Ed}{4k_BT\cos h^2[(E_F-E)/2k_BT]}, \quad (5)$$

where $P(q,0,E)$ is the polarizability at the temperature $T=0$, E is the electron energy, k_B is the Boltzmann constant, and E_F is the Fermi energy: $E_F=\pi\hbar^2N_s/2m^*$.

To eliminate the divergence of the integral as $\vartheta\to0$ in calculating the intensity of scattering by an ionized impurity according to Eq. (2), we choose a certain nonzero angle $\vartheta_{\min}$ as the lower limit of integration. Since the theoretical value of this angle is not known *a priori*, it can be estimated from the condition of compatibility of the results of Monte Carlo mobility calculations with experimental or analytical data obtained by other methods. As the required control mobility we adopt its maximum value of 2 $m^2/(V\cdot s)$, which was determined previously[23] at $T=4.2$ K, $N_i=3.5\times10^{23}$ m^{-3}, $L=1.5$ nm, and $\Delta=0.52$ nm for the same scattering mechanisms as in the present study, but without regard for the temperature dependence of the polarizability of the 2D electron gas.

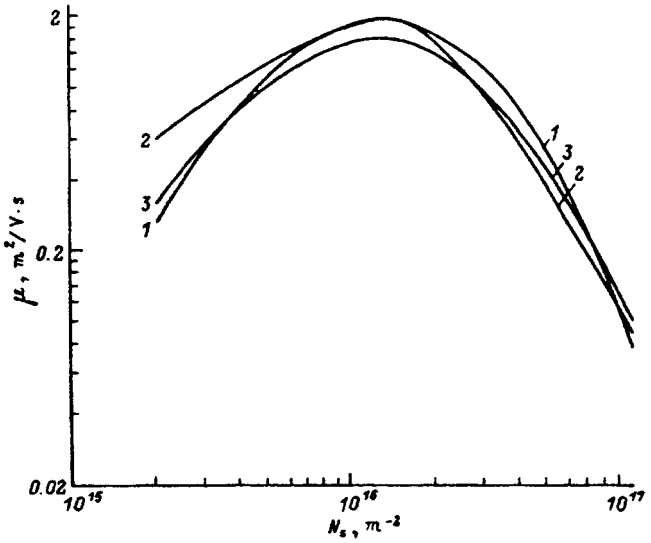

FIG. 1. Mobility μ vs surface density N_s of electrons in the inversion layer at the temperature $T=4.2$ K. *1*) Monte Carlo results, $E=10$ V/m; *2*) results from Ref. 23; *3*) according to Matthiessen's rule. Here $L=1.5$ nm, $\Delta=0.52$ nm, $N_i=3.5\times10^{23}$ m^{-3}, $\varepsilon_{sc}=11.7$, $\varepsilon_{ox}=4.1$, and $N_{\text{depl}}=1.92\times10^{16}$ m^{-2}.

To find the instantaneous values of ϑ, which must be chosen at random according to the specified angular distribution

$$P(\vartheta)d\vartheta\sim\frac{(1+q/b)^{-6}}{q^3\epsilon^2(q,T,N_s)}d\vartheta,$$

we use the sampling method in Ref. 11.

According to Refs. 1, 3, and 7, the intensity of scattering by surface roughness is calculated from the equation

$$W_{SR}(k)=\frac{m^*\Delta^2L^2}{2\hbar^2}\int_0^{2\pi}\frac{\Gamma^2(q,N_s)}{\epsilon(q,T,N_s)}\exp\left(-\frac{q^2L^2}{4}\right)d\vartheta, \quad (6)$$

where Δ is the average height of the roughness elements, L is the average distance between them, and for $q/b\gg1$ the function $\Gamma(q,N_s)$ is[3]

$$\Gamma(N_s)=\frac{e^2}{\varepsilon_{sc}\varepsilon_0}\left(\frac{N_s}{2}+N_{\text{depl}}\right). \quad (7)$$

As in the case of impurity scattering, statistical sampling is used to estimate the scattering angle ϑ from the angular distribution

$$P(\vartheta)d\vartheta\sim\frac{\exp(-q^2L^2/4)}{\epsilon^2(q,T,N_s)}d\vartheta.$$

Figure 1 shows the results of calculations of the mobility μ as a function of the surface density of electrons in the inversion layer N_s (curve 1) at the temperature $T=4.2$ K in a field $E=10$ V/m. Also shown on the same graph is a curve taken from Ref. 23 (curve 2) and a curve calculated by Matthiessen's rule (curve 3). It follows from the figure that

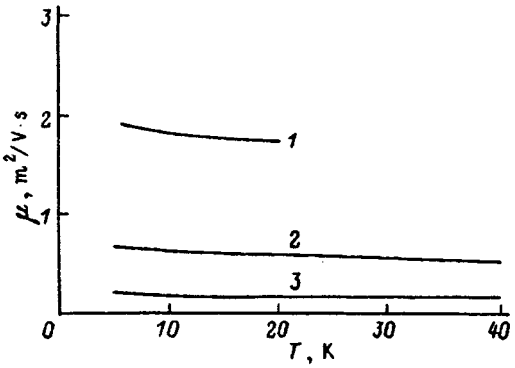

FIG. 2. Mobility μ vs temperature T for $E=100$ V/m and various densities N_s. *1)* $N_s=10^{16}$ m^{-2}; *2)* 5×10^{16} m^{-2}; *3)* 10^{17} m^{-2}. The parameters ε_{sc}, ε_{ox}, N_{depl}, L, Δ, and N_i have the same values as in Fig. 1.

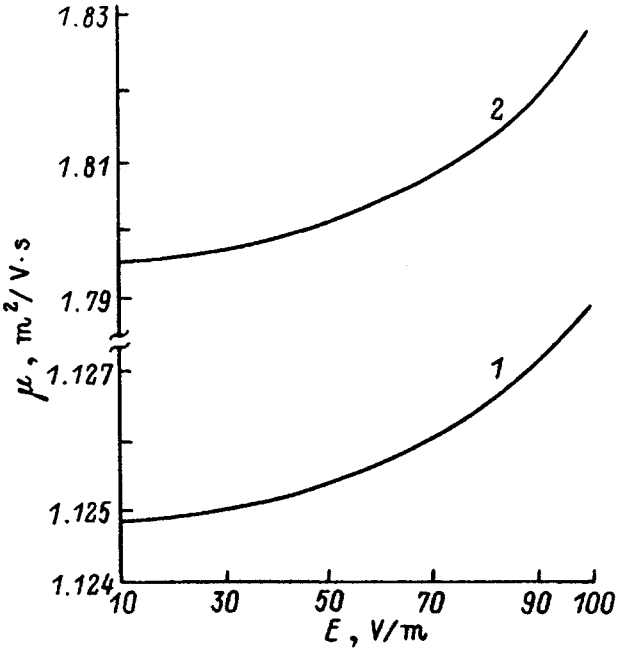

FIG. 3. Mobility μ vs electric field E at the temperature $T=4.2$ K for various densities N_s. *1)* $N_s=5\times10^{15}$ m^{-2}; *2)* 10^{16} m^{-2}. The parameters ε_{sc}, ε_{ox}, N_{depl}, L, Δ, and N_i have the same values as in Fig. 1.

curves 1 and 2 coincide at the point of the maximum, since at this point they are matched by appropriate selection of the angle $\vartheta_{\min}$ at equal temperatures, along with the parameters N_s, Δ, L, and N_i. The two curves also exhibit good agreement over the entire range of N_s except for $N_s<4\times10^{15}$ m^{-2}. Another fact worth noting is that curves 1 and 3 correlate with each other. This is reasonable in light of the fact that Matthiessen's rule must be valid at the temperature $T=4.2$ K (Ref. 4).

As an example, Fig. 2 shows the results of calculations of μ as a function of the temperature T for three values of N_s and a field $E=100$ V/m. It is evident from the figure that the mobility decreases slightly as the temperature increases. The decrease in mobility is attributable to the temperature dependence of the polarizability of the 2D gas.[4–6] This behavior of the curves is qualitatively consistent with results published earlier[4] for the same temperature range and the same scattering mechanisms, provided allowance is made for the temperature dependence of the polarizability of the 2D gas, but with the mobility calculated by suitable averaging of the relaxation time τ on the basis of a Fermi–Dirac distribution.

Finally, Fig. 3 shows the results of calculations of the mobility μ as a function of the field E at $T=4.2$ K in the presence of slight warming of the electron gas. This figure reveals a slight increase in the value of μ as the field is varied from 10 V/m to 100 V/m. The approximation of this dependence by a function of the form $\mu=\mu_0(1+\beta E^2)$, where μ_0 is the ''zero-field'' mobility, yields the following estimates for the coefficient β: $\beta_1=3.11\times10^{-7}$ m^2/V^2 for $N_{s1}=5\times10^{15}$ m^{-2} and $\beta_2=2.38\times10^{-6}$ m^2/V^2 for $N_{s2}=10^{16}$ m^{-2}. The value of β_2 agrees in order of magnitude with the results published in Ref. 24, according to which $\beta\simeq10^{-6}$ m^2/V^2 for $N_s<10^{16}$ m^{-6} at $T=4.2$ K.

We have thus demonstrated the effective applicability of the Monte Carlo method for calculating the low-temperature mobility of the 2D electron gas in an inversion layer of silicon MOS structures under conditions such that the electron gas is degenerate. We have relied on two principal scattering mechanisms: scattering by charges in the oxide and scattering by surface roughness elements. Despite the ample existing store of theoretical and experimental results describing electron transport in inversion layers at low temperatures, the approach discussed in this article has the advantage that it permits any number of significant scattering processes to be used in the calculations, and regardless of the complexity of the model description, it facilitates the incorporation of those mechanisms into the general simulation algorithm.

[1] T. Ando, A. B. Fowler, and F. Stern,''Electronic properties of two-dimensional systems,'' Rev. Mod. Phys. **54**, 437-672 (1982).
[2] S. É. Esipov and I. B. Levinson, Zh. Éksp. Teor. Fiz. **90**, 330 (1986) [Sov. Phys. JETP **63**, 191 (1986)].
[3] T. Ando, J. Phys. Soc. Jpn. **43**, 1616 (1977).
[4] F. Stern, Phys. Rev. Lett. **44**, 1469 (1980).
[5] A. Gold and V. T. Dolgopolov, J. Phys. C **18**, L463 (1985).
[6] E. A. Vyrodov, V. T. Dolgopolov, S. N. Dorozhkin, and N. B. Zhitenev, Zh. Éksp. Teor. Fiz. **94**(5), 234 (1988) [Sov. Phys. JETP **67**, 998 (1988)].
[7] V. K. Karavolas, M. J. Smith, T. M. Fromhold, P. N. Butcher, B. G. Mulimani, B. L. Gallagher, and J. P. Oxley, J. Phys. C **2**, 10401 (1990).
[8] G. I. Zebrev, Fiz. Tekh. Poluprovodn. **26**, 1550 (1992) [Sov. Phys. Semicond. **26**, 871 (1992)].
[9] V. M. Borzdov, F. F. Komarov, T. A. Petrovich, M. M. Vrubel, and O. G. Zhevnyak, Phys. Status Solidi B **183**, K47 (1994).
[10] V. M. Borzdov, F. F. Komarov, and T. A. Petrovich, Phys. Status Solidi B **188**, K5 (1995).
[11] C. Jacoboni and L. Reggiani, Rev. Mod. Phys. **55**, 645 (1983).
[12] P. K. Basu, Solid State Commun. **27**, 657 (1978).
[13] Chu-Hao, J. Zimmerman, M. Charef, R. Fauquembergue, and E. Constant, Solid–State Electron. **28**, 733 (1985).
[14] M. Shirahata, K. Taniguchi, and C. Hamaguchi, Jpn. J. Appl. Phys. **26**, 1447 (1987).
[15] S. Imanaga and Y. Hayafuji, J. Appl. Phys. **70**, 1522 (1991).
[16] M. V. Fischetti and S. E. Laux, Phys. Rev. B **48**, 2244 (1993).
[17] V. M. Borzdov, O. G. Zhevnyak, and F. F. Komarov, Fiz. Tekh. Poluprovodn. **29**, 193 (1995) [Semiconductors **29**, 95 (1995)].
[18] F. Stern and W. E. Howard, Phys. Rev. **163**, 816 (1967).

[19] C. Canali, C. Jacoboni, F. Nova, G. Ottaviani, and A. Alberigi-Quaranta, Phys. Rev. B **12**, 2265 (1975).
[20] S. Bosi and C. Jacoboni, J. Phys. C **9**, 315 (1976).
[21] F. F. Fang and W. E. Howard, Phys. Rev. Lett. **16**, 797 (1966).
[22] P. F. Maldaque, Surf. Sci. **73**, 296 (1978).
[23] Y. Matsumoto and Y. Uemura, in *Proceedings of the Second International Conference on Solid Surfaces* (1974), p. 367.
[24] F. F.Fang and A. B. Fowler, J. Appl. Phys. **41**, 1825 (1970).

Translated by James S. Wood

Study of PbTe photodiodes on a buffer sublayer of porous silicon

L. V. Belyakov

A. F. Ioffe Physicotechnical Institute, Russian Academy of Sciences, 194021 St. Petersburg, Russia

I. B. Zakharova, T. I. Zubkova, S. F. Musikhin, and S. A. Rykov

St. Petersburg State Technical University, 195251 St. Petersburg, Russia
(Submitted March 13, 1996; accepted for publication March 25, 1996)
Fiz. Tekh. Poluprovodn. **31**, 93–95 (January 1997)

The formation of epitaxial lead-telluride films on a silicon substrate with a porous-silicon sublayer is investigated. In these structures vertical-type infrared photodiodes were produced using ion doping. Despite a great mismatch in the lattice constants and the temperature expansion coefficients between silicon and lead telluride, the photodiode parameters are similar to those of photodiodes in the orienting substrates. © *1997 American Institute of Physics.* [S1063-7826(97)02001-2]

Lead-chalcogenide films deposited on silicon substrates can serve as a basis for the formation of a wide class of optoelectronic devices operating in the infrared in conjunction with silicon-based readout circuits. However, a serious obstacle to the growth of high-quality silicon epitaxial films is the great mismatch of the lattice constants (for lead telluride it is 17%) and the temperature expansion coefficients of lead and silicon, which makes it necessary to use buffer sublayers of calcium and barium fluoride. It is well known, however, that porous silicon (PS) can serve as the buffer sublayer in the growth of semiconducting epitaxial films on silicon. The porous-silicon layer in this case plays the role of an elastic matrix with nanosize voids which compensate for the elastic stresses of the polymorphic layer. Bondarenko *et al.*[1] recently reported a successful attempt to grow lead-sulfide films of a quality acceptable for optoelectronic devices on porous silicon by molecular-beam epitaxy. In the present paper we report the results of an experimental study of the formation of lead-telluride films by condensation from a gas-dynamic flow onto porous-silicon sublayers with various parameters, as well as the formation on such layers by ion implantation of vertical-type photodiodes with high photoelectrical characteristics.

Vertical-type photodiodes based on PbTe epitaxial films on a BaF_2 orienting substrate have several advantages over diodes with planar geometry[2] and exhibit a photosensitivity in the range 3–5 μm, near its limiting value, i.e., in the noise-limited regime. An obstacle to the formation of gratings or matrices of such photodiodes on a silicon substrate is the need for a high level of perfection of such films since in the case of polycrystalline PbTe films the crystallite boundaries shunt the p–n-junctions, leading to the growth of leakage currents, etc. It might be expected that the use of a porous-silicon buffer sublayer would make it possible to obtain high-quality epitaxial PbTe films and correspondingly highly-sensitive, vertical-type infrared photodiodes on a silicon substrate.

Porous-silicon layers of 0.5–1.0 μm thickness were formed on phosphorus-doped, n-type silicon substrates with resistivity $\rho = 1\ \Omega \cdot$cm and boron-doped, p-type silicon with resisitivty $\rho = 10\ \Omega \cdot$cm and orientation [100]. Anodization regimes with and without backlighting were used, with an anode current density of 5–20 mA/cm^2 in an electrolyte of 48% HF–isopropyl alcohol in the ratio 1:1. An MII-4 interferometer was used to determine the thickness of the porous-silicon layers after etching the porous silicon in a 5% solution of KOH at 50 °C. The structure of the porous-silicon layers so obtained was examined using a scanning tunneling microscope (STM) and a scanning electron microscope (SEM). To achieve electrical contact when carrying out the structural studies, a gold layer of 10 nm thickness was sputtered onto the porous-silicon surface. The results show that large-void layers with characteristic inhomogeneity size equal to 0.5–1 μm are formed on n-type silicon. On p-type silicon at current densities up to 10 mA/cm^2 in darkness for a porous-silicon layer thickness $\sim$1 μm the characteristic inhomogeneity size, revealed by the STM, is 30–40 nm (Fig. 1). Such layers have manifested intense photoluminescence with a wide maximum in the region 600–650 nm when illuminated with light in the wavelength range 300–400 nm (mercury lamp with a UFS-1 filter). The presence of such a luminescence can serve as a method for express monitoring of quality and uniformity of porous-silicon layers and their suitability for further epitaxy since the highest-quality PbTe layers have been obtained on such sublayers.

Using the method of condensation from a gas-dynamic

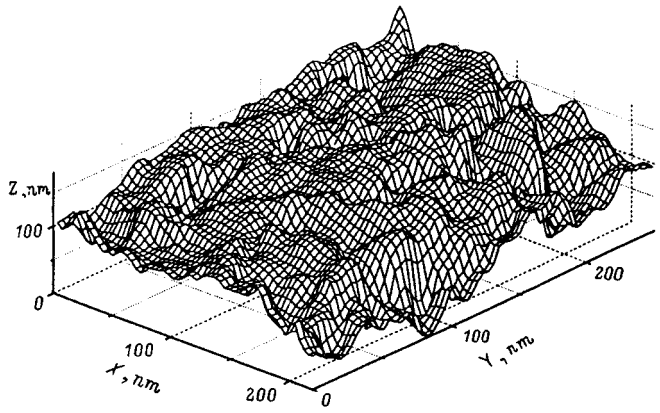

FIG. 1. Morphology of the porous-silicon buffer sublayer obtained by the STM method.

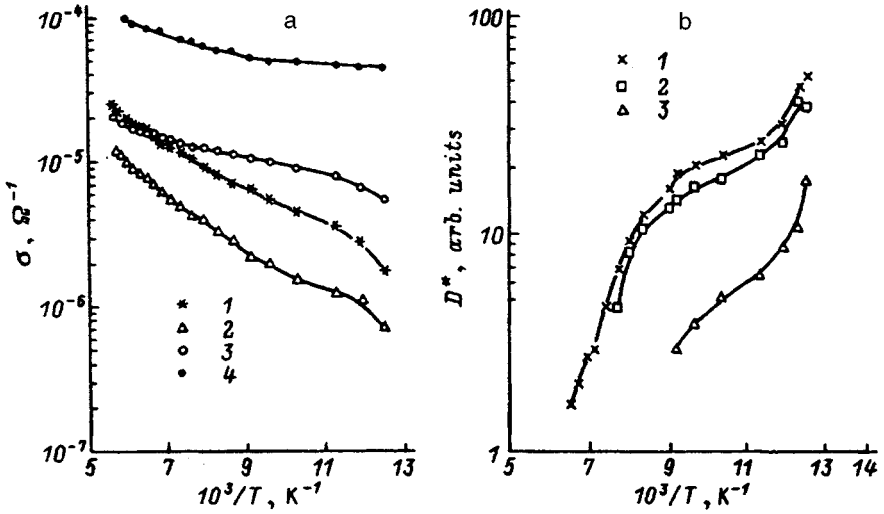

FIG. 2. a) Temperature dependence of the electrical conductivity of PbTe films on different substrates: *1*) on an amorphous substrate (photographic glass), *2*) on a porous-silicon silicon (*n*-type Si), *3*) on a substrate of porous-silicon substrate (*p*-type Si), *4*) on an orienting substrate (mica); b) temperature dependence of the specific detecting power of vertical infrared photodiodes on substrates of *1*) mica, *2*) porous silicon (*p*-type Si), and *3*) Si.

flow in a quasi-sealed space we obtained layers of compensated lead telluride of thickness 0.5–0.6 μm on both types of porous-silicon buffer layers, and also on control layers of silicon (unoriented substrate, which leads to condensation of polycrystalline PbTe films) and mica (oriented substrate; high-quality PbTe epitaxial films are formed on it). The regimes in which the PbTe films were obtained and the structure of the films on the orienting substrate and the silicon substrate are described in Ref. 3. Measurements of the temperature dependence of the electrical conductivity of the PbTe films over a wide temperature range (Fig. 2a) allowed us to determine the activation energy of conduction, from which we were able to estimate the drift barriers to current flow (E_d). For PbTe films with a porous-silicon buffer layer on *p*-type silicon E_d is equal to 13–15 meV, which is close to its value on high-quality epitaxial films on mica. On the other hand, for PbTe films deposited on *n*-type porous silicon E_d is 39–40 eV, which is the same as E_d of films on deposited silicon; the same value of E_d was observed for polycrystalline films of compensated PbTe on an amorphous unoriented substrate—photographic glass.[3]

We used the method of ion implantation to obtain vertical-type photodiodes. Since the intrinsic defects in lead chalcogenides are electrically active, when *p*-type PbTe films are implanted with Ar^+ ions, because of the formation in the implanted region of intrinsic defects a stable *n*-type region is formed with current-carrier concentrations up to 10^{18} cm^{-3} (Ref. 4). Here the depth of the layers in which the inversion of conductivity type is observed exceeds the calculated penetration depth of implanted ions by at least an order of magnitude. At ion energy of 100 keV the penetration depth is 0.2–0.6 μm. In our case, we used 60-keV N_2^+ ion implantation at an ion current density of 2 mA/cm^2 and obtained 1-mm-wide, vertical-type photodiodes. The optical area of the photodiode is governed by the collection length of the current carriers in the *n*- and *p*-type regions and stands at $(1-2)\times10^{-2}$ mm^2. Measurements of the current–voltage characteristics of the structures so obtained showed that for the indicated implantation regimes a *p*–*n* junction, with an energy barrier $\varphi\sim$60–120 meV and zero-bias resistance $R_0\approx$20–150 kΩ, is formed over the entire depth of the PbTe film (0.5 μm). The best values of the photodiode parameters were obtained for PbTe epitaxial films on mica and porous silicon. We measured the temperature dependence of the specific detecting power D^* of the photodiodes on an IChFR-11A ''blackbody'' setup in the presence of background radiation with a temperature of 300 K. The parameters of devices based on high-quality epitaxial PbTe films deposited on mica and on a buffer sublayer of porous silicon with nanosize voids essentially coincide over a wide temperature range (Fig. 2b), while without the porous-silicon buffer sublayer the photosensitivity of the diodes is one or two orders of magnitude lower.

We have determined the regularities of the growth of epitaxial lead-telluride films with a large mismatch of the lattice constants and large temperature expansion coefficient on a nanosize matrix of porous silicon of varying structure. The use of buffer sublayers of porous silicon has been shown to be promising for the formation on silicon of structures sensitive in the infrared region of the spectrum. By using ion doping we have obtained vertical-type infrared photodiodes with parameters approaching the parameters of photodiodes on an oriented substrate.

The authors express their deep gratitude to I. A. Abroyan for performing ion implantation of the lead-telluride films.

This work was carried out with the partial financial support of the Russian Fund for Fundamental Research (Grants 96-02-17200, 96-02-17197, and 96-02-17903).

[1] V. L. Bondarenko, N. N. Voronov, V. V. Dikarev, A. M. Dorofeev, V. I. Levchenko, L. I. Postnova, and G. N. Troyankov, Tech. Phys. Lett. **20**, 51 (1994).
[2] Z. M. Dashevskiĭ and M. P. Rudenko, Fiz. Tekh. Poluprovodn. **27**, 662 (1993) [Semiconductors **27**, 366 (1993)].
[3] I. B. Zakharova, T. I. Zubkova, S. A. Nemov, O. V. Rabizo, and V. N. Vydrik, Fiz. Tekh. Poluprovodn. **28**, 1802 (1994) [Semiconductors **28**, 998 (1994)].
[4] I. A. Abroyan, V. Z. Aliev, S. D. Imamkuliev, S. A. Kaz'min, V. I. Kaĭdanov, G. D. Kasamanli, and A. V. Suvorov, Fiz. Tekh. Poluprovodn. **17**, 611 (1983) [Sov. Phys. Semicond. **17**, 381 (1983)].

Translated by Paul F. Schippnick

High-frequency capacitance–voltage characteristic of GaAs-based, thin-film structures

N. B. Gorev, T. V. Makarova, E. F. Prokhorov, A. T. Ukolov, and V. I. Éppel'

Institute of Technical Mechanics, National Academy of Sciences of the Ukraine, 320600 Dnepropetrovsk, Ukraine

(Submitted November 2, 1993; accepted for publication March 26, 1996)
Fiz. Tekh. Poluprovodn. **31**, 96–99 (January 1997)

An analytical calculation of the high-frequency capacitance–voltage characteristic of a GaAs thin-film structure is carried out. It is shown that the peculiarities of this characteristic, namely an abrupt drop followed by a falloff to zero, are due to the merging of the depletion regions of the Schottky barrier and the film–substrate junction and to a lag in the recharging of deep centers in the substrate. © *1997 American Institute of Physics.* [S1063-7826(97)02101-7]

Manifestations of the role of the $n-\nu$ junction at the boundary of a film with substrate in GaAs-based structures are extremely varied in their nature[1] and, in particular, have a nontrivial effect on low-frequency $C-V$ (capacitance–voltage) measurements.[2] The latter, as is well known, make it possible to determine the concentration of the unfilled deep centers in the substrate.[3] Current thinking gives sufficient grounds to expect that the presence of an $n-\nu$ junction should also have a substantial effect on high-frequency $C-V$ measurements, which serve as the main method of obtaining information about the dopant impurity in the structure. However, despite the obvious relevance of this question, there is virtually nothing reported in the literature on this subject. We hope that the present work, dedicated to a study of the effect of the $n-\nu$ junction on high-frequency $C-V$ measurements, will to some extent fill this gap.

To determine the effect of the $n-\nu$ junction on the results of high-frequency $C-V$ measurements, it is first of all necessary to obtain an analytical description of the high-frequency barrier capacitance C under conditions in which the depletion region of the Schottky barrier is linked with the region of the film–substrate junction, i.e., when at some point on the film x_m the free electron concentration reaches its maximum value $n_m<N_0$, where N_0 is the concentration of the dopant impurity in the film.

In out further analysis it is more convenient to represent the barrier capacitance C in the form

$$C=\varepsilon\varepsilon_0 S\,\frac{\delta E_b}{\delta V}\,, \tag{1}$$

where S is the area of the barrier contact, δE_b is the amount by which the electric field E_b at the metal–semiconductor interface changes when the Schottky barrier bias changes by δV. When the depletion region of the Schottky barrier and the region of the film–substrate $n-\nu$ junction are joined, the magnitude of δE_b is determined by, among other factors, the change in the electric field E_j in the plane of the $n-\nu$ junction. In this regard, a well-known property of the $n-\nu$ junction of the type film–(semiconducting compensated substrate) becomes very important. This property has to do with the fact that the charge of the accumulation layer located in the substrate is formed by carriers bound to deep centers, since in the substrate the concentration of unfilled deep centers is 5–7 orders of magnitude higher than the concentration of free carriers. Therefore, in the case of the high-frequency capacitance a change in the barrier bias δV does not lead to a change in the charge of the accumulation layer of the $n-\nu$ junction and, consequently, it does not lead to a change in the electric field E_j; i.e.,

$$\delta E_j=0. \tag{2}$$

Using relations (1) and (2), we can obtain, using a method similar to that used in Ref. 3 to calculate the low-frequency capacitance, a parametric expression for the dependence of the high-frequency capacitance C on V (n_m serves as this parameter), valid for $N_0>n_m\gg n_j$, where n_j is the free carrier concentration in the plane of the $n-\nu_j$ junction:

$$\begin{aligned} C&=qS\left(\frac{2\varepsilon\varepsilon_0 N_0}{kT}\right)^{1/2}\frac{B}{2AB+N_0/n_m-1}\,,\\ V&=\frac{kT}{q}\left(\ln\frac{N_c}{n_m}+\frac{n_m}{N_0}+A^2\right)-\varphi_b\,, \end{aligned} \tag{3}$$

where

$$\begin{aligned} A&=\frac{h}{\sqrt{2}l_d}+2\left(\ln 3-\frac{n_m}{N_0}\right)^{1/2}\\ &\quad-\frac{\sqrt{2}}{\sqrt{1+2t}}\ln\frac{(\sqrt{1+3t}+\sqrt{1+2t})^2}{t}-D,\\ B&=\left(\ln 3-\frac{n_m}{N_0}\right)^{-1/2}+\frac{\sqrt{2}}{(1+2t)^{3/2}}\\ &\quad\times\ln\frac{(\sqrt{1+3t}+\sqrt{1+2t})^2}{t}+\frac{\sqrt{2}}{t(1+2t)\sqrt{1+3t}}\,,\\ D&=\left[\frac{N_t-N_s}{N_t-N_s+N_0}\left(\ln\frac{n_m}{n_i}-\frac{n_m}{N_0}\right)\right.\\ &\quad\left.-\frac{N_t}{N_t-N_s+N_0}\ln\frac{N_t}{N_s}\right]^{1/2},\\ t&=1-n_m/N_0. \end{aligned}$$

Here h is the film thickness, N_s, N_t, and n_i are the concentrations of the minority donors which compensate the deep centers in the substrate and the free carriers in the interior of the substrate, N_c is the density of states in the conduction band of the semiconductor, φ_b is the barrier height from the metal side, and $l_d=kT\varepsilon\varepsilon_0/q^2N_0$ is the Debye length in the film.

Analysis of relation (3) shows that as the concentration decreases, C falls abruptly and tends to zero as n_m/N_0. However, for a significant decrease of n_m (increase of V), when the junction begins to flatten out, the condition $n_m \geqslant n_j$, which restricts the applicability of relation (3), is violated. Nevertheless, this situation can be calculated analytically with sufficient accuracy.

The point is that by virtue of the large value of N_0/n_i this flattening out of the junction can commence only when $n_m \ll N_0$, i.e., when the film is almost completely depleted of its free carriers. In this case, as will be shown below, the high-frequency capacitance C becomes equal to zero. Indeed, for $n_m \ll N_0$ it follows from the Poisson equation that

$$E_b = E_j + (q/\varepsilon\varepsilon_0)N_0 h. \tag{4}$$

According to (1) and (2), it follows that C equals zero [the abrupt drop of C before it falls to zero, given by relations (3), obviously corresponds to the case in which n_m is still not small enough in comparison with N_0, and δE_b is governed in this case also by the variation of the free charge in the film]. Note that condition (2) remains valid as long as the accumulation layer of the film–substrate junction continues to exist, i.e., for $n_m > n_i$. Therefore, making use of the expression obtained in Ref. 3 for V in the case $n_m \ll N_0$ for the junction flatting out for $n_i < n_m \ll N_0$, we have

$$C = 0,$$

$$V = \frac{kT}{q}\left[\ln\frac{N_0}{n_j} + \frac{1}{2}\left(\frac{h}{l_d}\right)^2 - \frac{\sqrt{2h}}{l_d}\left(n_j - n_i + N_t \ln\frac{n_1+n_j}{n_1+n_i} - N_s \ln\frac{n_j}{n_i}\right)^{1/2}\right] - \varphi_b, \tag{5}$$

where $n_1 = N_c \exp(-E_t/kT)$ is the Shockley–Reed parameter, which is governed by the embedding depth of the deep center E_t.

Calculation shows that the two functional dependences $C(V)$, defined respectively by (3) and (5), practically coincide over a considerable interval in V in which the conditions $n_m \geqslant n_j$ and $n_m \ll N_0$ are simultaneously satisfied. This allows us, by joining these two forms in the indicated interval, to calculate the dependence $C(V)$ over a wide interval in V corresponding to the condition $n_i < n_m < N_0$.

With further increase of the reverse bias V, the film–substrate junction completely disappears, leaving only the depletion layer of the Schottky barrier, which covers the entire film and penetrates into the substrate. In this case, for the high-frequency barrier capacitance the customary expression is valid

$$C = \varepsilon\varepsilon_0 S/h_b, \tag{6}$$

where h_b is the width of the depletion layer of the Schottky barrier. Therefore, at the moment the junction disappears ($n_j = n_i$) a jump appears on the $C(V)$ curve from zero to the value of the capacitance given by expression (6). Here two cases are possible.

1. The Fermi level E_F in the interior of the substrate lies above the deep layer E_t, i.e., $n_i < n_1$. In such a situation the charge of the depletion layer of the Schottky barrier in the substrate is determined only by the minority impurity N_s since upon the escape of the free carriers the negatively charged, filled deep centers in this case are immediately wiped out and become neutral. The dependence $C(V)$ in this case is easily represented in the following parametric form (where $n_j \leqslant n_i$ serves as the parameter):

$$C = \varepsilon\varepsilon_0 s/(h + x_s),$$

$$V = \frac{kT}{q}\left(\ln\frac{N_c}{n_j} + \frac{1}{2}\left(\frac{h}{l_d}\right)^2 + \frac{x_s h}{l_d^2}\frac{N_s}{N_0}\right) - \varphi_b, \tag{7}$$

where

$$x_s = \left[\frac{2\varepsilon\varepsilon_0 kT \ln(n_i/n_j)}{q^2 N_s}\right]^{1/2}$$

is the width of the depletion layer of the Schottky barrier in the substrate.

2. $E_F < E_t$, i.e., $n_i > n_1$. In the depletion layer of the barrier in the substrate in this case, there is a part whose charge is determined only by the escape of free carriers without discharge of the deep centers. For $n_j > n_1$ this part spreads out over the entire depletion layer in the substrate and we now have for the dependence $C(V)$

$$C = \varepsilon\varepsilon_0 S/(h + x_s),$$

$$V = \frac{kT}{q}\left(\ln\frac{N_c}{n_j} + \frac{1}{2}\left(\frac{h}{l_d}\right)^2 + \frac{x_s h}{l_d^2}\frac{n_i}{N_0}\right) - \varphi_b, \tag{8}$$

where we now have

$$x_s = \left[\frac{2\varepsilon\varepsilon_0 kT \ln(n_i/n_j)}{q^2 n_o}\right]^{1/2}.$$

For $n_j < n_1$ the depletion layer in the substrate consists of a part, whose charge is determined only by the escape of free carriers without discharge of the deep centers ($n_1 < n < n_i$), and a part whose charge is determined by the minority impurity ($n_j < n < n_1$). In this case the dependence $C(V)$ is given by

$$C = \varepsilon\varepsilon_0 S/(h + x_s),$$

$$V = \frac{kT}{q}\left[\ln\frac{N_c}{n_j} + \frac{1}{2}\left(\frac{h}{l_d}\right)^2 + \frac{h}{l_d^2 N_0}(x_{s1} n_i + x_{s2} N_s)\right] - \varphi_b, \tag{9}$$

where

$$x_{s1} = \left[\frac{2\varepsilon\varepsilon_0 kT \ln(n_i/n_1)}{q^2 n_i}\right]^{1/2},$$

$$x_{s2} = -\frac{x_{s1}}{2} + \left[\frac{x_{s1}^2}{4} + \frac{2\varepsilon\varepsilon_0 kT \ln n_1/n_j}{q^2 N_s}\right]^{1/2}.$$

Relations (3), (5), and (7)–(9) allow us to calculate the dependence $C(V)$ over a very wide range of variation of V. Typical calculated results are shown in Fig. 1 (Fig. 1a corresponds to the case $n_i > n_1$, and Fig. 1b corresponds to the case $n_i < n_1$). The above-noted peculiarities of the high-frequency dependence $C(V)$ are clearly visible in these graphs, namely 1) the abrupt drop with subsequent drop to

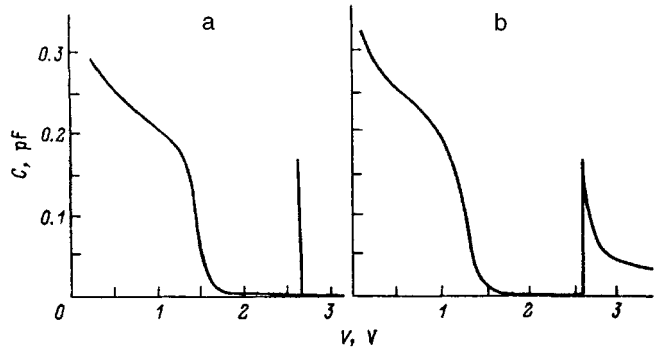

FIG. 1. Dependence of the high-frequency barrier capacitance C on the blocking voltage V across the Schottky barrier, calculated for $\varphi_b=0.8$ eV, $h=0.2$ μm, $S=300$ μm^2, $T=300$ K, $N_0=10^{17}$ cm^{-3}, $n_s=10^9$ cm^{-3}, and $N_t=5\times10^{16}$ cm^{-2} for $n_1=5\times10^8$ cm (a) and 4.9×10^{10} cm (b).

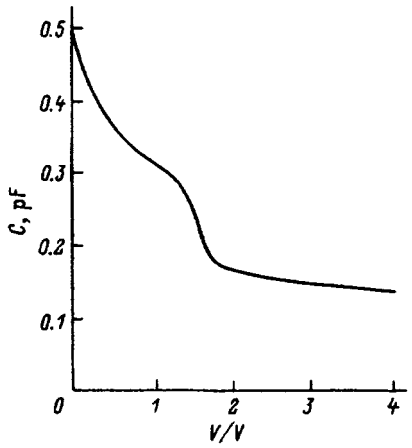

FIG. 2. Experimental dependence of the high-frequency barrier capacitance C on the blocking voltage V across the Schottky barrier; measurement frequency 1 MHz, $N_0\simeq10^{17}$ cm^{-3}.

zero, due to a combination of the depletion of the film of its free carriers and the zero variation of the charge of the accumulation layer of the film–substrate junction, and 2) the subsequent upward jump due to the removal of the film–substrate junction by the reverse bias of the Schottky barrier. Note that in the case $n_i>n_1$ this jump is in fact manifested as the upward jump of one point corresponding to the moment the film–substrate junction is removed, i.e., the point at which the concentration n_j reaches the value n_i since with further increase of V the dependence $C(V)$ defined by (8) and (9) very rapidly falls to zero by virtue of the smallness of n_i. Calculation shows that for typical values of the parameter of the film–substrate structure the width of this drop is of the order of 10^{-4} V.

Summing up the results of our theoretical analysis, we note two main features of the high-frequency barrier capacitance of the structure in question—1) the falloff of the capacitance to zero, due to the absence of any reaction of the junction's negative charge to the variable voltage, and 2) the jump in the capacitance due to the complete removal of the junction followed by a more or less rapid falloff to zero by virtue of the propagation of the space charge region into the depth of the lightly doped substrate. Here the width of the jump is connected mainly with the relation between n_1 and n_i and for $n_1<n_i$ it is so small that an experimental recording of the capacitance jump upon removal of the film–substrate junction is nearly impossible. However, real substrates actually satisfy such a relation between n_1 and n_i, since the compensating impurity here is either chromium or structural defects, both yielding the $EL2$ level, whose depth in each case lies in the range $0.5-0.6$ eV, which even for $n_i\simeq10^9$ cm^{-3} ensures the inequality $n_1<n_i$. Therefore, experimental curves, a typical example of which is shown in Fig. 2, are completely smooth. It is clear from the graph that the behavior of the experimental curve is similar to the calculated dependence (Fig. 1a) with the one exception that as V grows, the experimental curve does not fall to zero, but rather to some constant value. Here it is worth recalling that the above calculation pertains only to the barrier capacitance which is controlled by the space charge in the semiconductor and which naturally does not include the geometrical interelectrode capacitance, the elimination of which from the measurement results can be a nontrivial task and is nearly impossible when using sputtered contacts of complex shape. The $C-V$ dependences which are measured were made specifically in such a situation. Consequently, the constant to which the curve in Fig. 2 falls is the interelectrode capacitance of the sputtered contacts, which, as can be seen from the graph, is comparable to the barrier capacitance.

The determination of the interelectrode capacitance is necessary if we are to obtain the correct results from our $C-V$ measurements and all the more so if the results of these measurements are to be used to determine the impurity profile. It follows from the foregoing arguments that such a determination may be based on a measurement of the saturation value of the high-frequency dependence $C(V)$.

In conclusion we note that the zero level of variation of bound charge, which determines the zero value of the capacitance for deep linking is in no way connected with the nature of the doping of the film. Hence it follows that the drop of the high-frequency capacitance to zero, which we have established within the framework of the assumption of a constant impurity profile, is invariant with respect to the level and nature of the impurity profile of the film.

This work was carried out within the framework of the project ''Development of new methods for measuring electrical parameters of thin-film structures of III–V compounds,'' financed by the Ukraine State Committee on Science and Technology.

[1] S. A. Kostylev, E. F. Prokhorov, and A. T. Ukolov, *Current Transport Phenomena in Thin-Film Gallium-Arsenide Structures* [in Russian], Naukova Dumka, Kiev, 1990.
[2] N. B. Gorev, S. A. Kostylev, T. V. Makarova, E. F. Prokhorov, and A. T. Ukolov, Fiz. Tekh. Poluprovodn. **23**, 357 (1989) [Sov. Phys. Semicond. **23**, 220 (1989)].
[3] N. B. Gorev, T. V. Makarova, S. A. Kostylev, E. F. Prokhorov, and A. T. Ukolov, Fiz. Tekh. Poluprovodn. **26**, 861 (1992) [Sov. Phys. Semicond. **26**, 485 (1992)].

Translated by Paul F. Schippnick

Electrical properties of ZnSe/GaAs (100) heterostructures grown by photostimulated vapor-phase epitaxy

A. V. Kovalenko

Dnepropetrovsk State University, 320625 Dnepropetrovsk, Ukraine
(Submitted March 10, 1995; accepted for publication February 2, 1996)
Fiz. Tekh. Poluprovodn. **31**, 11–14 (January 1997)

Epitaxial layers of ZnSe were grown on GaAs (100) by photostimulated vapor-phase epitaxy, using a He–Cd laser (power $P \simeq 1$ mW/cm^2, $h\nu = 2.807$ eV) at a substrate temperature of $T =$ (175–300) K. The temperature dependences of the mobility of the majority charge carriers were studied in layers doped during growth, using such sources as $AlCl_3$, Zn, Al, and Ga. Based on an analysis of the thermally stimulated current and thermally stimulated depolarization curves, parameters were established for seven deep local levels that have a substantial effect on the electrical characteristics of the heterostructures. © *1997 American Institute of Physics.* [S1063-7826(97)01912-6]

The identical crystal structure and the closeness of the lattice parameters of the compounds ZnSe and GaAs make this pair of semiconductors nearly ideal for creating heterostructures, which have already become widely used in practice as photodetectors and solar cells.[1,2] Further improvement of the characteristics of devices based on ZnSe/GaAs heterostructures involves searching for a cheap and efficient technology that, on one hand, must provide economical mass production and, on the other hand, must satisfy the highest requirements on their quality.

An analysis of the results of studies of ZnSe/GaAs heterostructures obtained by high-temperature liquid-phase epitaxy of GaAs on a ZnSe substrate, the deposition of ZnSe on a GaAs substrate in a closed volume at $T = (750–800)\,^\circ$C, and the deposition of ZnSe from metallo-organic compounds at $T = 450^\circ$ and above, described in Ref. 3, showed that high-temperature techniques for obtaining heterostructures cause blurring of the layer–substrate boundary as a result of diffusion processes and the formation of the transitional compounds $Ga_2Se_3 \cdot 9ZnSe$ and $(ZnSe)_x(GaAs)_{1-x}$, where x depends on the deposition conditions. These data show that the electrical characteristics of heterostructures strongly depend on the transition-layer thickness, which in turn increases with increasing deposition temperature.

In Ref. 2, ZnSe/GaAs heterostructures were also obtained by depositing ZnSe on GaAs from metallo-organic compounds at even lower substrate temperatures, $T = (350–400)\,^\circ$C. However, a transition layer (0.1–0.2) μm thick with a high level of Ga doping was observed on the interface even in this case. This can be caused by diffusion of Ga from the substrate during growth and by the transfer of Ga by alkyl radicals formed during the decomposition of diethylzinc at the initial stages of film growth.

Substantial success in improving the quality of ZnSe/GaAs heterostructures has been achieved by such techniques as molecular-beam epitaxy (MBE), vapor-phase epitaxy from metallo-organic compounds (MOCVD), and atomic-layer epitaxy (ALE).[3–6] Because of the high purity of the materials used, the reliable system for monitoring the structure and chemical composition of the epitaxial layer, and the low temperature of the GaAs substrate ($T = 150–210\,^\circ$C (Ref. 4), $T = 320\,^\circ$C (Ref. 5) and $T = 300\,^\circ$C, Ref. 6), not only were high-quality single-crystal ZnSe layers,[3] but also spatially quantized structures of the single-quantum-well[4] and superlattice types,[5,6] for which the presence of a sharp layer–substrate interface is a fundamental condition.

The low-temperature technology of photostimulated vapor-phase epitaxy (PSVPE) is a particularly promising technology.[7–9] PSVPE is substantially less expensive than the MBE, MOCVD, and ALE technologies. However, it also makes it possible to obtain high-quality, single-crystal ZnSe films on GaAs without transition layers and with optical characteristics that are not inferior to similar layers grown by MBE.[7] The high potential of this technology is also shown by the fact that we were able to use it to synthesize spatially quantized structures of the single-quantum-well and superlattice types.[8] The low substrate temperature $T = (175–300)\,^\circ$C provided by forced-water cooling of the growth zone, combined with the high migration capability of the adsorbed atoms on the surface caused by weakening of the ionic bond due to perturbation of the sp^3 configuration of the atoms by resonance excitation of the growing ZnSe layer by He–Cd laser radiation (power $P \simeq 1$ mW/cm^2, $h\nu = 2.807$ eV), made it possible to obtain single-crystal, mirror-smooth ZnSe films. Their optical characteristics are considered in detail in Ref. 9, while the optimal technological growth parameters are evaluated in Refs. 10 and 11.

The reactor design and the growth technique of the ZnSe film using PSVPE make it possible to obtain an entire variety of ZnSe(n, p)/GaAs(n, p) heterostructures. Since the GaAs substrates, which are used with a (100) orientation, can be either n or p type, the control of the electrical characteristics of the epitaxial layer is an essential factor in this case. The standard growth technology[10,11] makes it possible to obtain single-crystal, n-type epitaxial layers. Their electrical characteristics, measured by the Van der Pauw method, indicated low resistivity [$\rho = (0.5–10^2)\ \Omega \cdot$cm], high concentration [$n = (10^{15}–10^{18})$ cm^{-3}], and relatively high mobility [$\mu = (110–130)$ cm^2/(V·s)] of the majority charge carriers, which is characteristic of high-quality ZnSe single crystals. The n-type conductivity is stabilized when the ZnSe films

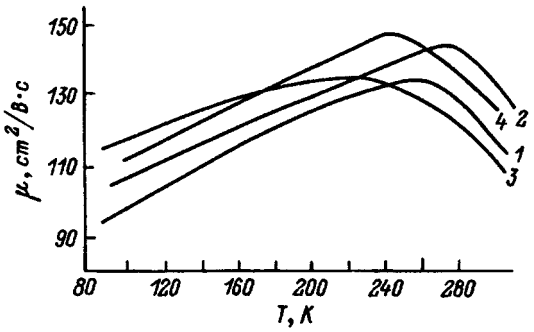

FIG. 1. Temperature dependences of the mobility of the majority charge carriers in ZnSe films on GaAs substrate with (100) orientation, doped during growth using $AlCl_3$ (*1*), Zn (*2*), Al (*3*), and Ga (*4*) sources.

are grown under a superpressure of Zn vapor, as well as when the film is doped during growth with impurities from such sources as Al, $AlCl_3$, and Ga. The temperature dependences of the charge-carrier mobility in such samples have a similar form, passing in the temperature region $T=210-280$ K through a distinct maximum (Fig. 1) caused by redistribution of the scattering mechanisms. In the high-temperature region we have $\mu \propto T^{-3/2}$, which is evidence that lattice scattering of the charge carriers predominates. Charge-carrier scattering at impurity centers, with $\mu \propto T^{3/2}$, predominates at low temperatures. This type of scattering imposes a limit on the mobility near the extremum, equal to $\mu=(130-150)$ cm^2/(V·s). The *n*-type ZnSe films were characterized by a high majority charge-carrier concentration [$n \simeq (10^{17}-10^{19})$ cm^{-3}] and low resistivity ($\rho \sim 5 \times 10^{-3}$ Ω·cm) of the epitaxial layer. The latter is extremely important for reducing the total series resistance of heterostructures used as solar cells. For all kinds of *n*-type samples, the ionization energy of the shallow donor levels was between 10 and 23 meV.

Growing epitaxial ZnSe films with a superpressure of Se increases their resistivity [$\rho \sim (10^9-10^{12})$ Ω·cm] and reduces the mobility and charge-carrier concentration. Changing the stoichiometry of the ZnSe film toward a Se excess can invert the conductivity type. We observed a similar effect on bulk crystals of ZnSe.[12] The *p*-type conductivity of an epitaxial ZnSe layer is also caused by doping the layer during growth with such an acceptor impurity as Li. We obtained control data concerning the introduction of acceptor and donor impurities into a crystal lattice by analyzing data on the nature of the photoluminescence bands of a ZnSe film.[9]

To obtain information on deep charge-carrier trapping levels in the ZnSe/GaAs heterostructure, we analyzed thermally stimulated current (TSC) curves (Fig. 2) and thermally stimulated depolarization (TSD) curves (Fig. 3). The studies were carried out on heterostructures with an epitaxial layer 1 μm thick, a substrate 300 μm thick, and a sample area of 10×10 mm. Platinum electrodes were deposited by cathode sputtering. First a sample at $T=300$ K was placed in an external polarizing electric field with a voltage of $U=100$ V for 3 min, creating a spatially inhomogeneous charge-carrier distribution (Maxwell–Wagner polarization). To increase the

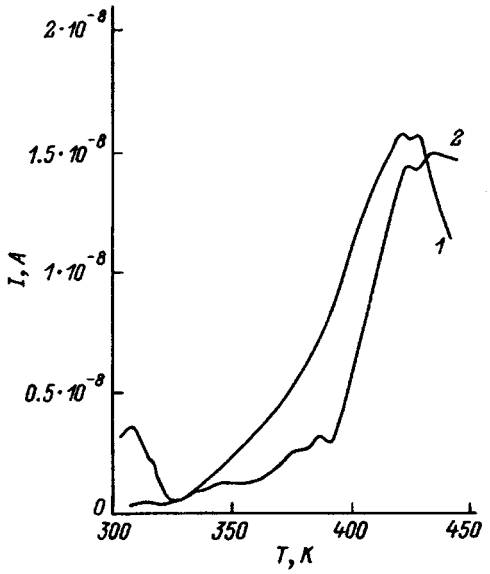

FIG. 2. TSC spectra for a ZnSe/GaAs heterostructure with (100) orientation, measured at different heating rates, deg/min: *1*—2.7, *2*—1.05.

degree of filling of the local centers, the heterostructure was illuminated during this period with light having a wavelength of $\lambda=0.66$ μm. After the electric field is removed, a metastable state is established in the sample. Subsequent heating of the short-circuited sample was accompanied by the appearance of TSC in the external circuit.[13] The TSC curves for an extracting field of $U=1$ V, measured at different heating rates (Fig. 2), indicate that several local centers are present. The thermogram recorded at a high heating rate lies in the region of large currents, and four extrema in all can be distinguished on it. At a lower heating rate, the TSC curve shifts toward lower currents, but at least six extrema can be distinguished on it. In the TSC method, the charge carriers migrate in a constant external electric field, which substantially reduces the sensitivity. In contrast with the TSC

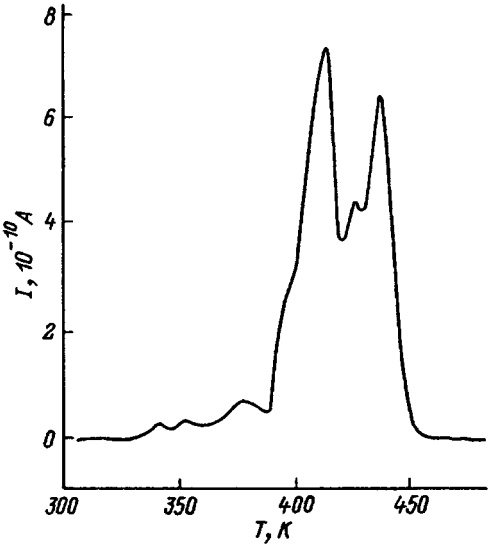

FIG. 3. TSD spectra for a ZnSe/GaAs heterostructure with (100) orientation.

TABLE I. Parameters of the individual Gaussian bands in the TSD spectrum of ZnSe/GaAs heterostructures with (100) orientation and the characteristics of the corresponding local centers.

No.	I_{max}, A	T_{max}, K	ΔE, eV	Q, C	N, cm^{-3}
1	2.79×10^{-11}	342	0.30	1.49×10^{-9}	9.34×10^{13}
2	3.43×10^{-11}	353	0.41	2.16×10^{-9}	1.35×10^{14}
3	7.07×10^{-11}	378	0.65	7.63×10^{-9}	4.76×10^{14}
4	1.51×10^{-10}	396	0.68	1.75×10^{-8}	1.09×10^{15}
5	6.52×10^{-10}	410	0.70	6.81×10^{-8}	4.25×10^{15}
6	3.04×10^{-10}	425	0.73	1.99×10^{-8}	1.24×10^{15}
7	5.71×10^{-10}	435	0.75	4.51×10^{-8}	2.81×10^{15}

method, the charge carriers during TSD migrate in an interior electric field that self-consistently varies during heating of the sample. All these factors increase the resolution, and seven extrema can be reliably distinguished on the TSD curve (Fig. 3). The method developed in Ref. 14 for analyzing the increments of the function $I=f(T)$ was used for processing the TSD curve. This provides the exact number of the individual bands and an approximate estimate of such parameters of the center as the activation energy ΔE of a local center, the total charge Q liberated from a local center during heating of the sample, and the concentration N of the centers. The TSD curve was mathematically processed on the assumption that the elementary extremum is described by a Gaussian contour. The activation energy was estimated by the initial-rise method (the Garlic–Gibson method). The main characteristics of the individual bands of the Gaussian spectra (I_{max} is the current in the region of an extremum of the TSD spectrum, and T_{max} is the temperature at which the extremum is observed in the TSD spectrum) and the corresponding parameters of the local centers (ΔE, Q, N) are shown in Table I.

It is quite difficult to determine the spatial localization of the identified centers, which can lie in the ZnSe and GaAs layers, as well as directly at the phase boundary. Comparison of the results with the data of Ref. 12, where the parameters of local centers in bulk ZnSe crystals were established, shows that the centers numbered 1, 2, and 7 in the table occur in the ZnSe layer.

I wish to thank A. Yu. Mekekechko and G. V. Snezhnyĭ for help in this study and for useful discussions.

[1] G. G. Devyatykh, B. V. Zhuk, A. A. Zlenko, A. M. Prokhorov, V. K. Khamylov, and G. P. Shipulo, Pis'ma Zh. Tekh. Fiz. **10**, 118 (1984) [Sov. Tech. Phys. Lett. **10**, 49 (1984)].
[2] B. V. Zhuk, I. A. Zhukov, and A. A. Zlenko, Fiz. Tekh. Poluprovodn. **19**, 1405 (1985) [Sov. Phys. Semicond. **19**, 864 (1985)].
[3] J. Gutowski, N. Presser, and G. Kudlek, Phys. Status Solidi A **120**, 11 (1990).
[4] T. Yao, M. Fujimoto, S. Chang, and H. Tanino, J. Crystal Growth **111**, 823 (1991).
[5] A. Shen, J. Cui, Y. Chen, and H. Wang, J. Crystal Growth **111**, 807 (1991).
[6] Y. Kawakami, T. Taguchi, and A. Hiraki, J. Crystal Growth **89**, 331 (1988).
[7] A. V. Kovalenko, A. Yu. Mekekechko, N. V. Bondar', V. V. Tishchenko, Yu. M. Shekochikhin, S. M. Rumyantseva, and I. S. Malashenko, Fiz. Tekh. Poluprovodn. **26**, 1251 (1992) [Sov. Phys. Semicond. **26**, 698 (1992)].
[8] M. S. Brodin, N. V. Bondar', A. V. Kovalenko, A. Yu. Mekekechko, and V. V. Tishchenko, Kvant. Elektron. (Moscow) **20**, 619 (1993) [Quantum Electron. **23**, 537 (1993)].
[9] A. V. Kovalenko, A. Yu. Mekekechko, V. V. Tishchenko, and N. V. Bondar', Fiz. Tverd. Tela (St. Petersburg) **36**, 1350 (1994) [Phys. Solid State **36**, 737 (1994)].
[10] A. V. Kovalenko and R. Lilleĭ, Neorg. Mater. **28**, 49 (1992).
[11] N. V. Bondar', A. V. Kovalenko, V. V. Tishchenko, and A. Yu. Mekekechko, Neorg. Mater. **27**, 2520 (1991).
[12] A. V. Kovalenko and N. D. Borisenko, Fiz. Tekh. Poluprovodn. **28**, 646 (1994) [Semiconductors **28**, 387 (1994)].
[13] Yu. A. Gorokhovatskiĭ, *Principles of Thermal Depolarization Analysis* (Nauka, Moscow, 1981).
[14] D. N. Glebovskiĭ, A. I. Krashenninikov, M. E. Berdina, and P. I. Zelikhman, Zh. Prikl. Spektrosk. **3**, 25 (1983).

Translated by W. J. Manthey

Quasiballistic model of current transport and formation of the *S*-type current–voltage characteristic in the lightly doped, double-barrier heterostructure $Al_xGa_{1-x}As$–GaAs–AlAs

A. M. Belyantsev and Yu. Yu. Romanova

Institute of the Physics of Microstructures, Russian Academy of Sciences, Nizhniĭ Novgorod, Russia
(Submitted March 6, 1996; accepted for publication April 4, 1996)
Fiz. Tekh. Poluprovodn. **31**, 100–103 (January 1997)

The quasiballistic model of current-carrier transport in the lightly doped, double-barrier heterostructure $Al_xGa_{1-x}As$–GaAs–AlAs is considered. Electron scattering into the *X*-valley in the GaAs layer, nonspecular electron reflection from the AlAs layer, and energy quantization in the pre-barrier region are all taken into account. The possibility of an S-shaped current–voltage characteristic in lightly doped, double-barrier heterostructures in the absence of electron–electron collision is demonstrated for a comparatively wide AlAs barrier.
 [S1063-7826(97)02201-1]

In the quasiballistic approximation of the motion of electrons in a lightly doped ($n<10^{15}$ cm^{-3}) GaAs layer Belyantsev *et al.*[1] showed that the current–voltage characteristic of the single-barrier heterostructure *n*-GaAs–*i*-$Al_{0.25}Ga_{0.75}As$ can be multivalued, and that the structure can possess a *S*-type negative differential conductivity (NDC) in the absence of electron–electron collisions. In their calculations they assumed that the barrier is thin and that for the electrons of all GaAs valleys it has a high tunneling transparency. The mechanism for the appearance of *S*-type NDC in such a structure owes its existence to changes in the lifetime of the electrons at the quantum-well level in the near-barrier region that accompany variation of the field in that region. As the barrier width (more than 100 Å) increases, this mechanism for the appearance of NDC in the considered heterostructure model becomes inefficient.[1] Higman *et al.*[2] have experimentally observed *S*-type NDC in a double-layer heterostructure with a wide AlAs barrier (on the order of 1000 Å) and lightly doped well (*n*-GaAs, $n<10^{15}$ cm^{-3}). They assumed that the transition of the system to the unstable state is connected with intervalley scattering, with the transition of the electrons from the Γ-valley to the *X*-valley of GaAs, from which they freely penetrate the AlAs barrier. The I–V characteristics of lightly doped, single- and double-barrier heterostructures with wide AlAs barriers and the possibility for the appearance of *S*-type NDC as a result of intervalley transitions were investigated by Belyantsev and Romanova[3] by the Monte Carlo method.

In what follows we assume a simple quasiballistic model of current transport in the lightly doped, double-barrier heterostructure $Al_xGa_{1-x}As$–GaAs–AlAs (see Fig. 1, inset), in which intervalley electron scattering is dominant. In contrast to Ref. 3, we allow for energy quantization in the near-barrier region. As was shown by Heiblum,[4] the mean free path of electrons in GaAs, injected with energies in the range 0.2–0.25 eV is on the order of 800−1000 Å. Therefore, in the structure under consideration for the cathode barrier height Δ_1 of the order of 0.2 eV and the width of the potential well (GaAs layer) less than 800 Å (see Fig. 1, inset) the motion of the cathode-barrier injected electrons in the GaAs potential well in weak fields is quasiballistic.

Clearly, the presence of a high and wide second barrier (the AlAs layer) hinders the passage of the injected electrons through the structure. Only some of the Γ-electrons will tunnel through the AlAs barrier, the specularly reflected electrons emerge from the potential well, and the diffusely scattered electrons pile up in front of the AlAs barrier. As the voltage on the structure is increased, the number of near-barrier electrons increases and energy quantization takes place in a narrow near-barrier region. In strong fields, when the voltage drop across the GaAs layer is of the order of 0.3 eV ($\varphi_3 \simeq \Delta_{\Gamma X} - \Delta_1$), the injected Γ-electrons are scattered into the *X* and *L* valleys. Since the *X* valley of AlAs lies below the *X* valley of GaAs, the *X* electrons from the GaAs layer pass through the AlAs barrier ''unhindered.'' The current through this structure correspondingly grows. The influx of electrons into the near-barrier region decreases while tunneling from the quantum-well level and tunneling of the free electrons are conserved and the voltage distribution over the structure changes. A decrease of the current takes place again at lower voltages on the heterostructure and is attributable mainly to the disappearance of electron flux above the AlAs barrier, to the accumulation of charge at the quantum-well level, and to a corresponding reversed voltage redistribution.

All these qualitative factors are taken into account in the proposed model of current transport in a double-barrier heterostructure. In the latter, however, we use the following approximations: in the calculation of the redistribution of the potential in the well we disregard the charge of the electrons ''captured'' by the well, with the exception of the quantum-well region, which is completely justified in the case of a lightly doped potential well ($n_0 \simeq 10^{15}$ cm^{-3}). Of all the scattering mechanisms we allow only for intervalley Γ–*X*-scattering, which tentatively drifts into the near-barrier region, quantum-well level is calculated in the triangular-well approximation, the probability of electron capture to a quantum-well level is determined by introducing a nonspecularity coefficient of the rectangular AlAs barrier. Note that the assumption of localization of Γ–*X*-scattering in a narrow near-barrier region allows us to take the traversal by the elec-

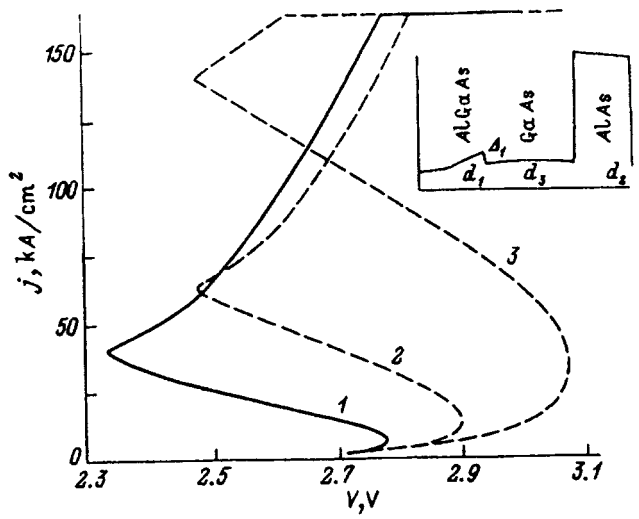

FIG. 1. Current–voltage characteristic of a double-barrier heterostructure (the potential well is shown in the inset) for different potential barrier heights Δ_1, eV: *1*) 0.2, *2*) 0.18, *3*) 0.15. Structure parameters: $n_0^+=10^{18}$ cm^{-3}, $n_0=10^{15}$ cm^{-3}, $\Delta_2=0.86$ eV, $d_1=200$ Å, $d_2=300$ Å, $d_3=500$ Å.

trons of most of the well to be ballistic. Obviously, transitions to the L valley can be disregarded in the calculations because of the smaller intervalley scattering coefficient ($\Xi_{\Gamma X}\simeq 0.5\times 10^9$ eV·s, $\Xi_{\Gamma L}\simeq 0.18\times 10^9$ eV·s; Ref. 5) and because of the smaller contribution from the L-valley electrons (in comparison with the X electrons) to the current through the AlAs barrier (for the latter it is transparent).

Γ–X scattering leads to a change in the concentration of the free electrons since the X electrons are substantially slower than the Γ electrons. Let us estimate the change in the potential $\varphi_{(1)}$ which occurs as a result of this circumstance, working from the linearized Poisson equation:

$$\varphi''_{(1)}+a(x)\varphi_{(1)}=e_0 n_x(x)/\varepsilon\varepsilon_0,$$

where

$$a(x)=\frac{j}{2\varepsilon\varepsilon_0}\sqrt{\frac{m^*}{2}}\,\frac{e_0}{(\Delta_1+e_0\varphi(x))^{1.5}},$$

$\varphi(x)$ is the potential in the absence of Γ–X scattering, ε is the dielectric constant of the GaAs lattice, $\varepsilon_0=8.85\times 10^{-12}$ F/m, m^* is the effective mass of the Γ-valley electrons, e_0 is the elementary charge of the electron, and n_x is the X-electron concentration. The characteristic scale of variation of $\varphi_{(1)}$ is

$$\lambda^{-1}=a(x)^{-1/2}. \tag{1}$$

At scales less than this value, localization of Γ–X scattering in the near-barrier region is justified. As will be shown below, this condition can easily be satisfied in real structures.

Given the above assumptions, the potential distribution $\varphi(x)$ in the GaAs layer outside the near-barrier region can be found from the Poisson equation in which the charge density is defined in terms of the current j^* and velocity of the electrons in the heterostructure potential well:

$$\frac{d^2\varphi}{dx^2}=\frac{j^*}{v(x)\varepsilon\varepsilon_0}=\frac{j^*}{\varepsilon\varepsilon_0}\sqrt{\frac{m^*}{2[\Delta_1+e_0\varphi(x)]}}. \tag{2}$$

Here $j^*=j_+ + j_-$ is the sum of the forward and reverse currents, which defines the electron density at that point $[n(x)=j^*/e_0 v(x)]$. The total current j is equal to the difference of the forward and reverse currents, $j=j_+-j_-$.

Equation (2) for the boundary conditions $\varphi(0)=0$, $\partial\varphi(0)/\partial x=E(0)=E_1$ (E_1 is the field strength at the first heterostructure barrier) is integrable and allows us to find the relation between the total current j and the field E_1. This relation is given implicitly by the equation

$$[2(y+2)-z][z+4(y-1)]^{0.5}-(z-6)z^{0.5}=6\sqrt{\frac{j}{j_0}}\,\frac{x_3}{x_0}. \tag{3}$$

Here $x_0^2=\varepsilon_0\varepsilon kT/e_0^2 n_0$, $j_0=e_0 n_0 v_\Delta$, $v_\Delta=\sqrt{2\Delta_1/m^*}$, $y=\sqrt{1+e\varphi(x_3)/\Delta_1}$, $z=(E_1^2 j_0)/(E_0^2 j^*)$, $E_0=\Delta_1/(e_0 x_0)$, x_3 is the boundary of the quantum-well region ($x_3\cong d_3$), j_+ is the forward thermal-emission current that flows through the first barrier:

$$j_+=e_0 n^+\,\exp\left(-\frac{\Delta_1+e_0E_1d_1}{kT}\right). \tag{4}$$

The total voltage on the heterostructure is

$$V=-E_1d_1-E_2d_2+V_3+W_0/e_0. \tag{5}$$

Here $V_3=\varphi(x_3)$, W_0 is the energy of the quantum-well level, and E_2 is the field strength at the second barrier. The field strength E_2 is given in terms of the charge density in the two-dimensional layer n_s and the field to the left of the two-dimensional layer E_3:

$$E_2=E_3-\frac{e_0 n_s}{\varepsilon\varepsilon_0}, \tag{6}$$

$$E_3=\frac{\partial\varphi(x_3)}{\partial x}=-\sqrt{E_1^2+4j\,\frac{E_0^2}{j_0}\left(\sqrt{1+\frac{e_0\varphi(x_3)}{\Delta_1}}-1\right)} \tag{7}$$

The energy of the quantum-well level W_0 is calculated in the triangular-well approximation[6]

$$W_0=\lambda_1\left(\frac{h^2}{2m^*}\right)^{1/3}\left(\frac{e_0^2 n_s}{2\varepsilon\varepsilon_0}\right)^{2/3}, \tag{8}$$

where $\lambda_1=2.34$ is the first node of the Airy function.

To find the total current through the structure, Eq. (3) must be supplemented by the equation of continuity for the near-barrier region, which we write in the form

$$j_+(x_3)=j_{2D}+j_{\rm tun}+j_-(x_3). \tag{9}$$

The quantity on the left side of Eq. (9) is the flow of Γ electrons into the near-barrier region (in which we have allowed for transitions of the electrons into the X valley)[1)]

$$j_+(x_3)=j_+\left[1-\exp\left(-\frac{x_3-x^*}{l_{\rm int}}\right)\right]. \tag{10}$$

The quantity j_{2D} on the right side of Eq. (9) is the current from the quantum-well level, which is assigned as in Ref. 8:

$$j_{2D}=e_0 n_3 \frac{W_0}{h} D(W_0), \tag{11}$$

where

$$D(W)=\exp\left\{-\frac{\sqrt{2m}^*(\Delta_2-W)^{3/2}}{3he_0|E_2|}\right\}$$

is the probability that an electron will traverse the second barrier of height Δ_2; j_{tun} is the tunneling current

$$j_{\text{tun}}=j_+(x_3)D(\Delta_1+e_0V_3), \tag{12}$$

and $j_-(x_3)$ is the current of the Γ-electrons reflected from the AlAs barrier:

$$j_-x_3=\alpha[j_+(x_3)-j_{\text{tun}}]. \tag{13}$$

Here $\alpha<1$ is the nonspecularity coefficient. The simultaneous solution of system of equations (3)–(13) allows us to find the I–V characteristic of the double-barrier heterostructure.

We have considered a heterostructure with a triangular cathode barrier with height on the order of 0.2 eV ($\Delta_1\simeq 0.15-0.2$ eV), width of the second barrier of rectangular shape on the order of 300 Å, and electron density in the potential well (GaAs layer of width on the order of 500 Å) not exceeding 10^{15} cm^{-3}. The large height of the first barrier affords the electrons flying into the potential well a high initial energy (on the order of 0.2 eV), which increases rapidly under the action of the electric field. Let us estimate the transit time of the above-barrier electrons:

$$\Delta t\cong\int_0^{d_3} v\,dx=\int_0^{d_3}\sqrt{\frac{m^*}{2[\Delta_1+e_0\varphi(x)]}}\,dx<5\times10^{-12}\ S.$$

Here d_3 is the width of the well. This time is comparable to the times of the intervalley transitions which predominate at the given energies, which allows us to use the quasiballistic approximation. The characteristic scale of variation of the correction to the potential $\varphi_{(1)}$ for the chosen parameters is of the order of 10^{-6} m [Eq. (1)], which is much greater than the width of the well $\sim 5\times10^{-8}$ m. The, localization of Γ–X scattering in the near-barrier region is therefore justifiable.

The current–voltage characteristics, calculated for the case $\alpha=0.5$, $l_{\text{int}}=500$ Å for three values of the height of the first barrier Δ_1, are shown in Fig. 1. As can be seen, the current densities of the currents flowing through the structure exceed 2×10^4 A/cm^2; i.e., for velocities on the order of 10^8 cm/s the concentration of the free electrons is greater than 2×10^{15} cm^{-3} and exceeds the equilibrium electron density in the well. Consequently, ignoring the equilibrium electron density in the Poisson equation is also justifiable. The I–V characteristic of the double-barrier heterostructure has an S-shape, i.e., the negative differential conductivity (NDC) in it, in contrast to the single-barrier heterostructure,[1] can exist even when the AlAs barrier is relatively wide ($d_2=300$ Å). However, the voltage which activates the flow of current at which the transition from the high to the low-resistivity branch of the I–V characteristic begins depends weakly on the probability of the intervalley transitions. A formal increase in the probability of intervalley scattering (a fivefold decrease in l_{int}) has hardly any effect on the magnitude of the current ''switch-on'' voltage. This is obviously due to the exclusion from the given model of all scattering mechanisms except the intervalley scattering mechanism with a corresponding ''exaggeration'' of the tunneling current of the Γ electrons in the AlAs barrier in high fields. Note that as the height of the first barrier is increased, the ''switch-on'' voltage and the maximum current on the high-resistivity branch of the I–V characteristic decrease. The upper branch of the I–V characteristic of the two-barrier heterostructure, as in the Monte Carlo calculations,[3] is governed to a greater extent by the above-barrier Γ electrons. At the same time, the X electrons play the leading role in the formation of the unstable branch. The contribution from the quantum-well level to the current turns out to be insignificant, although taking it into account alters the potential distribution.

We note in conclusion that the above-considered simple mathematical model of a double-barrier heterostructure with a lightly doped GaAs layer can be used to relatively easy to estimate the effect of the main parameters of the heterostructure on the appearance of S-type negative differential conductivity in it.

This work was carried out with the financial support of the MNTP [Ministry for Scientific and Technological Problems] (Project No. 1-030) and the International Scientific Fund (Project No. N0L000).

[1)] It is natural to write the probability of Γ–X scattering, allowing for the variation in the distance at which it may take place, in the simple form $P\sim\exp[-(d_3-x^*)/l_{\text{int}}]$, where x^* is the value of the x coordinate at which the potential φ_{x^*} is equal to $(\Delta_{\Gamma X}-\Delta_1)/e_0$, where $\Delta_{\Gamma X}$ is the energy gap between the Γ and X valleys and $l_{\text{int}}\geqslant 500$ Å is the mean free path for the intervalley transitions.[7]

[1] A. M. Belyantsev, E. V. Demidov, and Yu. A. Romanov, Lith. J. Phys. **32**, 31 (1992).
[2] T. K. Higman, L. M. Miller *et al.*, Appl. Phys. Lett. **53**, 1623 (1988).
[3] A. M. Belyantsev and Yu. Yu. Romanova, Fiz. Tekh. Poluprovodn. **29**, 1498 (1995) [Semiconductors **29**, 781 (1995)].
[4] M. Heiblum, Solid–State Electron. **31**, 617 (1988).
[5] A. Mitskyavichus and A. Reklaıtis, Fiz. Tekh. Poluprovodn. **20**, 1693 (1986) [Sov. Phys. Semicond. **20**, 1060 (1986)].
[6] T. Ando, A. Fowler, and F. Stern, Rev. Mod. Phys. **54**, 437 (1982).
[7] W. Fawcett, A. D. Broadman, and S. Swain, J. Phys. Chem. Solids **34**, 1963 (1970).
[8] A. Wacker and E. Scholl, Appl. Phys. Lett. **59**, 1702 (1991).

Translated by Paul F. Schippnick

Thermal stability of vertically coupled InAs–GaAs quantum dot arrays

A. E. Zhukov, A. Yu. Egorov, A. R. Kovsh, V. M. Ustinov, M. V. Maksimov, A. F. Tsatsul'nikov, N. N. Ledentsov, N. Yu. Gordeev, S. V. Zaĭtsev, P. S. Kop'ev, and Zh. I. Alferov

A. F. Ioffe Physicotechnical Institute, Russian Academy of Sciences, 194021 St. Petersburg, Russia

D. Bimberg

Institut für Festkörperphysik, Technische Universität Berlin, D-10623 Berlin, Germany
(Submitted March 22 1996; accepted for publication April 8 1996)
Fiz. Tekh. Poluprovodn. **31**, 104–108 (January 1997)

The effect of high-temperature annealing on the optical properties of vertically coupled InAs quantum dots in a GaAs matrix and on the performance of a quantum-dot laser are studied. A strong blue shift of the photoluminescence peak and lasing line, as well as changes in the photoluminescence intensity and temperature dependence of the threshold current density are observed. The reason for this behavior is probably a reduction in the carrier localization energy due to a partial mixing of the In and Ga atoms as well as an improvement in the quality of the low-temperature grown Ga(Al)As layers achieved by high-temperature annealing.
 [S1063-7826(97)02301-6]

Quantum dot arrays, formed in a matrix of wider-band material, are promising for use as the active region of injection lasers. Size quantization in all three directions leads to a modification of the density of states, which, as expected, affords a significant improvement in the device characteristics of semiconductor lasers. In particular, a lowering of the threshold current density and an increase in the characteristic temperature, which describes the temperature dependence of the current, have been predicted.[1]

The method we used to create quantum dot arrays is based on the decay of a highly strained layer of InAs, grown on a GaAs (100) surface, into coherent islands.

The properties of strained islands of (In,Ga)As can depend not only on the conditions under which the active region forms, but also on the growth regimes, first of all the temperature at which subsequent layers of the structure were deposited. In particular, Xie *et al.*[3] have shown that if the GaAs layer immediately covering the island array is grown at a temperature $\geqslant 530$ °C, practically complete disappearance of the ordered shape and size of the islands is observed. It was assumed that such behavior is due to strong mixing of the Ga and In atoms on the growing surface at enhanced temperatures. On the other hand, experiments on thermal annealing of strained InGaAs/(Al)GaAs quantum wells[4,5] indicate that such mixing may also be observed in an already completely grown structure which is subsequently subjected to high-temperature processing.

The importance of the thermal stability of these arrays is based, in particular, on the fact that an improvement in the degradation characteristics of injection lasers requires high growth temperatures for the regions that contain aluminum. In lasers with an active region based on strained InGaAs quantum wells, which have shown record-low threshold currents ($J_{th} < 1$ mA) for the formation of the emitter regions and gradient waveguides, a substrate temperature of 700 °C is used.[6] Besides, the low quality of the GaAs layer grown at low temperature in the immediate vicinity of the active region can lead to the appearance of additional nonradiative recombination channels. It was shown in Ref. 7 that deposition of the upper emitter and the gradient waveguide at 580 °C increases the laser threshold current density to 1 kA/cm^2 in comparison with 50 A/cm^2 for deposition at 700 °C.

We will investigate the thermal stability of InAs–GaAs quantum dot arrays and the effect of high-temperature growth on the characteristic features of injection lasers whose active regions are based on these arrays.

The investigated structures were grown by molecular beam epitaxy (MBE) on a Riber-32P setup. The active region was located in the center of a GaAs layer of thickness 200 nm, separated from the surface and the substrate by AlAs/GaAs superlattices with small spacing. The active region consists of an array of quantum dots, formed by deposition of three successive InAs monolayers separated by GaAs spacers of 5-nm thickness, with an effective thickness of 1.7 monolayers.

As was revealed by transmission electron microscopy, upon second deposition of InAs a new chain of islands is formed exactly above the tops of the islands of the previous layer.[8] When GaAs spacers are used to separate the series of dots, with thicknesses close to the height of the islands ($\lesssim 5$ nm), a new physical object is formed—an array of vertically coupled quantum dots (VCQD) characterized by a nonpyramidal shape and an increased height-to-base ratio in comparison with the case of a single series of dots. As we showed in Ref. 9, VCQD arrays, as a result of their increased optical limitation factor and carrier localization energy, allow an improvement in the characteristics of injection lasers with active regions based on quantum dots.

The substrate temperature was 485 °C during the deposition of the active region and the 10-nm-thick GaAs covering layer and 600 °C for the rest of the structure. At the end of the growth process, the wafer was separated into four parts, three of which were annealed in the MBE growth chamber in a stream of arsenic at a substrate temperature of 700 °C for 10, 30, and 60 min.

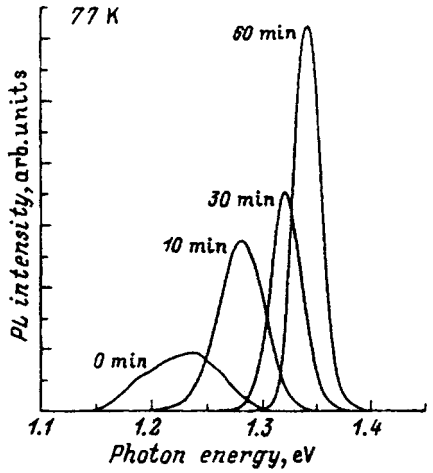

FIG. 1. Photoluminescence spectra of a structure containing a vertically coupled quantum-dot array at 77 K after annealing at 700 °C for durations as indicated.

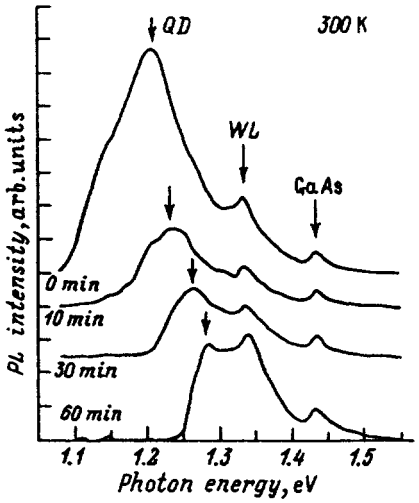

FIG. 2. Photoluminescence spectra at 300 K after annealing at 700 °C for durations as indicated. Arrows indicate lines due to carrier recombination at the quantum dots (QD) in the wetting layer (WL) and in the barrier (GaAs).

Photoluminescence spectra of the structure at 77 K after annealing are shown in Fig. 1 for the three annealing times and for no annealing. As is evident, high-temperature annealing leads to a regular shift of the photoluminescence maximum toward higher energies, a decrease in the width of the photoluminescence line, and an increase in its integrated intensity.

Different mechanisms may be responsible for the change in the transition energy achieved by high-temperature annealing.[5] First, the effective width of the band gap of the strained material decreases if annealing results in the formation of dislocations that remove the strain. Second, interdiffusion (mixing) of group-III atoms, which eliminates the initial sharpness of the heterostructures, leads to an increase in the transition energy.

The strong, short-wavelength shift of the photoluminescence line that we observed, which exceeds 100 meV after annealing for one hour, means that in the case of vertically coupled quantum dots the mechanism of mixing of Ga and In atoms predominates. The perduration of intense photoluminescence, in our opinion, proves the absence of plastic relaxation of strain. Moreover, an increase in the integrated photoluminescence intensity is observed probably as a result of curing of point defects, primarily in GaAs grown at low temperature. Such behavior was noted earlier in the case of fast thermal annealing of strained InGaAs quantum wells.[4]

As the observation temperature is increased, two additional shorter-wavelength peaks, which are associated with recombination in the GaAs barriers and through states in the so-called InAs ''wetting'' layer, appear in the photoluminescence spectra along with luminescence due to carriers localized in the quantum wells. Photoluminescence spectra recorded at 300 K are shown in Fig. 2. In contrast to the strong shift of the quantum dots photoluminescence line, the peak of the radiation from the wetting layer changes its spectral position hardly at all. Such behavior accords well with the expected weak effect of smearing of the quantum well profile on the weakly coupled states.

The strong, short-wavelength shift of the quantum dots photoluminescence line as a result of increasing the annealing time means that the localization energy of the carriers in the quantum wells decreases. Thus, the energy levels of the electrons (holes) in the quantum dots get closer to the corresponding levels in the wetting layer and closer to the edges of the GaAs bands. Consequently, as the observation temperature is increased, the relative population of states of the wetting layer and the GaAs barriers relative to the population of states of the quantum dots will increase faster in samples subjected to thermal annealing. As is shown in Fig. 3, an increase in the ratio of the intensity of the photoluminescence line of the wetting layer to the intensity of the photoluminescence line of the quantum dots ($I_{\mathrm{WL}}/I_{\mathrm{QD}}$) correlates well with a decrease in the energy difference between these two lines ($E_{\mathrm{PL}}^{\mathrm{WL}}-E_{\mathrm{PL}}^{\mathrm{QD}}$).

As we showed in Ref. 11, thermal ejection of carriers from the quantum dots is the main reason for the abrupt increase in the threshold current density of injection lasers at elevated observation temperatures. It can be assumed, therefore, that thermal annealing of vertically coupled quantum dots upon deposition of the injection-laser emitters at a substrate temperature of 700 °C will lead to a deterioration of the device characteristics due to a decrease in the localization energy of the carriers. On the other hand, an improvement in the quality of the low-temperature grown GaAs layers directly adjacent to the quantum dots and of the aluminum-containing layers may lead to the opposite effect.

We studied the effect of the deposition temperature of the emitter layers on the device characteristics of VCQD-based lasers. Heterolaser structures with separate limitation and gradient waveguide were grown. The active region was a VCQD array formed as described above. The substrate temperature, when growing the $Al_{0.4}Ga_{0.6}As$ emitter layers and $Al_xGa_{1-x}As$ waveguides ($x=0-0.4$), was 600 or 700 °C; these structures are denoted QD600 and QD700, respectively. The duration of deposition of the upper emitter layer in the QD700 structure was close to one hour. The contacts

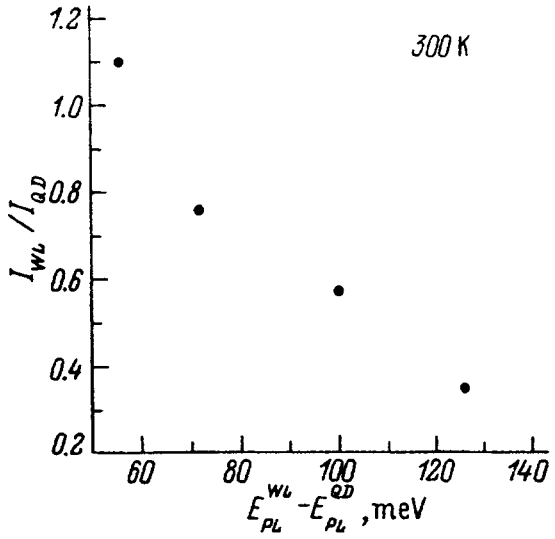

FIG. 3. Dependence of the ratio of the photoluminescence intensity of the wetting layer to the photoluminescence intensity of the quantum dots (I_{WL}/I_{QD}) on the energy difference between the positions of the photoluminescence lines of the wetting layer and the quantum dots ($E_{PL}^{WL}-E_{PL}^{QD}$).

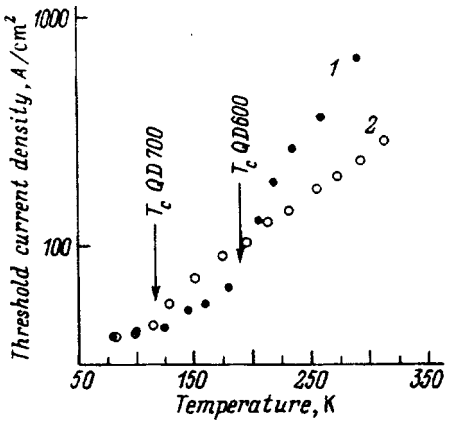

FIG. 4. Temperature dependence of the threshold current density J_{th} for (*1*) QD700 and (*2*) QD700 laser structures. The arrows indicate the critical temperature T_C corresponding to the onset of rapid increase of J_{th}.

to the laser diodes were formed by sputtering and fusing-in (450 °C) AuGe/Ni/Au and AuZn/Ni/Au metal layers to the n^+-GaAs substrate and p^+-GaAs contact layer, respectively. To reduce radiation losses, we chose as our objects of study lasers with four sheared faces. The measurements were carried out at temperatures in the range 77−300 K in the pulsed pump regime with a frequency of 5 kHz and a pulse duration of 100 ns.

Laser generation in a QD600 structure was observed at the wavelengths 996.7 and 1052.7 nm at 77 and 300 K, respectively. In the QD700 structure the laser line is strongly shifted toward shorter wavelengths and is located at 918.1 nm at 77 K and 950.0 nm at 300 K. The spectral position of the laser line over the entire investigated temperature range is close to the maximum of the observed photoluminescence line of the test structures discussed above: for the QD700 laser, the sample annealed at 700 °C, and for the QD600 laser, the unannealed sample.

The dependence of the threshold current density on the measurement temperature is plotted for both structures in Fig. 4. For the QD600 structure in the low-temperature region J_{th} is essentially constant and varies from 40 to 45 A/cm^2. The temperature dependence is characterized by the characteristic temperature $T_0=430$ K. The low temperature sensitivity of the threshold current density is a consequence of the zero-dimensional nature of the limitation of carriers in quantum dots. At temperatures above the critical temperature and equal to 180 K an abrupt increase in J_{th} is observed as a consequence of thermal ejection of scatterers from the quantum-dot states.

In the QD700 structure the values of J_{th} in the low-temperature region nearly coincide with the corresponding quantity measured in the QD600 structure. However, the critical temperature corresponding to the onset of the rapid increase of J_{th} is substantially lower and is equal to 120 K. We think the decrease in the critical temperature in the QD700 structure is a direct consequence of the decrease in the energy distance between the ground state of the quantum dots and the states in the wetting layer and barrier as a result of high-temperature annealing of VCQD's during the deposition of the upper emitter layer.

At 300 K the QD700 structure is characterized by a lower value of J_{th} in comparison with the QD600 structure (see Fig. 4). We think this is due to an improvement in the quality of the low-temperature grown GaAs layer immediately adjacent to the active region. At the same time, J_{th} is observed to coincide in both structures at 77 K. This means, as we see it, that an improvement in quality of the low-temperature grown GaAs layers and the Al-containing layers does not have a noticeable effect on the threshold current density when the nonradiative recombination rate in these layers is reduced by lowering the observation temperature.

In summary, we have investigated the effect of high-temperature annealing on the optical properties of vertically coupled InAs quantum-dot arrays in a GaAs matrix, and also the effect of the deposition temperature of the emitter layers on the device characteristics of an injection laser with a quantum-dot array based active medium. We have found that in structures subjected to annealing and also in an injection laser in the case where the upper emitter is deposited at 700 °C a strong, short-wavelength shift of the photoluminescence maximum and of the laser line is observed. Such behavior is apparently the result of a decrease of the localization energy of the carriers in the quantum dots resulting from partial mixing of the In and Ga atoms. Deposition of the upper emitter layer at 700 °C leads to a decrease of the onset temperature of the rapid increase of the threshold current density as a result of a decrease of the energy distance between the ground state of the quantum dots and the states in the wetting layer and the barrier. An improvement in the quality of the low-temperature grown GaAs layers and the Al-containing layers resulting from high-temperature annealing leads to a decrease of the threshold current density at room temperature, whereas in the low temperature region its effect on the device characteristics is insignificant.

This work was carried out with the support of the Russian Fund for Fundamental Research (Grant No. 96-02-17824) and the program INTAS (Project No. 94-1028).

[1] Y. Arakawa and H. Sakaki, Appl. Phys. Lett. **40**, 939 (1982); E. Kapon, M. Water, J. Christen, M. Grundmann, C. Caneau, D. M. Hwang, E. Colas, R. Bhat, G. H. Song, and D. Bimberg, Superlattices Microstruct. **12**, 491 (1992).
[2] D. Leonard, M. Krishnamrthy, C. M. Reaves, S. P. Den Baars, and P. M. Petroff, Appl. Phys. Lett. **63**, 3203 (1993); A. Yu. Egorov, A. E. Zhukov, P. S. Kop'ev, N. N. Ledentsov, M. V. Maksimov, and V. M. Ustinov, Fiz. Tekh. Poluprovodn. **28**, 1439 (1994) [Semiconductors **28**, 809 (1994)].
[3] Q. Xie, P. Chen, A. Kalburge, A. Nayfonov, T. R. Ramachandran, A. Konkar, and A. Madhukar, in *Proceedings of the Eighth International Conference on MBE* (Osaka, Japan, 1994), p. 383.
[4] K. Kaviano, J. Chen, K. Hu, L. Chen, and A. Madhukar, J. Vac. Sci. Technol. B **10**, 793 (1992).
[5] L. P. Sandwich, D. C. Streit, W. L. Jones, C. W. Kim, and R. J. Hwu, IEEE Trans. Electron Devices **ED-39**, 50 (1992).
[6] T. R. Chen, L. E. Eng, B. Zhao, Y. H. Zhuang, and A. Yariv, Appl. Phys. Lett. **63**, 2621 (1993).
[7] N. Chand, E. E. Becker, J. P. van der Ziel, S. N. G. Chu, and N. K. Dutta, Appl. Phys. Lett. **58**, 1704 (1991).
[8] A. Yu. Egorov, A. E. Zhukov, P. S. Kop'ev, N. N. Ledentsov, M. V. Maksimov, V. M. Ustinov, A. F. Tsatsul'nikov, N. A. Bert, A. O. Kosogov, D. Bimberg, Zh. I. Alferov, Fiz. Tekh. Poluprovodn. **30**, 1682 (1996) [Semiconductors **30**, (1996)].
[9] V. M. Ustinov, A. Yu. Egorov, A. E. Zhukov, N. N. Ledentsov, M. V. Maksimov, A. F. Tsatsul'nikov, N. A. Bert, A. O. Kosogov, P. S. Kop'ev, D. Bimberg, Zh. I. Alferov, in *Proceedings Vater. Research Society, Fall Meeting* (Boston, 1995), Paper EE3.6.
[10] N. N. Ledentsov, V. A. Shchukin, M. Grundmann, N. Kirstaedter, J. Bohrer, O. Schmidt, D. Bimberg, V. M. Ustinov, A. Yu. Egorov, A. E. Zhukov, P. S. Kop'ev, Zh. I. Alferov, A. I. Borovkov, A. O. Kosogov, S. S. Ruvimov, U. Gossele, and J. Heydenreich, Phys. Rev. Lett. (to be published).
[11] D. Bimberg, N. N. Ledentsov, N. Kirstaedter, O. Schmidt, M. Grundmann, V. M. Ustinov, A. Yu. Egorov, A. E. Zhukov, M. V. Maximov, P. S. Kop'ev, Zh. I. Alferov, S. S. Ruvimov, U. Gossele, and J. Heydenreich, in *Proceedings 1995 of the International Conference on Solid State Devices and Materials* (Osaka, 1995), p. 716.

Translated by Paul F. Schippnick

Modulation of a quantum well potential by a quantum-dot array

A. F. Tsatsul'nikov, A. Yu. Egorov, A. E. Zhukov, A. R. Kovsh, V. M. Ustinov, N. N. Ledentsov, M. V. Maksimov, A. V. Sakharov, A. A. Suvorova, P. S. Kop'ev, and Zh. I. Alferov

A. F. Ioffe Physicotechnical Institute, Russian Academy of Sciences, 194021 St. Petersburg, Russia

D. Bimberg

Institut für Festkörperphysik, Technische Universität Berlin, D-10623 Berlin, Germany
(Submitted April 3, 1996; accepted for publication April 8, 1996)
Fiz. Tekh. Poluprovodn. **31**, 109–113 (January 1997)

The possibility of locally varying the potential energy of the electrons and holes localized in a quantum well by a quantum-dot array deposited in the immediate vicinity of the quantum well is demonstrated. These changes in the potential energy are induced when a strain arises in the quantum-dot region. © *1997 American Institute of Physics.* [S1063-7826(97)02401-0]

Considerable attention in semiconductor physics has recently been given to the study of quantum dots (QD) of narrow-band materials in a wide-band matrix. The most promising method of obtaining quantum dots is spontaneous decay of a strained layer of a semiconductor material grown on the surface of another semiconductor material with different lattice constant. The properties of (In,Ga,Al)As islands on a (Ga,Al)As surface have been studied extensively.[1–5] The quantum dots obtained as a result are dislocation-free and are characterized by a high photoluminescence efficiency. Injection lasers based on (In, Ga)As quantum dots in a GaAs matrix with high temperature stability have been fabricated.[6,7]

In the present paper we investigate the possibility of locally varying the potential energy of the electrons and holes localized in an InGaAs quantum well (QW) with the help of an InAlAs quantum-dot array which is deposited in the immediate vicinity of the quantum well (the parameters of the investigated structures are listed in Fig. 1). Since for the chosen parameters the electron and hole levels in such quantum dots lie higher than in the quantum well,[4,5] recombination of nonequilibrium carriers takes place in the quantum well. Because of the effect of elastic strains caused by the mismatch of the lattice constants of the materials of the quantum dots and the barrier, and also because of a change in the height of the potential barrier near the quantum dots, a local variation in the potential energy of the carriers takes place in the regions of the quantum well near the quantum dots.

The investigated structures were grown by molecular beam epitaxy on GaAs (100) semiconducting substrates. A detailed description of the growth regimes is given, for example, in Ref. 3. The sequence of layers in the investigated structure (SQDW) is shown in Fig. 1. We also grew samples analogous to SQDW, but in which either the layer of dots was absent (SQW samples) or the quantum wells were absent (SQD samples) (Fig. 1). Photoluminescence was excited by an Ar^+ laser (wavelength $\lambda = 488$ nm) with excitation power density equal to ~ 150 W/cm^2 and was recorded by a cooled photomultiplier.

Figure 2 shows a planar image of quantum dots in an SQD structure, obtained by transmission electron microscopy (TEM). The TEM studies were carried out on a Philips EM420 electron microscope with an accelerating voltage of 100 keV. The quantum-dot array was observed in the [001] projection. The quantum dots had a characteristic size of $\sim 100-150$ Å and the array was distinguished by a high dot density $\sim 2\times 10^{11}$ cm^{-2}, which is significantly higher than the dot density of (In,Ga)As quantum dots on a GaAs surface.[3] In the SQDW structure the dot density is lower and stands at $\sim 1\times 10^{11}$ cm^{-2}. This may be connected with the different effective thickness of the $In_{0.5}Al_{0.5}As$ layer in the SQDW and SQD structures. At the same time, the character-

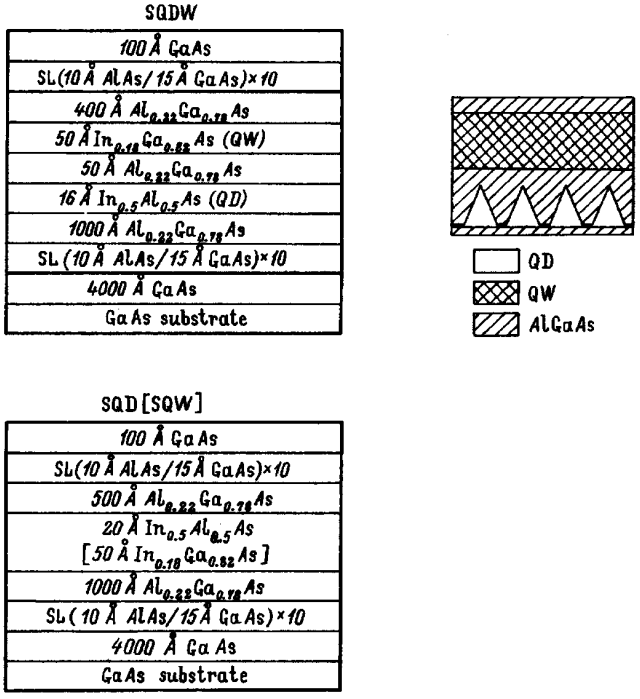

FIG. 1. Schematic representation of the sequence of layers in SQDW, SQD, and SQW structures. For the SQDW structure a schematic representation of the cross section of a layer with quantum dots (QD) and quantum wells (QW) is shown.

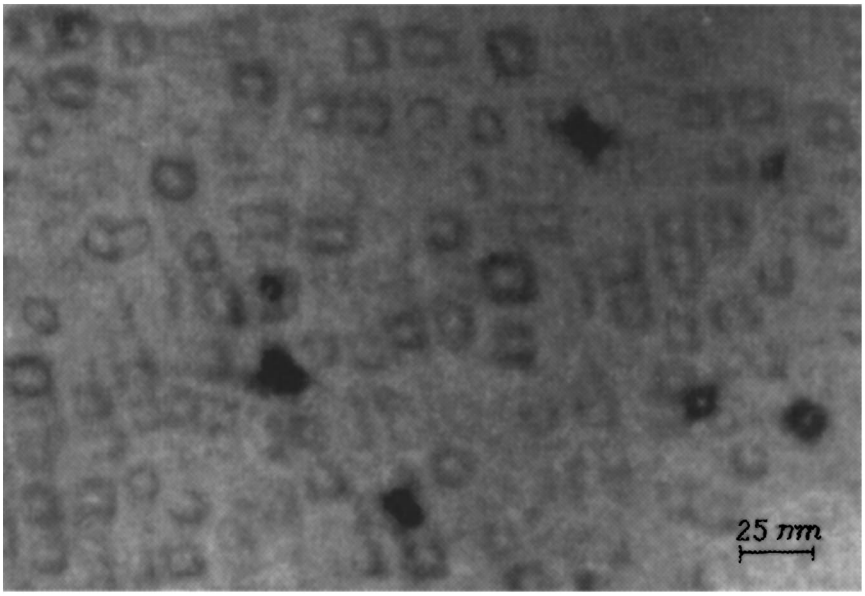

FIG. 2. Quantum dots (QD) shown in a SQD structure along the [100] direction, obtained by transmission electron microscopy.

istic size of the dots in SQDW differs only slightly from the size of the dots in the SQD structure.

Figure 3 presents the photoluminescence spectra of the investigated structures at $T=77$ K. As can be seen, in the spectrum of the SQD sample a wide line with a maximum near 1.57 eV, which is associated with recombination of nonequilibrium carriers through the quantum-dot states, is visible. The width of the line is ~100 meV, which is attributable to the spread in the sizes of the dots. In the spectrum of the SQDW structure, in addition to the QW line with a maximum at ~1.4 eV, which is observed in the spectrum of the SQW sample, a long-wavelength line QW_D with a maximum at ~1.35 eV is also present. The appearance of this band is due, in our opinion, to the recombination of carriers in the local minima of the potential in the QW plane, where these minima are associated with the presence of quantum dots in the immediate vicinity of the quantum well. Lowering the temperature to ~5 K leads to a drop in the QW line intensity and a shift of the QW_D line toward shorter wavelengths. Such behavior of the photoluminescence stems from the fact that there is a great spread in the localization energy of the carriers for different minima. At 77 K, the probability of thermal ejection of carriers from weakly localized states and their relaxation to deeper minima is increased. This accounts for the fact that the line which is associated with the recombination of carriers in these minima being the dominant line. An increase in the thermal ejection of carriers also causes an increase in the intensity of the QW line, which is associated with the recombination of nonequilibrium electrons and holes in the QW regions between the energy minima. Lowering the temperature to 5 K suppresses the rates of thermal ejection of carriers and increases the probability of recombination through the energy minima with low localization energy. This results in a significant decrease from the QW line intensity and an increase in the intensity from short-wavelength side of the QW_D band, which leads to a shift of the maximum toward higher energies.

Figure 4 shows spectra of the photoluminescence spectra of the SQDW structure, taken at different intensities of the exciting light and normalized to the photoluminescence intensity at the maximum of the QW line. As can be seen, lowering the excitation intensity leads to an increase in the intensity of the QW_D line relative to the intensity of the QW line. Figure 5a plots the dependence of the total intensity of the QW_D and QW lines on the intensity of the exciting light. The rate of saturation of the QW_D line intensity exceeds the rate of saturation of the QW line intensity; however, up to a power density of the exciting light ~150 W/cm^2 the QW_D line continues to predominate in the photoluminescence spectrum. An increase in the intensity of the exciting light causes a short-wavelength shift of the QW_D line and an in-

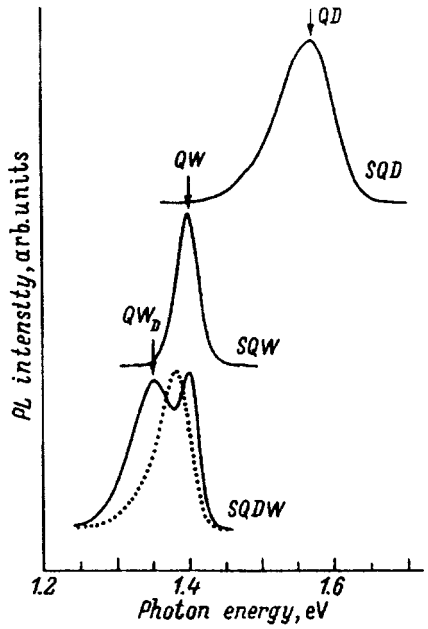

FIG. 3. Photoluminescence (PL) spectra of the examined structures. Power density of the exciting radiation is ~150 W/cm^2.

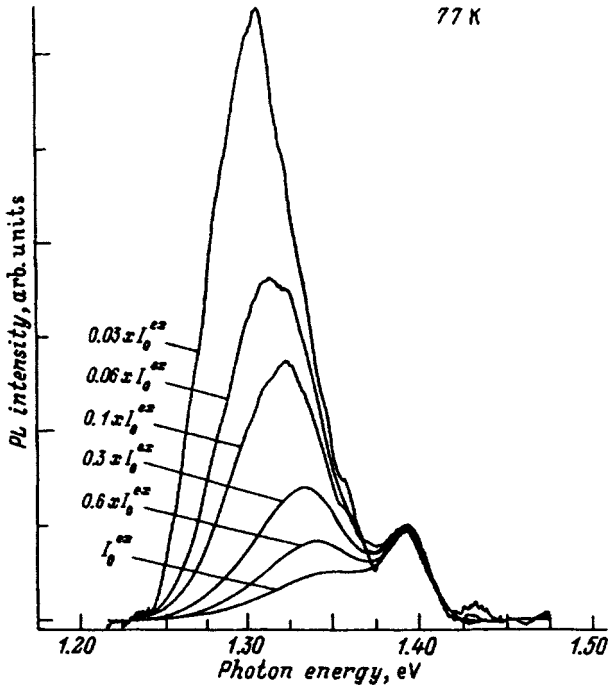

FIG. 4. Photoluminescence (PL) spectra of the SQDW structure at 77 K for different power densities of the exciting radiation I_0^{ex}. $I_0^{ex}=150$ W/cm^2.

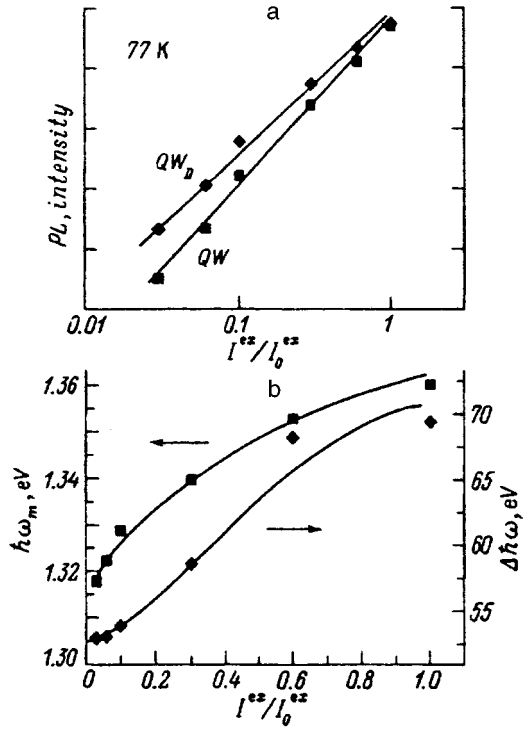

FIG. 5. Dependence of a) the total photoluminescence (PL) intensity of the QW_D and QW lines and b) the position of the maximum $\hbar\omega_m$ and the FWHM $\Delta\hbar\omega_m$ of the QW_D line on the power density of the exciting radiation I^{ex}/I_0^{ex}, $I_0^{ex}=150$ W/cm^2.

crease in its width (Fig. 5b). Such behavior of the photoluminescence is probably due to an increase in the recombination of nonequilibrium carriers through minima with lower localization energy, and also through possible excited states in the local energy minima.

Let us consider possible reasons for modulation of the QW potential. First, near the region of a quantum dot the height of the potential barriers for the electrons and holes is lowered. Let us estimate the possible change in the energy of an optical transition associated with a change in the quantum-well energy. Toward this end, we will use the approximation of a quantum well with walls of finite height, allowing for the difference in the effective electron and hole masses in the barrier and in the quantum well. The calculation of the effect of elastic strains on the band diagram was based on the analysis in Ref. 8. The parameter values used in the calculations for $In_{0.18}Ga_{0.82}As$ are given in Table I.[8–10] For an $In_{0.18}Ga_{0.82}As$ quantum well of 50 Å thickness, enclosed between $Al_{0.22}Ga_{0.78}As$ barriers, the width of the band gap allowing for the effect of deformation E_g^{strain} is equal to 1.307 eV, the quantum-well energy for the electrons E_e is equal to 77 meV, and for the heavy holes E_{hh} it is 25 meV. Thus, the energy of the optical transition, not allowing for the exciton binding energy E_{PL}, is equal to 1.409 eV, in good agreement with the experimental results. The maximum variation of the quantum-well energy can be estimated by assuming that near a quantum dot the width of the quantum well is ~100 Å. For an $In_{0.18}Ga_{0.82}As$ quantum well of width 100 Å $E_e'=32$ meV and $E_{hh}'=8$ meV. As can be seen from the calculation, the photoluminescence line shift associated with the change in the quantum-well energy in this case is $(E_e-E_e')+(E_{hh}-E_{hh}')\simeq 60$ meV. This value is smaller than the experimentally observed distance between the QW_D and QW lines, which for low excitation intensities is equal to ~80 meV. Such a considerable difference in the energies of the optical transitions is apparently due to the strong effect of the elastic distortions on the position of the energy levels near a quantum dot. A change in the energy levels of the InGaAs quantum well due to elastic deformation during deposition in the immediate vicinity of the quantum wells of the InP islands was observed in other studies.[11,12] We estimate the distance between the QW_D and QW bands by assuming that on the $Al_{0.22}Ga_{0.78}As$/

TABLE I. Values of the material constants.

Material	a_0, Å	C_{11}, 10^{12} dyn/cm^2	C_{12}, 10^{12} dyn/cm^2	a_c, eV	a_v, eV	b, eV	m_e^*/m_0	m_{hh}^*/m_0	m_{lh}^*/m_0
$In_{0.18}Ga_{0.82}As$	5.726	1.12	0.52	−6.92	1.13	−1.72	0.056	0.357	0.07
$Al_{0.22}Ga_{0.78}As$	5.653	–	–	–	–	–	0.078	0.371	0.088

Note: C_{11} and C_{12} are elastic constants; a_0 is the lattice constant; a_c, a_v, and b are the deformation potential constants; and m_e^*, m_{hh}^*, and m_{lh}^* are the effective masses of the electron and of the heavy and light holes.

$In_{0.18}Ga_{0.82}As$ heteroboundary near a quantum dot the barrier lattice constant corresponds to the lattice constant of bulk $In_{0.5}Al_{0.5}As$ ($a_0' = 5.859$Å). Since a_0' exceeds the lattice constant of $In_{0.18}Ga_{0.82}As$, a sign change takes place in the relative deformation in comparison with the unstrained $Al_{0.22}Ga_{0.78}As/In_{0.18}Ga_{0.82}As$ heteroboundary; i.e., a tensile stress acts on a quantum well near a quantum dot. It should be noted that in this case the light-hole state becomes the ground state for the hole. The width of the $In_{0.18}Ga_{0.82}As$ band gap, allowing for the elastic deformation, is $(E_g^{\text{strain}}) = 1.017$ eV, the quantum-well energy of the electron is $E_e' = 103$ meV, the light hole energy is $E_{lh}'' = 74$ meV, and the energy of the optical transition is $E_{\text{PL}}'' \simeq 1.2$ eV. The obtained value of E_{PL}'' significantly differs from the experimentally observed position of the QW_D line and is an upper bound on the possible variation of the energy of the optical transition since we have assumed that in a large region of the barrier near the dots the material has the lattice constant of $In_{0.5}Al_{0.5}As$ and does not vary after deposition of the quantum well. However, the lattice constant of the barrier can be equal to an intermediate value between the lattice constants of GaAs and $In_{0.5}Al_{0.5}As$, which leads to less significant variation of the potential energy of the electrons and holes. We also ignored the effect of the shape of the quantum dots and the exciton bond energy on the energy levels. In addition, differences in the lattice constant on different segments of the surface before deposition of the InGaAs layer can also lead to the formation near the quantum dots of InGaAs regions with high indium content in the layer. All these factors also affect the energy of the optical transitions.

In summary, we have shown that deposition of an InAlAs quantum-dot array in the immediate vicinity of an $In_{0.18}Ga_{0.82}As$ of 50 Å width leads to a local decrease in the potential energy of the electrons and holes near a quantum dot. As our estimates show, this change probably is mainly due to the effect of elastic strain arising in the region of the quantum dot.

This work in different parts was supported by the Russian Fund for Fundamental Research (Grant No. 96-02-17824), the Volkswagen Fund, and a grant from INTAS (Grant No. 94-1028).

[1] L. Goldstein, F. Glass, J. Y. Marzin, M. N. Charasse, and G. Le Roux, Appl. Phys. Lett. **47**, 1099 (1985).
[2] P. M. Petroff and S. P. Den Baars, Superlattices Microstruct. **15**, 15 (1994).
[3] N. N. Ledentsov, M. Grundmann, N. Kirstaedter, O. Schmidt, R. Heitz, J. Böhrer, D. Bimberg, V. M. Ustinov, V. A. Shchukin, A. Yu. Egorov, A. E. Zhukov, S. V. Zaitsev, P. S. Kop'ev, Zh. I. Alferov, S. S. Ruvimov, A. O. Kosogov, P. Werner, U. Gösele, J. Heydenreich, Solid–State Electronics **40**, 785 (1996).
[4] S. Fafard, R. Leon, D. Leonard, J. L. Merz, and P. M. Petroff, Phys. Rev. B **50**, 8086 (1994).
[5] S. Fafard, R. Leon, D. Leonard, J. L. Merz, and P. M. Petroff, Phys. Rev. B **52**, 5752 (1995).
[6] Zh. I. Alferov, N. A. Bert, A. Yu. Egorov, A. E. Zhukov, P. S. Kop'ev, A. O. Kosogov, I. L. Krestnikov, N. N. Ledentsov, A. V. Lunev, M. V. Maksimov, A. V. Sakharov, V. M. Ustinov, A. F. Tsatsul'nikov, Yu. M. Shchernyakov, and D. Bimberg, Fiz. Tekh. Poluprovodn. **30**, 351 (1996) [Semiconductors **30**, 194 (1996)].
[7] Zh. I. Alferov, N. Yu. Gordeev, S. V. Zaĭtsev, P. S. Kop'ev, V. V. Komin, I. L. Krestnikov, N. N. Ledentsov, A. V. Lunev, M. V. Maksimov, S. S. Ruvimov, N. A. Bert, A. Yu. Egorov, A. E. Zhukov, A. V. Sakharov, and A. F. Tsatsul'nikov, Fiz. Tekh. Poluprovodn. **30**, 357 (1996) [Semiconductors **30**, 197 (1996)].
[8] M. P. C. Krijn, Semicond. Sci. Technol. **6**, 27 (1991).
[9] S. Adachi, J. Appl. Phys. **53**, 8775 (1982).
[10] S. H. Pan, H. Shen, Z. Hang, F. H. Pollak, W. Zhuang, Q. Xu, A. P. Roth, R. A. Masut, C. Lacelle, and D. Morris, Phys. Rev. B **38**, 3375 (1988).
[11] M. Sopanen, H. Lipsanen, and J. Abopelto, Appl. Phys. Lett. **66**, 2364 (1995).
[12] M. Sopanen, H. Lipsanen, and J. Abopelto, Phys. Rev. B **51**, 13868 (1995).

Translated by Paul F. Schippnick

Cathodoluminescence of $p-n-p$ microstructures in $CuInSe_2$ crystals

S. G. Konnikov, G. A. Medvedkin, M. M. Sobolev, and S. A. Solov'ev

A. F. Ioffe Physicotechnical Institute, Russian Academy of Sciences, 194021 St. Petersburg, Russia
(Submitted April 26, 1996; accepted for publication May 22, 1996)
Fiz. Tekh. Poluprovodn. **31**, 114–119 (January 1997)

Microstructures in p–$CuInSe_2$ single crystals tailored by the strong electric field have been studied using the method of local ($d \leqslant 1\ \mu$m) cathodoluminescence (CL). The shortest-wavelength radiation ($\hbar\omega = 1.023$ eV) has been observed from the n-type layer and longer-wavelength radiation ($\hbar\omega = 1.006$ eV)—from the p-type regions. An analysis of the cathodoluminescence spectra has allowed us to attribute the experimental features to optical transitions associated with donor and acceptor levels of V_{Cu}, V_{Se}, and Cu_i point defects in the crystal. Test measurements of EBIC, the $C-V$ characteristics, and the DLT spectra confirm the cathodoluminescence data and reveal additional features of the $p-n-p$ microstructures. © *1997 American Institute of Physics.* [S1063-7826(97)02501-5]

1. INTRODUCTION

The electronic and optical properties of $CuInSe_2$ crystals are mainly determined by point defects associated with the individual atoms forming the ternary compound. The chemical nature of each chemical element entering into the makeup of a semiconductor, as well as the chemical nature of the material as a whole, determines the stability of the compound to external factors such as a strong electric field. The diamond-like lattice of $CuInSe_2$, like that of other ternary compounds of the diamond-like series, plays a key role in the high stability of these semiconductor materials.[1] However, as a consequence of the significant polar component in the ionic–covalent bonds of these compounds, they should also exhibit some ionic conductivity, for example, in a strong electric field. If we compare $CuInSe_2$ and HgCdTe with the (not diamond-like) chalcogenide material Cu_xSe, which has also been successfully used in photovoltaic applications, then we may discover a significantly smaller ionic component in the electric current for the compounds of the diamond-like series.[2–5]

The recent discovery and comprehensive study of weak ionic conductivity in ternary chalcogenides[6,7] has underscored the important role of copper ions (and silver ions), and also V_{Cu} (and V_{Ag}) vacancies in the electronic and electrochemical properties of $CuInSe_2$, $AgInSe_2$ and $(Cu,Ag)InSe_2$. In particular, a tendency has been demonstrated for the diffusion coefficient of the Cu^+ ions to increase (all the way to 10^{-7}cm^2/s) when the concentration of the IB metal is decreased in copper-poor crystals of $CuInSe_2$.

2. STABILITY OF THE ELEMENTS IN $CuInSe_2$

Let us consider briefly the effect of each chemical element in $CuInSe_2$ on the stability of the compound as a whole and from the viewpoint of the effect of strong external forces on its properties. (1). It is well known that copper diffuses strongly in a $CuInSe_2$ crystal in the presence of a strong electric field, i.e., it participates in ionic drift (with a coefficient of chemical diffusion as high as 10^{-7}cm^2/s). (2). It is also well known that indium provides a factor of stability for $CuInSe_2$ in processes associated with the strong effects of temperature, electric field, and oxidants. (3). At the same time, selenium is the lightest component of this ternary compound and does not guarantee stability in the presence of strong physical or chemical agents.

These three statements are supported by the following facts.

1. First, ionic conductivity occurs, in particular, because of Cu^+ ions;[2,6,7] second, copper has a small covalent radius,[8] and, third, the highest diffusion coefficient was identified in copper-poor samples.[2] *Conclusion*: diffusion of Cu^+ ions is large in $CuInSe_2$ and proceeds preferentially by a vacancy mechanism.[2] Copper, as a chemical element, does not lend stability to $CuInSe_2$.

2. Second, indium is strongly oxidized, in comparison with the other elements, in thermal oxidation processes;[9–11] second, indium has a large covalent radius, 0.144 nm, and a large atomic weight, 114.82 a.m.u. (compare Cu–In–Se: 0.135–0.144–0.114 nm/63.55–114.82–78.96 a.m.u.);[8] third, in substitution reactions indium displaces copper, e.g., $Cu_2O + In \rightarrow In_2O_3 + Cu$;[12] and, fourth, indium forms more-covalent bonds than copper and selenium in diamond-like semiconductors; i.e., indium is found closer to the axis of the periodic table and participates in the formation of more-covalent and less-ionic diamond-like compounds than copper and selenium.[1] *Conclusion*: indium is the stabilizing element in $CuInSe_2$.

3. Third, there is the higher vapor pressure of selenium (10^{-3} Pa at $T = 100$ °C) in comparison with the vapor pressures of copper and selenium, which are negligible at $T = 100$ °C. At $T = 550$ °C the vapor pressure of copper is $< 10^{-9}$ Pa, and of indium, 10^{-5} Pa, and selenium, 10^{-4} Pa;[13] in addition, heat processing of $CuInSe_2$ crystals and films in vacuum leads to surface selenium depletion;[14] furthermore, selenium has the smallest covalent radius, 0.114 nm, and a low atomic weight. *Conclusion*: selenium does not give stability to $CuInSe_2$ and selenium diffusion should increase radically with temperature, as well as in a strong electric field.

A strong electric field in the crystal creates radically nonequilibrium conditions for the mobile charge carriers (e,h) and the low-mobility carriers (Cu^+ and Se^{2-} ions and

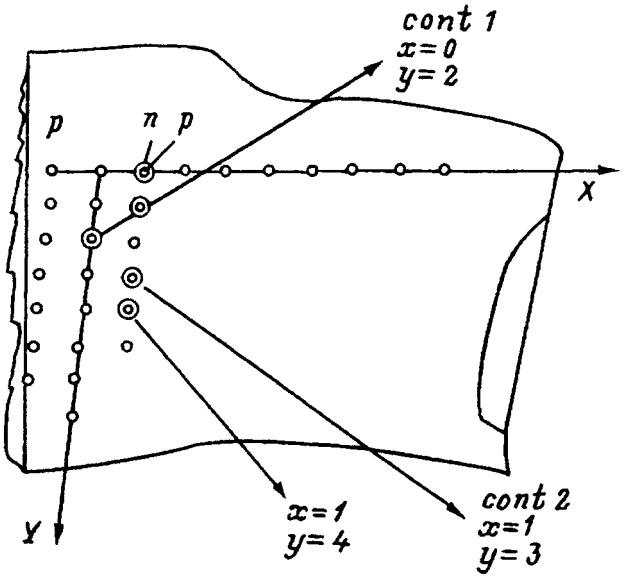

FIG. 1. Sample of a $CuInSe_2$ single crystal with linear arrays of gold contacts and $p-n-p$ microstructures formed by a strong field. CL and EBIC were measured at the point $(x,y)=(1.0,0.2)$. The $C-V$ characteristic and DLTS were measured at points 2 and 3: $(x,y)=(0.2,1.1)$.

V_{Cu} and V_{Se} vacancies). Taking into account elemental stability and ion migration, both of which have been studied for the chalcogenides,[2] it is possible to imagine two stages in the process of the action of an electric field on a $CuInSe_2$ crystal: 1) an electric stage (consisting mainly of Cu^+ ion transport) and 2) a Joule (thermal) stage, when Se^{2-} ion transport also kicks in.

The Se^{2-} ion transport intensifies with increasing heat liberation. In a region with enhanced resistivity, a large amount of heat will be liberated and more and more selenium atoms will abandon their lattice sites. The Se^{2-} ions will drift in the counter direction to the Cu^+ ions along the force lines of the electric field. It is also possible to speak of a movement of V_{Cu} and V_{Se} vacancies if we consider them as charged point defects.

3. EXPERIMENTAL PART

To a first approximation we may consider there to be two subsystems of acceptor- and donor-type point defects present in the crystal simultaneously. A strong external electric field applied to the gold point contacts on the sample acts on these two different types of point defects differently. The most mobile point defects, i.e., the interstitial atoms, vacancies of the intrinsic elements, etc. participate in weak ionic conduction leading to the formation of the concentration profile and layers which are depleted in one or another type of ligand. In order to estimate the predominance of the dopant point defect in each layer, we measured the micro-cathodoluminescence at the $C-V$-characteristics in Au/$p-n-p$ structures fabricated on single-crystal p-$CuInSe_2$ samples. The samples were prepared at the Weizmann Institute of Science in the laboratory of Professor David Cahen (Fig. 1).

A. Study of local cathodoluminescence

The experimental conditions for obtaining local cathodoluminescence (CL) spectra were the following: temperature 78–80 K, energy of the electron beam 10–15 keV, beam current 50–100 nA, exciting spectral region 0.6–1.0 μm. The cathodoluminescence emitted from the micro-region was collected by mirror optics, after which it was transmitted via an achromatic infrared light guide to an MDR-23 spectrophotometer. To detect the signal, we used a synchronous output amplifier (modulation frequency 10 kHz) and cooled germanium detector (EO-817, sensitivity 5×10^9 V/W). The spectral resolution of the setup was better than 3 meV.

The local cathodoluminescence spectra were measured for three different types of micro-regions. 1) The electron beam excited a region near the gold point contact or fell directly on the 20-nm metallic layer and excited luminescence from under the contact. In both cases the emitted infrared radiation gave an identical spectral distribution and originated from the p-type layer. 2) The electron beam excited the n-type layer, i.e., the region around the gold contact, adjacent to the above-mentioned p-type layer. Since the shape of the boundary of the $n-p$-junction in some of the $p-n-p$ structures was not ideally spherical, we performed additional alignment within this micro-region so that the electron beam excited the point with the shortest-wavelength cathodoluminescence maximum. 3) The electron beam excited the p-type region far from the gold contacts, i.e., the radiation originated from the interior of the single crystal.

The measurements performed with the electron beam positioned within micro-regions of types 1, 2, and 3 were equivalent or similar to one another within the limits of experimental accuracy. Note that for some structures it was not possible to reliably record the presence of the thin p-type layer adjacent to the metal, and in this case aided by CL or EBIC measurements it was possible only to observe the $n-p$ junction. In addition, evidence for a diode-type $n-p$ structure was found in the $C-V$ characteristics at room temperature, while at low temperatures a transistor-type $p-n-n$ structure was recorded. Figure 2 presents cathodoluminescence spectra for the three above-indicated $p-n-p$ structures. The shape of the spectral bands differs markedly for these three regions, but they are all relatively wide: the full width at half-maximum (FWHM) averages out to 50–70 meV, which is characteristic of level–band and level–level transitions. The broadening of the short-wavelength tail to energies exceeding the band gap $E_g=1.04$ eV in $CuInSe_2$ is due to the high level of electron pumping in the cathodoluminescence measurements.

Analysis of the luminescence spectra shows them to be nonelementary and allows us to separate them into two separate bands. The main band reaches its maximum in the short-wavelength region for the n-type layer while the main peaks for the p-type layer and the base p-type type crystal are found to lie in the long-wavelength region. The spectral features of these bands are characterized briefly in Table I. The intensity of the infrared radiation from the p-type layer adjoining the metal contact was several times lower than from the n-type layer or from the p-type type bulk crystal. This probably has to do with the more defective microstructure of

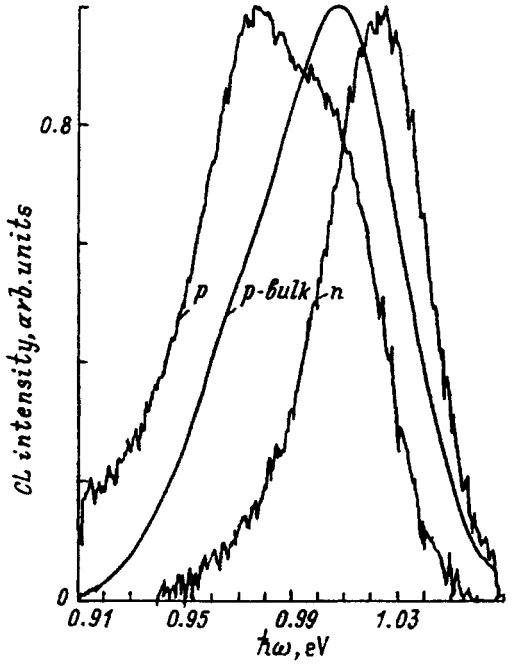

FIG. 2. Cathodoluminescence spectra for $p-n-p$ microstructures at $T=80$ K.

the layers adjoining the gold contact and the enhanced concentration of defects formed as a result of application of a strong electric field. As a result, the appearance of nonradiative recombination centers leads to a drop in the luminescence quantum yield in the p-type layer.

The radiative transition with photon energy 1.006 eV may be associated with an acceptor level lying 34 meV above the $CuInSe_2$ valence band. Indeed, the presence of a shallow acceptor level in the crystal was indicated by our $C-V$-measurements (see below). The thermal activation energy differs from the optical activation energy by several meV and in our measurements was equal to $E_{\text{therm}}=25$ meV, and the concentration of the corresponding states was approximately 10^{17} cm^{-3}. These acceptor states can be assigned to copper vacancies, which are located 35–45 meV above the edge of the valence band.[15] At the same time, there is also another radiative transition, which probably occurs through the V_{In} and Cu_{In} defect levels, whose activation energies are nearly the same. The long-wavelength extremum indicates the presence of a deeper level with an optical activation energy of 65 meV, which can be assigned to several types of point defects: V_{Se}, Cu_i, Se_i, and Cu_{In}. However, basing ourselves on the foregoing discussion of the stability of the chemical elements in $CuInSe_2$, we think that the most probable candidates are the donor defects V_{Se} and Cu_i.

TABLE I. Spectral features of the CL spectra for three regions of the $p-n-p$ structure and corresponding point defects.

Region	Peak energy, eV	E_{act}, meV	Type of point defect
p-crystal	1.006	34	A: V_{Cu}, V_{In}, Cu_{In}
	0.975 (shoulder)	65	A: Se_i, Cu_{In}; D: V_{Se}, Cu_i
n-layer	1.023	17	D: In_{Cu}, V_{Se}
	0.99 (limb)	41	D: In_{Cu}; A: V_{Cu}, Cu_{In}
p-layer	1.006 (knee)	34	A: V_{Cu}, V_{In}, Cu_{In}
	0.975	65	A: Se_i, Cu_{In}; D: V_{Se}, Cu_i
	0.92 (limb)	120	A: Se_i

TABLE II. Two-band fitting parameters of cathodoluminescence spectra and radiative transitions in a $CuInSe_2$ $p-n-p$-structure.

Region	Peak energy, eV	FWHM, meV	$I/I_{\max}$	Transitions
p-crystal	1.013	51	0.77	$CB\rightarrow V_{\text{Cu}}$ $(A3)$
				$\text{CB}\rightarrow\text{CuIn}$, V_{In}
	0.978	61	0.45	$\text{In}_{\text{Cu}}\rightarrow V_{Cu}$
				$\text{In}_{\text{Cu}}\rightarrow\text{Cu}_{\text{In}}$, V_{In}
				$(V_{Se}\rightarrow VB)*$
n-layer	1.024	40	0.80	V_{Se}, $\text{In}_{\text{Cu}}\rightarrow VB$
p-layer	1.003	60	0.25	$CB\rightarrow V_{\text{Cu}}$, Cu_{In}
	1.015	28	0.25	$CB\rightarrow V_{\text{Cu}}$ $(A3)$
				$CB\rightarrow\text{Cu}_{\text{In}}$, V_{In}
	0.979	65	0.97	$\text{In}_{\text{Cu}}\rightarrow V_{\text{Cu}}$
				$\text{In}_{\text{Cu}}\rightarrow\text{Cu}_{\text{In}}$, V_{In}
				$(V_{\text{Se}}\rightarrow VB)$*
p-type (without fitting)	0.92	-	0.10	$CB\rightarrow\text{Se}_i$ $(V_{\text{Se}}\rightarrow VB)$

*_Note_: The transition in parentheses is either insignificant or weak.

The radiative band for the n-layer is shifted toward shorter wavelengths and has a peak at 2.023 eV and a spectral limb with a feature at 0.99 eV. These optical transitions may be associated with the substitution defect levels In_{Cu} and Cu_{In} or with the acceptor level V_{Cu}.

The radiative band for the p-layer, in comparison with the foregoing cases, is broadened toward longer wavelengths and exhibits a spectral feature in the form of a limb at 0.92 eV. The corresponding optical transitions may be associated with a deep level of interstitial selenium whose concentration is not as large as that of the point defects Cu_i, V_{Cu}, and V_{Se}, which give stronger luminescence.

From a comparison of the spectra it follows that such intense radiative transitions are present in the original p-type substrate and in the electric, field-induced p-type layer. In addition, in this p-layer a long-wavelength limb also appears, which is characteristic of Se_i defects. As a result of the high level of electron pumping, the cathodoluminescence spectra are broadened into the region of high photon energies, e.g., in comparison with the photoluminescence spectra in Ref. 5, although many spectral features of cathodoluminescence are the same as those of photoluminescence. The short-wavelength edge in our cathodoluminescence spectra is well fit by a Gaussian distribution. For this reason we used Gaussian fitting curves to separate the experimental spectra into the two above-mentioned elementary bands. The band fitting parameters are listed in Table II. All maxima of the fitted bands are found to be in good agreement with the main peaks and the spectral features in the experimental curves (Fig. 1). The data in Tables I and II reveal, on the one hand, distinct spectral differences between the n-layer and the p-regions and, on the other, a similarity between the p-layer and the p-substrate. This fact indicates that the very

same point defects are responsible for radiation in p-type material, irrespective of its nature, but the application of a strong electric field leads to the appearance of additional point defects of the Se_i type in the p-type layer.

Scanning an electron beam across the structure traced out the variation of the relative amplitude of the two main cathodoluminescence bands for the scan p-layer $\rightarrow$ n-layer $\rightarrow$ p-substrate. However, as a consequence of the high sensitivity of the technique to microdamage (artifacts) of the crystal surface, which caused the pump power and luminescence yield to vary, the continuous scan measurements did not always give the correct result. Obviously, better results can be obtained on a transverse cleavage of the structure and by systematic continuous scan measurements. The difference in the spectral position of the bands highlights differences in the nature of the point defects in the n- and p-type regions. Guided by the review in Ref. 15 for the donor and acceptor ionization energies, we have attributed specific radiative transitions to our cathodoluminescence data (Table II). We think, however, that only some of the types of listed defects can be considered as real candidates for these strong electric field-processed structures.

First of all, copper vacancies predominate in the bulk crystal while interstitial copper atoms and selenium vacancies predominate in the n-type layer. This accords well with earlier studies of ion migration and the action of an electric field on the electronic properties of these crystals.[2,3,6,7] Second, interstitial selenium atoms appear in the p-type layers in addition to copper vacancies and In_{Cu} substitution defects. This also accords with the above discussion of elemental stability.

B. EBIC measurements

Measurements of an electron-beam-induced current (EBIC) were made to characterize the boundaries of the $n-p$-type junctions in the prepared structures. They demonstrate the existence of one or two junctions with oppositely directed internal electric fields. Two junctions are observed, but not always distinctly and not for every scan. The EBIC profile exhibits a significantly drawn-out falloff of the current amplitude as the electron beam is scanned across the $n-p$ junction. The effective diffusion length, estimated to be >10 μm, exceeds the actual diffusion length L_{diff} in homogeneous $CuInSe_2$ by more than an order of magnitude.[16] It is well known that such behavior is observed for the corresponding dopant profiles, which are characteristic of a diffusion-type $n-p$ junction or a layer of space charge because of the ''frozen'' ions and charged vacancies.

4. $C-V$ AND DLTS MEASUREMENTS

Capacitance–voltage ($C-V$) characteristics and deep-level transient spectroscopy (DLTS) were employed to investigate $CuInSe_2$ $p-n-p$ structures in the temperature range 430–82 K. The $C-V$ measurements were made at voltages of both polarities from 0.0 to 7.8 V at 100 kHz. The curves so obtained in the coordinates $(1/C^2)-V$ exhibit a nearly linear dependence, which indicates an abrupt $n-p$ junction. The general characteristic feature—the temperature dependence of the capacitance—is typical of all the measured junctions. The capacitance was found to increase as the temperature was raised. The capacitance increased only slightly as a function of the reverse bias applied to the sample. This behavior can be attributed to the presence of states at the interface distributed deep into the band gap or to the localized states of deep levels in the region of the $n-p$ junction.

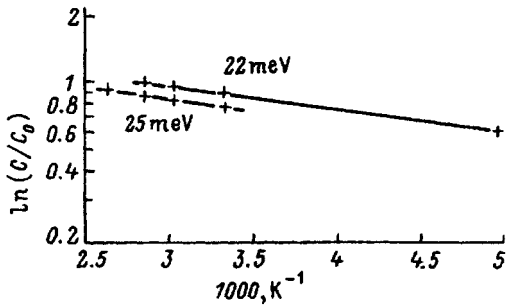

FIG. 3. Temperature dependence of the capacitance of an $n-p$ transition for microstructures 2 (25 meV) and 3 (22 meV).

The concentration of these states is comparable with the concentration of free charge carriers in the bulk crystal and is close to 10^{17}cm^{-3}. The thermal activation energy of the carriers from these states was determined from the relation $C=C_0\exp(-E_a/kT)$ at zero bias $u_0=0$. Independent measurements on the two gold contacts give the values 22 and 25 meV (Fig. 3). The activation energy characterizes the position of the Fermi level if it is assumed that distributed states exist at the interface, and it characterizes the localization energy if localized states exist there. The thermal activation energy characterizes the levels of the V_{Cu} point defects, which have an ionization energy of 30–35 eV, according to the photoluminescence data.[15]

We examined the behavior of the $C-V$ curves for $CuInSe_2$ $p-n-p$ structures for both biases. Diode-type characteristics were obtained only at room temperature. Lowering the temperature transforms the $C-V$ branches in such a way that they become mirror-symmetric for reverse bias at liquid-nitrogen temperature. This suggests a transistor-type structure at low temperatures. Such a transformation of the structure can be explained by the ''switching on'' of deep metastable acceptor levels[17] as a result of lowering of the Fermi level and a change in the degree of donor–acceptor compensation, which leads to a change in the type of conductivity in the highest-resistivity region of the microstructure. Obviously, this acceptor level can be attributed to a definite type of point defect, e.g., Se_i with activation energy $E_{\text{act}}=120$ meV (Table I).

DLTS measurements were performed for one of the $CuInSe_2$ $p-n-p$ structures. The DLTS spectra yielded the thermal emission energy from the deep donor level $E_{\text{em}}=171$ meV and the charge-carrier capture cross section $\sigma_e=2.08\times10^{-19}\text{cm}^2$ for this level. The level is distributed over the entire volume of the $CuInSe_2$ single crystal and its concentration is estimated to be 5×10^{15} cm^{-3}.

5. CONCLUSIONS

Studies of cathodoluminescence of $p-n-p$ microstructures in $CuInSe_2$ crystals show that the emission and spectral makeup of the original bulk p-crystal is markedly different from that of the n- and p-layers formed by a strong electric field. The postulated types of point defects agree with a previous study of ion migration and with the discussion of chemical elemental stability presented at the beginning of this article. EBIC, $C-V$, and DLTS test measurements reveal the characteristic features of the fabricated structures and confirm the cathodoluminescence measurement results.

This work was supported, in particular, by the International Rich Foundation, Paris. The authors express their gratitude to Professor D. Cahen of the Weizmann Institute of Science for providing samples.

[1] N. A. Goryunova, *Composite Diamond-like Semiconductors* [in Russian], Sovetskoe Radio, Moscow, 1968.
[2] G. Dagan, T. F. Ciszek, and D. Cahen, J. Phys. Chem. **96**, 11 009 (1992).
[3] K. Gartsman, L. Chernyak, J. M. Gilet, D. Cahen, and R. Triboulet, Appl. Phys. Lett. **61**, 2428 (1992).
[4] M. Savelli, J. Bougnot, F. Guastavino, J. Marucchi, and H. L. Luquet, *Solar Energy Conversion Solid-State Physics Aspects*, edited by B. O. Seraphin (Springer Verlag, Berlin, 1979), Ch. 5, p. 189.
[5] R. Hill and J. D. Meakin, *Current in Photovoltaics*, edited by T. J. Coutts and J. D. Meakin (Academic Press, London, 1985), Ch. 5, Sec. 5.5 Cell Stability, p. 286.
[6] A. Jakubowicz, G. Dagan, C. Schmitz, and D. Cahen, Adv. Mater. **4**, 741 (1992).
[7] D. Cahen, J.-M. Gilet, L. Chernyak, K. Gartsman, and A. Jakubowicz, Science **258**, 271 (1992).
[8] C. Kittel, *Introduction to Solid State Physics*, 5th Ed. (Wiley, New York, 1976).
[9] M. E. Boiko and G. A. Medvedkin, in *Proceedings of the First World Conference on Photovoltaic Energy Conversion*, Waikoloa, Hawaii, Dec. 5–9, 1994, IEEE, 1995, Vol. 1, p. 258.
[10] G. A. Medvedkin, R. A. Bekimbetov, T. L. Makarova, A. D. Smirnova, and V. I. Sokolova, Zh. Tekh. Fiz. **57**, 960 (1987) [Sov. Phys. Tech. Phys. **32**, 583 (1987)].
[11] G. A. Medvedkin, R. A. Bekimbetov, and A. A. Yakovenko, A. S. SSSR No. 1321141 (Priority 10 June, 1985).
[12] G. A. Medvedkin, G. A. Ambrazyavichyus, and A. A. Yakovenko, Poverkhnost'. Fizika, Khimiya, Mekhanika, No. 2, 81 (1987).
[13] *Handbook of Thin-Film Technology*, edited by L. I. Maissel and R. Glang (McGraw–Hill, New York, 1970), Pt. I.
[14] L. L. Kazmerski, M. Hallerdt, P. J. Ireland, R. A. Mickelsen, and W. S. Chen, J. Vac. Sci. Technol. A **1**, 395 (1983).
[15] G. Dagan, F. Abou-Elfotouh, D. J. Dunlavy, R. J. Matson, and D. Cahen, Chem. Mater. **2**, 286 (1990).
[16] L. L. Kazmerski and S. Wagner, ''Solar Cells on Ternary Cu-Compounds with Calcopyrite Structure,'' Ch. 2, in *Current Topics in Photovoltaics*, edited by T. J. Coutts and J. D. Meakin (Academic Press, London, 1985), p. 62.
[17] P. M. Mooney and T. N. Theis, Commun. Condens. Matt. Phys. **16**, 167 (1992).

Translated by Paul F. Schippnick